Block Copolymer Nanocomposite Membranes for CO_2 Separation

Dissertation with the aim of achieving a doctoral degree (Dr. rer. nat.)

Institute of Physical Chemistry, Department of Chemistry

University of Hamburg

Submitted by

Md. Mushfequr Rahman

Hamburg, 2014

This study was conducted between February 2011 and July 2014 at the Institute of Polymer Research, Helmholtz-Zentrum Geesthacht under the supervision of Prof. Dr. Volker Abetz.

Prof. Dr. Volker Abetz (First reviewer)

Prof. Dr. Horst Weller (Second reviewer)

Date of Oral Defense: 19.12.2014

Table of Content

List of Figures …… v
List of Tables ……. x
List of Scheme ……... xi
List of Symbol …… xi
List of Abbreviations ……. xiii

Part – A:
Chapter 1. Introduction ……..……. 1
1.1. Objective ……. 2
1.2 Poly(ethylene oxide) based membranes for CO_2 separation …… 5
1.3 Strategy of the research and outline of the thesis ……. 7

Part – B:
Chapter 2. Theoretical Framework ……..……... 10
2.1. Fundamental of gas separation process ……... 11
2.1.1. Gas separation membranes ……. 11
2.1.2. Solution-diffusion model ……... 12
2.1.3. Gas sorption and diffusion in glassy and rubbery polymer membranes …… 14
2.1.4. Gas transport through semicrystalline polymers …… 18
2.1.5. Influence of temperature on transport parameters …….. 20
2.2. Block copolymers & block copolymer nanocomposites ……. 22
2.2.1. Block copolymer …….. 22
2.2.2. Block copolymer nanocomposites ……... 25

Part - C:
Chapter 3. Experimental ……..…… 29
3.1. Materials …….. 30
3.2. Functionalization of nanoparticles …….. 30
3.2.1. Functionalization of POSS ……. 30
3.2.1.1. Grafting methoxy poly(ethylene glycol) (Mn = 350) via epoxide ring opening reaction ....…….. 30
3.2.1.2. Acylation & Mesylation of PEG grafted POSS nanoparticles ……... 31
3.2.1.3. Azidation of PEG grafted POSS nanoparticles …….. 32
3.2.2. Functionalization of MWCNT ……... 32
3.2.2.1. Oxidation of MWCNT ……... 32
3.2.2.2. Chlorination of oxidized MWCNT …… 32

3.2.2.3. Grafting poly(ethylene glycol) to the chlorinated MWCNT via esterification…….. 33
3.3. Preparation of nanocomposite membranes ……. 33
3.3.1. PEG functionalized POSS incorporated PEBAX® membrane …….. 33
3.3.2. PEG functionalized POSS incorporated PolyActive™ membrane …… 34
3.3.3. PEG functionalized MWCNT incorporated PEBAX® membrane ……. 34
3.4. Characterization …….. 35
3.4.1. Time-lag method …… 35
3.4.2. Fourier transformation infrared spectroscopy (FT-IR) …… 36
3.4.3. Nuclear magnetic resonance spectroscopy (NMR) ……. 37
3.4.4. Raman spectroscopy …….. 37
3.4.5. Differential scanning calorimetry (DSC) ……. 37
3.4.6. Thermogravimetric analysis (TGA) …….. 38
3.4.7. Scanning electron microscopy (SEM) …….. 38
3.4.8. Atomic force microscopy (AFM) ……. 38

Part – D:

Chapter 4. PEBAX® with PEG functionalized POSS as nanocomposite membranes for CO_2 separation …….. 39
4.1. Introduction ……. 40
4.2. Results ……. 41
4.2.1. Chemical structure and composition ……. 41
4.2.2. Gas separation performance …….. 43
4.2.3. Thermal analysis ……... 54
4.2.4. Surface topography ……... 59
4.2.5. SEM and EDS analysis …….. 63
4.3. Discussion ……... 67
4.3.1. Correlation between thermal and gas separation properties …….. 67
4.3.2. Correlation between surface topography and gas separation properties …… 69
4.4. Conclusion …….. 70
Chapter 5. Influence of poly(ethylene glycol) segment length on CO_2 permeation and stability of PolyActive™ membranes and their nanocomposites with PEG POSS® …. 71
5.1. Introduction ……. 72
5.2. Results ……. 73
5.2.1. Composition of three grades of PolyActive™ ……... 73
5.2.2. Thermal characterization …… 76
5.2.3. Gas separation performance ……... 81
5.2.3.1. CO_2 permeation ……. 81
5.2.3.2. CO_2 selectivity over light gases …… 85
5.2.4. Morphology …… 89
5.3. Discussion ……... 95

5.4. Conclusion …….. 99
Chapter 6. Functionalization of POSS nanoparticles and fabrication of block copolymer nanocomposite membranes for CO_2 separation …… 101
6.1. Introduction ……. 102
6.2. Results & Discussion …….. 103
6.2.1. Modification of glycidyl POSS® and glycidyldimethylsilyl POSS® with methoxy poly(ethylene glycol) …….. 103
6.2.2. Influence of solvent upon the structure of functionalized POSS nanoparticles ……... 106
6.2.3. Gas separation performance of the nanocomposite membranes …… 113
6.4. Conclusion …….. 119
Chapter 7. Influence of temperature upon properties of tailor made PEBAX® MH 1657 nanocomposite membranes for post combustion CO_2 capture ….……..… 121
7.1. Introduction ……. 122
7.2. Results ……. 123
7.2.1. Location of the nanoparticles in the prepared nanocomposite membranes via atomic force microscopy …… 123
7.2.2. Gas separation performance ……... 128
7.2.3. Differential scanning calorimetry …….. 136
7.3. Discussion ……... 142
7.3.1. Influence of structural features of the nanofillers upon gas permeation …… 142
7.3.2. Influence of nanofiller upon selectivity of CO_2 over N_2 and H_2 …… 143
7.3.3. Influence of temperature upon stability of the membrane ……. 145
7.4. Conclusion …….. 146
Chapter 8. Functionalization of Carbon Nanotube and Fabrication of Nanocomposite Membrane ……. 148
8.1. Introduction ……. 149
8.2. Functionalization of Carbon Nanotube with poly(ethylene glycol) (Mn=200 g/mol) … 150
8.2.1. TGA and TGA-FTIR study …… 151
8.2.2. Raman spectroscopy …….. 153
8.3. PEBAX® MH 1657 nanocomposite membranes with FutureCarbon-MWCNT-PEG ……. 156
8.4. Polyurathane based electromagnetic interference (EMI) shielding foam ……... 158
8.5. Conclusion …….. 159

Part – E:
Chapter 9. Outlook …… 160
9.1. Post modification of PEG-GLY-POSS-Toluene ……. 161

Part – F:
Chapter 10. Summary ……... 166

10.1. Summary ……... 167
10.2. Zusammenfassung ……. 170

Part – G:
Chapter 11. References …… 174
Chapter 12. Acknowledgement ……... 184
Chapter 13. Appendix ……..……... 187
Appendix A …… 188
13.1. List of NMR Peaks …… 188
13.2. Composition of PEG functionalized POSS nanoparticles …… 190
13.3. DSC thermograms ……. 191
Appendix B …… 194
13.4. Conductive Foam …….. 194
Appendix C …… 195
13.5. Toxicity of Chemicals ……... 195

List of Publications…….. 197

Curriculum Vitiate……..…… 199

Declaration on oath……. 200

List of Figures

Figure 1.1: Schematic diagram of flue gas clean up in coal fired power plant ……..... 3

Figure 1.2: Main topics involved in membrane performance development …….. 4

Figure 2.1: Schematic representation of gas permeation through porous and nonporous membranes ……... 11

Figure 2.2: Gas permeation through a nonporous membrane ……..... 13

Figure 2.3: Schematic representation of transport of a gas molecule through a rubbery polymer membrane …….. … 15

Figure 2.4: Schematic representation of transport of Henry's law sorption isotherm 16

Figure 2.5: Schematic representation of transport of a gas molecule through a glassy polymer membrane …….. 17

Figure 2.6: Schematic representation of transport of dual mode sorption isotherm ……... 18

Figure 2.7: Schematic representation of transport of a gas molecule through a semi crystalline polymer membrane ……. 19

Figure 2.8: a) Schematic representation of microphase separated morphologies in an A-B diblock copolymer as a function of volume fraction of the A-block b) Theoretical phase diagram of A-B diblock copolymer predicted by self-consistent mean field theory. CPS and CPS' are closely packed spheres, S and S'are body-centered-cubic spheres, C and C'are hexagonally packed cylinders, G and G'are bicontinuous gyroids and L is lamellae …….. 23

Figure 2.9: Schematic representation of a functionalized nanoparticle in an A-B diblock copolymer matrix ……. 27

Figure 3.1: Time-lag measurement of gas permeation ……..... 35

Figure 4.1: Composition of PEG POSS® (a) Structure provided by manufacturer (b) Thermogravimetric analysis ……..... 41

Figure 4.2: Single gas permeability as a function of PEG POSS® content in PEBAX® MH1657. Permeability of N_2, O_2, CH_4 and H_2 are plotted on left ordinate and that of CO_2 right ordinate …….. 43

Figure 4.3: CO_2 selectivity over light gases as a function of PEG POSS® content in PEBAX® MH1657 ……..... 43

Figure 4.4: Diffusion coefficient and solubility of CO_2 as a function of PEG POSS® content in PEBAX® MH1657 …….. 44

Figure 4.5: Single gas permeability as a function of PEG POSS® content in PEBAX® 2533. Permeability of N_2, O_2, CH_4 and H_2 are plotted on left ordinate and that of CO_2 right ordinate ……. 45

Figure 4.6: CO_2 selectivity over light gases as a function of PEG POSS® content in PEBAX® 2533 ……. 46

Figure 4.7: Diffusion coefficient and solubility of CO_2 as a function of PEG POSS® content in PEBAX® MH1657 ……. 47

Figure 4.8: Permeability of gases as a function of temperature of PEBAX® MH1657 and PEBAX® 2533 before and after 30 wt% PEG POSS® incorporation 48

Figure 4.9: CO_2 selectivity over light gases as a function of temperature of PEBAX® MH1657 and PEBAX® 2533 before and after incorporation of 30 wt% PEG POSS® ……. 50

Figure 4.10: Diffusion coefficient and solubility of CO_2 as a function of temperature of PEBAX® MH1657 and PEBAX® 2533 before and after 30 wt% PEG POSS® incorporation ……..... 51

Figure 4.11: DSC thermograms of PEBAX® MH1657 and its PEG POSS® incorporated nanocomposites – a) second heating trace b) second cooling trace …… 55

Figure 4.12: DSC thermogram of PEBAX® 2533 and its PEG POSS® incorporated nanocomposites a) second heating trace b) second cooling trace …… 57

Figure 4.13: Surface topography via AFM a) 3D- image of PEBAX® MH1657 c) 3D-image of 30 wt% PEG POSS® incorporated PEBAX® MH1657 b) Height image of PEBAX® MH1657 d) Height image of 30 wt% PEG POSS® incorporated PEBAX® MH1657 ……. 60

Figure 4.14: Surface topography via AFM a) 3D- image of PEBAX® 2533 c) 3D-image of 30 wt% PEG POSS® incorporated PEBAX® 2533 b) Height image of PEBAX® 2533 d) Height image of 30 wt% PEG POSS® incorporated PEBAX® 2533 ……. 61

Figure 4.15: Surface morphology and surface spectra of PEBAX® nanocomposite membranes containing 30 wt% PEG POSS. a) SEM micrograph of PEBAX® MH1657 nanocomposite membrane; b) SEM micrograph of PEBAX® 2533 nanocomposite membrane; c) EDS spectra of two areas of PEBAX® MH1657 nanocomposite membrane; d) EDS spectra of two areas of PEBAX® 2533 nanocomposite membrane …….. 63

Figure 4.16: SEM micrograph of the cross section of - a) PEBAX® MH1657 nanocomposite membrane containing 30 wt% PEG POSS® and b) PEBAX® 2533 nanocomposite membrane containing 30 wt% PEG POSS® ……... 65

Figure 4.17: Cross section morphology of a PEBAX® MH1657 nanocomposite membrane containing 30 wt% PEG POSS® a) SEM micrograph b) Si element map c) C element map d) O element map …….. 65

Figure 4.18: Cross section morphology of a PEBAX® 2533 nanocomposite membrane containing 30 wt% PEG POSS® a) SEM micrograph b) Si element map c) C element map d) O element map ……..... 66

Figure 5.1: a) Structure of poly(butylene terephthalate) (PBT) and poly(ethylene glycol terephthalate) (PEGT); b) ^{1}H-NMR of P 1500; c) ^{1}H-NMR of P 3000; d) ^{1}H-NMR of P 4000 ……..... 74

Figure 5.2: a) Chemical structure b) DSC curves (second heating and cooling trace) of PEG POSS®…….. 76

Figure 5.3: DSC curves (second heating and cooling trace) of the three grades of PolyActive™ and their nanocomposites with PEG POSS® ……. 77

Figure 5.4: CO_2 permeability as a function of temperature in three grades of PolyActive™ and their nanocomposites with PEG POSS® ……. 81

Figure 5.5: CO_2 diffusivity as a function of temperature in three grades of PolyActive™ and their nanocomposites with PEG POSS® …… 83

Figure 5.6: CO_2 solubility as a function of temperature in three grades of PolyActive™ and their nanocomposites with PEG POSS® …… 84

Figure 5.7: CO_2/N_2 selectivity as a function of temperature in three grades of PolyActive™ and their nanocomposites with PEG POSS® ……. 86

Figure 5.8: CO_2/CH_4 selectivity as a function of temperature in three grades of PolyActive™ and their nanocomposites with PEG POSS® ……. 87

Figure 5.9: CO_2/H_2 selectivity as a function of temperature in three grades of PolyActive™ and their nanocomposites with PEG POSS® ……. 88

Figure 5.10: Surface morphology – a) SEM micrograph of P 1500, secondary electrons (SE) b) Oxygen elemental map of P1500 c) Silicon elemental map of P 1500 d) SEM micrograph of P 1500 + 20 wt% PEG POSS® e) Oxygen elemental map of P 1500 + 20 wt% PEG POSS® f) Silicon elemental map of P 1500 + 20 wt% PEG POSS® g) SEM micrograph of P 1500 + 30 wt% PEG POSS® h) Oxygen elemental map of P 1500 + 30 wt% PEG POSS® i) Silicon elemental map of P 1500 + 30 wt% PEG POSS®. The accelerating voltage is 5 kV for all measurements ……. 89

Figure 5.11: Cross section morphology – a) SEM micrograph of P 1500 b) Oxygen elemental map of P1500 c) Silicon elemental map of P 1500 d) SEM micrograph of P 1500 + 20 wt% PEG POSS® e) Oxygen elemental map of P 1500 + 20 wt% PEG POSS® f) Silicon elemental map of P 1500 + 20 wt% PEG POSS® g) SEM micrograph of P 1500 + 30 wt% PEG POSS® h) Oxygen elemental map of P 1500 + 30 wt% PEG POSS® i) Silicon elemental map of P 1500 + 30 wt% PEG POSS®. The accelerating voltage is 5 kV for all measurements ……. 90

Figure 5.12: Cross section of P 1500 – a) SEM image, accelerating voltage 800V, energy selective backscattered electrons b) AFM image (3 μm × 3 μm) c) AFM image (1 μm × 1 μm) …… 92

Figure 5.13: Cross section of P 1500 + 20 wt% PEG POSS® – a) SEM image, accelerating voltage 800V, energy selective backscattered electrons b) AFM image (3 μm × 3 μm) c) AFM image (1 μm × 1 μm) ……... 93

Figure 5.14: Cross section of P 1500 + 30 wt% PEG POSS® – a) SEM image, accelerating voltage 800V, energy selective backscattered electrons b) AFM image (3 μm × 3 μm) c) AFM image (1 μm × 1 μm) …….. 94

Figure 6.1: (a) Reaction scheme and chemical structures (b) ^{13}C-DEPTQ-135 NMR spectra of – (i) glycidyl POSS® (ii) methoxy poly(ethylene glycol) (PEG) (iii) PEG modified glycidyl POSS …….. 104

Figure 6.2: FT-IR spectra of – (i) glycidyl POSS® (ii) methoxy poly(ethylene glycol) (PEG) (iii) PEG modified glycidyl POSS ……..... 105

Figure 6.3: ^{1}H NMR spectra of – (a) PEG-GLY-POSS-Chloroform (b) PEG-GLY-POSS-Toluene (c) PEG-GLY-POSS-THF (d) PEG-GDMS-POSS-Chloroform (e) PEG-GDMS-POSS-Toluene (f) PEG-GDMS-POSS-THF … 107

Figure 6.4: ^{13}C-DEPTQ-135 NMR spectra of – (a) PEG-GLY-POSS-Chloroform (b) PEG-GLY-POSS-Toluene (c) PEG-GLY-POSS-THF (d) PEG-GDMS-POSS-Chloroform (e) PEG-GDMS-POSS-Toluene (f) PEG-GDMS-POSS-THF ……..... 108

Figure 6.5: Quantitative ^{13}C (inverse gated decoupled) NMR spectra of – (a) PEG-GLY-POSS-Chloroform (b) PEG-GLY-POSS-Toluene (c) PEG-GLY-POSS-THF (d) PEG-GDMS-POSS-Chloroform (e) PEG-GDMS-POSS-Toluene (f) PEG-GDMS-POSS-THF ……..……. 109

Figure 6.6: Thermogravimetric analysis of – i) glycidyl POSS® ii) PEG-GLY-POSS-Toluene iii) PEG-GLY-POSS-Chloroform iv) PEG-GLY-POSS-THF v) methoxy poly(ethylene glycol) (PEG) ……. 111

Figure 6.7: Thermogravimetric analysis of – i) glycidyldimethylsilyl POSS® ii) PEG-GDMS-POSS-Toluene iii) PEG-GDMS-POSS-Chloroform iv) PEG-GDMS-POSS-THF v) methoxy poly(ethylene glycol) (PEG) ……. 112

Figure 6.8: Single gas permeability as a function of – a) PEG-GLY-POSS-Chloroform content b) PEG-GLY-POSS-Toluene content c) PEG-GLY-POSS-THF content d) PEG-GDMS-POSS-Chloroform content e) PEG-GDMS-POSS-Toluene content f) PEG-GDMS-POSS-THF content. Permeability of N_2 and H_2 are plotted on left Y axis and that of CO_2 right Y axis ……... 114

Figure 6.9: Diffusion and solubility coefficients of CO_2 as a function of – a) PEG-GLY-POSS-Chloroform content b) PEG-GLY-POSS-Toluene content c) PEG-GLY-POSS-THF content d) PEG-GDMS-POSS-Chloroform content e) PEG-GDMS-POSS-Toluene content f) PEG-GDMS-POSS-THF content. Permeability of N_2 and H_2 are plotted on left Y axis and that of CO_2 right Y axis ……... 116

Figure 6.10: CO_2 selectivity over light gases as a function of – a) PEG-GLY-POSS-Chloroform content b) PEG-GLY-POSS-Toluene content c) PEG-GLY-POSS-THF content d) PEG-GDMS-POSS-Chloroform content e) PEG-GDMS-POSS-Toluene content f) PEG-GDMS-POSS-THF content …….. 117

Figure 7.1: TappingMode™ AFM phase image (3 μm ×3 μm) of the cross section of a PEBAX® MH1657 membrane ……..….. 123

Figure 7.2: TappingMode™ AFM phase image (3 μm ×3 μm) of the cross section of PEBAX® MH 1657 nanocomposite containing 40 wt% of – a) PEG-GLY-POSS-Chloroform b) PEG-GLY-POSS-Toluene c) PEG-GLY-POSS-THF d) PEG-GDMS-POSS-Chloroform e) PEG-GDMS-POSS-Toluene f) PEG-GDMS-POSS-THF ……..…… 124

Figure 7.3: SEM micrograph of the surface of the PEBAX® MH 1657 nanocomposites containing 40 wt% of – (a) PEG-GLY-POSS-Chloroform (b) PEG-GLY-POSS-Toluene (c) PEG-GLY-POSS-THF (d) PEG-GDMS-POSS-Chloroform (e) PEG-GDMS-POSS-Toluene (f) PEG-GDMS-POSS-THF 126

Figure 7.4: SEM micrograph of the cross section of the PEBAX® MH 1657 nanocomposites containing 40 wt% of – (a) PEG-GLY-POSS-Chloroform (b) PEG-GLY-POSS-Toluene (c) PEG-GLY-POSS-THF (d) PEG-GDMS-POSS-Chloroform (e) PEG-GDMS-POSS-Toluene (f) PEG-GDMS-POSS-THF …….. 127

Figure 7.5: Permeability of gases as a function of temperature of PEBAX® MH 1657 and nanocomposites containing 40 wt% nanofiller ……. 128

Figure 7.6: CO_2 permeability selectivity over N_2 and H_2 as a function of temperature of PEBAX® MH 1657 and nanocomposites containing 40 wt% nanofiller ……. 130

Figure 7.7: Solubility and diffusion coefficient of CO_2 as a function of temperature of PEBAX® MH 1657 and nanocomposites containing 40 wt% nanofiller ……. 131

Figure 7.8: Solubility and diffusion coefficient as a function of temperature of PEBAX® MH 1657 and nanocomposites containing 40 wt% nanofiller – a) N_2 and b) H_2 ……. 134

Figure 7.9: Solubility selectivity and diffusion selectivity as a function of temperature of PEBAX® MH 1657 and nanocomposites containing 40 wt% nanofiller – a) CO_2/N_2 and b) CO_2/H_2 …… 135

Figure 7.10: DSC thermogram of synthesized nanofillers – a) 2nd heating trace b) 2nd cooling trace ……. 137

Figure 7.11: a) Temperature protocol of DSC run b) DSC thermogram of PEBAX® MH 1657 …….. 139

Figure 7.12: DSC thermogram (second cooling trace) of the nanocomposites of PEBAX® MH 1657 containing – (a) PEG-GLY-POSS-Chloroform (b) PEG-GLY-POSS-Toluene (c) PEG-GLY-POSS-THF (d) PEG-GDMS-POSS-Chloroform (e) PEG-GDMS-POSS-Toluene (f) PEG-GDMS-POSS-THF … 140

Figure 8.1: Thermogravimetric Analysis at 10 K/min (mass loss (%) at 600 ºC) of unfunctionalized, oxidized and PEG grafted – a) CSIC-MWCNT and b) FutureCarbon-MWCNT ……. 151

Figure 8.2: TGA-FTIR – a) CSIC-MWCNT after oxidation b) CSIC-MWCNT after PEG functionalization c) Comparison of pure PEG with CSIC-MWCNT PEG ……. 152

Figure 8.3: Raman spectra – a) CSIC-MWCNT before functionalization b) CSIC-MWCNT after functionalization c) FutureCarbon-MWCNT before functionalization d) FutureCarbon-MWCNT after functionalization ……. 154

Figure 8.4: Gas separation performance of PEBAX® MH 1657 membranes before and after 2 wt% FC-MWCNT-PEG incorporation as a function of temperature – a) Permeability b) Selectivity of CO_2 over other gases …… 156

Figure 9.1: FT-IR spectra – i) PEG-GLY-POSS ii) PEG-GLY-POSS after acylation iii) PEG-GLY-POSS after mesylation ……..…….. 162

Figure 9.2: ^{13}C-DEPTQ-135 NMR spectra – i) PEG-GLY-POSS-Toluene ii) PEG-GLY-POSS after acylation iii) PEG-GLY-POSS after mesylation …….. 162
Figure 9.3: FT-IR spectra – i) Mesylated-PEG-GLY-POSS ii) Azide -PEG-GLY-POSS 163
Figure 9.4: ^{13}C- NMR spectra – i) Mesylated-PEG-GLY-POSS ii) Azide -PEG-GLY-POSS ……. 164
Figure 13.1: DSC thermograms (first cooling trace) of PEBAX® MH 1657 and its nanocomposites containing – a) PEG-GLY-POSS-Chloroform b)PEG-GLY-POSS-Toluene c)PEG-GLY-POSS-THF d) PEG-GDMS-POSS-Chloroform e)PEG-GDMS-POSS-Toluene f)PEG-GDMS-POSS-THF …… 191
Figure 13.2: DSC thermograms (second heating trace) of PEBAX MH 1657 and its nanocomposites containing – a) PEG-GLY-POSS-Chloroform b)PEG-GLY-POSS-Toluene c)PEG-GLY-POSS-THF d) PEG-GDMS-POSS-Chloroform e)PEG-GDMS-POSS-Toluene f)PEG-GDMS-POSS-THF ……. 192
Figure 13.3: DSC thermograms (second cooling trace) of PEBAX MH 1657 and its nanocomposites containing – a) PEG-GLY-POSS-Chloroform b)PEG-GLY-POSS-Toluene c)PEG-GLY-POSS-THF d) PEG-GDMS-POSS-Chloroform e)PEG-GDMS-POSS-Toluene f) PEG-GDMS-POSS-THF …….. 193

List of Tables

Table 4.1: Composition of two grades of PEBAX®…….. 41
Table 4.2: E_P, E_D and ΔH_S (Chapter 2, equation 2.11, 2.12, 2.14 and 2.15) of CO_2 through PEBAX® MH1657 and PEBAX® 2533 before and after 30 wt% PEG POSS® incorporation ……... 52
Table 4.3: Glass transition temperature of PEBAX® MH1657 and PEBAX® 2533 as a function of PEG POSS® content …….. 54
Table 4.4: Onset, peak and endset temperature of crystallization of polyether domain of PEBAX® MH1657 as a function of PEG POSS® content ……... 56
Table 4.5: Roughness parameters of PEBAX® MH1657 and its nanocomposite after incorporation of 30 wt% PEG POSS® ……. 60
Table 4.6: Roughness parameters of PEBAX® 2533 and its nanocomposite after incorporation of 30 wt% PEG POSS® ……. 61
Table 5.1: Acronym of three grades of PolyActive™ …….. 73
Table 5.2: Comparison of the three different grades of PolyActive™ from ^{1}H NMR …. 75
Table 5.3: The melt onset, melt peak, melt endset, enthalpy of melting and crystallinity (second heating) of the polyether blocks of three grades of PolyActive™ …. 78
Table 5.4: The onset, peak, endset, and enthalpy of crystallization (second cooling) of the polyether blocks of three grades of PolyActive™ ……... 79
Table 5.5: N_2, CH_4, and H_2 permeability in three grades of PolyActive™ and their nanocomposites with PEG POSS® …….. 85

Table 6.1: Acronyms of the products of epoxide ring opening reaction …….. 106
Table 7.1: Comparison of E_P, E_D and ΔH_S (Chapter 2, equation 2.11, 2.12, 2.14 and 2.15) of CO_2 transport through nanocomposites containing different nanofillers …… 132
Table 7.2: Glass transition temperature of PEBAX® MH 1657, the nanofillers and the nanocomposites …… 136
Table 8.1: Average ratio of area and standard deviation of D-band to G-band …… 155
Table 13.1: Composition of functionalized POSS nanoparticles after modification with PEG …….. 190
Table 13.2: Conductivity values as a function of density, MWCNT type and dispersion protocol …… 194
Table 13.3: List of chemicals with GHS symbol, H- and P-data …… 195

List of Schemes

Scheme 1.1: General structure of PolyActive™ …….. 6
Scheme 1.2: General structure of PEBAX® ……. 6
Scheme 6.1: Structure of – (a) glycidyl POSS® (b) glycidyldimethylsilyl POSS® ……. 102
Scheme 6.2: Epoxide ring opening reaction mechanism S_N1 and S_N2 …… 103
Scheme 8.1: Schematic diagram of grafting oligomeric hydroxyl terminated poly(ethylene glycol) chain on pristine MWCNT ...…… 150
Scheme 9.1: Post modification of PEG-GLY-POSS- i) Acylation ii) Mesylation ……... 161
Scheme 9.2: Azidation of mesylated PEG-GLY-POSS-Toluene ……. 163
Scheme 9.3: Copper catalyzed “Click”reaction of Azide-PEG-GLY-POSS ……... 164

List of Symbol

b	Langmuir hole affinity parameter
C	Concentration of a gas
C'_H	Langmuir capacity parameter
C_1	Gas concentration on the downstream side
C_2	Gas concentration on the uptream side
C_D	Gas concentration based on Henry’s law sorption
CED	Cohesive energy density of the polymer
C_H	Gas concentration based on Langmuir sorption
d	Kinetic cross sectional area of a penetrant
d_{total}	Total diameter of the nanoparticle
d_{core}	Diameter of core of the nanoparticle

D	Diffusion coefficient of a gas
D_a	Diffusivity of a gas for a completely amorphous polymer
D_o	Diffusion coefficient of a gas at infinite high temperature
E_D	Activation energy of diffusivity
E_P	Activation energy of permeation
f_A	Volume fraction of block A
J	Flux of a gas
k_D	Henry's solubility constant
l	Thickness of membrane
N	Degree of polymerization
N_o	Avogadro constant
p	Pressure of a gas
p_1	Gas pressure on the downstream side
p_2	Gas pressure on the uptream side
P	Permeability of a gas
P_a	Gas permeability in the amorphous phase of a semicrystalline polymer
P_o	Permeability of a gas at infinite high temperature
R	Ideal gas constant
S	Solubility coefficient of a gas
S_a	Solubility coefficient of a pure amorphous polymer
S_o	A pre-exponential factor
T	Temperature (unit kelvin)
t_{corona}	Thickness of surface grafted ligand of the nanoparticle
T_g	Glass transition temperature
$\alpha_{A/B}$	Ideal selectivity of a gas A over gas B
β	Chain immobilization factor
ΔG	Change in free enthalpy in bulk block copolymer nanocomposite
$\Delta H_{ligand\text{-}polymer}$	Enthalpic contribution of the interaction between the segment of the block copolymer and the ligand attached to the nanoparticle in bulk block copolymer nanocomposite
ΔH_S	Enthalpy of sorption
ΔS_{con}	Change in conformational entropy of the polymer chains
ΔS_{trans}	Entropic contribution due to the number of distinguishable physical arrangements of the nanoparticles in the nanocomposite
λ	Length of diffusive jump
τ	Tortuosity factor
Φ_a	Volume fraction of the amorphous phase
χ	Flory-Huggins-Staverman-parameter
χ_{PA}	Enthalpic interactions between the ligand of the nanoparticle and the monomeric unit of A block of a A-B diblock copolymer
χ_{PB}	Enthalpic interactions between the ligand of the nanoparticle and the monomeric unit of B block of a A-B diblock copolymer

List of Abbreviations

AFM	Atomic force microscopy
BT	butylene terephthalate
C and C’	Hexagonally packed cylinders
CPS and CPS’	Closely packed spheres
CSIC	Consejo Superior de Investigaciones Científicas
DCM	dichloromethane
DSC	Differential scanning calorimetry
EGT	ethylene glycol terephthalate
EMI	Electomagnetic interference
EsB	Energy selective backscattered
FT-IR	Fourier transform infrared spectroscopy
G and G’	Bicontinuous gyroids
IMDS	Intermaterial dividing surface
IPDS	Interparticle domain surface
L	Lamellae
MWCNT	Multiwalled carbon nanotube
NMR	Nuclear magnetic resonance spectroscopy
PA	polyamide
PBT	poly(butylene terephthalate)
PE	polyether
PEG	poly(ethylene glycol)
PEG-GDMS-POSS	PEG modified Glycidyldimethylsilyl POSS
PEG-GLY-POSS	PEG modified Glycidyl POSS
PEGT	poly(ethylene glycol terephthalate)
PEO	poly(ethylene oxide)
POSS	polyhedral oligomeric silsesquioxane
PTFE	poly(tetrafluoroethylene)
S and S’	Body-centered-cubic spheres
SE	Secondary electron
SEM	Scanning electron microscopy
TBAI	tert-butylammonium iodide
TEA	triethylamine
TGA	Thermogravimetric analysis
THF	Tetrahydrofuran
TPE	Thermoplastic elastomer

Part –A:

Chapter 1. Introduction

1.1. Objective

Global warming and climate change has compelled us to look for economically feasible and energy efficient processes to prevent the CO_2 from reaching the atmosphere. At present fossil fuel accounts for 80% of the global energy needs.[1] A fossil fuel based power plant generates steam to run the turbine by burning coal, oil, natural gas etc. This combustion turbine process leads to emission of enormous amount of CO_2. In spite of the tremendous development of alternative energy production technologies (e.g. solar energy, wind power, biomass energy etc.) the ever growing energy requirement is expected to depend on fossil fuels at least for the next few decades.[1, 2] Among the three major fossil fuel (i.e. coal, gas and oil) coal constituents about 65% of the fossil fuel reserve and is expected to be the only remaining fossil fuel after 2042.[1] Due to the availability and low cost a large percentage of electricity production will certainly be dependent upon combustion of coal.[3] The existing coal fired power plants emit around 2 billion tons of CO_2 per year.[4] Therefore, it is obvious that CO_2 capture from the fossil fuel based power plants is the key issue to ensure sustainable utilization of the fossil fuel resource.

CO_2 can be captured from power plants using three different pathways- oxy-fuel combustion, pre combustion and post combustion. In the post combustion carbon capture technology CO_2 is captured from the flue gas after the combustion of fossil fuel in air. CO_2 is purified up to a target specification followed by transportation and storage. The advantage of using this process is that it allows retrofitting the existing power plants with some modification.[5]

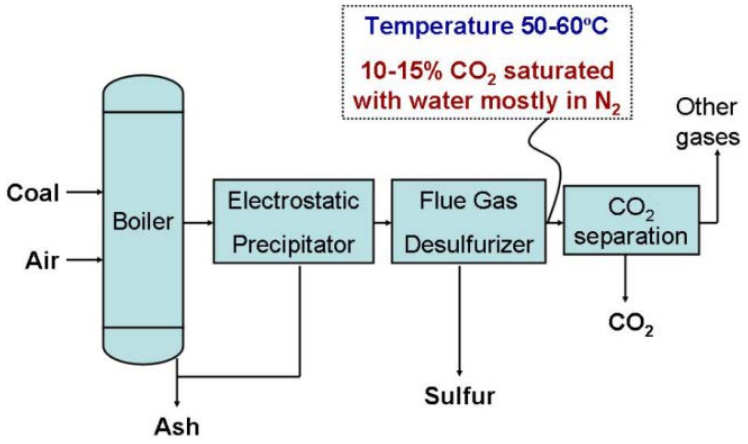

Figure 1.1: Schematic diagram of flue gas clean up in a coal fired power plant.[3]

Figure 1.1 depicts a schematic representation of the flue gas treatment of a typical coal fired power plant. In average a 600 MW coal fired power plant generates 500 m^3/s of flue gas. In a typical coal fired power plant, the flue gas after leaving the boiler is passed through an electrostatic precipitator (to remove particulates), a desulfurizer (to remove SO_2 gas), and then CO_2 can be separated. At this stage the water saturated flue gas is at about 50 ºC, nearly atmospheric pressure and has CO_2 content as low as 10-15% or CO_2 partial pressure of 100-150 mbar. [3] It is necessary to adopt an economically feasible CO_2 separation process for successful implementation of post combustion CO_2 capture technology. Traditional methods used to separate CO_2 from gas mixture are solvent adsorption, pressure swing adsorption, cryogenic distillation etc. These conventional technologies require a gas to liquid phase change which increases the energy cost of the separation process substantially. In the last two decades membrane technology has become an attractive choice for gas separation. Membrane technology enjoys an inherent advantage of high energy efficiency since it does not require a phase change. In addition it offers less mechanical complexity and less capital investment.[4, 6] However, use of membrane separation technology to separate CO_2 in post combustion capture technology is

confronted with some limitations in terms separation efficiency. To increase the performance of membrane separation process, development is required in system design, module design and material selection (Figure 1.2).[7]

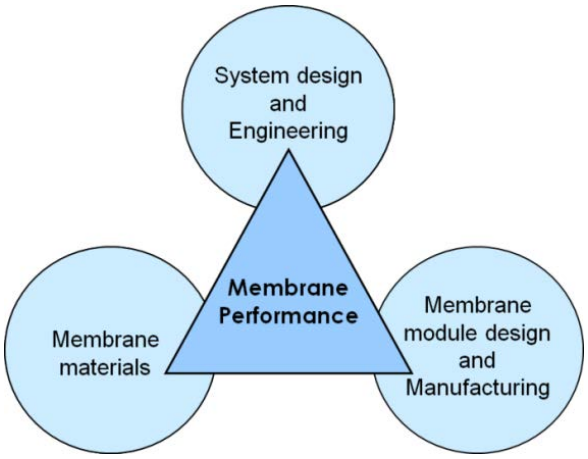

Figure 1.2: Main topics involved in membrane performance development. [7]

Polymers have so far been the most attractive choice for commercial gas separation membrane materials. A vast array of potential polymeric materials have been explored to fulfill the desired requirements concerning CO_2/N_2 separation efficiency for the post combustion carbon capture.[3] From an application point of view the most basic requirements of a membrane material is to have a high gas permeation rate maintaining the desired selectivity. An increase of membrane permeance reduces the membrane area required for a desired separation which results in reduced footprint and investment costs. However, a major drawback of polymer based membranes has been the naturally counteracting permeability and selectivity. The development of new membrane materials with improved permeability and selectivity is required to overcome this drawback in order to improve the process efficiency for industrial application. Nonetheless,

the material selection criterion also involves durability (e.g. mechanical integrity) at the operating conditions. A balance between these features to maintain high separation efficiency makes the task of material selection quite difficult. Therefore, the search for robust materials with better separation performance at the operating conditions is still going on.[8-11] The aim of this PhD research is to contribute to the continuing trend of the development of polymeric membrane materials for post combustion carbon capture.

1.2. Poly(ethylene oxide) based membranes for CO_2 separation

Polymers containing the polar ethylene oxide groups have a strong affinity for CO_2 due to dipole-quadrupole interaction.[12] Thus the poly(ethylene oxide) (PEO) has attracted lots of attention to prepare a CO_2 selective membrane through which CO_2 passes faster than the light gases such as H_2, CH_4, N_2 etc. The major prerequisite for fabrication of this class of membrane is that the PEO must be in an amorphous state at the temperature of application. A polar ether group usually increases the chain packing efficiency, but the densely packed crystallites of the polyether are impermeable and non-sorbing. For this reason the homopolymers of ethylene oxide (PEO) are not suitable for membrane fabrication. Block copolymers containing alternating series of an amorphous PEO block and a rigid or even crystalline block (such as polyamide, polyester, polystyrene etc.) have carved out a reputation as suitable alternative materials.[12, 13] Two commercial block copolymer families namely PolyActive™ (scheme 1.1) [14, 15] and PEBAX® (scheme 1.2) [16] have already proven to be suitable CO_2 selective membrane materials. These block copolymers have microphase separated structure where the crystalline block hinders the crystallization of PEO block and provides mechanical strength while gas transport effectively

occurs through the amorphous PEO block. A variety of different concepts have also been successfully implemented to further improve the separation performance of these commercial polymers e.g. crosslinking, incorporation of filler etc.[17, 18]

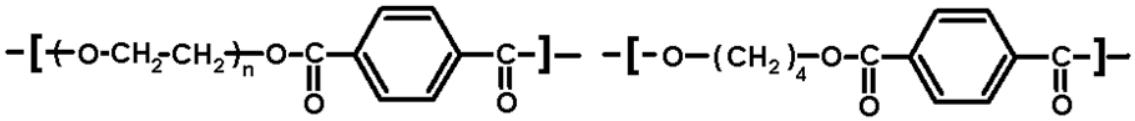

EGT **BT**

EGT = Ethylene glycol terephthalate

BT = Butylene terephthalate

Scheme 1.1: General structure PolyActive™.

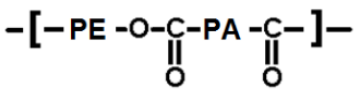

PE = Polyether

PA = Polyamide

Scheme 1.2: General structure PEBAX®.

PS: Note that in this work commercial block copolymers and nanoparticles produced by different manufacturers are used. In this thesis poly(ethylene oxide) (PEO) and poly(ethylene glycol) (PEG) both names are used to address the segment of polymer or ligand of nanoparticle having the -CH_2-CH_2-O- repeating unit.

A fundamental approach to improve the CO_2 separation performance is to increase the total amorphous PEO content in the membrane. In this regard several works have also been reported upon successful blending of the low molecular weight poly(ethylene glycol) (PEG) with these commercial block copolymers which leads to an increase of gas permeability. [14, 19-21]

1.3. Strategy of the research and outline of the thesis

In order to achieve the potential of membrane separation technology a molecular level control of the membrane material is required. Incorporation of nanofillers in polymer membranes is a facile and efficient way towards this endeavor. This class of membranes referred to as polymer nanocomposite membranes or mixed matrix membranes has recently been extensively explored for gas separation applications.[22-27] The nanosized fillers can impart desirable structural and functional properties in a polymer nanocomposite material. The surface functionality of the nanofillers governs the spatial distribution and mediates the interaction with the polymer segments in immediate vicinity of the surface of the nanofiller. Surface functionality is the key to take benefit of the nanosize of the filler and to control the bulk property of the polymer nanocomposite.[28, 29] In a non-porous polymer membrane properties of both the penetrant and the polymer determine the transport of gases.[12] Additionally, in polymer nanocomposite membranes interaction between the surface of the nanofiller with the surrounding polymer chains as well as with the permeating gases contributes to the gas transport to a great extent. Hence, one of the biggest concerns in nanocomposite membrane preparation is to decorate the surface of the nanoparticle with suitable functional group by covalent or noncovalent functionalization which

not only contribute to homogeneous filler dispersion, but also create an opportunity to tune the transport of penetrants through the membrane. [27, 30]

Taking into account the above mentioned facts, in this research work PEG functionalized nanoparticles are incorporated in commercially available multiblock copolymers PolyActive™ and PEBAX® to prepare CO_2 separation nanocomposite membranes. Two types of nanoparticles are employed to prepare the nanocomposite membranes – polyhedral oligomeric silsesquioxane (POSS) and multiwalled carbon nanotube (MWCNT). The biggest challenge of preparing the nanocomposites are- i) location of the nanoparticle must be in the polyether domain of the block copolymer matrix and ii) the prepared nanocomposite membranes must be stable in the temperature range of application for post combustion carbon capture. Both of these challenges are achieved to a good extent by choosing a surface functionality of the nanoparticle which is compatible with the polyether domain of the polymer matrix and a block copolymer matrix where the polyether domains do not undergo thermal transition in the temperature range of application. A major part of this research is assigned to the fundamental understanding of the structure-property relationship of the nanocomposite membranes which is an integral part of the material development.

The thesis is organized as follows – a theoretical background (Part-B) of gas separation membranes and block copolymer nanocomposites is given in chapter 2. The experimental procedure (Part-C) of functionalization of nanoparticles & membrane preparation is summarized in chapter 3. This chapter also contains specification of the equipment which was used for characterization. The obtained results are presented and discussed in detail (Part-D) in chapter 4

to 8. These chapters are divided by topic. An introduction and conclusion is included in each of these chapters. The distribution is as follows- i) Chapter 4 reports the nanocomposite membranes prepared by incorporation of commercial PEG POSS® in multiblock copolymers PEBAX® MH 1657 and PEBAX® 2533. ii) Chapter 5 presents the nanocomposite membranes prepared by incorporation of PEG POSS® in PolyActive™ 1500PEGT77PBT23, PolyActive™ 3000PEGT77PBT23 and PolyActive™ 4000PEGT77PBT23. iii) Chapter 6 reports functionalization of glycidyl POSS® and glycidyldimethylsilyl POSS® with methoxy poly(ethylene glycol) and their influence on the CO_2 separation properties on PEBAX® MH 1657 at 30 ºC iv) Chapter 7 deals with the morphology and influence of temperature on the separation performance and stability of the membranes presented in chapter 6. v) Chapter 8 presents the functionalization of multiwalled carbon nanotubes and their influence on the gas separation performance of PEBAX® MH 1657. The outlook (Part-E) of the thesis i.e. the future direction of the research work together with some initial experimental work is presented in chapter 9. Chapter 10 portrays the summary of the whole thesis (Part-F). Chapter 11, 12 and 13 are references, acknowledgement and appendix respectively (Part-G).

Part - B:

Chapter 2. Theoretical framework

2.1 Fundamental of gas separation membrane process

2.1.1 Gas separation membranes

A gas separation membrane is a selective semipermeable barrier that allows different gases to permeate through it at different rates. Both porous and dense membranes can be employed for separation of gases.

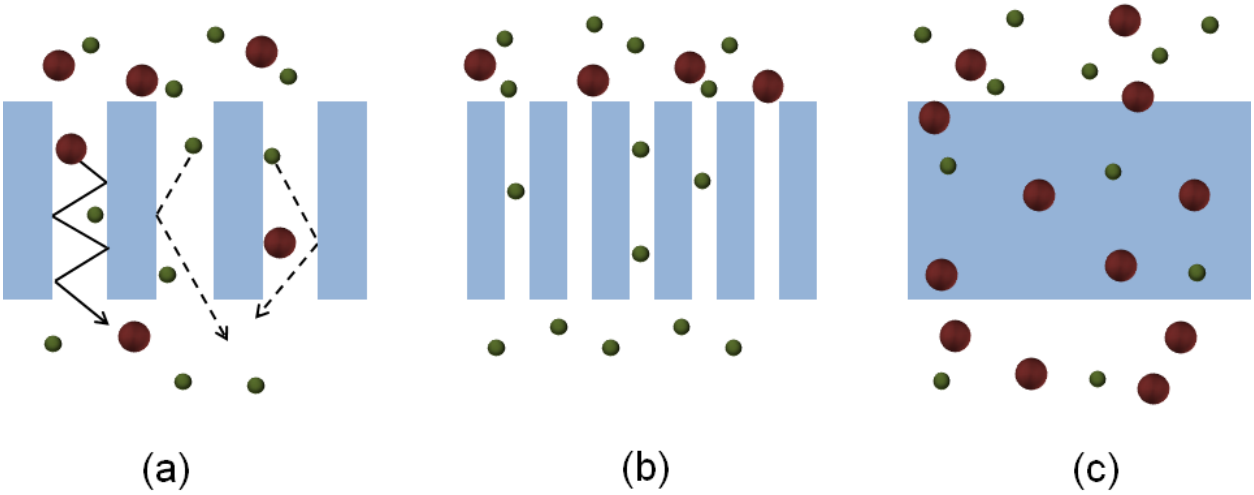

Figure 2.1: Schematic representation of gas permeation through porous and nonporous membranes.[31]

The overall mass transport of gas across the membrane is termed as “permeation”. Gas permeation through porous (depending on the pore size) and nonporous membranes is illustrated in Figure 2.1. Gases permeate through membranes of pore size 0.1 to 10µm by convective flow and separation does not take place. Gas separation occurs only if the pores are smaller than 0.1 µm. In this case the pore diameter is equal to or smaller than the mean free path of gas molecules. Gases pass through such pores by Knudsen diffusion (Figure 2.1a). Gases can be

separated according to their molecular size if the pores of the membrane are within 5-20Å (Figure 2.1b). At present all the commercial membranes used for gas separation are nonporous or dense membranes. Gas transport through nonporous or dense membranes is based on the solution diffusion mechanism (Figure 2.1c). [32]

2.1.2 Solution-diffusion model

Gas permeation through nonporous polymer membrane is a complex interplay of dissolution and diffusion of gases in the polymer referred to as "solution-diffusion mechanism". When gas pressure is applied to the feed side of the membrane, the transport of gas molecules is considered to take place by the following sequence of events –

i) The gas molecule is adsorbed at the feed side or upstream side of the membrane.

ii) The gas molecule being transported is molecularly dissolved in the polymer and diffuses through the thickness of the membrane.

iii) Finally the gas molecule is desorbed or released from the permeate side or downstream side of the membrane.[33]

A fundamental basis for permeation of gas molecules through a polymer membrane may be derived by considering a plane of polymer with thickness l separating two regions filled with a gas. The gas pressure and concentration on the downstream side are p_1 and C_1, while those on the upstream side are p_2 and C_2, respectively. At steady sate, the permeability of a pure gas (P), which is the pressure and thickness normalized gas flux through the membrane, can be expressed as-

$$P = \frac{Jl}{p_2 - p_1} = \frac{C_2 - C_1}{p_2 - p_1} D \qquad (2.1)$$

where, J is the gas flux and D is the average effective diffusion coefficient.

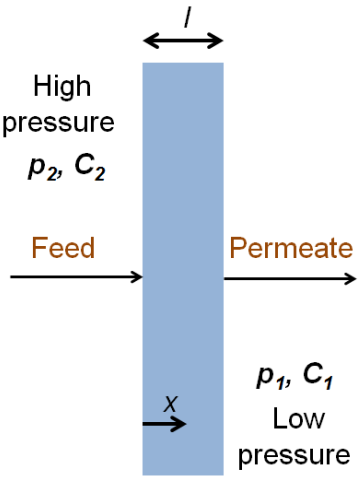

Figure 2.2: Gas permeation through a nonporous membrane. [34]

When the pressure and concentration of the upstream side is much greater than those of the downstream side, then equation 2.1 can be simplified as follows-

$$P = \frac{C_2}{p_2} D \qquad (2.2)$$

The solubility coefficient (S) of a gas is the ratio between the concentration of a gas dissolved in the polymer (C) and the pressure of the gas (p).

$$S = \frac{C}{p} \qquad (2.3)$$

From equations 2.2 and 2.3 we get the following relation –

$$P = DS \qquad (2.4)$$

Where S is evaluated at the upstream side of the membrane (i.e. $S=C_2/p_2$). Hence, P is a product of two factors- 1) a kinetic term i.e. diffusion coefficient, D which represents the mobility of the gas molecule as they diffuse through the membrane and 2) a thermodynamic term i.e. solubility coefficient, S which represents the number density of gas molecules dissolved in the polymer. Hence, P is an intrinsic property of a gas polymer system which depends upon the number of gas molecule dissolved in the polymer membrane and their rate of migration. [34, 35] The ideal selectivity ($\alpha_{A/B}$) of a gas A over gas B is defined as the ratio of the pure gas permeabilities.

$$\alpha_{A/B} = \frac{P_A}{P_B} = \frac{D_A}{D_B} \times \frac{S_A}{S_B} \qquad (2.5)$$

Where, D_A/D_B is referred to as the diffusivity selectivity and S_A/S_B is termed as the solubility selectivity. [34-36]

2.1.3 Gas sorption and diffusion in glassy and rubbery polymer membranes

Polymeric membrane materials can be broadly classified into two categories depending on their physical state at the application temperature – a) Rubbery polymers and b) Glassy polymers.

a) Rubbery polymer membranes:

If the polymer membrane is at a temperature higher than the glass transition (T_g), the segments of the polymer backbone have sufficient energy to rotate around their axis and the thermal motion of the segments makes the polymer membrane rubbery and flexible.[32] The rubbery polymers respond promptly to any external stress that tend to change their physical condition because they have a very short relaxation time compared to the glassy polymers. For example- if the

temperature is changed the polymer responds immediately and shifts to a new equilibrium state (e.g. a new volume). A similar immediate adjustment is made when the penetrant gas molecules are adsorbed by the rubbery polymer membrane (at constant temperature and pressure) and adsorption (solution) equilibrium is rapidly established. Segmental mobility due to internal chain motions i.e. chain rotation, translational motion and vibrational motion creates transient free-volume which allows a gas molecule to diffuse through the polymer. [33, 37, 38] The gas molecule makes diffusive jumps from one equilibrium site to another in the direction of decreasing concentration i.e. from the feed side to the permeate side of the membrane (Figure 2.3). The free volume undergoes rapid fluctuations in this kind of polymer since it originates from segmental mobility. The difference between the measurement temperature and T_g has a strong effect on free volume. Several authors have demonstrated good correlations of *D* and *P* of gas molecules in rubbery polymers with T_g as it serves as a crude indicator of segmental mobility.[34]

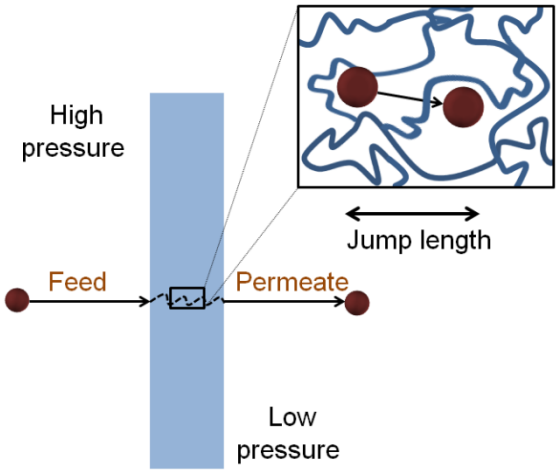

Figure 2.3: Schematic representation of transport of a gas molecule through a rubbery polymer membrane.

The sorption of gas molecules in a rubbery polymer is typically governed by Henry's law.

$$C = k_D.p \qquad (2.6)$$

where C is the concentration of gas in the polymer, k_D is the Henry's solubility constant for the particular polymer gas pair and p is the gas penetrant pressure. The sorption isotherm is linear.

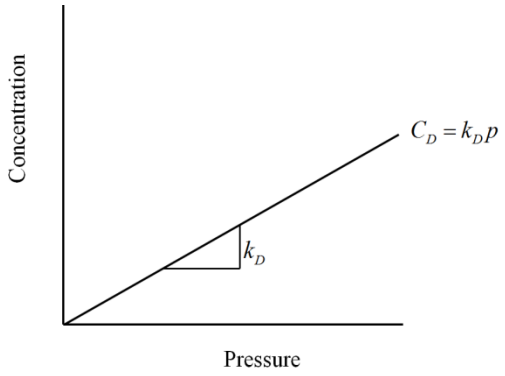

Figure 2.4: Schematic representation of transport of Henry's law sorption isotherm.

b) Glassy polymer membranes:

When the temperature range of application is below the glass transition (T_g) the polymer membrane is in a glassy state. The free rotation of the polymer segments around their axis is essentially prohibited in this type of polymer.[32] The relaxation time of a glassy polymer is extremely long and the polymer is not in a state of true thermodynamic equilibrium. The polymer is eventually trapped in a non-equilibrium state.[38] The rigidity of the polymer backbone does not allow efficient packing of the polymer chains which creates unrelaxed free volume or cavities in glassy polymers. The gas molecule jumps from one cavity to another in the direction of lower concentration and eventually crosses the thickness of the membrane (Figure 2.5). The

size, shape and distribution of these cavities or free volume control the diffusion of gas molecules through the glassy polymers.

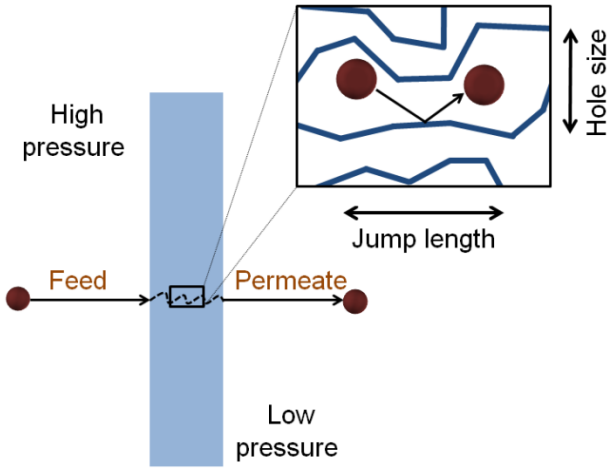

Figure 2.5: Schematic representation of transport of a gas molecule through a glassy polymer membrane.

The sorption of gas molecules in glassy polymer is complex. The gas sorption isotherm in glassy polymer generally exhibits nonlinear pressure dependence. The isotherm is concave to the pressure axis. This behavior is described by the dual-mode sorption which is an additive combination of Henry's law sorption and Langmuir sorption. The dual-mode sorption is expressed as-

$$C = C_D + C_H = k_D p + \frac{C'_H bp}{1 + bp} \qquad (2.7)$$

Where C is the total gas concentration in glassy polymer, C_D is the gas concentration based on Henry's law sorption, C_H is the gas concentration based on Langmuir sorption, k_D is the Henry's law coefficient, C'_H is the Langmuir capacity parameter and b is the Langmuir hole affinity

parameter. The Langmuir term stems from the non-equilibrium character of the polymer in the glassy state. [39]

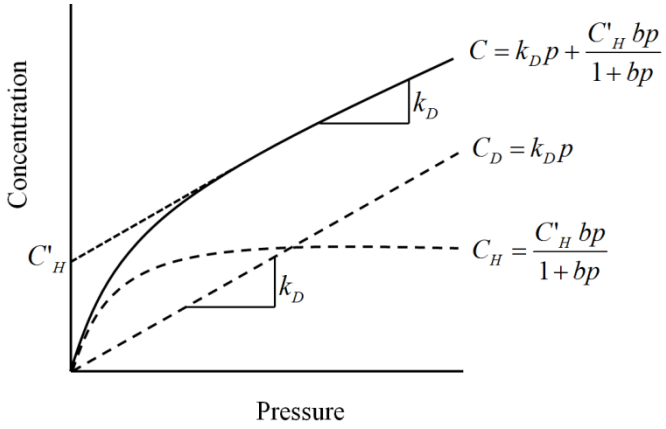

Figure 2.6: Schematic representation of transport of dual mode sorption isotherm. [39]

2.1.4 Gas transport through semicrystalline polymers

Semicrystalline polymers can be considered as a two phase system which has discrete regions of regularly ordered chains dispersed in the disordered amorphous phase. Gases are insoluble in the crystalline regions. As the polymer chains are three dimensionally packed, mass transfer of the gas molecule through the crystallites is also not possible. Therefore the presence of the crystallites results in a decrease of the effective cross-sectional area for the diffusion of a gas molecule in semicrystalline polymers. The path length of the diffusing gas molecule increases as it has to follow a rather tortuous path (Figure 2.7). Moreover, these crystallites also reduce the mobility of the polymer chains of the neighboring amorphous regions. Therefore, the rate of permeation of gas through a semicrystalline polymer membrane decreases with the increase of volume fraction of crystallites.[33]

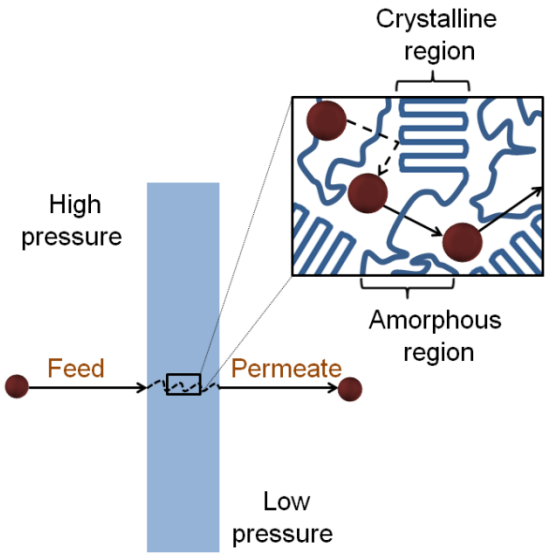

Figure 2.7: Schematic representation of transport of a gas molecule through a semi crystalline polymer membrane.

The solubility of gases in a semicrystalline polymer with a random distribution of crystallites is given as –

$$S = S_a.\phi_a \qquad (2.8)$$

where S_a is the solubility coefficient of the pure amorphous polymer and Φ_a is the volume fraction of the amorphous phase. The diffusion coefficient of gases through a semicrystalline polymer can be defined as-

$$D = \frac{D_a}{\tau\beta} \qquad (2.9)$$

where D_a is the diffusivity of the gas for a completely amorphous polymer, τ is the tortuosity factor and β is the chain immobilization factor. When there is no restricted segmental mobility in

the amorphous phase caused by the presence of the crystallites i.e. $\beta = 1$, the gas permeability is given by-

$$P = \frac{P_a}{\tau\beta}\phi_a \qquad (2.10)$$

where P_a is the gas permeability in the amorphous phase of the semicrystalline polymer.[36]

2.1.5 Influence of temperature on transport parameters

Generally, increasing temperature leads to higher gas permeability. A correlation of the kinetic and thermodynamic factors of permeability i.e. the diffusion coefficients and solubility coefficient with temperature provides ample insight into the gas transport phenomenon of the membrane. The permeability and diffusion of gases are correlated with temperature by Arrhenius relationships, in order to explore the temperature dependence of gas transport. According to Arrhenius relationship-

$$P = P_o \exp^{\frac{-E_P}{RT}} \qquad (2.11)$$

$$D = D_o \exp^{\frac{-E_D}{RT}} \qquad (2.12)$$

where P_o and D_o correspond to the respective values at infinite high temperature, E_P and E_D are activation energy of permeability and diffusivity, respectively. Typically in glassy polymer membranes the values of E_P and E_D are independent of temperature. But in rubbery and semicrystalline polymer membranes the values of this activation energy depend on temperature especially when the polymer undergoes a thermal transition in the temperature range of

measurement. The activation energy for permeation of the polymer membrane tends to increase with the transition from glassy to rubbery state due to increased intersegmental motion. E_D is the energy required for a gas molecule to make a diffusive jump. The size of the penetrant and the polymer chain packing determines the value of E_D. In a rubbery polymer an increase of temperature increases the large scale polymeric chain motion and eventually larger transient chain gaps are produced which facilitates the diffusive jumps of a gas molecule. Moreover, E_D is a function of molecular size of the penetrants. This phenomenon is illustrated by an expression given by Meares as follows-

$$E_D = 0.25 N_o \pi d^2 \lambda CED \qquad (2.13)$$

Where N_o is the Avogadro constant, d is the kinetic cross sectional area of a penetrant, λ is the length of diffusive jump and CED is the cohesive energy density of the polymer. Equation 2.13 narrates that E_D is dependent on d^2 which leads to a decrease in gas diffusivity with increasing penetrant size.

The Van't Hoff equation illustrates the temperature dependence of sorption of gases in polymer membranes as follows-

$$S = S_o \exp^{\frac{-\Delta H_S}{RT}} \qquad (2.14)$$

Here, S_o is a pre-exponential factor ΔH_S is the enthalpy of sorption. Typically, solubility of the gases decreases with increasing temperature and consequently ΔH_S has a negative value. Equations 2.4, 2.11, 2.12 and 2.14 imply that E_P is simply the sum of E_D and ΔH_S.

$$E_P = E_D + \Delta H_S \qquad (2.15)$$

Over a temperature range where thermal transitions of the polymer membrane are not involved E_P and E_D can be calculated from a logarithmic plot of P and D versus T^{-1}, respectively, and ΔH_S from equation 2.15. [34, 40]

2.2 Block copolymers & block copolymer nanocomposites

2.2.1 Block copolymer

"*Block copolymers are polymers, in which different homo or random copolymers are connected into one macromolecule. Block copolymers not only combine the properties of constituting blocks but may display new properties, depending on the way the different blocks are combined into one macromolecule, the strength of incompatibility between different blocks and their respective molecular weights.*"[41]

The block copolymers based on soft and hard blocks where one block has a low glass transition temperature (T_g) or melting temperature and the other has high glass or melting temperature are widely known as thermoplastic elastomer (TPE) block copolymers. The hard blocks act as a physical crosslink sites for the soft blocks at a temperature below the T_g or melting temperature of the hard block. Due to the covalent link between the chemically dissimilar blocks a three dimensional network of the physical crosslinks is created which is comparable with a covalently crosslinked system. Unlike covalently crosslinked polymers the hard block of a TPE block copolymer also melts at elevated temperature which allows easy processing (like a thermoplastic polymer). The combined properties of glassy or semicrystalline thermoplastic phase and soft

elastomers together with the ease of processing make TPE block copolymers highly attractive for commercial applications. A prominent example is the commercial TPE multiblock copolymer poly(ether-*b*-amide) well-known under the trade name PEBAX®. [42, 43]

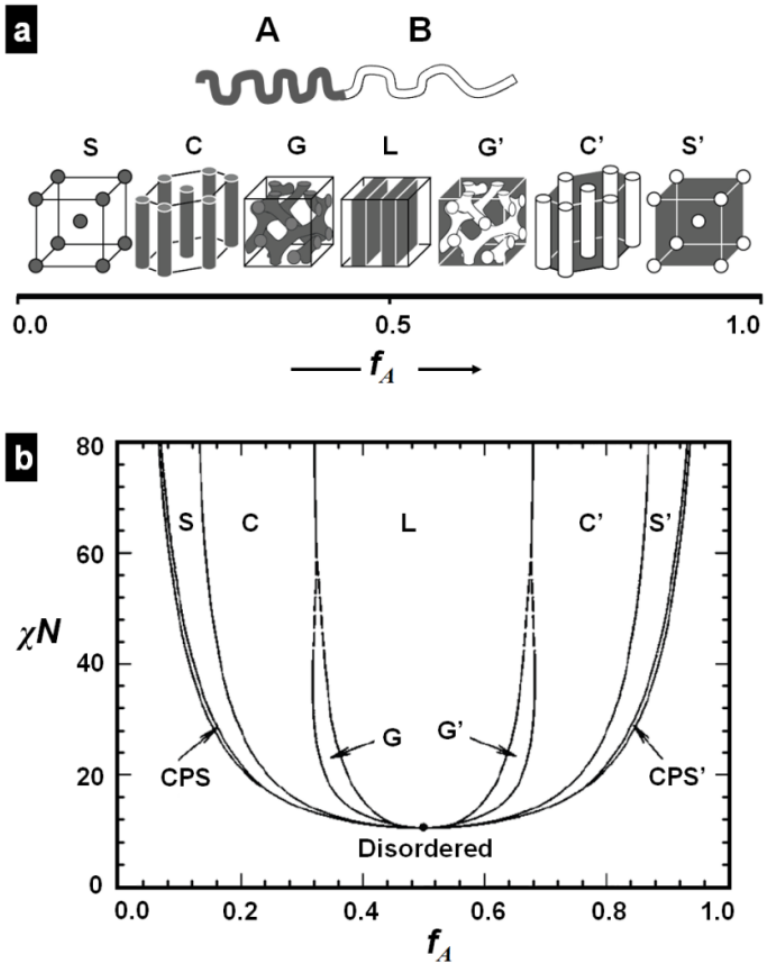

Figure 2.8: a) Schematic representation of microphase separated morphologies in an A-B diblock copolymer as a function of volume fraction of the A-block b) Theoretical phase diagram of A-B diblock copolymer predicted by self-consistent mean field theory. CPS and CPS' are closely packed spheres, S and S'are body-centered-cubic spheres, C and C'are hexagonally packed cylinders, G and G'are bicontinuous gyroids and L is lamellae. [44, 45]

An interesting feature of the block copolymers is their ability to form well defined microphase separated structures due to thermodynamic incompatibility of the covalently attached blocks. The well-known microphase separated equilibrium morphologies of a linear A-B diblock copolymer (namely sphere, cylinder, gyroid and lamella) as a function of volume fraction of block A (f_A) are depicted in figure 2.8a. [45, 46] The theoretical phase diagram for the diblock copolymer is illustrated in figure 2.8b. The term χN, i.e the product of Flory-Huggins-Staverman-parameter χ and the degree of polymerization N, refers to the degree of incompatibility between the blocks.[41] At equilibrium the chains of the A-B diblock copolymer is arranged in minimum free energy configurations. If either χ or N are small enough (when the value of $\chi N << 10$) the entropic factor dominates and the block copolymer is in a disordered state. If N is sufficiently high an increase of the value of χ favors a reduction in A-B monomer contact and local compositional ordering takes place due to loss of entropy. As the value of χN increases a disorder-to-order phase transition occurs due to a balance between enthalpic and entropic factors.[47] However, at very low and very high f_A the block copolymer is in a disordered state for all values of χN. For a fixed value of χN above the disorder-to-order transition, with an increase of f_A the order-to-order transition starts from closely packed spheres (CPS), passing through body-centered cubic spheres (S), hexagonally packed cylinders (C) and bicontinuous gyroid (G) to lamella (L). For further increase of the value of f_A morphological inversion takes place as follows L → G' → C' → S' → CPS'→ disordered. [45]

2.2.2 Block copolymer nanocomposites

"Since the first reports in the late 1980s, the term "polymer nanocomposite" has evolved to refer to a multicomponent system in which the major constituent is a polymer or blend thereof and the minor constituent has at least one dimension below 100 nm."[48] The physical and chemical properties of the constituent materials (i.e. the polymer matrix and the filler), the length scale and the morphological details of the dispersion determine the ultimate properties of a nanocomposite material. Therefore, a homogenous dispersion of the nanoparticle in the polymer matrix is the prerequisite to explore the potential of the polymer nanocomposite. From a thermodynamic point of view the dispersion of nanoparticles in a polymer creates a polymer-particle interface which eventually leads to a compromise between the decrease in polymer conformational entropy and the gain in translational entropy of the nanoparticle. Theoretical studies suggest that the potential application of the block copolymer nanocomposite can reach far beyond the nanocomposites prepared from homopolymers. However, the dispersion of nanoparticles in a block copolymer matrix and precise control of the final morphology is associated with a complex synergy of enthalpy and entropy. [49-51]

Functionalization of the nanoparticle with polymeric ligands compatible with one of the blocks creates an enthalpic driving force for localization of nanoparticle in a selective domain. Besides this, there is also the possibility of an entropic driving force, if the conformational entropy of a polymer is increased. Molecular weight, areal density and nature of the ligands are key variables in controlling the enthalpic and conformational entropic interactions. The other important factor,

i.e. the translational entropy depends upon the ratio between the nanoparticle and the block copolymer domain size.

The change in free enthalpy in bulk block copolymer nanocomposites due to incorporation of functionalized nanoparticles can be stated as-

$$\Delta G = \Delta H_{ligand-polymer} - T(\Delta S_{con} + \Delta S_{trans}) \qquad (2.16)$$

where $\Delta H_{ligand\text{-}polymer}$ is the enthalpic contribution of the interaction between the segment of the block copolymer and the ligand attached to the nanoparticle, ΔS_{con} is the change in conformational entropy of the polymer chains ΔS_{trans} is entropic contribution due to the number of distinguishable physical arrangements of the nanoparticles in the nanocomposite. [52] The enthalpic interactions between the ligand of the nanoparticle and the respective monomeric unit of A and B block of a A-B diblock copolymer can be expressed by χ_{PA} and χ_{PB}, respectively. The location of the functionalized nanoparticles is expected to be in A block of the microphase separated diblock copolymer matrix for a negative value of χ_{PA} and a positive the value of χ_{PB}. The design of the ligand of nanoparticles having a favorable mixing enthalpy with one of the blocks of a A-B diblock copolymer is a current research topic. Upto now only $\chi_{PA} = 0$, $\chi_{PB} > 0$ has been achieved.[49]

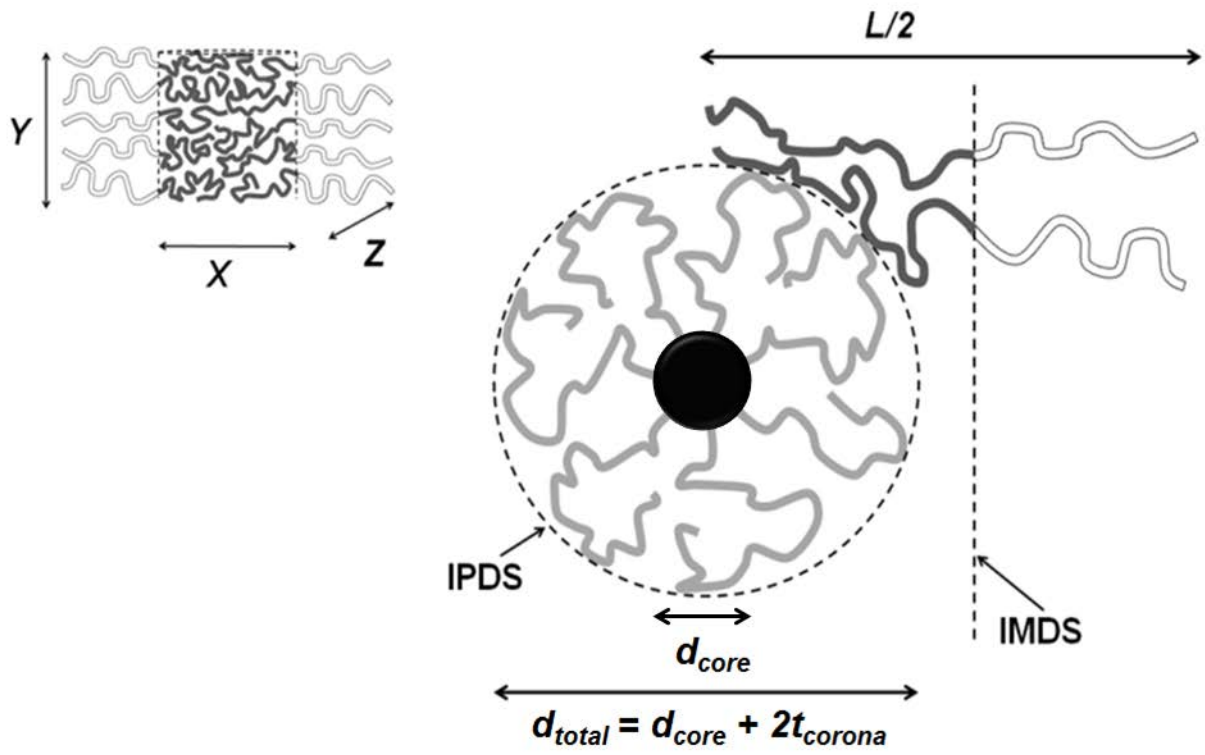

Figure 2.9: Schematic representation of a functionalized nanoparticle in an A-B diblock copolymer matrix.[49]

Figure 2.9 represents a functionalized nanoparticle within a block copolymer matrix. The width, height and depth of the block copolymer domain is given by X, Y and Z, respectively. The junction points of the blocks are located at the intermaterial dividing surface (IMDS). The core of the nanoparticle is rigid and has a diameter of d_{core}. The corona region comprised of surface grafted ligands has a thickness t_{corona}. Depending on the grafting density and size of the ligands the corona can undergo limited shape distortions. The circumferential area of the relevant particle size $d_{total} = d_{core} + 2t_{corona}$ determines the contact area of the particle with the surrounding block copolymer domain i.e. the interparticle domain surface (IPDS). At least one of the dimensions of the microdomain should be large enough to accommodate the functionalized

nanoparticle. Thus, there is a limiting size of particle which can be accommodated in a polymer domain for a given chemical composition of the nanoparticle ligand and block copolymer segment (which defines the mixing enthalpy). Accommodation of a large particle in a block copolymer microdomain requires formation of a highly curved IMDS (the curvature decreases with particle size) and the associated chain conformational distortions. Therefore the large particles tend to aggregate and macrophase separate from the block copolymer matrix. [49]

Part - C:

Chapter 3. Experimental

3.1. Materials

PEBAX® MH 1657 and PEBAX® 2533 were purchased from ARKEMA, France. PolyActive™ 1500PEGT77PBT23, PolyActive™ 3000PEGT77PBT23 and PolyActive™ 4000PEGT77PBT23 were purchased from PolyVation®, The Netherlands. PEG POSS®, glycidyl POSS® and glycidyldimethylsilyl POSS® were purchased from Hybrid Plastics®, USA. Boron triflouride diethyletharate, triethyl amine, acetyl chloride, mesyl chloride, *tert*-butylammonium iodide, thionyl chloride, sodium azide, methoxy poly(ethylene glycol) (M_n=350 g/mol) and poly(ethylene glycol) (M_n=200 g/mol) were purchased from Sigma-Aldrich. Multiwalled carbon nanotubes were supplied by FutureCarbon GmbH, Germany and Consejo Superior de Investigaciones Científicas (CSIC), Spain. Sodium hydroxide, hydrocholoric acid, dichloromethane, *N*,*N*-dimethylformamide, chloroform, toluene, tetrahydrofuran, butanol and ethanol were purchased from Merck KGaA, Germany. All chemicals were used as received without any further purification.

3.2. Functionalization of nanoparticles

3.2.1. Functionalization of POSS

3.2.1.1. Grafting methoxy poly(ethylene glycol) (Mn = 350) via epoxide ring opening reaction

4 g (3 mmol) glycidyl POSS® and 30g (86 mmol) methoxy polyethylene glycol (PEG) (M_n=350 g/mol) were dissolved in 200g solvent (chloroform, toluene or tetrahydrofuran). Approximately

400 µl of boron triflouride diethyletharate catalyst were added to the reaction mixture and stirred for 48 hours at room temperature. The solvent was removed from the reaction mixture using a rotary evaporator. The reaction mixture was dissolved in dichloromethane (DCM) and 100 g 2 wt% aqueous solution of NaOH was added to convert the remaining catalyst into salt. The unreacted PEG and the salt were removed from the mixture by DCM and water extraction. Extraction was continued until the entire unreacted PEG fraction was removed (confirmed by ^{13}C NMR spectra). The PEG modified glycidyl POSS was collected in the organic phase. The organic phase was dehydrated using $MgSO_4$ salt and filtered. Finally, DCM was evaporated to collect the product. Using the same procedure PEG (M_n=350 g/mol) modified glycidyldimethylsilyl POSS® was also synthesized.

3.2.1.2. Acylation & mesylation of PEG grafted POSS nanoparticles

PEG functionalized glycidyl POSS (using toluene as solvent) was dissolved in DCM. The solution was cooled down using an ice bath and triethylamine (TEA) was added. At this point acetyl chloride (when acylation was performed) / mesyl chloride (when mesylation was performed) was added. Then the ice bath was removed and the reaction was kept at room temperature for 1 day. The reaction mixture was first filtered to remove the salts which precipitated during the reaction and washed with solution of 500 ml 1 M hydrochloric acid (HCl), 500 ml 1 M sodium hydroxide (NaOH) and 500 ml 1 M sodium chloride (NaCl), respectively. The organic layer was collected and finally dicholoromethane was removed using a rotary evaporator and the product was obtained.

3.2.1.3. Azidation of PEG grafted POSS nanoparticles

Mesylated PEG functionalized POSS nanoparticles were dissolved in *N*,*N*-dimethylformamide (DMF). Sodium azide and *tert*-butylammonium iodide (TBAI) were sequentially added. The reaction was continued at 60 ºC for 48 hours. Then the reaction mixture was filtered and DMF was removed by rotary evaporation. The mixture was dissolved in DCM and washed extensively with distilled water to remove the remaining TBAI.

3.2.2. Functionalization of MWCNT

3.2.2.1. Oxidation of MWCNT

Multiwalled carbon nanotubes (MWCNT) supplied by FutureCarbon and CSIC were used without further purification. 4 g MWCNT was added in 600 ml 65 v% HNO_3 and sonicated for 30 minutes using a water bath. The mixture was then stirred in an oil bath at 65 ºC for 48 h under reflux. The mixture was then transferred to a filtration funnel and filtered with deionized water until the pH of the filtrate was identical to the deionized water used for the filtration. Finally the oxidized MWCNT (obtained as residue) was dried in vacuum oven at 100 ºC for 48 hours.

3.2.2.2. Chlorination of oxidized MWCNT

300ml thionyl chloride ($SOCl_2$) was added in 4 g of MWCNT and stirred at 65 ºC for 24 h. The flask was connected to a trap system containing 4 wt% NaOH aqueous solution (to trap SO_2 and HCl vapour). The reaction mixture was filtered using a Sartorius Type 118 PTFE filter and

washed extensively with THF. The filtrate was neutralized by dropwise addition of 4 wt% NaOH aqueous solution. The chlorinated MWCNT was obtained as residue and dried in a vacuum oven at room temperature for 48 hours.

3.2.2.3. Grafting poly(ethylene glycol) to the chlorinated MWCNT via esterification

300 ml poly(ethylene glycol) (PEG) of Mn = 200 g/mol were added in 4 g chlorinated MWCNT. The mixture was stirred at 120 ºC for 48 h under condensation. Then the reaction mixture was cooled down and filtered using a Sartorius Type 118 PTFE filter and washed with THF. Washing was continued until all the unreacted PEG molecules were removed from the system (confirmed by thermogravimetric analysis).

3.3. Preparation of nanocomposite membranes

3.3.1. PEG functionalized POSS incorporated PEBAX® membrane

Dense membranes were prepared by solution casting in Teflon molds. Mixtures of PEG POSS® and PEBAX® MH 1657 were dissolved in a mixture of ethanol/water (70/30 wt %) under reflux (80 ºC) for 2h. Similarly, mixtures of PEG POSS® and PEBAX® 2533 were dissolved in *n*-butanol at 70 ºC for 2h. The concentration of the solution was 3 wt% and the PEG POSS® content was varied from 10-50 wt% of the polymer. After cooling to room temperature the obtained homogeneous solution was poured into Teflon molds. The solutions of PEBAX® MH 1657 and PEG POSS® were dried for 24 hours, while those of PEBAX® 2533 and PEG POSS®

were dried for 48 hours at 40 ºC. The films were dried under vacuum overnight at 30 ºC. The Membrane thicknesses were measured by a digital micrometer and they varied from 100 to 200 μm.

3.3.2. PEG functionalized POSS incorporated PolyActive™ membrane

PolyActive™ membranes and their nanocomposites with PEG POSS® were prepared by a solution casting method. 3 wt% solutions of pure polymer and the mixture with PEG POSS® were prepared using chloroform as solvent. The obtained homogeneous solution was filtered and poured into a Teflon® mold and kept at room temperature for film formation. The molds were covered with a glass Petri dish to ensure slow evaporation of solvent. PEG POSS® content was varied in the range 10-30 wt% with respect to the total weight of the nanocomposite.

3.3.3. PEG functionalized MWCNT incorporated PEBAX® membrane:

PEG functionalized MWCNTs were dispersed in a mixture of ethanol/water (70/30 wt %) using tip sonication. Then PEBAX® MH 1657 was added (3 wt% of the solvent mixture) to the dispersion and dissolved under reflux (80 ºC) for 2 h. The obtained solution was poured in a Teflon mold and dried at 40 ºC for 24 h. The MWCNT content was varied from 0.5-2 wt% of the polymer.

3.4. Characterization

3.4.1. Time-lag method

"Time-lag method" is a standard method for determination of permeability and diffusion coefficient of a gas in a membrane. If the membrane is free of penetrant molecules at the beginning of permeation, the feed pressure is constant and much larger than the permeate pressure, the amount of penetrant per unit membrane passing through a membrane is given by-

$$\frac{Q_t}{l.c_h} = \frac{Dt}{l^2} - \frac{1}{6} - \frac{2}{\pi^2}\sum_{n=1}^{\infty}\frac{(-1)^n}{n^2}\exp\left[\frac{-Dn^2\pi^2 t}{l^2}\right] \qquad (3.1)$$

During the initial stage of permeation, Q_t increases non linearly with t. A steady state is approached when t→∞, and the relation between Q_t vs t becomes linear.[53]

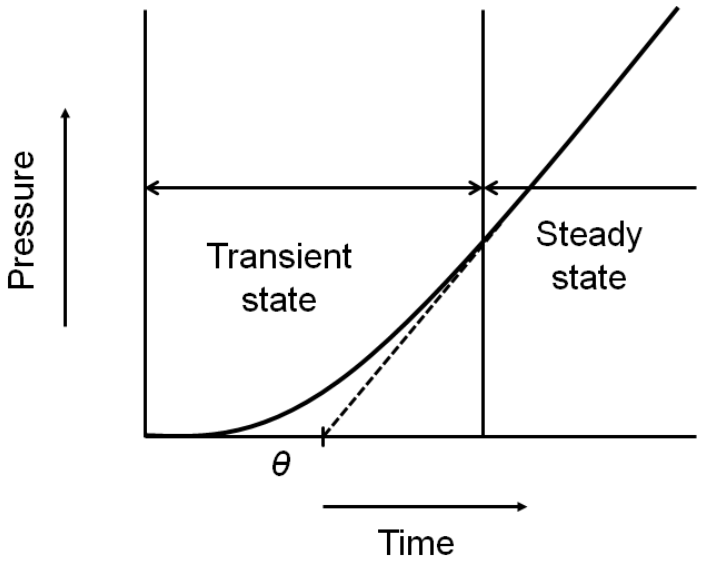

Figure 3.1: Time-lag measurement of gas permeation.

By extrapolating the steady state permeation curve, the intercept (θ) on time axis can be obtained, which is referred to as the time-lag. Permeability (P), diffusion coefficient (D) and solubility (S) were determined in the temperature range of 30 - 70 ºC using an in-house built highly automated measurement facility using the following equations:

$$P = D \cdot S = \frac{V_p \cdot l}{A \cdot R \cdot T \cdot \Delta t} \ln \frac{p_f - p_{p1}}{p_f - p_{p2}} \quad (3.2)$$

$$D = \frac{l^2}{6\theta} \quad (3.3)$$

where, V_p is the permeate volume, l is the membrane thickness, A is the membrane area, R is the gas constant, p_f is the feed pressure considered constant in the time range Δt, p_{p1} and p_{p2} are permeate pressures at time moment 1 and 2, Δt is the time difference between two points (1 and 2) on the pressure curve, and θ is the time-lag.

3.4.2. Fourier transformation infrared spectroscopy (FT-IR)

FT-IR spectra were recorded in an attenuated total reflectance (ATR-diamond crystal) mode with a Bruker ALPHA FT-IR spectrometer in a spectral range of 400 - 4000 cm^{-1} with a resolution of 2 cm^{-1} and average of 32 scans.

3.4.3. Nuclear magnetic resonance spectroscopy (NMR)

NMR spectroscopic measurements were performed on a Bruker AV300 spectrometer at a sample temperature of 298 K using $CDCl_3$ as solvent. ^{1}H NMR spectra were recorded applying a 10 ms 90º pulse. ^{13}C NMR spectra were recorded using DEPTQ-135 sequences employing a waltz-16 decoupling scheme to determine multiplicity. Quantitative ^{13}C NMR spectra were recorded using an inverse gated decoupled sequence.

3.4.4. Raman spectroscopy

A Bruker Senterra Raman microcope was used to record the Raman spectra. 532 nm laser and 10 fold objective was used to measure multiple sample areas by applying a square array 300 μm X 300 μm.

3.4.5. Differential scanning calorimetry (DSC)

A DSC 1 (Star system) from Mettler Toledo was used to study the thermal transitions of prepared membranes in the temperature range of -100 to 250 ºC using nitrogen as a purge gas stream (60 mL/min). All DSC runs were performed at the scan rate of 10 K/min.

3.4.6. Thermogravimetric analysis (TGA)

Thermogravimetric analysis was carried out between 25 ºC to 1000 ºC using a TGA device Netzsch TG209 F1 Iris device at a constant argon pressure with a flow rate of 20 mL/min.

3.4.7. Scanning electron microscopy (SEM)

A scanning electron microscope (Merlin, Zeiss) equipped with an EDS system (Oxford) was used to characterize both surface and cross section morphology of the samples with secondary electrons (SE) and X-rays.

3.4.8. Atomic force microscopy (AFM)

A Veeco (now Bruker) MultiMode NanoScope IV atomic force microscope (AFM) operating in TappingMode™ at room temperature using commercial silicon AFM tips were used to study the surface and cross section of the membranes.

Part – D:

Chapter 4. PEBAX® with PEG functionalized POSS as nanocomposite membranes for CO_2 separation

4.1. Introduction

Commercially available thermoplastic elastomers poly(ether-*block*-amide) under the trade name PEBAX® having flexible polyether and rigid polyamide segments can be used to separate CO_2 from light gases (e.g. H_2 or N_2). The polymers containing less polar poly(tetramethylene oxide) (PTMO) blocks have higher gas permeability compared to those containing more polar poly(ethylene oxide) (PEO) blocks. But the selectivity of CO_2 over the light gases is higher in the polymers which have higher content of polar groups.[54] Studies have been reported to increase the permeability of a hydrophilic grade PEBAX® MH 1657 (60 wt% PEO and 40 wt% polyamide 6) without affecting the selectivity by incorporation of low molecular weight poly(ethylene glycol) (PEG).[55, 56] Moreover, a low molecular weight copolymer containing 20 wt% of polydimethylsiloxane as a backbone and 80 wt% of poly(ethylene glycol) as a side chain was reported to increase the permeability even more than pure PEG.[57] Recently, molecular level mixed matrix membranes comprising PEBAX® and polyhedral oligomeric silsesquioxanes (POSS) have been reported to exhibit simultaneous enhancement in CO_2 permeability and CO_2/H_2 selectivity at extremely low POSS loadings.[58] POSS molecules have a rigid cage-like structure which is intermediate between silica and siloxane. The empirical formula can be rendered as $(RSiO_{1.5})_n$, n = 6 - 12, where R is some functional group. A small particle (molecule) size in the range of 1 - 3 nm and the possibility of tailoring properties by introduction of various functional groups makes POSS an attractive candidate for organic inorganic hybrid nanocomposites. [59] This chapter deals with the effect of incorporation of a commercial nanoparticle PEG POSS® (poly(ethylene glycol) modified polyoctahedral oligomeric silsesquioxanes) upon CO_2 separation performance, thermal properties and morphology of two different grades of PEBAX®.

4.2. Results

4.2.1. Chemical structure and composition

Table 4.1: Composition of two grades of PEBAX®.

Grade of PEBAX®	Polyether Phase	Polyether Content (wt%)	Polyamide Phase	Polyamide Content (wt%)
PEBAX® MH 1657	-$(CH_2$-CH_2-$O)_n$- Poly(ethylene oxide)	60	-$(NH$-$(CH_2)_5$-$CO)_n$- Polyamide 6	40
PEBAX® 2533	-$(CH_2$-CH_2-CH_2-CH_2-$O)_n$- Poly(tetramethylene oxide)	80	-$(NH$-$(CH_2)_{11}$-$CO)_n$- Polyamide 12	20

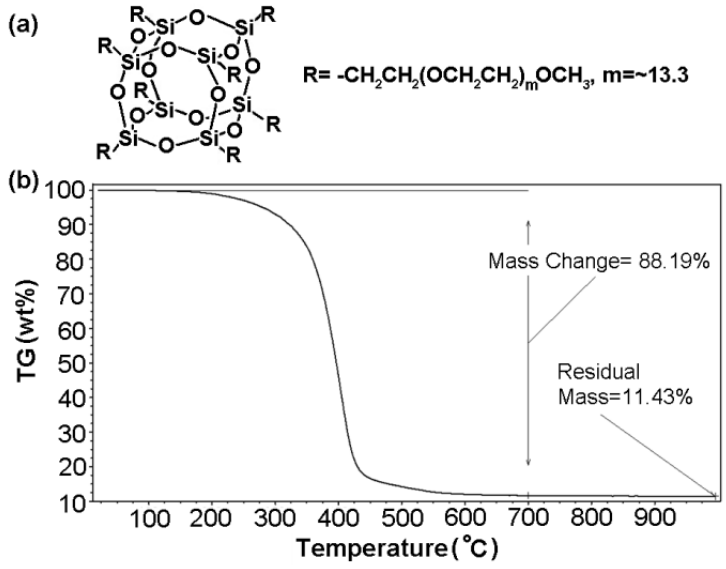

Figure 4.1: Composition of PEG POSS® (a) Structure provided by manufacturer (b) Thermogravimetric analysis.

The compositions of PEBAX® polymers used for this study are summarized in Table 4.1. [54, 55, 60] POSS used as nanofiller for this study (the structure available from manufacturer is presented in Figure 4.1a) is functionalized with PEG which has the same chemical structure as that of the amorphous phase of PEBAX® MH 1657. But in the other case (i.e PEBAX® 2533) the amorphous phase is composed of a different polyether i.e. PTMO.

From the structure and molecular weight provided by the supplier, the weight percentage of PEG surrounding the POSS was calculated. According to the calculation PEG POSS® consists of approx. 92 wt% PEG. Thermogravimetric analysis (TGA) of PEG POSS® is presented in Figure 4.1(b). In TGA 88 % mass loss was observed between 100 - 700 ºC and 11.5 % residue was left at 995 ºC, which is in accordance with the calculation made from the structure. The mass loss reveals that the commercial PEG POSS® is decorated with approximately 88 wt% PEG which degraded between 100 - 700 ºC and the residual mass comes from the cage structure of oligomeric silsesquioxanes as well as some carbonaceous residues. Hence, the commercial PEG POSS® contains higher weight percentage of polyether than both PEBAX® MH 1657 and PEBAX® 2533 which means incorporation of PEG POSS® increases the total polyether content of the nanocomposite prepared by both the grades of PEBAX® significantly.[61]

4.2.2. Gas separation performance

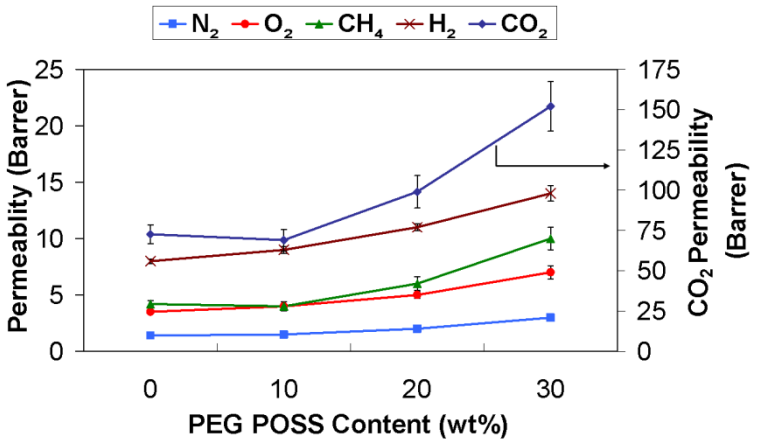

Figure 4.2: Single gas permeability as a function of PEG POSS® content in PEBAX® MH1657. Permeability of N_2, O_2, CH_4 and H_2 are plotted on left ordinate and that of CO_2 right ordinate.

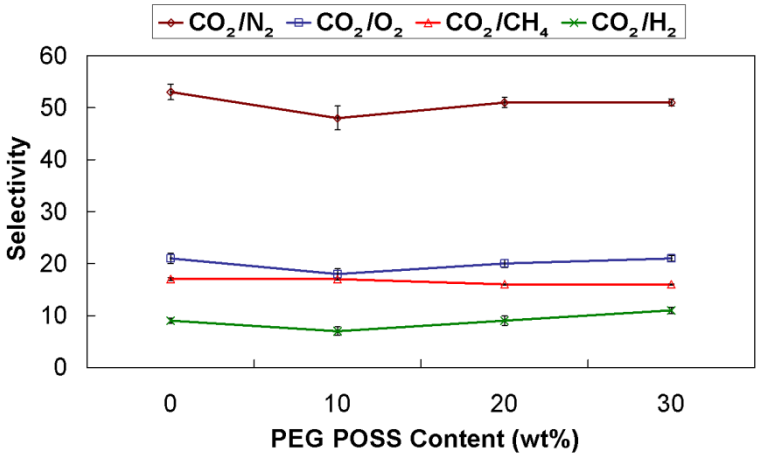

Figure 4.3: CO_2 selectivity over light gases as a function of PEG POSS® content in PEBAX® MH1657.

Figure 4.2 shows the values of single gas permeabilities of pure PEBAX® MH 1657 and the composites prepared by incorporation of PEG POSS® as a function of PEG POSS® content. Significant increase in permeability of all the gases was observed up to 30 wt% PEG POSS® incorporation. The permeability of CO_2 increased from 73 to 152 barrer, this means that the permeability of a nanocomposite membrane containing 30 wt% PEG POSS® was two times higher than of pure PEBAX® MH 1657. For higher amounts of PEG POSS® (40 wt% and 50 wt%) the membranes became too soft to be fixed in the measurement cell of the time-lag measurement facility. Figure 4.3 clearly shows that, due to 10 % incorporation of PEG POSS® the selectivity of the membrane decreased slightly but as the PEG POSS® content was increased to 20 and 30 wt%, similar selectivity like PEBAX® MH 1657 was found for all four gas pairs. The loss of selectivity at 10 wt% PEG POSS® loading, in spite of increase in total polyether content may be related with the crystallinity of the polyether domain (discussed in section 4.3).

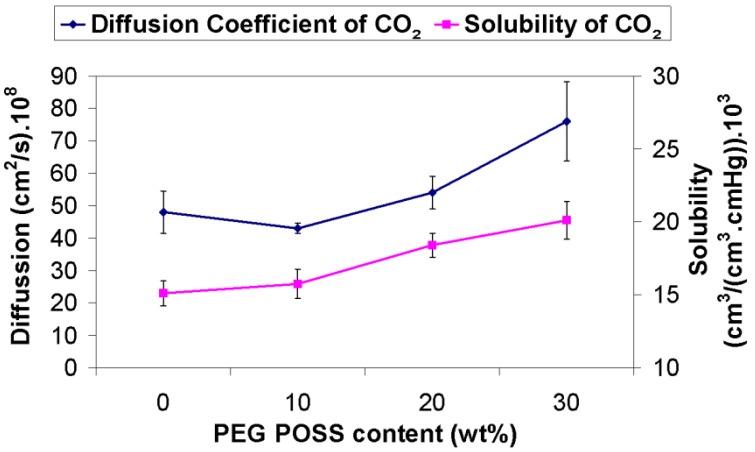

Figure 4.4: Diffusion coefficient and solubility of CO_2 as a function of PEG POSS® content in PEBAX® MH1657.

To gain insight into the effect of PEG POSS® incorporation upon the gas transport mechanism through the membrane, diffusion coefficient and solubility of CO_2 are plotted as a function of PEG POSS® content in Figure 4.4. It was observed that at a loading with 10 wt% PEG POSS® the diffusion coefficient was slightly lower than for pure PEBAX® MH 1657. However, as the error bars overlap each other, the decrease in diffusion of CO_2 in the membrane is actually not significant. But at higher loadings of PEG POSS® a significant increase of the diffusion coefficient was observed. The solubility of CO_2 appeared to increase with increasing of PEG POSS® content. It is already well established that ethylene oxide units provide very good solubility of condensable CO_2 gas in the polymer membrane due to affinity of the polar ether oxygen and quadrapolar CO_2 gas.[12] Hence, the solubility of CO_2 is directly related with the increase of ether oxygen in the nanocomposite membrane.

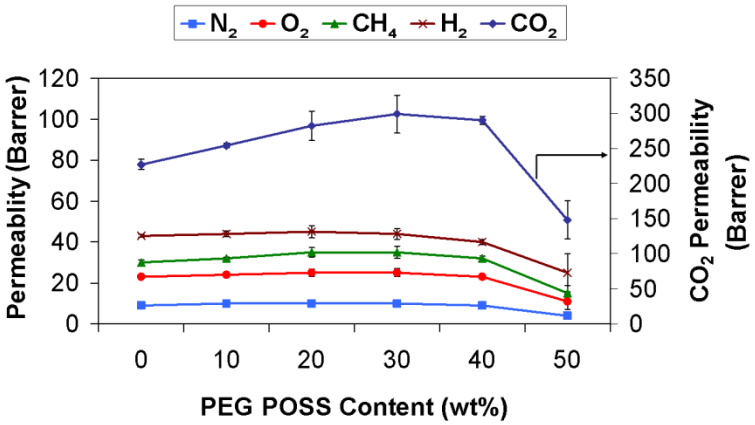

Figure 4.5: Single gas permeability as a function of PEG POSS® content in PEBAX® 2533. Permeability of N_2, O_2, CH_4 and H_2 are plotted on left ordinate and that of CO_2 right ordinate.

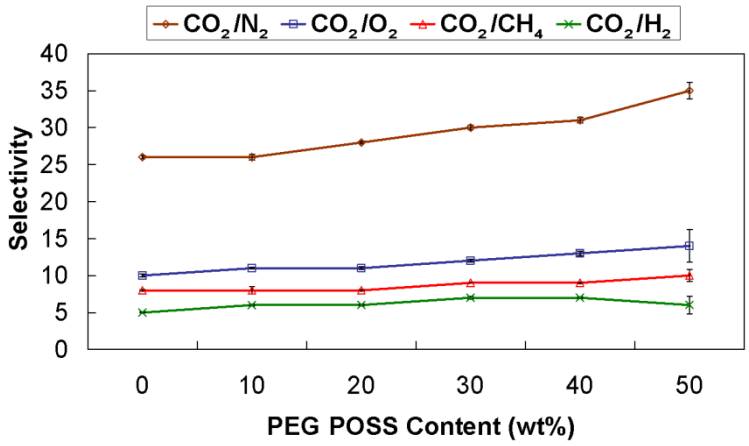

Figure 4.6: CO_2 selectivity over light gases as a function of PEG POSS® content in PEBAX® 2533.

Incorporation of PEG POSS® in PEBAX® 2533 also increased the permeability of the membranes up to 30 wt% loading, as represented in Figure 4.5. But, the increase in permeability was not as significant as in case of PEBAX® MH 1657. 30 wt% PEG POSS® loading in PEBAX® 2533 leads to 32 % higher permeability of CO_2 than that of pure PEBAX® 2533. For higher PEG POSS® content, permeability of the gases showed a decreasing trend and after incorporation of 50 wt% PEG POSS® the permeability of the gases through the nanocomposite membrane was well below the permeability through the pure polymer membrane, although the ether oxygen content is higher in 50 wt% PEG POSS® containing nanocomposite membrane than that of pure PEBAX® 2533. In contrast to what was observed in the case of PEBAX® MH 1657, incorporation of PEG POSS® leads to an increase in selectivity of the membrane in PEBAX® 2533, as evident from Figure 4.6. The selectivities of CO_2/N_2, CO_2/O_2, CO_2/CH_4 and CO_2/H_2 of the pure PEBAX® 2533 were found to be 26, 10, 8, and 5, respectively, while those of

PEBAX® 2533 with 50 wt% PEG POSS® nanocomposite membrane increased to 35, 14, 10, and 6, respectively.

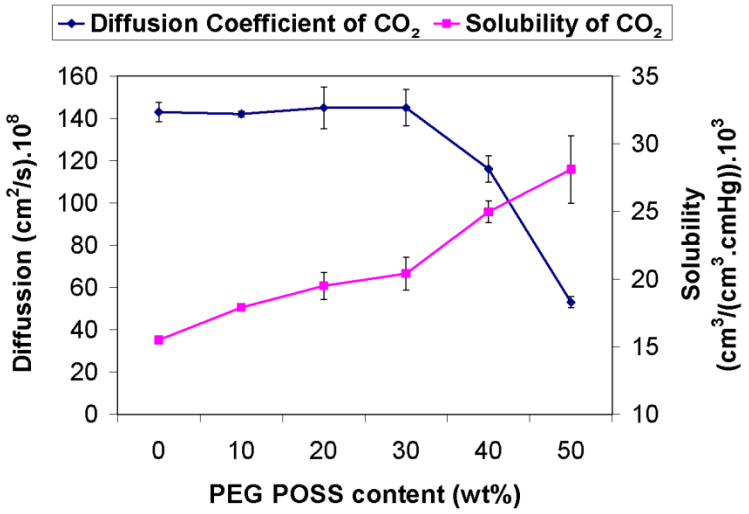

Figure 4.7: Diffusion coefficient and solubility of CO_2 as a function of PEG POSS® content in PEBAX® MH1657.

From Figure 4.7 it is also clear that an incorporation of PEG POSS® into PEBAX® 2533 has a different impact upon the gas transport mechanism through the membrane compared to that in PEBAX® MH 1657. In this case diffusion of CO_2 remains unchanged upto incorporation of 30 wt% PEG POSS® and at higher loadings it drops significantly. However, the solubility of CO_2 increases significantly with the increase of PEG POSS® content what is similar to what was observed for PEBAX® MH 1657. These observations elucidate the fact that at PEG POSS® loadings higher than 30 wt% the permeability of CO_2 shows a decreasing trend (Figure 4.5) because of the significant drop of diffusion through the membrane (Figure 4.7). The steady

increase of CO_2 selectivity for all four gas pairs (Figure 4.6), with the incorporation of PEG POSS® content stems from the increase of CO_2 solubility (Figure 4.7) in the membrane.

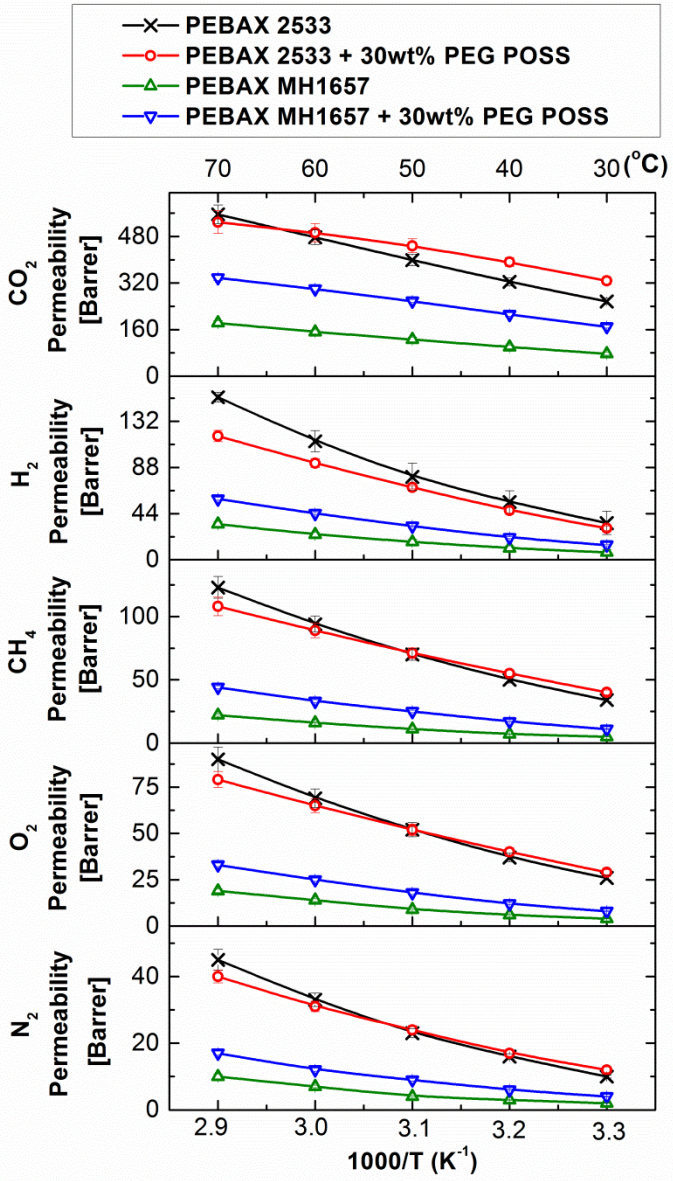

Figure 4.8: Permeability of gases as a function of temperature of PEBAX® MH1657 and PEBAX® 2533 before and after 30 wt% PEG POSS® incorporation.

Since at 30 ºC the best gas separation performance was observed for 30 wt% PEG POSS® loading in both grades of PEBAX®, this composition was chosen to study the effect of temperature upon CO_2 separation. The membranes were heated from 30 ºC to 70 ºC and the permeability of N_2, O_2, CH_4, H_2 and CO_2 were measured at every 10 ºC interval (plotted in Figure 4.8). Then the measurement cell was cooled down from 70 ºC to 30 ºC and the membranes were taken out of the cell. The gas permeability was determined only during heating the measurement cell. The measurements were not repeated during cooling. The permeability of all the gases increases with increasing temperature in pure PEBAX® as well as in PEG POSS® containing nanocomposite membranes. But a careful examination reveals that, although the nanocomposite membrane prepared from PEBAX® 2533 has a higher permeability of CO_2 and similar permeability of other gases (N_2, O_2, CH_4 and H_2) at relatively low temperatures (e.g. 30 ºC and 40 ºC), the increase of gas permeability with the increase of temperature for the nanocomposite membrane is not as significant as that of the pure polymer membrane. Especially, the permeability of H_2 is considerably lower in the nanocomposite membrane at 70 ºC. On the other hand, in PEBAX® MH 1657 the permeability of all the gases is higher in the nanocomposite membrane than in the pure polymer membrane at all temperatures.

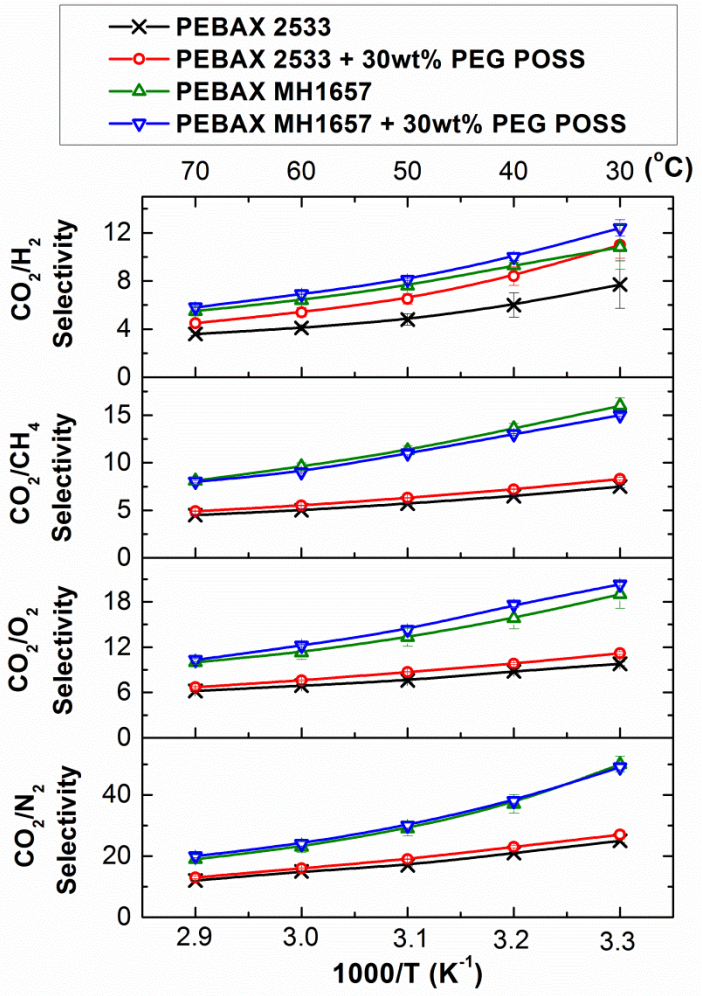

Figure 4.9: CO_2 selectivity over light gases as a function of temperature of PEBAX® MH1657 and PEBAX® 2533 before and after incorporation of 30 wt% PEG POSS®.

Polyether based membranes are notorious for loss of CO_2 selectivity over light gases with the increase of temperature. Figure 4.9 shows that both grades of PEBAX® have lost CO_2 selectivity significantly for all four gas pairs with the increase of temperature with and without incorporation of 30 wt% PEG POSS®. Hence, incorporation of PEG POSS® did not prevent the loss of CO_2 selectivity at high temperature. However, the selectivity of CO_2 over H_2 of

PEG POSS® containing PEBAX® 2533 nanocomposite membrane was found to be slightly higher than for the pure polymer membrane up to 50 ºC.

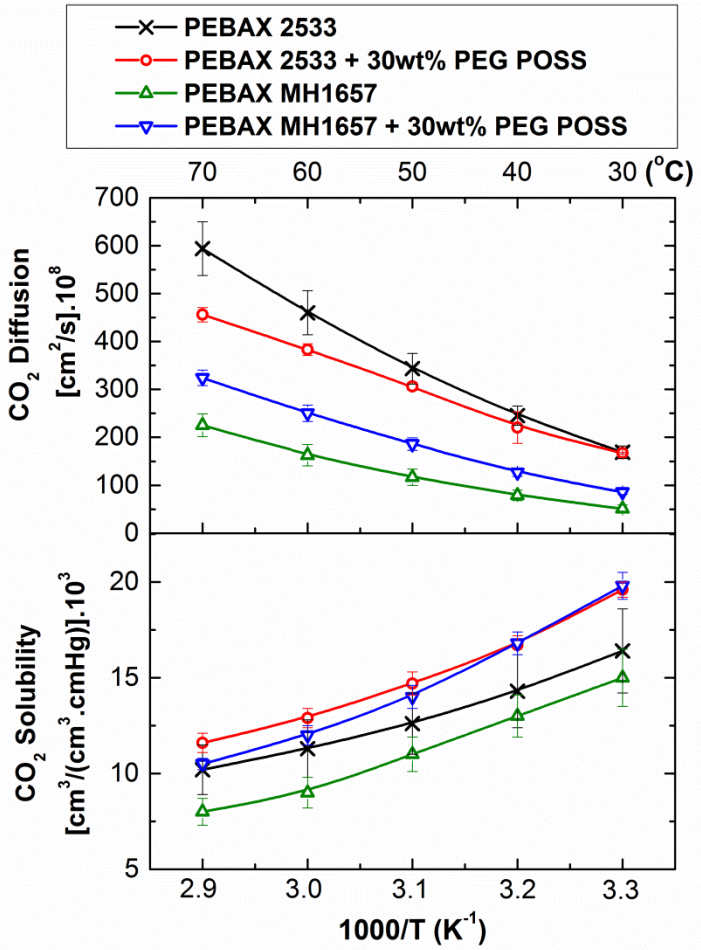

Figure 4.10: Diffusion coefficient and solubility of CO_2 as a function of temperature of PEBAX® MH1657 and PEBAX® 2533 before and after 30 wt% PEG POSS® incorporation.

Figure 4.10 shows that for all four membranes diffusion of CO_2 increases substantially while solubility of CO_2 undergoes a dramatic decrease with the increase of temperature. Interestingly, it was observed that diffusion of CO_2 increased much more significantly with the increase of

temperature in the PEBAX® 2533 membrane than the corresponding nanocomposite membrane. However, for PEBAX® MH 1657, the diffusion coefficient seemed to have slightly higher value at all temperatures after PEG POSS® incorporation.

Table 4.2: E_P, E_D and ΔH_S (Chapter 2, equation 2.11, 2.12, 2.14 and 2.15) of CO_2 through PEBAX® MH1657 and PEBAX® 2533 before and after 30 wt% PEG POSS® incorporation.

Composition	E_p of CO_2 (Kj/mol)	E_D of CO_2 (Kj/mol)	ΔH_S of CO_2 (Kj/mol)
PEBAX® 2533	16.7	27.2	-10.5
PEBAX® 2533 + 30 wt% PEG POSS®	10.3	22.2	-11.9
PEBAX® MH 1657	18.6	32	-13.4
PEBAX® MH 1657 + 30 wt% PEG POSS®	14.9	28.8	-13.9

E_P calculated from the slope of *ln P* vs *1000/T* (using equation 2.11), E_D calculated from the slope of *ln D* vs *1000/T* (using equation 2.12) and ΔH_S calculated from equation 2.15 are plotted in Table 4.2. A positive value of E_P is attributed to the increase of permeability with the increase of temperature. A significant drop of E_P can be noticed in PEG POSS® incorporated nanocomposite membranes compared to the pure polymer membrane. Therefore, the rate of increase of CO_2 permeability as a function of temperature is lower in the nanocomposite membranes compared to the pure polymer membrane (although CO_2 permeability is higher at all temperatures within 30 ºC to 70 ºC for the PEG POSS® containing PEBAX® MH 1657 nanocomposite membrane). For PEBAX® 2533 the drop of E_P of CO_2 was more significant (around 36 %) than that of PEBAX® MH 1657 (around 20 %). Comparing the values of E_D and ΔH_S it is clear that, change of both E_D and ΔH_S of CO_2 contributed to the observed change of E_P.

E_D corresponds to the energy required for a penetrant to make a diffusive jump from one equilibrium site to another. Lower values of E_D of CO_2 in the nanocomposite membranes are a result of lower rate of increase of CO_2 diffusion as a function of temperature after 30 wt% PEG POSS® incorporation in both grades of PEBAX®. As in the case of PEBAX® 2533 incorporation of 30 wt% PEG POSS® led to a drop of both diffusion coefficient as a function of temperature and E_D of CO_2; it can be assumed that the degree of freedom involved in the diffusion process is less in the nanocomposite membrane.[62, 63] A negative value of ΔH_S is the characteristic for decrease of sorption with increase of temperature which is in accordance with the loss of solubility observed in Figure 4.10. A more negative ΔH_S value or higher change of enthalpy in the nanocomposites compared to the pure polymer elucidates the fact that PEG POSS® provided a favorable sorption environment for the polar CO_2 due to the increase of polar ether oxygen content in both grades of PEBAX®. As the polyether segments of PEBAX® 2533 are composed of the relatively less polar repeating unit (tetramethylene oxide), the incorporation of PEG POSS®, containing more polar repeating units of the functional group (ethylene oxide), makes a more significant contribution to this behavior in this polymer compared with PEBAX® MH 1657.[61]

4.2.3. Thermal analysis

Table 4.3: Glass transition temperature of PEBAX® MH1657 and PEBAX® 2533 as a function of PEG POSS® content.

PEG POSS® Content (wt%)	Glass transition temperature (ºC)	
	PEBAX® MH 1657	PEBAX® 2533
0	-52.0	-77.1
10	-52.9	-76.9
20	-53.6	-78.2
30	-57.8	-78.9
40	-	-78.2
50	-	-78.7

In Table 4.3 the effect of PEG POSS® content upon glass transition temperature (T_g) obtained from DSC is shown. The T_gs that correspond to the polyether blocks were observable in all the samples, while the T_gs for polyamide blocks were impossible to detect by DSC. But the melting points of both polyether and polyamide blocks are visible. It was observed that the glass transition temperature of PEBAX® 2533 was significantly lower than that of PEBAX® MH 1657. T_gs gradually decreased with the increase of PEG POSS® content in PEBAX® MH 1657 upto 30 wt% and for higher PEG POSS® content T_g was not clearly observable. However, in the case of PEBAX® 2533 no substantial influence was observed upon the glass transition temperature due to incorporation of PEG POSS®. Hence, PEG POSS® acts as a plasticizer for PEBAX® MH 1657 but not for PEBAX® 2533.

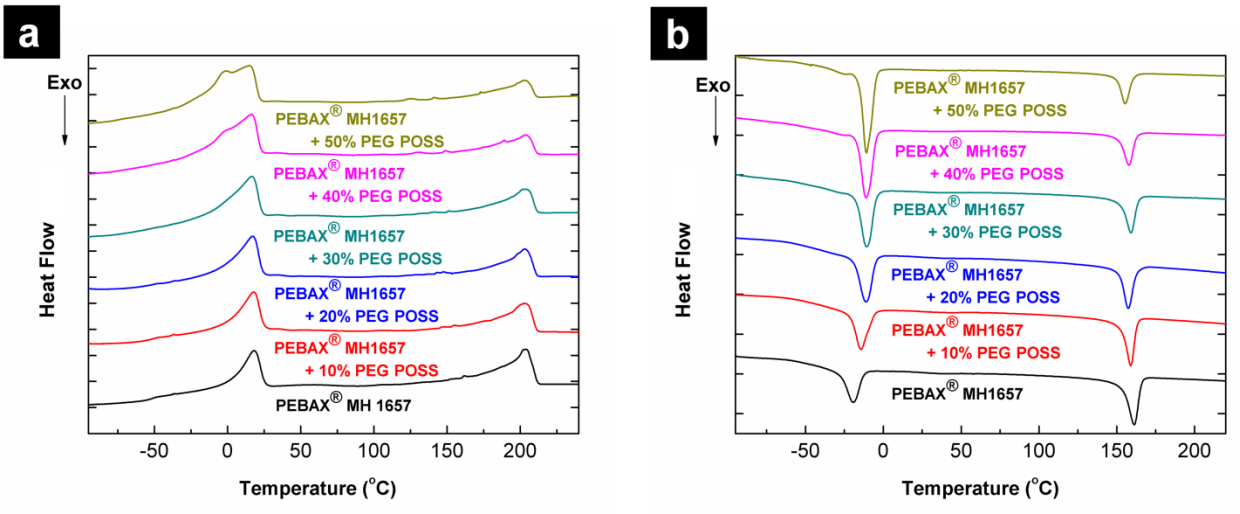

Figure 4.11: DSC thermograms of PEBAX® MH1657 and its PEG POSS® incorporated nanocomposites – a) second heating trace b) second cooling trace.

Figure 4.11a shows the effect of PEG POSS® content in PEBAX® MH1657 content upon the melting of polyether and polyamide domains (second heating cycle of the DSC thermogram). In pure PEBAX® MH1657 two characteristic melting endotherms were observed, which is consistent with the microphase separated structure of the block copolymer.[60] The melting endotherm observed with an onset, peak and endset temperature of 2 ºC, 18 ºC and 25 ºC, respectively, is attributed to the melting of the polyether domains and proves their molten nature at 30 ºC (gas permeability was measured within 30 ºC to 70 ºC). The other melting endotherm with an onset temperature at 190 ºC, peak temperature at 203 ºC and endset temperature at 212 ºC comes from the melting of the polyamide domains. The thermal transition of the polyamide blocks does not seem to be affected by the incorporation of PEG POSS®, as the onset, peak and endset temperatures were not significantly influenced after addition of PEG POSS®. On the other hand, significant changes were observed on the melting of the polyether domains due to incorporation of PEG POSS®. With the increase of PEG POSS® content the onset temperature of

the melting endotherm shifted to -0.6, -3.5, - 9.1, - 16.1 and -16.9 ºC, respectively. At 40 and 50 wt% loading a small shoulder is visible at lower temperature in the melting endotherm. This phenomenon reveals the fact that the polyether of PEG POSS® starts to melt at a lower temperature than that of PEBAX® MH1657, indicating that it might not be homogeneously mixed into the polyether domains at these higher loadings. The cooling scan of pure PEBAX® MH1657 in Figure 4.11b shows that crystallization of polyamide block starts at 166 ºC upon cooling from the melt and as the temperature is decreased further, crystallization of the polyether blocks starts at -12 ºC. Table 4.4 shows the onset, peak and endset temperatures of the crystallization attributed to the polyether domains as a function of PEG POSS® content.

Table 4.4: Onset, peak and endset temperatures of crystallization of polyether domain of PEBAX® MH1657 as a function of PEG POSS® content.

PEG POSS® Content (wt%)	Crystallization exotherm of polyether domain		
	Onset (ºC)	Peak (ºC)	Endset (ºC)
0	-12.3	-19.1	-27.5
10	-6.1	-14.3	-21.3
20	-4.6	-11.1	-18.7
30	-4.3	-10.5	-17.3
40	-4.3	-11.7	-16.8
50	-4.3	-10.7	-15.4

It was observed that the crystallization exotherm of polyether domains shifted to higher temperatures due to incorporation of PEG POSS® upto 20 wt%, i.e. the crystallization of polyether blocks occurred at a higher temperature while cooling down from the melt after incorporation of PEG POSS®. This observation elucidates the fact that PEG POSS® acts as a

nucleating agent on the polyether domain of this type of PEBAX. However, for higher loading (30, 40 and 50 wt%) of PEG POSS®, no further shift was observed.

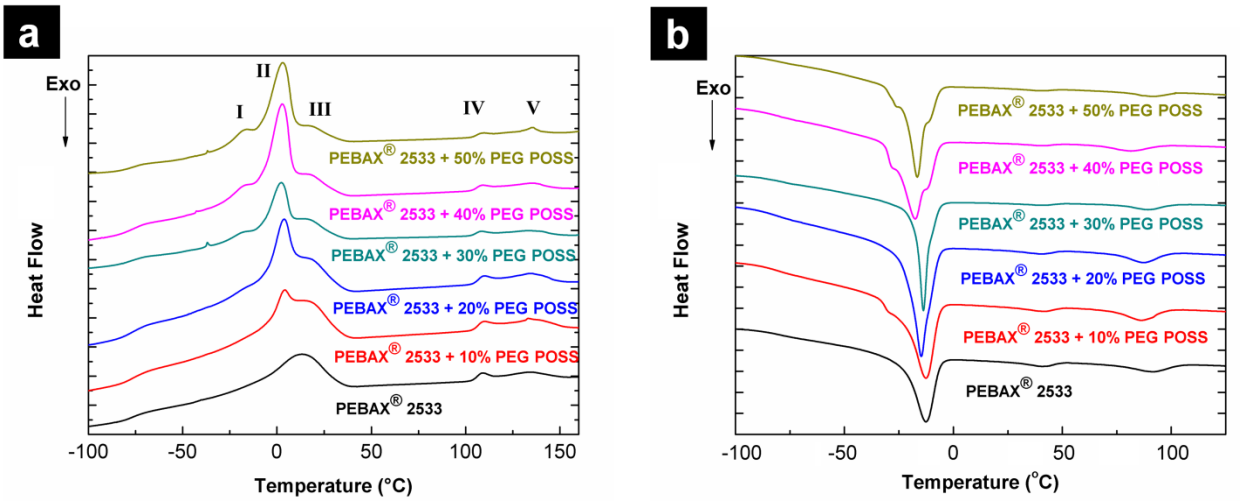

Figure 4.12: DSC thermogram of PEBAX® 2533 and its PEG POSS® incorporated nanocomposites a) second heating trace b) second cooling trace.

The heating cycles of DSC thermograms representing the effect of PEG POSS® content in PEBAX® 2533 upon melting are plotted in Figure 4.12a. To discuss the multiple melting endotherms in this figure the peaks are designated as I, II, III and so on with the increase of their position on the temperature scale. The endothermic peak observed between -14 ºC to 34 ºC having the maximum at 12.7 ºC (peak III) for pure PEBAX® 2533 is attributed to the melting of the polyether domains. Two adjacent melting endotherms (peak IV and V) observed above 100 ºC come from the melting of the polyamide domains. The endothermic transition (peak IV) prior to the main melting peak (peak V) refers to the existence of secondary crystallization phenomenon inside the polyamide phase. Peak IV might be attributed to the melting of poorly ordered small polyamide crystals.[64, 65] Even after incorporation of PEG POSS® both peaks IV

and V were visible at the same temperatures and the shape remained unchanged. On the other hand, significant changes were observed on the melting of the polyether domains due to incorporation of PEG POSS®. At 10 wt% loading a small new peak (peak II) appears at lower temperature. With the increase of PEG POSS® content peak II becomes bigger, but its position in the temperature scale remains constant. Although peak III becomes smaller with the increase of PEG POSS® content, it is clearly distinguishable from peak II even after 50 wt% PEG POSS® loading. This phenomenon reveals the fact that the ether of PEG POSS® melts at a lower temperature than the ether of PEBAX® which is in accordance with PEBAX® MH 1657 observed in Figure 4.11a. However, after 20 wt% loading another endothermic peak (peak I) starts to appear and becomes non-negligible at 30, 40 and 50 wt% loading. This refers to the PEG ligands of PEG POSS®, as it also was observed for the PEBAX® MH 1657 nanocomposite membrane. Figure 4.12b shows the effect of PEG POSS® content in PEBAX® 2533 upon the cooling cycle of the DSC thermogram. Upon cooling from the melt, the major portion of polyamide starts to crystallize just below 105.0 ºC, while a small fraction of polyamide can only crystallize at much lower temperature (below 55 ºC). No change of the shape or position in the temperature scale of polyamide peaks was observed after incorporation of PEG POSS®. The crystallization peak for polyether domains was -12.3 ºC for pure PEBAX® 2533 and it shifted to -12.4 ºC, -14.3 ºC, -13.4 ºC, -17.2 ºC and -16.3 ºC with the increase of PEG POSS® content up to 50 wt%. However, at 40 and 50 wt% loading multiple peaks were observed and it is clearly visible from the position of the multiple peaks at the temperature scale that a part of the polyether domains crystallizes exactly at the same temperature as pure PEBAX® 2533. The appearance of multiple peaks at heating and cooling traces leads to the hypothesis that at higher

PEG POSS® loadings a fraction of PEG POSS® is ejected from the polyether domains of PEBAX® 2533 and exist as aggregates.[61]

4.2.4. Surface topography

The surface topography of the films was characterized by AFM. Nevertheless, only 30 wt% PEG POSS® incorporated nanocomposite membranes were compared with the pure PEBAX® of both grades to study the effect of incorporation of nanoparticles upon the surface roughness. The maximum height, R_{max}, the route mean square deviation of height, R_q and the average deviation of height, R_a are determined.

$$R_a = \frac{1}{L}\int_0^L |Z(x)|dx \qquad (4.1)$$

$$R_q = \sqrt{\frac{1}{L}\int_0^L |Z^2(x)|dx} \qquad (4.2)$$

$$R_{\max} = |\max Z(x)| \quad \text{for } 0 \le x \le L \qquad (4.3)$$

where the function *Z(x)* describes the surface profile of the sample over the evaluation length, *L* analyzed in terms of height, *Z* and position, *x*.[66]

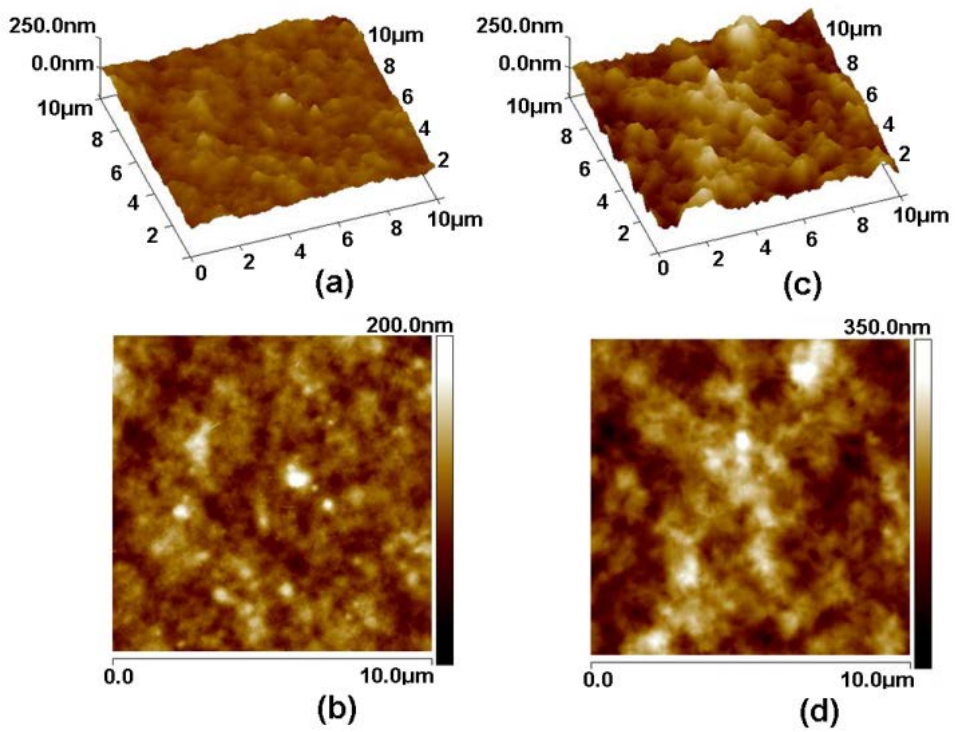

Figure 4.13: Surface topography via AFM a) 3D- image of PEBAX® MH1657 c) 3D-image of 30 wt% PEG POSS® incorporated PEBAX® MH1657 b) Height image of PEBAX® MH1657 d) Height image of 30 wt% PEG POSS® incorporated PEBAX® MH1657.

Table 4.5: Roughness parameters of PEBAX® MH1657 and its nanocomposite after incorporation of 30 wt% PEG POSS®.

Composition	R_{max} (nm)	R_q (nm)	R_a (nm)
PEBAX® MH1657	182	18.1	14
PEBAX® MH1657 + 30 wt% PEG POSS®	304	43.6	35

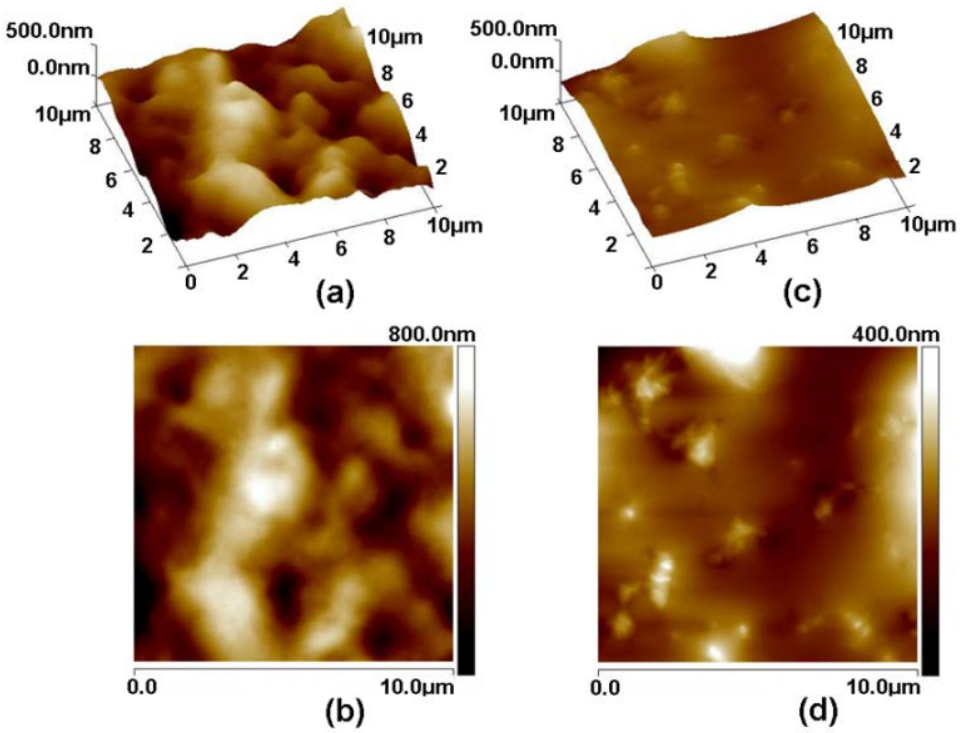

Figure 4.14: Surface topography via AFM a) 3D- image of PEBAX® 2533 c) 3D-image of 30 wt% PEG POSS® incorporated PEBAX® 2533 b) Height image of PEBAX® 2533 d) Height image of 30 wt% PEG POSS® incorporated PEBAX® 2533.

Table 4.6: Roughness parameters of PEBAX® 2533 and its nanocomposite after incorporation of 30 wt% PEG POSS®.

Composition	R_{max} (nm)	R_q (nm)	R_a (nm)
PEBAX® 2533	888	131	108
PEBAX® 2533 + 30 wt% PEG POSS®	224	39.7	32.7

The 3D images obtained by AFM from a sample area of 10 μm x 10 μm are presented in Figure 4.13a and c for PEBAX® MH1657 and PEBAX® MH1657 with 30 wt% PEG POSS®, respectively. The 3D images reveal the presence of nanoscale roughness on the surface of both pure PEBAX® MH 1657 and the nanocomposite membrane. It is evident from the 3D images that no clusters or agglomerates appeared on the surface of the nanocomposite membrane even for this rather high level of loading with PEG POSS®. This shows the compatibility of the nanoparticles with the polymer matrix. The height images corresponding to Figure 4.13a and c are presented in Figure 4.13b and d, which show that the nanocomposite samples have more bright and dark spots which correspond to the highest and lowest points of the surface. Moreover, the maximum vertical distance between the highest and lowest point for pure PEBAX® MH1657 is 182 nm compared to that of the nanocomposite sample which is 304 nm (Table 4.5). Hence, it is evident that in the case of the nanocomposite membrane with 30 wt% PEG POSS® nanoparticles the surface roughness is higher which might have occurred due to surface reorganization of the polymer chains due to the presence of nanoparticles.

In contrary to PEBAX® MH1657, no nanoscale roughness was observed in PEBAX® 2533. From the 3D and corresponding height images (Figure 4.14a and b) it is visible that the roughness present on the surface of PEBAX® 2533 is on a micrometer scale. Figure 4.14c shows that after incorporation of PEG POSS® the surface topography has changed and the roughness disappeared across a large part of the surface. Meanwhile some irregular nanoscale bumps were observed on the surface of the membrane of PEBAX® 2533 with 30 wt% PEG POSS®. The roughness calculation of these images is presented in Table 4.6. Hence, although some new nanoscale roughness appeared, the overall surface became smoother after incorporation of PEG POSS®

compared to that of pure PEBAX® 2533. These results indicate that the distribution of the nanofillers is different in the two types of PEBAX® and therefore further investigations were carried out by scanning electron microscopy.[61]

4.2.5. SEM and EDS analysis

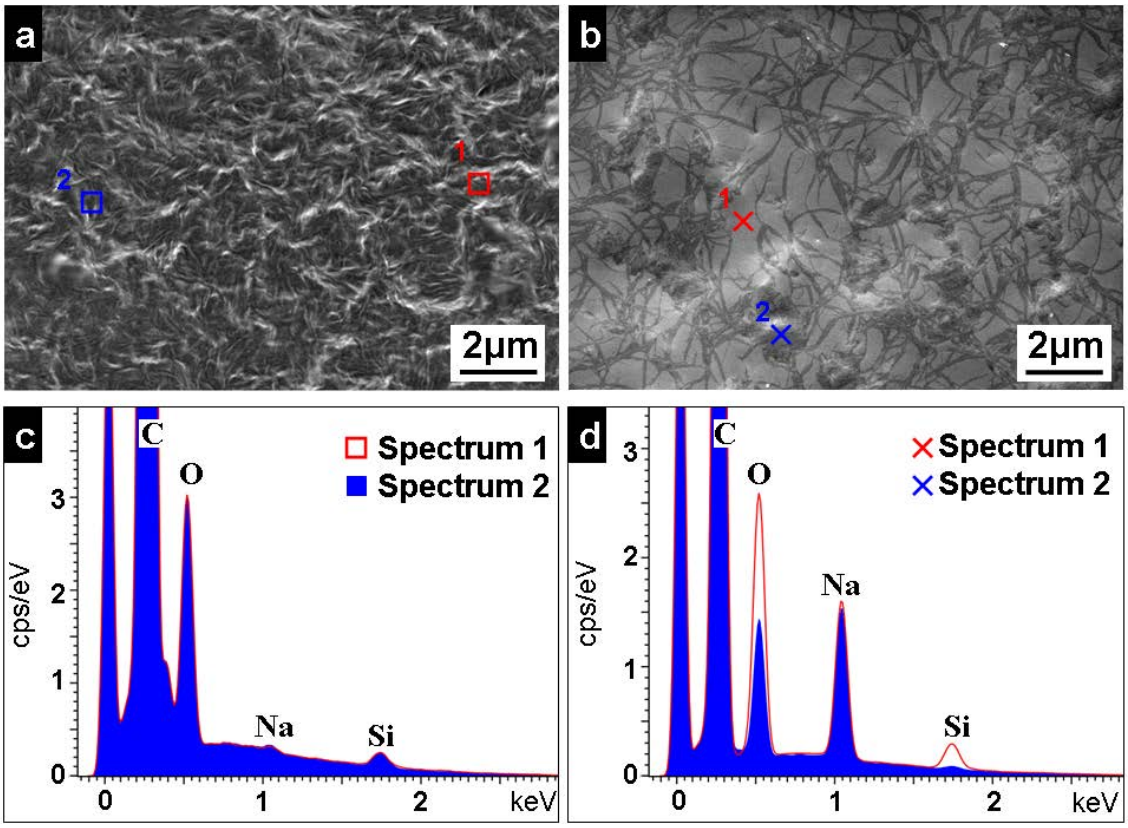

Figure 4.15: Surface morphology and surface spectra of PEBAX® nanocomposite membranes containing 30 wt% PEG POSS®. a) SEM micrograph of PEBAX® MH1657 nanocomposite membrane; b) SEM micrograph of PEBAX® 2533 nanocomposite membrane; c) EDS spectra of two areas of PEBAX® MH1657 nanocomposite membrane; d) EDS spectra of two areas of PEBAX® 2533 nanocomposite membrane.

The surface morphology and also the EDS spectra of representative areas are shown in Figure 4.15 for nanocomposite membranes of PEBAX® MH 1657 (Figure 17 a, c) and PEBAX® 2533 (Figure 4.15 b, d), respectively. Both nanocomposite membranes contain 30 wt% PEG POSS®. For the PEBAX® MH 1657 nanocomposite membrane the surface revealed a needle like structure which is due to the crystalline polyamide (Polyamide 6) part of the polymer. The regions in between these needles correspond to the polyether blocks i.e. the poly(ethylene oxide) blocks, which contribute 60 wt% to the multiblock copolymer. The lateral segregation of these two domains is too small to reveal the selective localisation of PEG POSS® in the polyether microdomains. However, DSC results shown in section 4.3 indicate that polyamide blocks melt at the same temperature in the nanocomposite membrane as it does in pure PEBAX® MH 1657. Therefore the EDS spectra presented in Figure 4.15c show a homogeneous distribution of PEG POSS® all over the surface (or surface near regions) within the polyether domains of the mutiblock copolymer. Hence, it is evident that the PEG ligands of the PEG POSS® nanofiller introduced miscibility with the polyether domains of the multiblock copolymer PEBAX® MH 1657. In contrast, the surface of the PEBAX® 2533 nanocomposite membrane showed distinct darker regions with a needle like structure and other, smoother regions appeared bright. The needle like structure corresponds to polyamide (Polyamide 12) blocks, the crystalline component contributing 20 wt% to this multiblock copolymer, while the smoother areas correspond to locations, where the amorphous poly(tetramethylene oxide) blocks cover the surface. In this sample rich and poor regions of PEG POSS® are clearly distinguishable from the comparison of the characteristic X-ray peaks for Si and O of the spectra recorded in a bright and dark regions, respectively (Figure 4.15d). The strong appearance of Na is probably due to impurities.

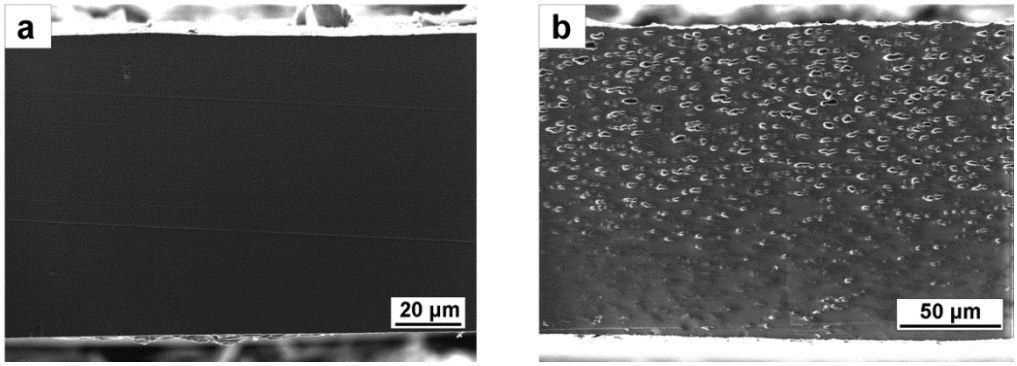

Figure 4.16: SEM micrograph of the cross section of - a) PEBAX® MH1657 nanocomposite membrane containing 30 wt% PEG POSS® and b) PEBAX® 2533 nanocomposite membrane containing 30 wt% PEG POSS® .

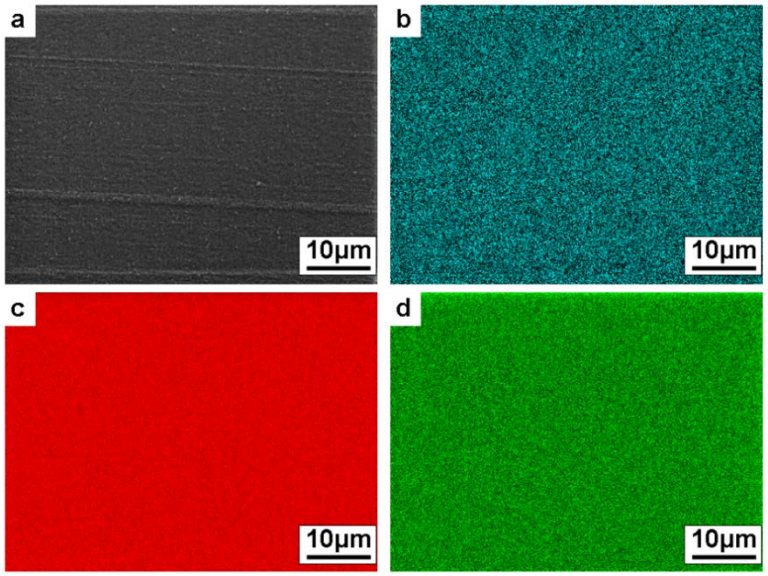

Figure 4.17: Cross section morphology of a PEBAX® MH1657 nanocomposite membrane containing 30 wt% PEG POSS® a) SEM micrograph b) Si element map c) C element map d) O element map.

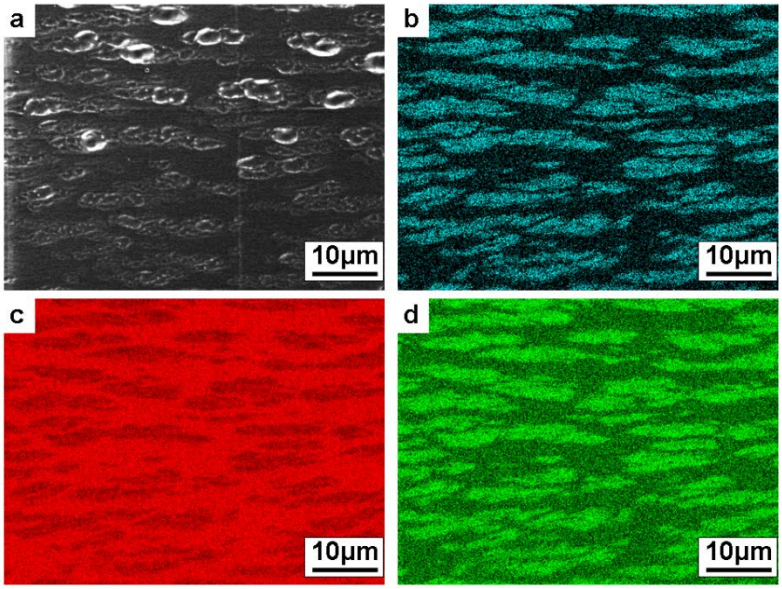

Figure 4.18: Cross section morphology of a PEBAX® 2533 nanocomposite membrane containing 30 wt% PEG POSS® a) SEM micrograph b) Si element map c) C element map d) O element map.

Another important issue is the distribution of PEG POSS® all over the thickness of the membranes. The cross-sectional morphologies of these two samples are shown in Figures 4.16a and b. Figure 4.16a shows a homogeneous morphology of the PEBAX® MH 1657 nanocomposite membrane, while Figure 4.16b shows an inhomogeneous structure with ellipsoidal inclusions for the PEBAX® 2533 nanocomposite membrane. These inclusions are located all over the cross section of the membrane, and they are larger and more numerous versus the top of the membrane. They are a result of the poor miscibility of PEG POSS® with the poly(tetramethylene oxide) domains, what becomes more evident from the elemental mappings shown in Figure 4.18. Figures 4.17a-d show a section of the cross sectional morphology of the PEBAX® MH 1657 nanocomposite membrane, and the corresponding elemental mappings of C,

Si and O, respectively. These images show that the nanofillers are homogeneously distributed within the sample, at least on the length scale of spatial resolution of the EDS analysis. The analogous investigation for the PEBAX® 2533 nanocomposite membrane is shown in Figure 4.18. The elemental maps reveal two clearly separated areas of PEBAX® 2533 and PEG POSS®. Due to the incompatibility of the PEG-ligands with both components of this multiblock copolymer a macroscopic demixing is clearly seen, which is the reason for the occurrence of the inclusions discussed before.[61]

4.3. Discussion

4.3.1. Correlation between thermal and gas separation properties

It has been reported that blending low molecular PEG in PEBAX® MH1657 leads to a decrease in glass transition and melting temperature of the PEG domains and consequently the permeability of the membrane increases.[54, 60] A similar trend was observed after the incorporation of PEG POSS® into PEBAX® MH1657. In the case of PEBAX® 2533 the incorporation of PEG POSS® does not lead to a significant decrease of the glass transition temperature and the increase of gas permeability with the increase of PEG POSS® content at 30 ºC is also much less than in the case of PEBAX® MH1657 (section 4.2.2). The influence of the change in glass transition temperature on the gas transport mechanism is clear from comparison of the diffusion behavior of CO_2 at 30 ºC through both grades of PEBAX® nanocomposite membranes with loadings upto 30 wt% PEG POSS® (Figures 4.4 and 4.7). In the case of PEBAX® MH1657 the incorporation of PEG POSS® leads to a significant decrease of T_g

or in other words it increased the flexibility of the polyether blocks. Consequently the diffusion of CO_2 also increases substantially after incorporation of 30 wt% PEG POSS®. On the other hand, PEG POSS® has no significant influence on the T_g of PEBAX® 2533 and the diffusion of CO_2 remains unchanged upto 30 wt% PEG POSS® loading. Since, PEG POSS® used for this study is decorated with low molecular weight PEG chains of the same chemical structure as the polyether blocks of PEBAX® MH1657 and different from the polyether blocks of PEBAX® 2533 (section 4.2.1) it is expected that the compatibility of the PEG ligand of the nanoparticle with the polyether blocks of these two different grades of PEBAX® is also different. Hence, a strong correlation between gas transport through the membrane and impact on the glass transition temperature due to different compatibility of the ligand of the nanoparticle with the polyether blocks of the block copolymer is evident. This argument seems to be further justified by the observation that incorporation of 30 wt% PEG POSS® into PEBAX® 2533 resulted in a lower diffusion of CO_2 at elevated temperature (e.g. 60 ºC and 70 ºC) while in the case of PEBAX® MH1657 it led to a higher diffusion of CO_2 between 30 ºC and 70 ºC (Figure 4.10). Moreover, Figures 4.5 and 4.7 reveal the fact that at 40 and 50 wt % PEG POSS® loading in PEBAX® 2533 the permeability of CO_2 decreases dramatically at 30 ºC due to decrease of diffusion through the nanocomposite membrane but the solubility shows an increasing trend. Meanwhile, DSC studies show multiple peaks during heating and cooling cycles at these compositions (section 4.2.3) and EDS analysis proved the existence of aggregates of PEG POSS® in PEBAX® 2533 (section 4.2.5). From all these observations it seems reasonable to assume that PEG POSS® did not plasticize the polyether blocks of PEBAX® 2533, rather it existed as agglomerates which provided favorable adsorption sites for polar CO_2 molecules but led to higher diffusion resistance

(or hindered the diffusive jump from one site to another) due to the presence of an interphase between the agglomerated nanoparticles and polymer matrix.

On the other hand, it was observed (section 4.2.5) that PEG POSS® is homogeneously dispersed in PEBAX® MH1657 and acts as a nucleating agent for the crystallization of the polyether domain (section 4.2.3). Since the polyether blocks of PEBAX® MH1657 and the ligand of PEG POSS® have the same repeating unit, it is expected that the PEG POSS® will be compatible with the polyether domains which might facilitate the crystal formation in the during the cooling from the melt. Hence, incorporation of PEG POSS® in PEBAX® MH1657 leads to two phenomena which counteract each other; increase of low molecular weight PEG content (which leads to plasticization or decrease of T_g) and too much compatibility of the ligand of the nanoparticle with the polymer segment (which leads to nucleation). Gases are virtually insoluble in the crystalline regions of the polymer when compared to amorphous rubbery regions.[67] However, it must also be considered that the single gas permeability of the membranes was measured between 30 ºC and 70 ºC and the nucleation of the polyether domain by PEG POSS® was observed below 0 ºC. Figure 4.11a shows the molten nature of the polyether domain at 30 ºC. Thus, it is expected that the nucleating effect of PEG POSS® is irrelevant at any temperature in which gas transport measurements were carried out.[61]

4.3.2. Correlation between surface topography and gas separation properties

Gas transport through dense polymeric membranes is believed to occur in three successive steps- sorption of the penetrant at the feed side of the membrane, diffusion of the penetrant through the

membrane, and desorption at the permeate side.[68] The first step is likely to be related with available adsorption sites. The presence of roughness on the surface of the membrane provides more available adsorption sites than a completely smooth surface. In section 4.2.4 it was described that incorporation of 30 wt% PEG POSS® seemed to have increased the surface roughness of PEBAX® MH1657 and decreased that of PEBAX® 2533. Meanwhile, the increase of gas permeability of the membrane was also significantly lower in case of PEBAX® 2533 than PEBAX® MH1657 after incorporation of 30 wt% PEG POSS®. For example, an increase of CO_2 permeability of ca. 100% was observed in PEBAX® MH1657 while in PEBAX® 2533 it was only ca. 30%. In spite of the strong correlation between the change in glass transition temperature with increase of gas permeability (section 4.3.1), these observations suggest that increase of surface area which stems from the roughness of the surface might also have an impact on the gas transport through these membranes.[61]

4.4. Conclusion

Commercial PEG POSS® is able to alter the gas separation performance of different grades of PEBAX® membranes significantly. The gas transport after incorporation of PEG POSS® is strongly related with the thermodynamic properties, while the surface roughness may also play a role. PEBAX® MH1657 with 30 wt% PEG POSS® showed substantial improvement in gas permeability without any significant change in selectivity in the temperature range 30 - 70 ºC. Hence, it can be concluded that PEG POSS® is a suitable nanofiller to improve the commercial viability of PEBAX® membranes containing PEO as a soft segment.[61]

Chapter 5. Influence of poly(ethylene glycol) segment length on CO_2 permeation and stability of PolyActive™ membranes and their nanocomposites with PEG POSS®

5.1. Introduction

Nanocomposite membranes containing nanosized fillers embedded in a polymer matrix has the potential to be used for industrial gas separation due to the low cost and simplicity of fabrication.[69] But the choice of the matrix-filler combination plays a vital role in the separation performance and stability of the membranes. From chapter 4 it is evident that commercial PEG POSS® (poly(ethylene glycol) functionalized polyoctahedral oligomeric silsesquioxanes) is a suitable nanofiller for PEBAX® MH 1657 which contains alternating series of poly(ethylene glycol) and polyamide-6 segments. However, the degrees of polymerization of the polyether blocks of PEBAX® multiblock copolymers are not available from the manufacturer. Therefore, PEG POSS® is incorporated in another polyether based block copolymer family PolyActive™. Three grades of commercial PolyActive™ having polyether segments of 1500, 3000 and 4000 g/mol namely PolyActive™ 1500PEGT77PBT23, PolyActive™ 3000PEGT77PBT23 and PolyActive™ 4000PEGT77PBT23, respectively are chosen for the study. The CO_2 gas separation performance of these three grades of commercial polymers and their nanocomposites with PEG POSS® in the temperature range from 30 to 70 ºC are reported in this chapter. In this regard, single gas permeabilities of N_2, H_2, CH_4, and CO_2 are measured via the time-lag method in the temperature range from 30 to 70 ºC. The thermal transitions of the prepared membranes are studied by differential scanning calorimetry (DSC). Morphology of PolyActive™ 1500PEGT77PBT23 and its nanocomposites containing PEG POSS® is thoroughly investigated using scanning electron microscopy (SEM) and atomic force microscopy (AFM). The gas transport properties are correlated with the thermoanalytical and morphological characteristics of the membranes. The aim is to demonstrate how the length of the poly(ethylene glycol) segment influences the separation performance and the stability of the three grades of

PolyActive™ and the nanocomposites based on them in the temperature range of post combustion carbon capture.

5.2. Results

5.2.1. Composition of three grades of PolyActive™

The commercial block copolymer PolyActive™ consists of two building blocks namely poly(ethylene glycol terephthalate) (PEGT) and poly(butylene terephthalate) (PBT). The three grades chosen for this study consist of approximately 77 wt% of PEGT and 23 wt% of PBT. The molecular weight of the poly(ethylene glycol) segments in these polymers are 1500, 3000 and 4000 g/mol, respectively. Since the ratio of weight content of PEGT and PBT is almost the same in these three polymers, they are addressed in terms of length of the PEG segment in this chapter. The commercial names and the acronyms are listed in Table 5.1.

Table 5.1: Acronym of three grades of PolyActive™.

Commercial Name	Acronym
PolyActive™ 1500PEGT77PBT23	P 1500
PolyActive™ 3000PEGT77PBT23	P 3000
PolyActive™ 4000PEGT77PBT23	P 4000

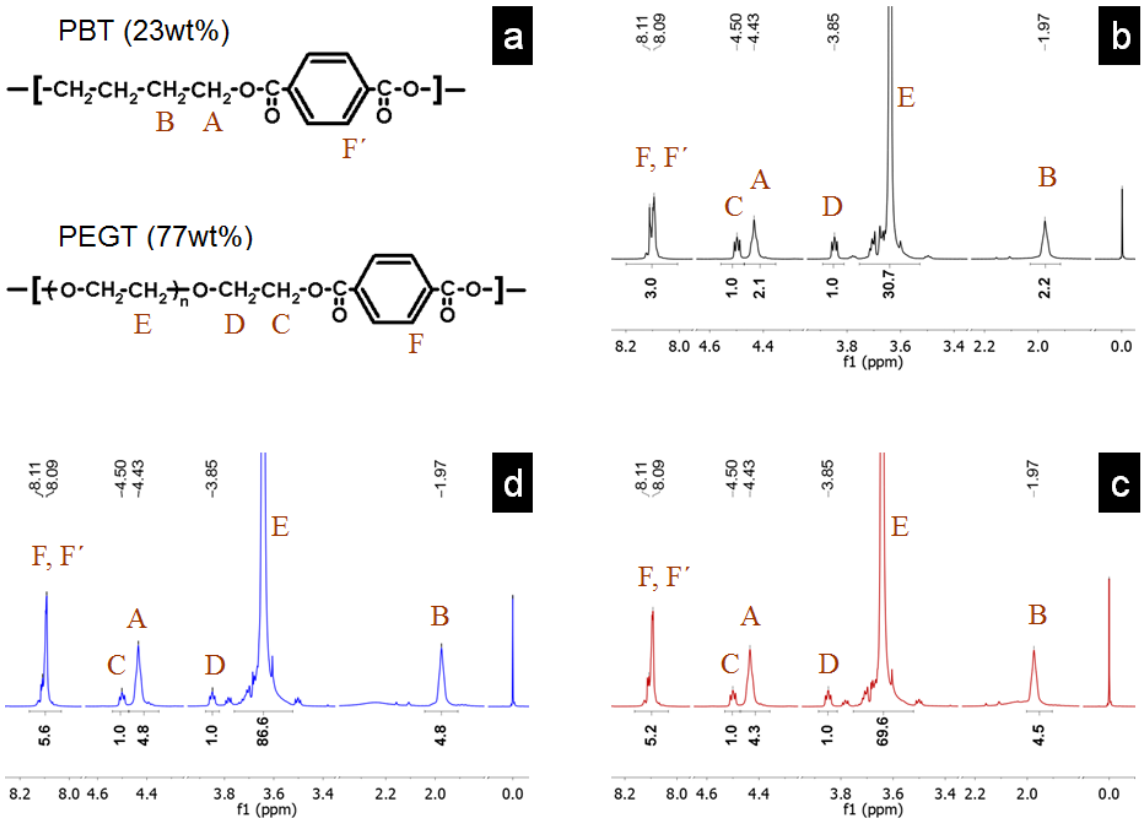

Figure 5.1: a) Structure of poly(butylene terephthalate) (PBT) and poly(ethylene glycol terephthalate) (PEGT); b) ^{1}H-NMR of P 1500; c) ^{1}H-NMR of P 3000; d) ^{1}H-NMR of P 4000.

The ^{1}H-NMR spectra of three grades of PolyActive^{TM} are illustrated in Figure 5.1. The peaks A and B at 4.43 and 1.97 ppm, respectively, originate from the butylene units of PBT. The peaks C & D at 4.5 and 3.85 ppm are attributed to the protons of the first repeating unit of PEG which is attached to the terephthalate unit i.e. the neighboring –CH_2–CH_2–O– group of terephthalate unit. The rest of the repeating units of PEG blocks give the peak E at 3.64 ppm. The aromatic protons of the terephthalate units of PEGT and PBT blocks (peak F and F') appear at 8.11 and 8.09 ppm, respectively[70]. From the ratios of integral areas of these peaks three rational number x_1, x_2 and x_3 are determined (listed in Table 5.2) using the following equations:

$$x_1 = \frac{I_E}{I_D} \quad (1)$$

$$x_2 = \frac{I_C + I_D}{I_A + I_B} \quad (2)$$

$$x_3 = \frac{I_C + I_D + I_E}{I_A + I_B + I_F + I_{F'}} \quad (3)$$

where *I* represents the integral area of a peak.

Table 5.2: Comparison of the three different grades of Polyactive^{TM} from ^{1}H NMR.

Polymer	x_1	x_2	x_3
P 1500	30.7	0.46	4.5
P 3000	69.6	0.23	5.1
P 4000	86.6	0.20	5.8

x_1 + 2 is the average number of ethylene oxide repeating units in PEG segments so the value increases in the following order P 1500 < P 3000 < P 4000. x_2 is the ratio of number of PEG segments to that of butadiene segments. The rational number x_3 is related to the PEG content of the polymer as it is the ratio between the sums of the integral areas of resonance for protons of the PEG segment to that of all other protons. From Table 5.2 it is evident that a variation of the PEG length changes the polymer composition, although the PEGT and PBT weight content is equal. The PEG content in the polymer (represented by x_3) increases with increase in the length of the PEG segments (represented by x_1) while the number of PEG segments (represented by x_2) decreases.[71]

5.2.2. Thermal characterization

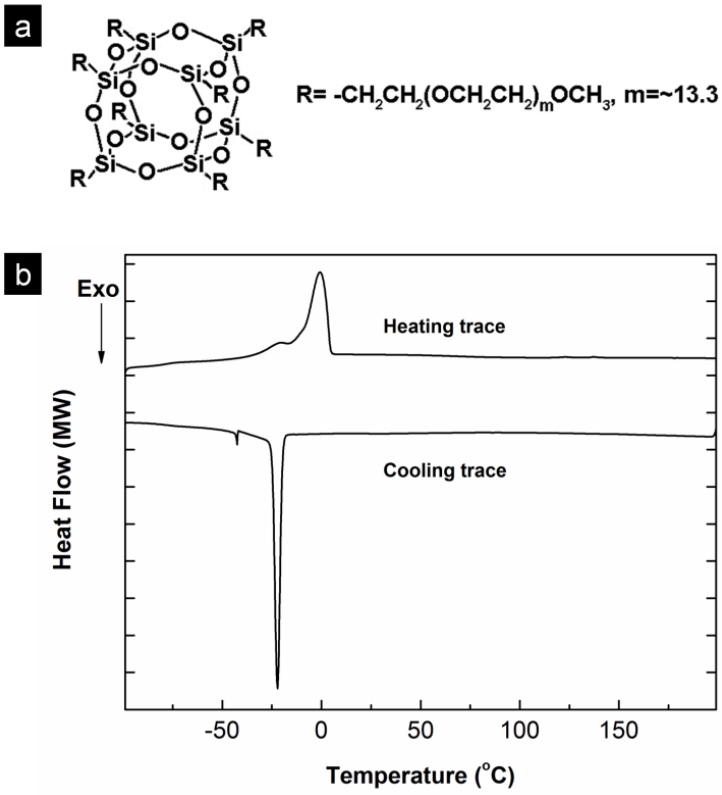

Figure 5.2: a) Chemical structure b) DSC curves (second heating and cooling trace) of PEG POSS®.

Figure 5.2a depicts the structure of PEG POSS® provided by the supplier. It contains a cage structure of silsesquioxane as core and the poly(ethylene glycol) ligands attached to every Si atom of the cage. According to the structure each of the PEG ligands of PEG POSS® is ca. 645 g/mol and the PEG content is ca. 92 wt%[61]. The thermal transitions of PEG POSS® in the second heating and cooling scan of DSC are presented in Figure 5.2b. In the heating scan the melting starts at approx. -10 ºC and the major melting peak has a peak temperature of -1 ºC. The

small shoulder prior to the major melting peak refers to some poorly ordered crystals. In the cooling run the crystallization exotherm is observed at approx. -22 ºC.

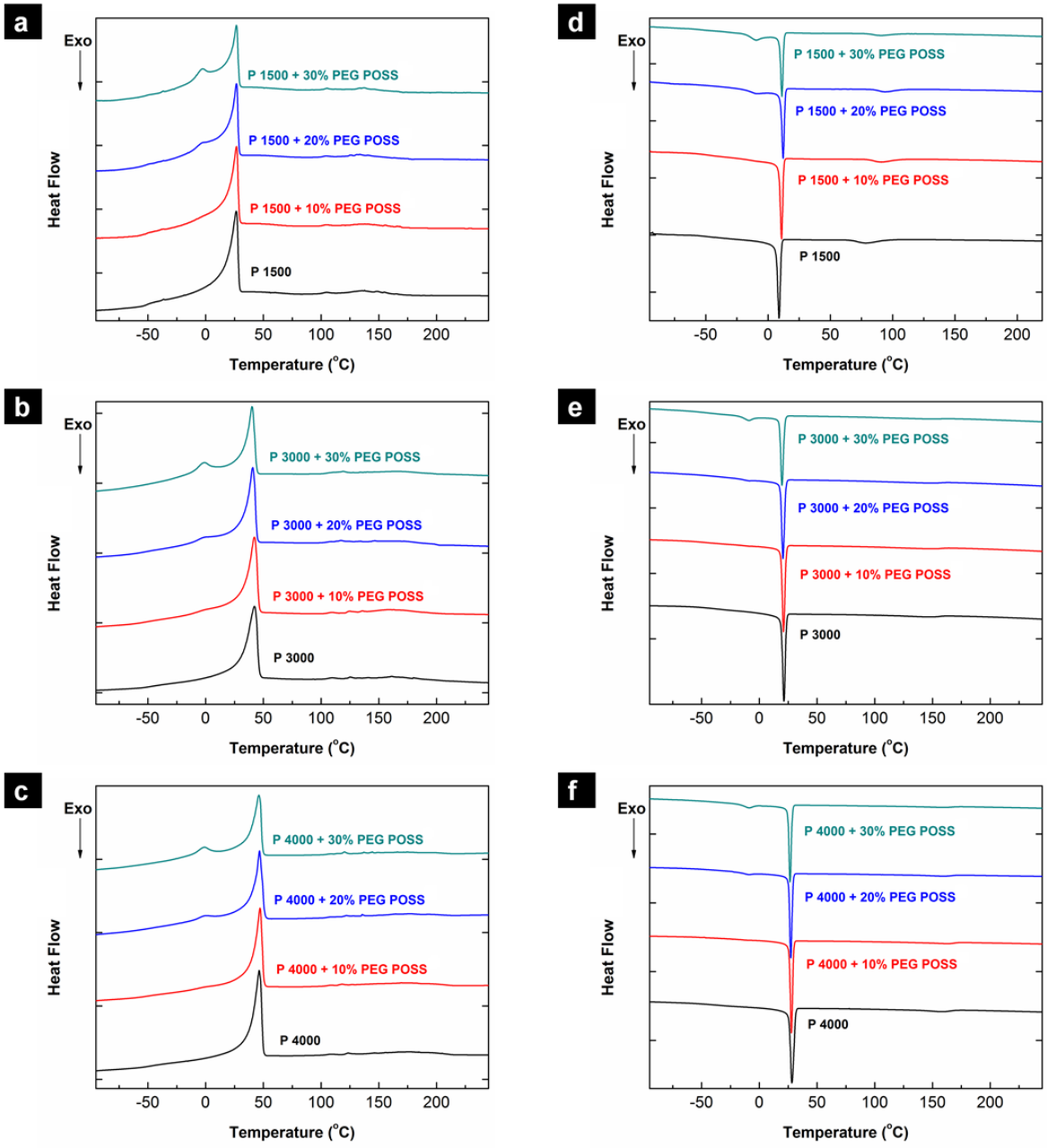

Figure 5.3: DSC curves (second heating and cooling trace) of the three grades of PolyActive™ and their nanocomposites with PEG POSS®.

Figure 5.3 shows the thermal transitions (second heating and cooling scans) of the three grades of PolyActive™ and their nanocomposites with PEG POSS®. The onset, peak, endset and melting enthalpy of the polyether blocks of the three grades of PolyActive™ are listed in Table 5.3. The crystallinity, X_c of the polyether block (listed in Table 5.3) is determined as:

$$X_c = \frac{\Delta H}{\Delta H_c} \qquad (4)$$

where ΔH is the is the melting enthalpy of polyether blocks obtained from the second heating scan of DSC run and ΔH_c is the theoretical value for melting enthalpy of 100% crystalline poly(ethylene oxide) [13]. The ΔH_c value of 166.4 J/g suggested by Simon and Rutherford is used for calculation [72].

Table 5.3. The melt onset, melt peak, melt endset, enthalpy of melting and crystallinity (second heating) of the polyether blocks of three grades of PolyActive™.

	Melt onset temperature (ºC)	Melt peak temperature (ºC)	Melt endset temperature (ºC)	Enthalpy, ΔH (J/g)	Crystallinity, X_c (%)
P 1500	18 ± 0.5	28 ± 0.9	32 ± 1.1	62 ± 1.4	37
P 3000	32 ± 0.3	41 ± 0.6	44 ± 0.7	90 ± 1.2	54
P 4000	40 ± 0.7	46 ± 1.3	50 ± 1.3	95 ± 1.0	57

Table 5.3 shows that the crystallinity of the polyether block increases and the melting endotherm (onset, peak and endset) shifts to a higher temperature as the length of polyether segment increases. A comparison of the onset temperatures suggests that the melting of the crystals start at a higher temperature when the polyether segment is longer. Figures 5.3a, b and c show that the melting endotherm of the polyether block of the polymers appears exactly at the same temperature also after incorporation of PEG POSS®. A new melting endotherm is observed around 0 ºC in cases of 20 and 30 wt% loaded nanocomposites. This new endothermic peak appears at the temperature for all the nanocomposites. Hence it is evident that it appears from the melting of poly(ethylene glycol) chains of the nanofiller PEG POSS® .

Table 5.4: The onset, peak, endset, and enthalpy of crystallization (second cooloing)of the polyether blocks of three grades of PolyActive™.

	Crystallization onset temperature (ºC)	Crystallization peak temperature (ºC)	Crystallization endset temperature (ºC)	Enthalpy (J/g)
P 1500	11 ± 0.2	9 ± 0.3	7 ± 0.4	61 ± 0.1
P 3000	24 ± 0.5	22 ± 0.5	18 ± 0.7	84 ± 1.6
P 4000	30 ± 0.1	28 ± 0.1	25 ± 0.4	91 ± 1.0

Table 5.4 shows the crystallization onset, crystallization peak, crystallization endset and enthalpy of crystallization of the polyether blocks of the three grades of PolyActive™ while cooling down from the melt. The onset, peak and endset have the following order: P 4000 > P 3000 > P 1500. Hence, crystallization of the polyether block starts at a higher temperature when the polyether segment is longer. Figure 5.3d shows that the crystallization of polyether block occurs at slightly higher temperature in the nanocomposites of P 1500 compared to the pure polymer. This indicates a nucleating effect of the nanofiller as we also showed in a previous work where PEG POSS® acted as a nucleating agent for the commercial multiblock copolymer PEBAX® MH 1657 [61].

However, this phenomenon is not observed in the nanocomposites of P 3000 and P 4000. For 20 and 30 wt% PEG POSS® loaded nanocomposites a separate crystallization exotherm at a peak temperature of approx. -10 ºC is observed. Although this peak appears at a higher temperature compared to the crystallization exotherm of pure PEG POSS® (Figure 5.3a), with increase of PEG POSS® content it becomes bigger and the position in the temperature scale is the same for both 20 and 30 wt% PEG POSS® loaded nanocomposites. Thus it is evident that this peak is attributed to the crystallization of the PEG ligand of PEG POSS® in the PolyActive™ matrices.

Hence, the DSC study shows that variation of PEG segment length has a pronounced influence on the thermal transition (melting and crystallization) of the polyether blocks of pure P 1500, P 3000 and P 4000. Moreover, in the nanocomposites the PEG ligand of the nanofiller and the PEG segment of the block copolymer matrices melt and crystallize separately.[71]

5.2.3. Gas separation performance

5.2.3.1. CO_2 permeation

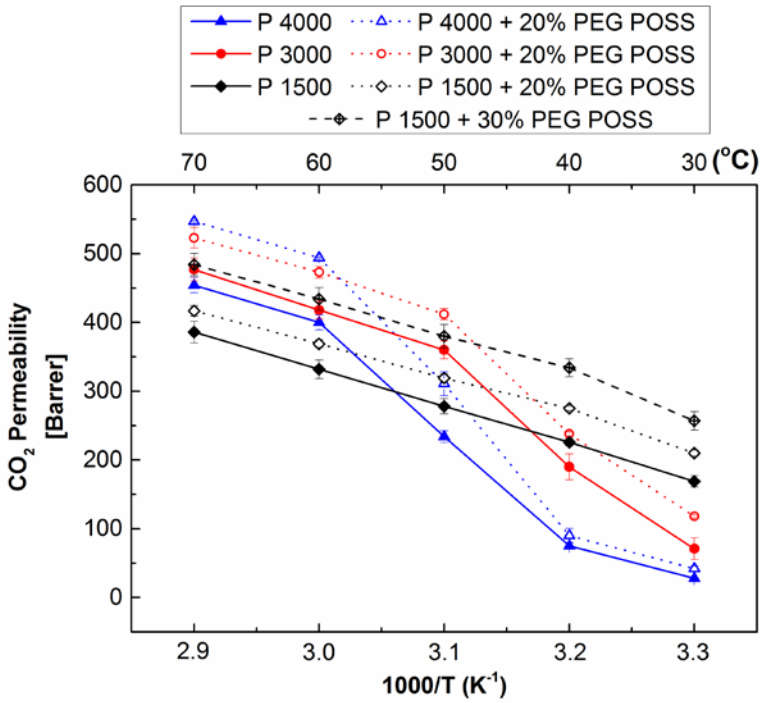

Figure 5.4. CO_2 permeability as a function of temperature in three grades of PolyActive™ and their nanocomposites with PEG POSS®.

The permeability of N_2, CH_4, H_2 and CO_2 through P 1500, P 3000 & P 4000 and their nanocomposites with PEG POSS® was measured between 30 - 70 ºC via time-lag method. The gas permeability was determined only during heating from 30 ºC to 70 ºC at every 10 ºC interval. Then the measurement cell was cooled down to 30 ºC to take out the sample. The gas permeability was not determined while cooling the measurement cell from 70 ºC to 30 ºC. The permeability of CO_2 through the membranes is plotted as a function of temperature in Figure 5.4.

At 30 ºC P 1500 shows higher permeability than P 3000 & P 4000. But between 50 - 70 ºC P 3000 become higher CO_2 permeability than other two grades of pure polymer. It is evident that the trend of increase of gas permeability with the increase of temperature is different in the different grades of PolyActive™. P 1500 shows a gradual increase of permeability with increase of temperature. For P 3000 the increase of permeability in the range of 30 - 50 ºC is significantly high but in the range of 50 - 70 ºC the trend is similar to that of P 1500. P 4000 also shows a similar behavior like P 3000 but at a higher temperature range. Incorporation of PEG POSS® in P 1500 leads to an increase in permeability. The trend of increase of permeability with the increase of temperature for both 20 and 30 wt% PEG POSS® incorporated nanocomposites is analogous to that of pure P 1500. 20 wt% PEG POSS® incorporation in P 3000 also shows increase of permeability. In case of 20 wt% PEG POSS® loaded in P 4000 the CO_2 permeability of the nanocomposite is similar to that of pure P 4000 membrane at 30 ºC and 40 ºC. But as the temperature increases the CO_2 permeability through the nanocomposite becomes significantly higher compared to that of the P 4000 membrane. After the gas permeability measurements via time-lag method from 30 ºC to 70 ºC the measurement cell was cooled down to 30 ºC again to take out the sample. It is important to be mentioned here that a small amount of PEG POSS® (confirmed by FT-IR) was observed on top of the nanocomposites of P 3000 after the gas transport tests while the nanocomposites of P 4000 were found broken into pieces. Since reproducible time-lag curves were observed until the last gas was passed through the membrane at 70 ºC, it is evident that the nanocomposites of P 4000 broke into pieces while cooling down (from 70 ºC to 30 ºC). In case of P 1500 stable nanocomposite membranes were obtained from up to 30 wt% loading of PEG POSS®. Since 20 wt% PEG POSS® incorporated P 3000 and P 4000 nanocomposites are not stable in the temperature range of 30 - 70 ºC, single gas

permeability measurement data of 30 wt% PEG POSS® loaded nanocomposites (which are also unstable) are not mentioned in this thesis.

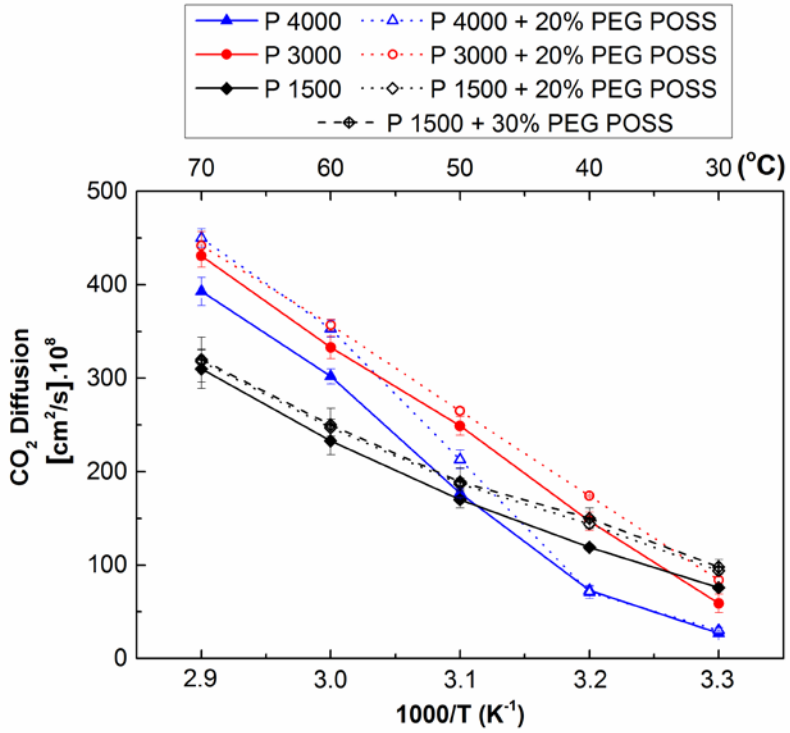

Figure 5.5: CO_2 diffusivity as a function of temperature in three grades of PolyActive™ and their nanocomposites with PEG POSS®.

Diffusion of the membranes is plotted as a function of temperature in Figures 5.5. It is evident that CO_2 has a slightly higher diffusion coefficient in P 1500 than in P 3000 at 30 ºC. Between 40 and 70 ºC the diffusion coefficient of CO_2 is highest for P 3000 among three pure grades of polymer. The higher CO_2 diffusion coefficient with increasing temperature in P 3000 compared to P 1500 is clearly related with the length of the polyether segment. It is clear from section 5.2.1 that although the ratio of weight content of PEGT and PBT is almost the same, the total polyether content (i.e. the only PEG part without the terephthalate units at two ends of PEGT

blocks) is higher in P 3000 than in P 1500. P 4000 has the longest polyether segment and highest polyether content among the three grades of pure polymer. However, the CO_2 diffusion coefficient is lower in P 4000 than P 3000 within the range of 30 - 70 ºC. At 30 and 40 ºC it is even lower than that of P 1500. From the change of slope at 40 ºC it is clear that the thermal transition has an influence upon the diffusion of CO_2 in this polymer (discussed in section 5.3).

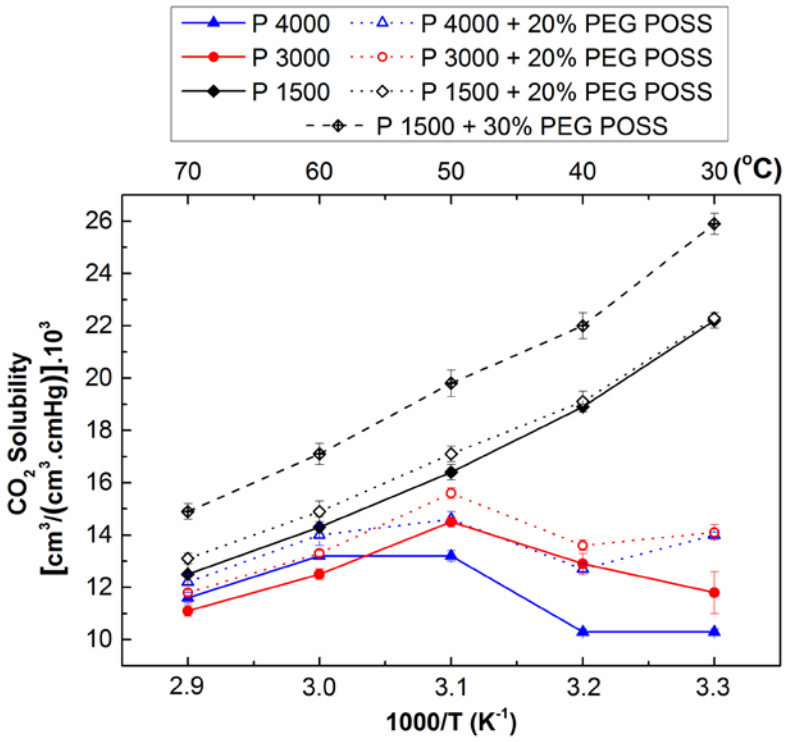

Figure 5.6: CO_2 solubility as a function of temperature in three grades of PolyActive™ and their nanocomposites with PEG POSS®.

Solubility of CO_2 in the membranes is plotted as a function of temperature in Figures 5.6. It shows that the different trend of increase of CO_2 permeability with the increase of temperature is largely due to the difference in CO_2 solubility. At 30 ºC the CO_2 solubility in P 1500 is significantly higher compared to P 3000 and P 4000. The CO_2 solubility decreases in P 1500

with the increase of temperature. In the other two pure polymers the CO_2 solubility increases up to 50 ºC. At higher temperature P 3000 shows a decreasing trend. In P 4000 a loss of solubility was observed only at 70 ºC.[71]

5.2.3.2. CO_2 selectivity over light gases

Table 5.5: N_2, CH_4, and H_2 permeability in three grades of PolyActive™ and their nanocomposites with PEG POSS®.

Gas	Temperature (ºC)	Permeability (Barrer)						
		P 1500	P 1500 + 20% PEG POSS®	P 1500 + 30% PEG POSS®	P 3000	P 3000 + 20% PEG POSS®	P 4000	P 4000 + 20% PEG POSS®
N_2	30	3 ± 0.1	4 ± 0.2	5 ± 0.3	1 ± 0.3	2 ± 0.1	1 ± 0.1	1 ± 0.1
	40	6 ± 0.1	7 ± 0.1	9 ± 0.5	5 ± 0.4	6 ± 0.2	2 ± 0.3	2 ± 0.2
	50	9 ± 0.2	10 ± 0.3	12 ± 0.8	11 ± 0.5	12 ± 0.4	8 ± 0.7	10 ± 0.7
	60	13 ± 0.3	14 ± 0.5	17 ± 1.1	16 ± 0.7	17 ± 1.1	15 ± 0.4	17 ± 0.2
	70	18 ± 0.5	18 ± 0.7	23 ± 1.4	22 ± 1.2	22 ± 1.1	22 ± 0.6	23 ± 0.1
CH_4	30	10 ± 0.4	13 ± 0.3	17 ± 1.0	4 ± 1.0	8 ± 0.4	2 ± 0.2	3 ± 0.2
	40	16 ± 0.3	22 ± 0.4	27 ± 1.4	14 ± 1.5	19 ± 0.2	6 ± 0.5	7 ± 1.4
	50	23 ± 1.9	27 ± 0.6	33 ± 1.7	30 ± 1.4	35 ± 0.9	18 ± 1.0	24 ± 1.2
	60	33 ± 2.4	37 ± 0.9	45 ± 2.3	41 ± 1.5	49 ± 2.0	39 ± 0.7	51 ± 0.5
	70	45 ± 3.4	49 ± 1.5	58 ± 2.6	54 ± 2.0	62 ± 1.9	52 ± 1.3	65 ± 0.6
H_2	30	17 ± 0.7	19 ± 0.5	23 ± 1.1	8 ± 1.2	12 ± 0.1	4 ± 0.2	5 ± 0.3
	40	26 ± 0.6	29 ± 1.1	35 ± 1.4	21 ± 1.7	25 ± 0.3	10 ± 0.6	11 ± 0.6
	50	37 ± 1.2	40 ± 0.9	47 ± 2.3	44 ± 1.8	48 ± 1.2	35 ± 3.1	44 ± 2.4
	60	51 ± 2.0	54 ± 1.1	63 ± 2.7	60 ± 2.3	66 ± 0.2	55 ± 1.5	66 ± 0.5
	70	69 ± 3.2	71 ± 1.6	81 ± 3.1	80 ± 3.2	83 ± 2.6	73 ± 1.8	85 ± 0.6

Single gas permeability of N_2, CH_4 and H_2 are presented in Table 5.5. The ideal selectivity of CO_2 over N_2, CH_4 and H_2 (plotted in Figure 5.7, 5.8 and 5.9, respectively) of the membranes is determined according to equation 2.5 (mentioned in chapter 2).

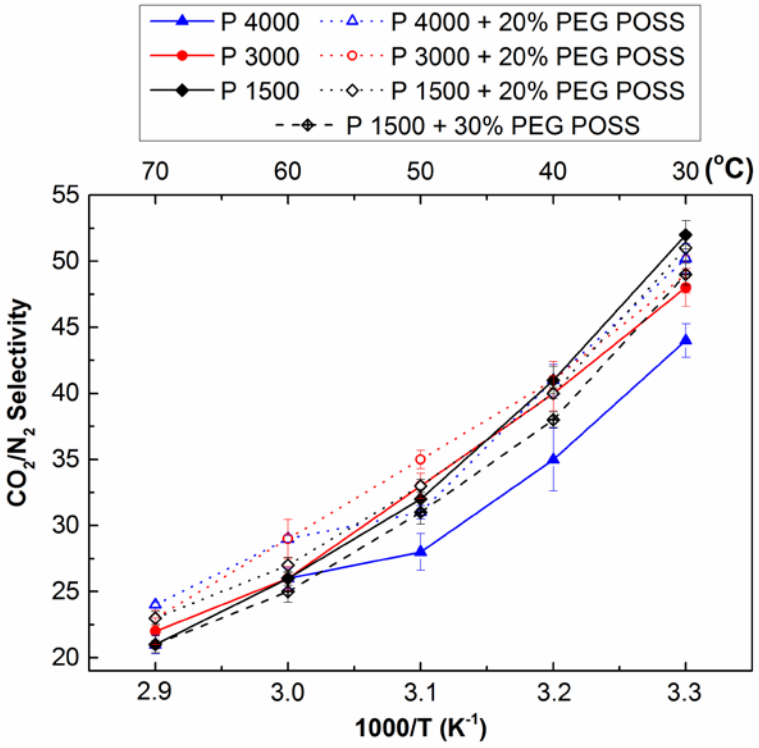

Figure 5.7: CO_2/N_2 selectivity as a function of temperature in three grades of PolyActive™ and their nanocomposites with PEG POSS®.

Figure 5.7 shows that CO_2/N_2 selectivity decreases with increasing temperature for all the membranes. At 30 ºC the CO_2/N_2 selectivity of P 3000 is slightly lower than that of P 1500. Between 40 - 70 ºC the CO_2/N_2 selectivity of these two grades of polymer are equal. P 4000 shows a lower CO_2/N_2 selectivity than the other two grades of polymer up to 50 ºC. Incorporation of PEG POSS® in P 1500 and P 3000 does not alter the CO_2/N_2 selectivity of the

membrane significantly. But 20 wt% PEG POSS® incorporated P 4000 showed better selectivity than that of the corresponding pure polymer membrane.

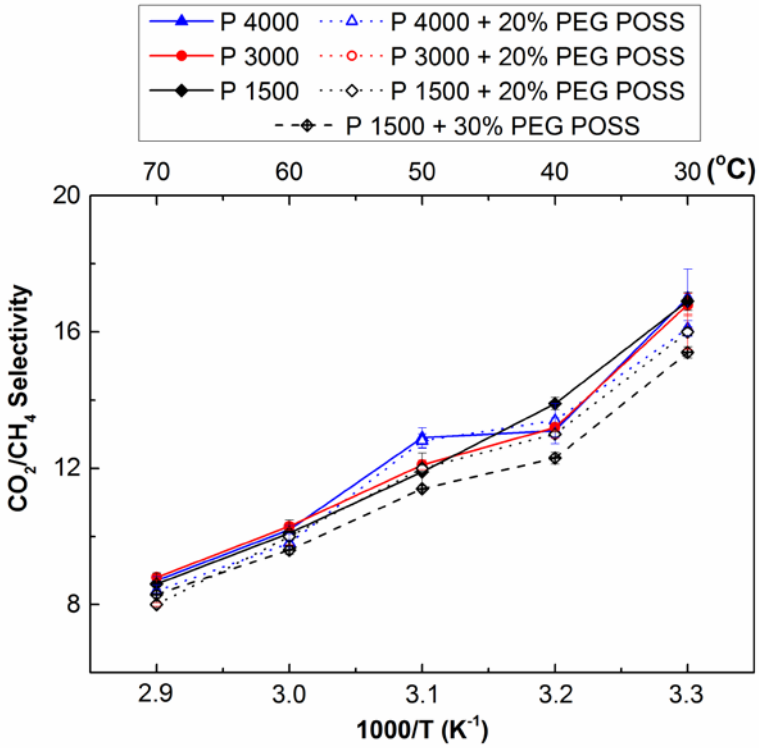

Figure 5.8: CO_2/CH_4 selectivity as a function of temperature in three grades of PolyActive™ and their nanocomposites with PEG POSS®.

Figure 5.8 shows that CO_2/CH_4 selectivity also decreases with increasing temperature. There is no significant difference in CO_2/CH_4 selectivity of these three grades of pure polymer membranes. 20 wt% PEG POSS® incorporated nanocomposites do not show any significant change in CO_2/CH_4 selectivity compared to the pure polymers. However, 30 wt% PEG POSS® incorporated P 1500 showed significantly lower selectivities at 30 and 40 ºC.

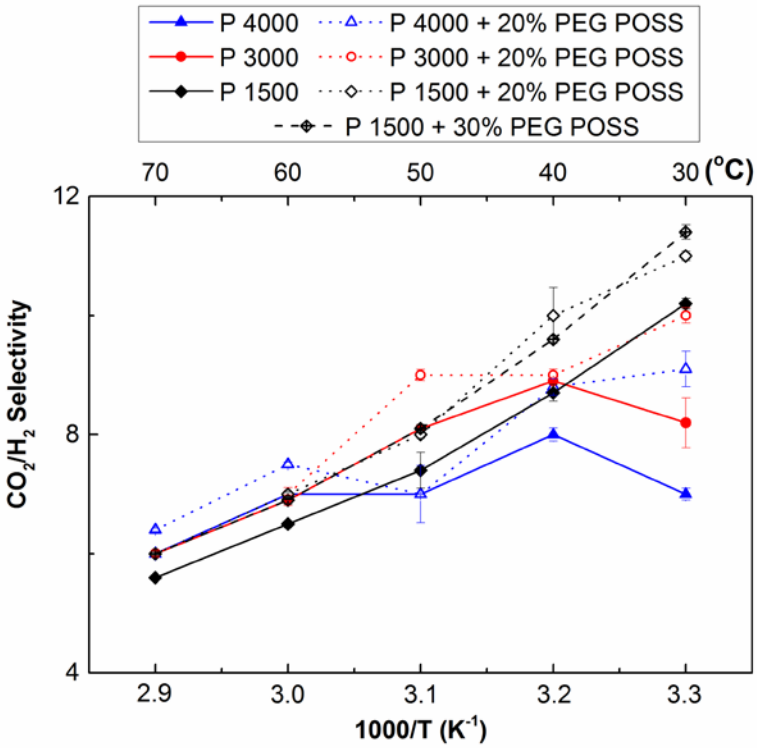

Figure 5.9: CO_2/H_2 selectivity as a function of temperature in three grades of PolyActive™ and their nanocomposites with PEG POSS®.

Figure 5.9 shows that an increase of PEG segment length leads to a lower CO_2/H_2 selectivity at 30 ºC. With the increase of temperature the CO_2/H_2 selectivity of P 1500 shows a gradual decrease. However, for P 3000 and P 4000 at 40 ºC the CO_2/H_2 selectivity increases and then shows a decreasing trend with increasing temperature. Incorporation of PEG POSS® increases the CO_2/H_2 selectivity slightly for P 1500. However, no significant difference was observed between 20 and 30 wt% PEG POSS® incorporated P 1500 nanocomposites. 20 wt% PEG POSS® incorporated P 3000 and P 4000 nanocomposites have significantly higher CO_2/H_2 selectivities at 30 ºC compared to the pure polymers. The trend of decrease of CO_2/H_2 selectivity with increase of temperature in these nanocomposites is different from that of P 3000 and P 4000.[71]

5.2.4. Morphology

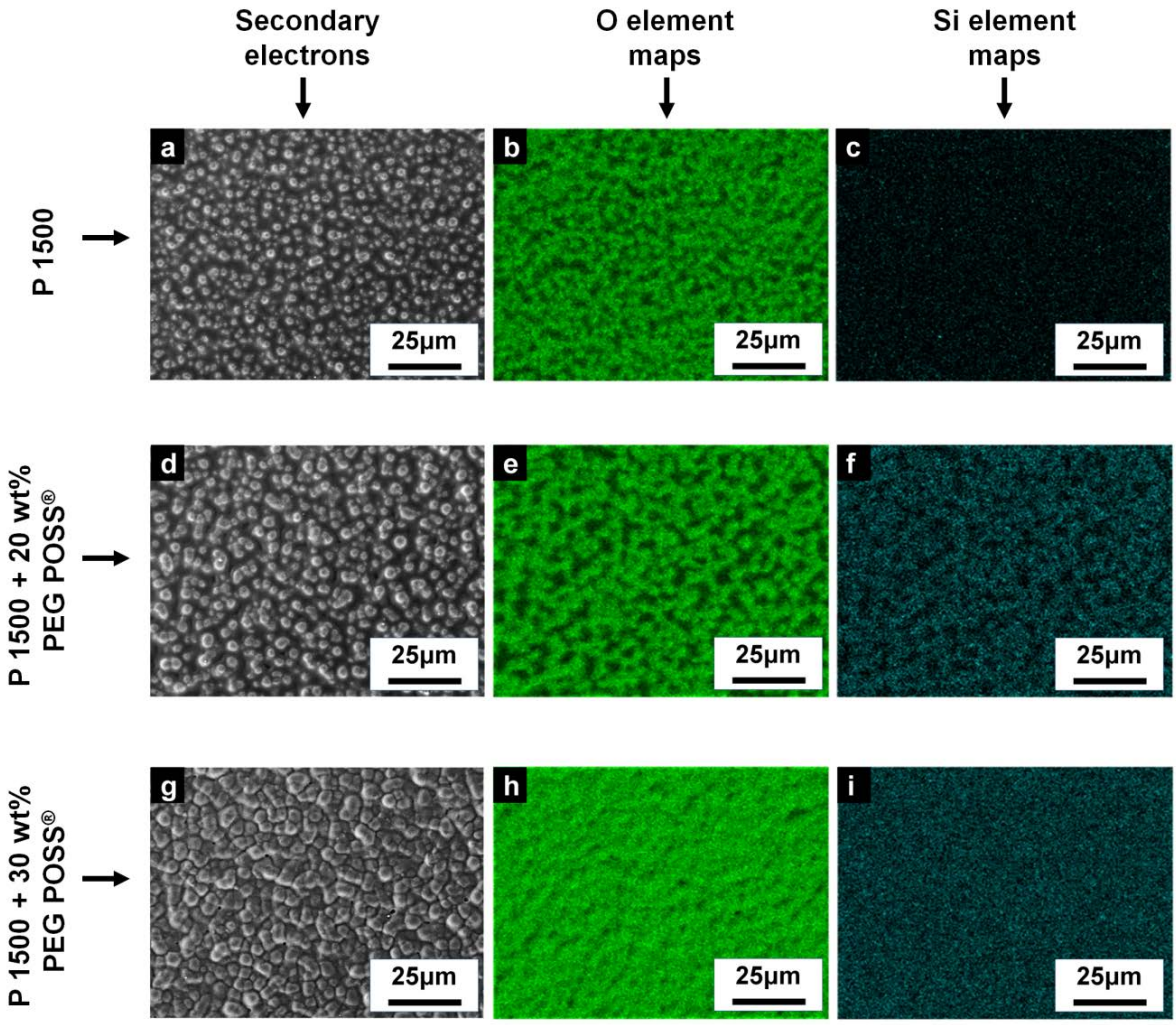

Figure 5.10: Surface morphology – a) SEM micrograph of P 1500 b) Oxygen elemental map of P 1500 c) Silicon elemental map of P 1500 d) SEM micrograph of P 1500 + 20 wt% PEG POSS® e) Oxygen elemental map of P 1500 + 20 wt% PEG POSS® f) Silicon elemental map of P 1500 + 20 wt% PEG POSS® g) SEM micrograph of P 1500 + 30 wt% PEG POSS® h) Oxygen elemental map of P 1500 + 30 wt% PEG POSS® i) Silicon elemental map of P 1500 + 30 wt% PEG POSS®. The accelerating voltage is 5 kV for all measurements.

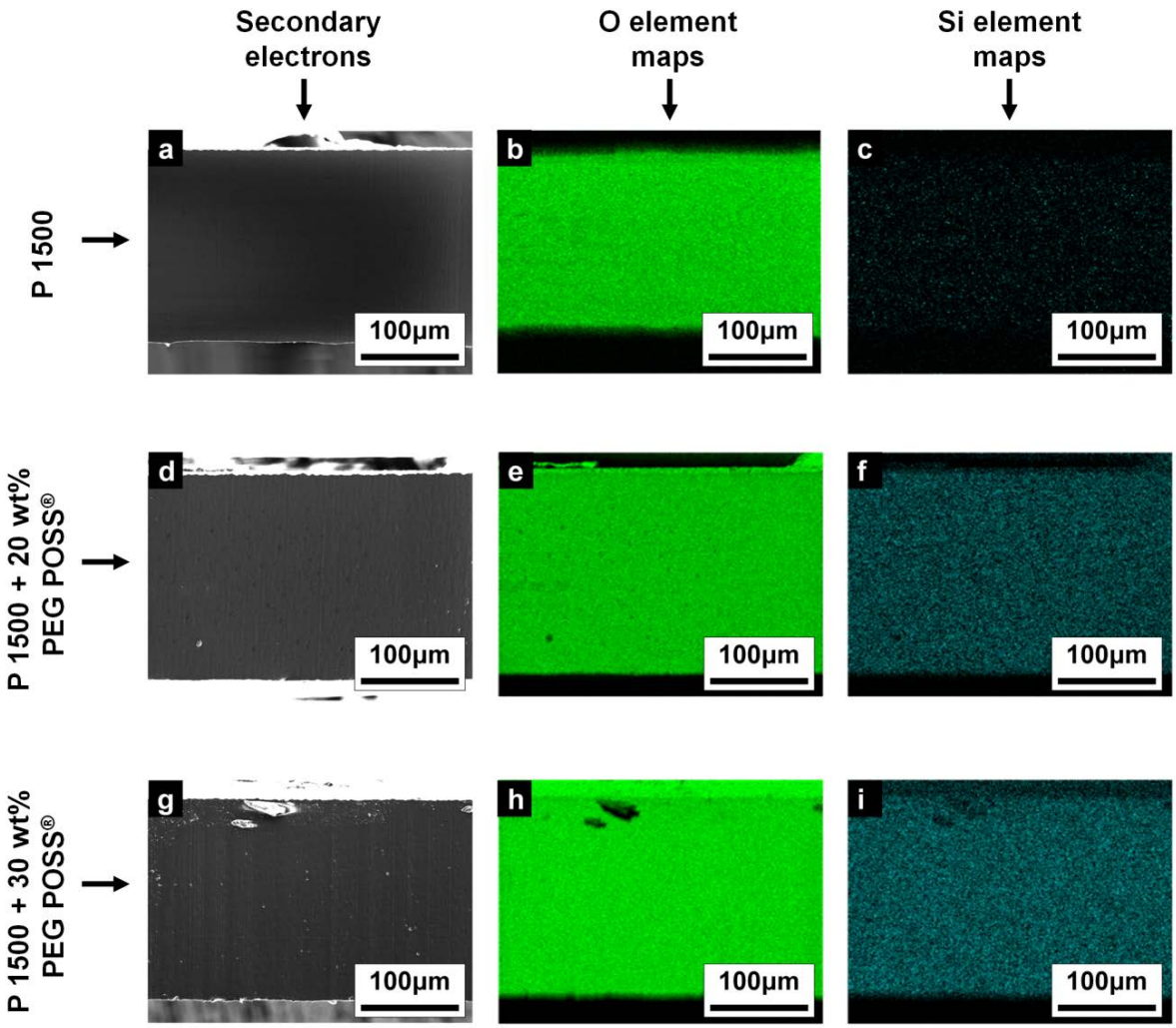

Figure 5.11: Cross section morphology – a) SEM micrograph of P 1500 b) Oxygen elemental map of P 1500 c) Silicon elemental map of P 1500 d) SEM micrograph of P 1500 + 20 wt% PEG POSS® e) Oxygen elemental map of P 1500 + 20 wt% PEG POSS® f) Silicon elemental map of P 1500 + 20 wt% PEG POSS® g) SEM micrograph of P 1500 + 30 wt% PEG POSS® h) Oxygen elemental map of P 1500 + 30 wt% PEG POSS® i) Silicon elemental map of P 1500 + 30 wt% PEG POSS®. The accelerating voltage is 5 kV for all measurements.

The morphology of P 1500 and its nanocomposites containing 20 and 30 wt% PEG POSS® is studied using SEM and AFM. Figure 5.10 shows the SEM micrographs, oxygen and silicon elemental maps of the surface of P 1500 and the nanocomposite membranes taken at an accelerating voltage of 5kV. P 1500 has spherical regions rich in oxygen (Figures 5.10a and b) which are attributed to the polyether blocks of the multiblock copolymer. Similar morphological features are observed in the nanocomposite membrane containing 20 wt% PEG POSS® although the size of these oxygen rich regions increases (Figures 5.10d and e). The silicon elemental map (Figure 5.10f) reveals that the PEG POSS® preferentially resides within these oxygen rich regions. Upon further increase of PEG POSS® *i.e.* in the nanocomposite membrane containing 30 wt% nanofiller, the oxygen rich regions no longer form discrete microdomains (Figure 5.10h). The silicon elemental map (Figure 5.10i) also shows that PEG POSS® is distributed all over the surface of this nanocomposite membrane.

The SEM micrographs and elemental mappings of the cross sections of these membranes are depicted in Figure 5.11. The SEM micrographs of Figures 5.11a, d and g show that the morphological features are indiscernible at a macroscopic level on the cross section of the membranes. Moreover, the oxygen and silicon elemental mappings exhibit that PEG POSS® is homogeneously distributed at this spatial resolution in both nanocomposites with 20 and 30 wt% PEG POSS®, respectively. Interesting structural features are observed in the SEM micrographs of higher magnification presented in Figures 5.12a, 5.13a and 5.14a. Taking advantage of an energy selective backscattered (EsB) incolumn detector at an accelerating voltage of 800V, it was possible to distinguish the PEG POSS® rich domains (bright colored areas) and PBT domains on a larger scale.

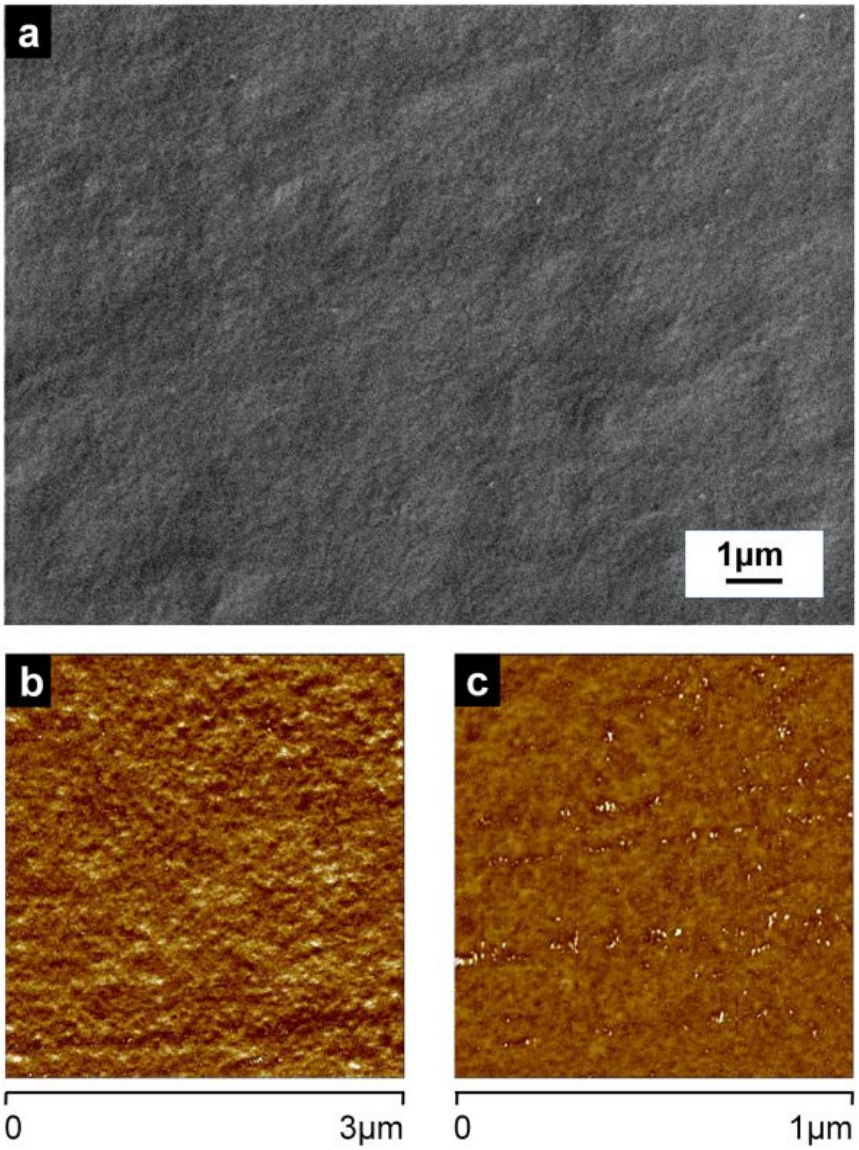

Figure 5.12: Cross section of P 1500 – a) SEM image, accelerating voltage 800V, energy selective backscattered electrons b) TappingMode™ AFM phase image (3 µm ×3 µm) c) TappingMode™ AFM phase image (1 µm ×1 µm).

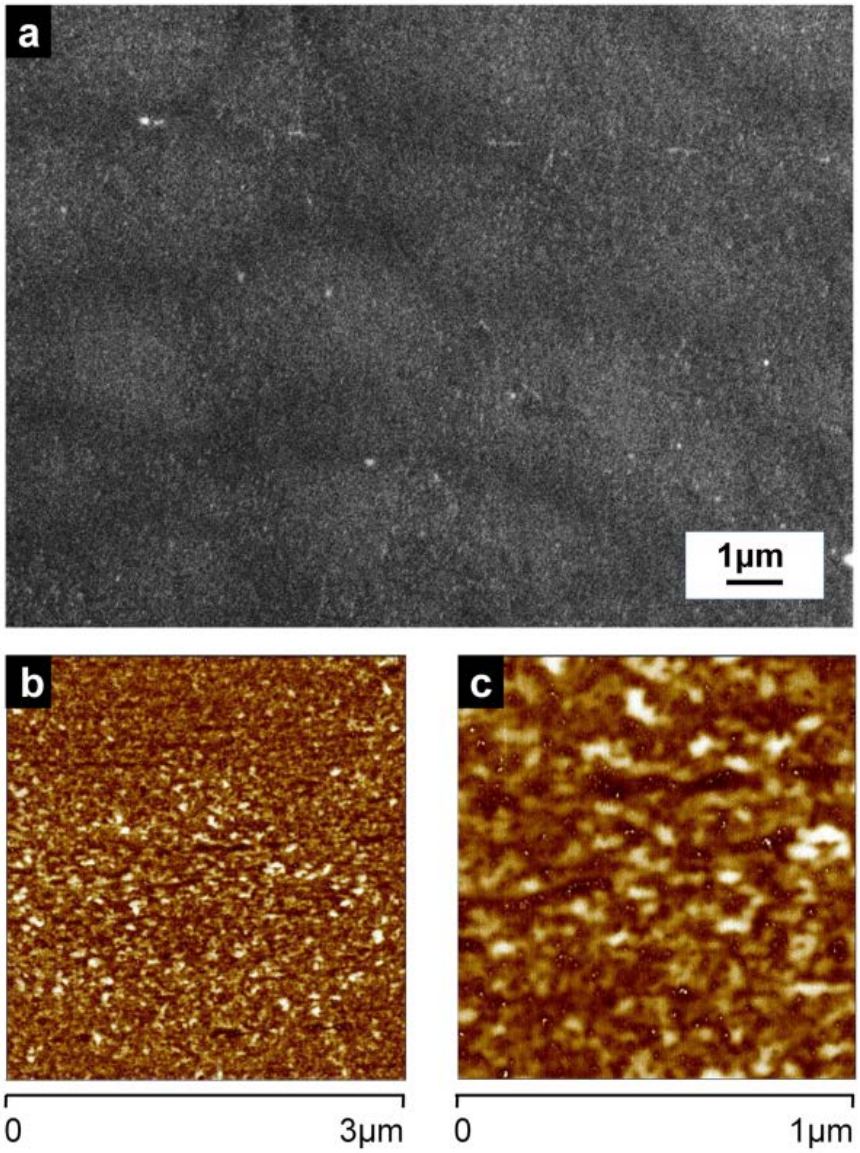

Figure 5.13: Cross section of P 1500 + 20 wt% PEG POSS® – a) SEM image, accelerating voltage 800V, energy selective backscattered electrons b) TappingMode™ AFM phase image (3 µm ×3 µm) c) TappingMode™ AFM phase image (1 µm ×1 µm).

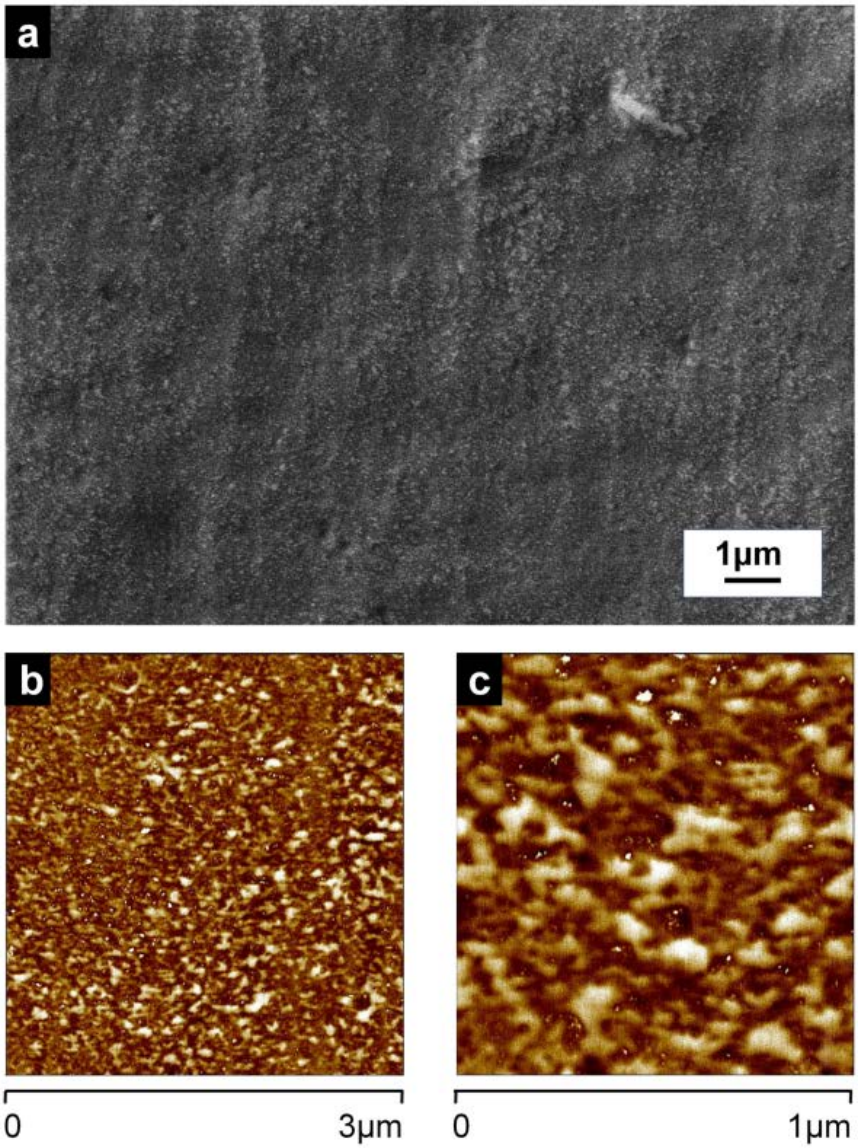

Figure 5.14: Cross section of P 1500 + 30 wt% PEG POSS® – a) SEM image, accelerating voltage 800V, energy selective backscattered electrons b) TappingMode™ AFM phase image (3 µm ×3 µm) c) TappingMode™ AFM phase image (1 µm ×1 µm).

Figure 5.13a shows an array of discrete elliptical domains rich in nanofiller content in the nanocomposite membrane containing 20 wt% PEG POSS®. These elliptical features disappear

and the PEG POSS® rich domains become interconnected when the nanofiller content is 30 wt% (Figure 5.14a). Owing to the low magnification, necessary to observe these morphological features over a large area, the nanoscopic microphase separation of the block copolymer is not discerned in the SEM micrographs. The microphase separation of polyether and polyester domains of the P 1500 multiblock copolymer is visible in the 1 μm ×1 μm AFM phase image (Figure 5.12c). The dark brown regions correspond to the amorphous PEG domains while the light brown regions are attributed to the polyester domains. The white spots surrounded by the dark brown region are attributed to the crystallites of PEG. Appearance of these white spots suggests that the polyether domains are not completely amorphous under the measurement condition of AFM. PEG POSS® appears as white spots in TappingMode™ AFM phase images. The 3 μm ×3 μm AFM images presented in Figures 5.13b and 5.14b show both the PEG POSS® rich regions and the regions depleted of PEG POSS® in the nanocomposites. These images are in agreement with the SEM results. The microphase separated structure embedded underneath these PEG POSS® depleted regions is only visible in AFM. Figures 5.13c and 5.14c show the 1 μm ×1 μm AFM phase images of the regions which are rich in PEG POSS® content. Both of these images show that although PEG POSS® exists as agglomerates on a nanoscopic level, the nanofillers are not rejected by the polyether microdomains of both nanocomposite membranes.[71]

5.3. Discussion

The gas permeability increases with temperature in a polymer membrane. Typically diffusion (i.e the kinetic factor of permeability) increases while solubility (i.e the thermodynamic factor)

shows a decreasing trend with increasing temperature [40]. In a rubbery polymer membrane this phenomenon is attributed to higher chain mobility in the polymer membrane and higher kinetic energy of the permeating gas molecules. This trend is observed only in P 1500 among the three grades of PolyActive^{TM} investigated here. Hence, it seems that the polyether blocks of P 1500 are in the amorphous state between 30 and 70 ºC and no thermal transition occurs in this temperature range. In P 3000 and P 4000 another key feature dominates the transport of CO_2 through the membranes. It is apparently well known that diffusion of gases through a semicrystalline polymer is lower than through an amorphous polymer. Crystallites of semicrystalline polymers typically act as impermeable and non-sorbing phase. Gas molecules are effectively soluble in and diffuse through only the amorphous phase. Hence the presence of crystallites increases the tortuosity of the gas diffusion path. Moreover these crystallites cause chain immobilization of the neighboring amorphous phase to some extent [12, 33]. From the CO_2 permeation behavior (section 5.2.3.1) it is evident that the polyether blocks of P 3000 and P 4000 are in a semicrystalline state at 30 ºC. With the increase of temperature the crystallites start to melt (i.e. the polymer undergoes thermal transition) and the total amount of amorphous polyether increases. P 3000 shows the typical behavior of a rubbery polymer within 50 - 70 ºC range. Hence it seems reasonable to argue that melting of the crystallites of P 3000 is complete as the temperature increases from 30 ºC to 50 ºC for a single gas permeation measurement. But for P 4000 the CO_2 permeation trend (Figure 5.4) reveals that some crystallites are still present in the polyether blocks at 50 ºC. However, section 5.2.2 shows that according to DSC measurements at a scan rate of 10 K/min the melting of the polyether block of P 1500, P 3000 and P 4000 is completed at approximately 32, 44 and 50 ºC, respectively. It must be noted that the onset and endset temperatures of the melting endotherms cannot be used directly to explain the behavior of

the CO_2 permeation behavior observed at a particular temperature presented in section 5.2.3.1. Because the temperature recorded in DSC is a function of the scan rate and the rate of increase of temperature of the single gas permeability measurements (via time-lag method) is not comparable to that of the DSC scan.

Metz et al. [15] have extensively studied the poly(ethylene oxide) poly (butylene terephthalate) (PEO-PBT) multiblock copolymers and reported the CO_2 permeability of 1000PEO75PBT25, 2000PEO75PBT25 and 4000PEO75PBT25 (having polyether segments of 1000, 2000 and 4000 g/mol, respectively). It was found that 4000PEO75PBT25 at 50 ºC exhibits the highest CO_2 permeability among the studied polymers. A comparison of the three grades of PolyActive™ (containing approximately 77 wt% of PEGT and 23 wt% of PBT) investigated here suggests that if the application temperature is 50 ºC or slightly higher as is expected in case of post combustion carbon capture [3], P 3000 would be the ideal polymer among the three grades of PolyActive™ investigated here. However, if the application temperature is below 50 ºC the CO_2 permeability of P 3000 decreases dramatically as the polyether blocks are not in a completely amorphous state. In this case the nanocomposite of P 1500 containing 30 wt% PEG POSS® is a better choice since it gives the highest CO_2 permeability within 30 - 70 ºC temperature range.

A careful comparison of the transport of CO_2 through the nanocomposites (presented in section 5.2.3.1) unravels some interesting phenomenon. Incorporation of 20 wt% PEG POSS® in P 1500 and P 3000 leads to an increase of permeability. The CO_2 permeability (Figure 5.4) increased significantly as the PEG POSS® content of the nanocomposite based on P 1500 was increased from 20 wt% to 30 wt%. CO_2 diffusion coefficients for these two nanocomposite membranes are

analogous and higher than that of pure P 1500 (Figure 5.5). It can mean that the polymer-filler system has reached an upper limit for the diffusive jumps of the penetrating CO_2 molecule. The increase of permeability stems from a substantial increase of CO_2 solubility (Figure 5.6) in the nanocomposite membrane. Surprisingly the CO_2 solubility changes significantly when PEG POSS® content increases from 20 wt% to 30 wt% although it remains unchanged between 0 wt% to 20 wt%. This observation implies that additional sites for CO_2 dissolution is formed only upon increase of PEG POSS® content from 20 wt% to 30 wt%. This hypothesis is consistent with the morphological features of the membranes presented in section 5.2.4. The microscopic investigation shows that there exists a saturation threshold of PEG POSS® content between 20 wt% and 30 wt% in P 1500 after which further incorporation of PEG POSS® leads to morphological change of the nanocomposite. Isolated PEG POSS® rich regions are observed both in surface and cross section of the nanocomposite containing 20 wt% PEG POSS®. In the 30 wt% PEG POSS® containing nanocomposite the surface has a more homogeneous distribution of ether oxygen which may lead to favorable sorption of CO_2 molecules. Moreover, the PEG POSS® rich regions become continuous (i.e. percolated) in the bulk of this nanocomposite membrane. Hence, more PEG is accessible in the bulk of the nanocomposite for the penetrating CO_2 molecules due to a good interconnection of PEG POSS® rich regions. Thus the morphology of the PEG POSS® incorporated P 1500 nanocomposites has substantial influence upon the gas permeation through the membranes. The nanocomposites of P 3000 and P 4000 are not interesting from an application point of view since they do not show stable properties under experimental conditions. From the gas transport behavior observed in section 5.2.3.1 for pure polymer membranes it is clear that both P 3000 and P 4000 undergo thermal transition in the temperature range of 30 - 70 ºC while P 1500 does not. Section 5.2.2

demonstrates that the polyether of PEG POSS® melts and crystallizes separately from the polyether of all three grades of PolyActive™ during heating and cooling scans run in the DSC. Moreover, the polyether of P 1500 has a lower crystallinity compared to P 3000 and P 4000 (Table 5.3). Thus the nanocomposite of P 1500 is stable in the temperature range of 30 - 70 ºC because the polyether domains do not undergo any thermal transition in this temperature range. Moreover, only 37% of the polyether of P 1500 is able to crystallize. Hence, there is always enough amorphous polyether of the block copolymer present in the matrix to accommodate the PEG POSS® nanofiller. These observations lead to the conclusion that the nanocomposites of PolyActive™ containing PEG POSS® are not stable in a temperature range where the polyether blocks undergo any thermal transition in case when the crystalline phase content is big enough to force the dispersed PEG POSS® out of the polymer matrix. Hence the application of PEG POSS® incorporated PolyActive™ nanocomposites having high crystallization degree as selective material of the gas separation membrane is only possible in a temperature range where no thermal transition takes place. Although we report this phenomenon here only for blends of PolyActive™ and PEG POSS® this trend will be very likely true also for other PEO based block copolymer and filler combinations as well.[71]

5.4. Conclusion

The influence of the PEG segment length of three grades of PolyActive™ upon separation of CO_2 from light gases was investigated. Commercial PEG POSS® was used as nanofiller to prepare the nanocomposite membranes. A correlation between the thermal transition observed in the DSC run and the gas permeation phenomenon in the temperature range from 30 - 70 ºC

elucidates some essential features which may facilitate the selection of appropriate membrane material for post combustion carbon capture. The length of the PEG segment regulates the content of the crystalline polyether phase at a particular temperature which has a pronounced influence on the gas separation efficiency of the membrane. Commercial PEG POSS® as nanofiller can increase the gas permeability, but the polymer matrix must be carefully chosen depending on the lengths of the PEG segments and the temperature range of the application. The possible application of the PEG POSS® containing nanocomposite membranes based on PolyActive™ with a high crystalline polyether microphase content is limited to a temperature range where no thermal transition of the polyether block microphase takes place.[71]

Chapter 6. Functionalization of POSS nanoparticles and fabrication of block copolymer nanocomposite membranes for CO_2 separation

6.1. Introduction

A variety of POSS containing reactive functionalities which are suitable precursors for grafting or further modification are commercially available. The flexibility to tune the compatibility between the nanoparticle and the polymer matrix by altering the functional group is quite appealing for the researchers to design polymer composite materials with improved properties by incorporating functionalized POSS nanoparticles [29, 73-78]. Chapter 4 represents the influence of PEG POSS® incorporation in two grades of the commercial poly(ether-*block*-amide) thermoplastic elastomer PEBAX® upon CO_2 separation performance. In this chapter we extend that concept to PEG functionalized POSS nanoparticles containing additional functionality in between the PEG ligand and the silsesquioxane cage core as filler for PEBAX® MH 1657 membrane. In what follows, first we aim to provide a comprehensive account of the influence of three different solvents (chloroform, toluene and tetrahydrofuran) upon modification of glycidyl POSS® (Scheme 1a) and glycidyldimethylsilyl POSS® (Scheme 1b) with methoxy poly(ethylene glycol) (PEG) via epoxide ring opening reaction. Next we compare the CO_2 separation performance of the nanocomposite membranes fabricated by using the obtained functionalized nanoparticles as filler for PEBAX® MH 1657.

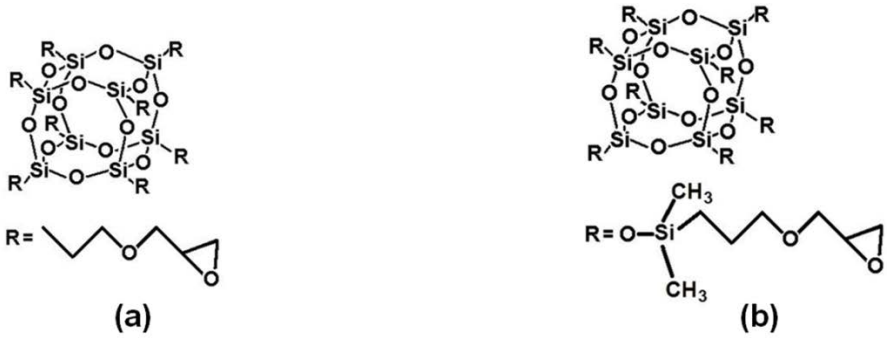

Scheme 6.1: Structure of – (a) glycidyl POSS® (b) glycidyldimethylsilyl POSS®.

6.2. Results & Discussion

6.2.1. Modification of glycidyl POSS® and glycidyldimethylsilyl POSS® with methoxy poly(ethylene glycol):

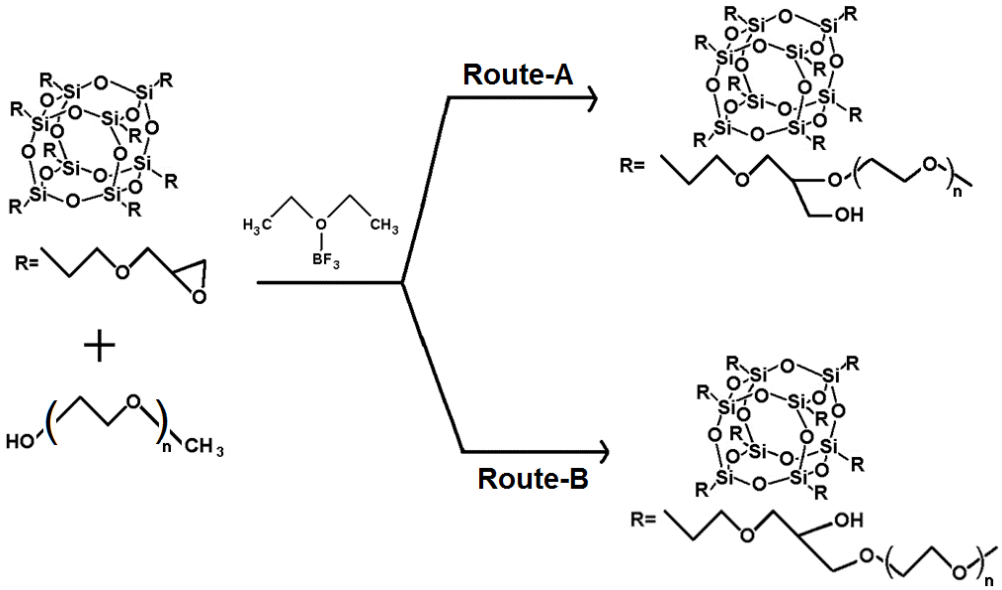

Scheme 6.2: Epoxide ring opening reaction mechanism S_N1 and S_N2.

Epoxides (three membered oxiranes) are extremely strained and reactive systems. Scheme 6.2 illustrates the two possible routes of an asymmetric epoxide ring opening reaction. One is following the S_N1 mechanism (Scheme 6.2, Route A) where nucleophilic substitution occurs at the more substituted carbon. In this reaction pathway the breaking of C-O bond creates a carbocation and the nucleophile attacks this carbocation. Hence, the stability of the carbocation determines the nucleophilic attack at this position to a great extent. The other possibility is that the reaction follows the S_N2 mechanism (Scheme 6.2, Route B) where the nucleophile attacks the less substituted carbon. Under acidic conditions the position of attack of the nucleophile is determined both by the steric hindrance and the carbocation stability. [79] To justify the epoxide

ring opening and subsequent attachment of PEG ligand, the synthesis was monitored by NMR and FT-IR spectroscopy.

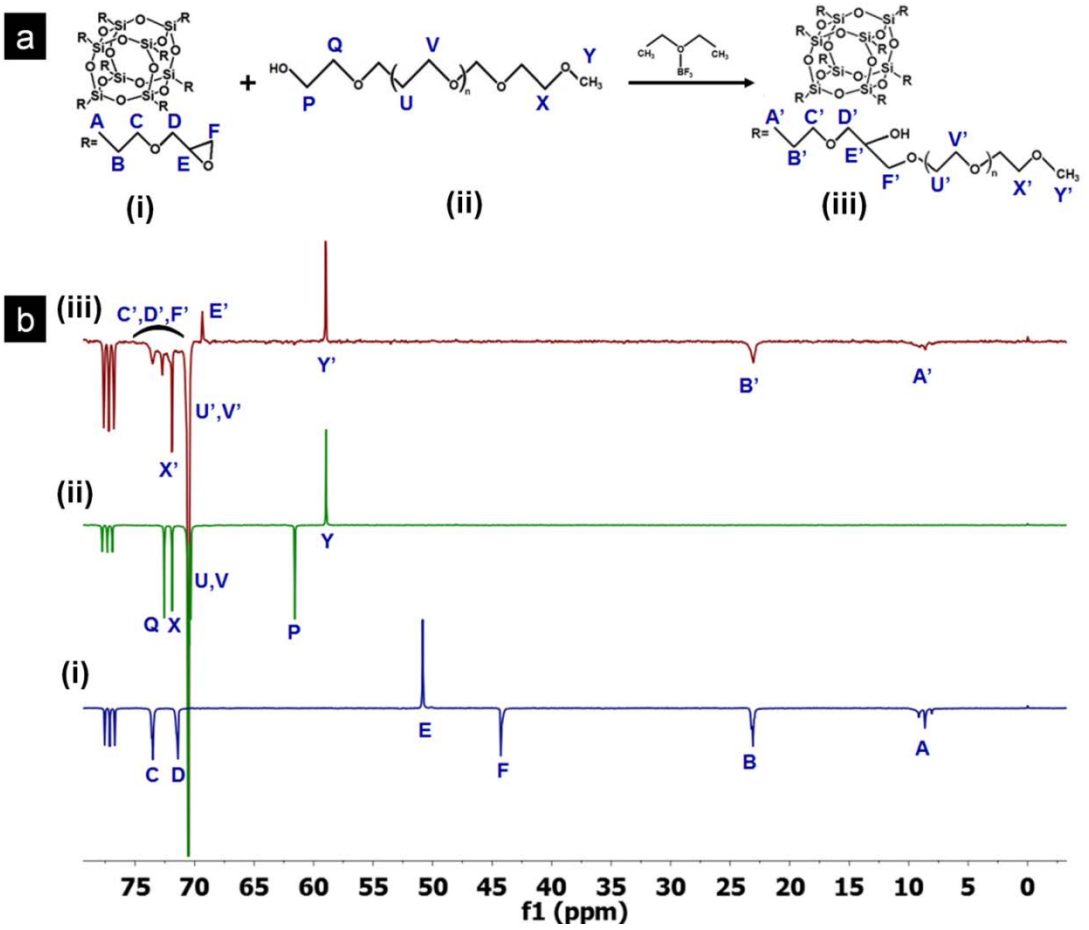

Figure 6.1: (a) Reaction scheme and chemical structures (b) ^{13}C-DEPTQ-135 NMR spectra of – (i) glycidyl POSS® (ii) methoxy poly(ethylene glycol) (PEG) (iii) PEG modified glycidyl POSS.

Figure 6.1b and Figure 6.2 illustrates the ^{13}C-DEPTQ-135 NMR and FT-IR spectra of glycidyl POSS® (i), PEG (ii) and PEG functionalized glycidyl POSS using toluene as solvent (iii). In the ^{13}C-DEPTQ-135 NMR spectra of Figure 1b the –CH and –CH_3 peaks are pointing upwards and

the $–CH_2$ peaks are pointing downwards. The peaks E and F (at 44.3 ppm and 50.9 ppm, respectively) in spectrum (i) originate from the epoxide ring of glycidyl POSS®. The peak P (at 61.6 ppm) in spectrum (ii) is attributed to the neighboring $–CH_2$ of –OH group of PEG. The disappearance of the peaks E, F &P in spectrum (iii) and the strong appearance of the peaks Y', U' and V' (at 59 ppm and 70.5 ppm) which originate from the $–CH_3$ end group and the $–CH_2$-O-CH_2- repeating unit of PEG, respectively, proves the successful modification of glycidyl POSS® with PEG. Spectrum (iii) shows only one –CH peak at 69.3 ppm (peak E'). Hence, the reaction followed one particular route of Scheme 2 (either S_N1 or S_N2 mechanism). The position of the peak E' suggests that in the present case the epoxide ring opening occurred via route B i.e S_N2 mechanism. Because in the other case, (S_N1 mechanism) the –CH peak is expected to appear more downfield.

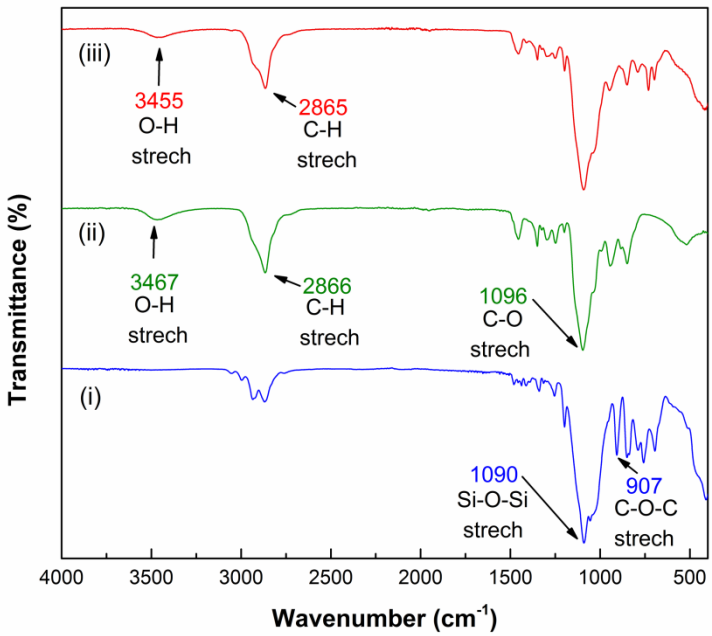

Figure 6.2: FT-IR spectra of – (i) glycidyl POSS® (ii) methoxy poly(ethylene glycol) (PEG) (iii) PEG modified glycidyl POSS.

In the FT-IR spectrum of glycidyl POSS® (Figure 6.2, spectrum (i)) the Si–O–Si stretching vibration of the POSS cage and the C–O–C stretching vibration of the epoxide group are detected at 1090 cm^{-1} and 907cm^{-1}, respectively. [80] The stretching vibration of –OH group, C–H stretching vibration of the methylene group and C–O stretching vibration of the $–CH_2–O–CH_2–$ repeating unit of PEG are observed at 3467cm^{-1}, 2866cm^{-1} and 1096cm^{-1}, respectively, (Figure 6.2, spectrum (ii)). In the FT-IR spectrum of the PEG modified glycidyl POSS (Figure 6.2, spectrum (iii)) Si–O–Si stretching vibration of POSS and C–O stretching vibration of the $–CH_2–O–CH_2–$ repeating unit of PEG overlap each other and the presence of –OH group is evident from the band at 3455 cm^{-1}. Since the peak P (the neighboring $–CH_2$ peak of –OH group of PEG) completely disappeared in the NMR spectra (Figure 6.1b, spectrum (iii)) there is no unreacted PEG left. A new –OH group originates after epoxide ring opening which gives the broad peak at 3455 cm^{-1} in the FT-IR spectrum (Figure 6.2, spectrum (iii)). The combination of ^{13}C-NMR and FT-IR results leads to the conclusion of structure (iii) of Figure 6.1a.[81]

6.2.2. Influence of solvent upon the structure of functionalized POSS nanoparticles:

Both glycidyl POSS® and glycidyldimethylsilyl POSS® are successfully modified with PEG using three different solvents (chloroform, toluene and THF). For further discussion the product of these reactions are given acronyms (listed in table 6.1).

Table 6.1. Acronyms of the products of epoxide ring opening reaction.

Reactant	Solvent	Acronym of product
Glycidyl POSS and PEG	Chloroform	PEG-GLY-POSS-Chloroform
Glycidyldimethylsilyl POSS and PEG	Chloroform	PEG-GDMS-POSS-Chloroform
Glycidyl POSS and PEG	Toluene	PEG-GLY-POSS-Toluene
Glycidyldimethylsilyl POSS and PEG	Toluene	PEG-GDMS-POSS-Toluene
Glycidyl POSS and PEG	THF	PEG-GLY-POSS-THF
Glycidyldimethylsilyl POSS and PEG	THF	PEG-GDMS-POSS-THF

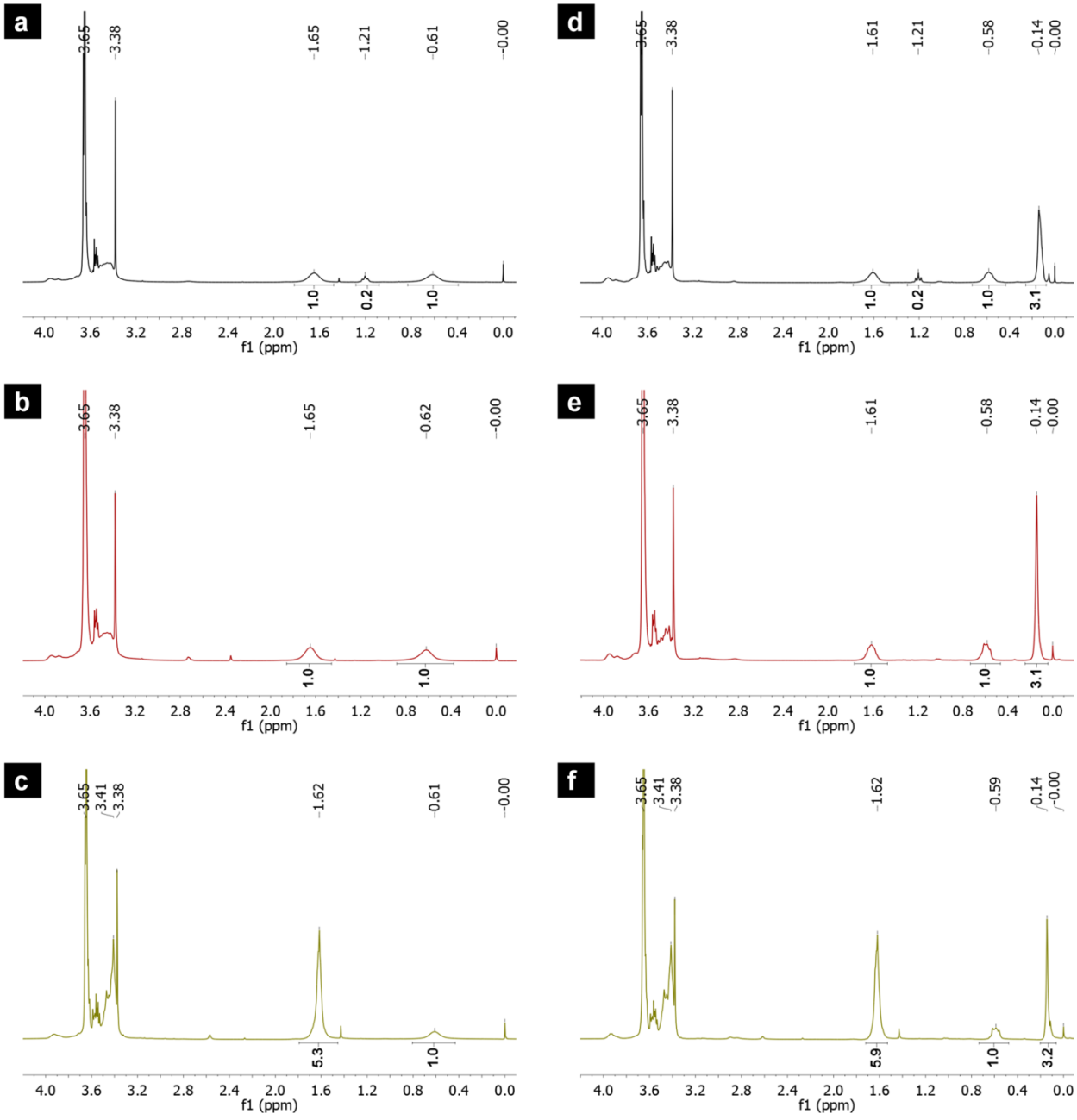

Figure 6.3: ^{1}H NMR spectra of – (a) PEG-GLY-POSS-Chloroform (b) PEG-GLY-POSS-Toluene (c) PEG-GLY-POSS-THF (d) PEG-GDMS-POSS-Chloroform (e) PEG-GDMS-POSS-Toluene (f) PEG-GDMS-POSS-THF.

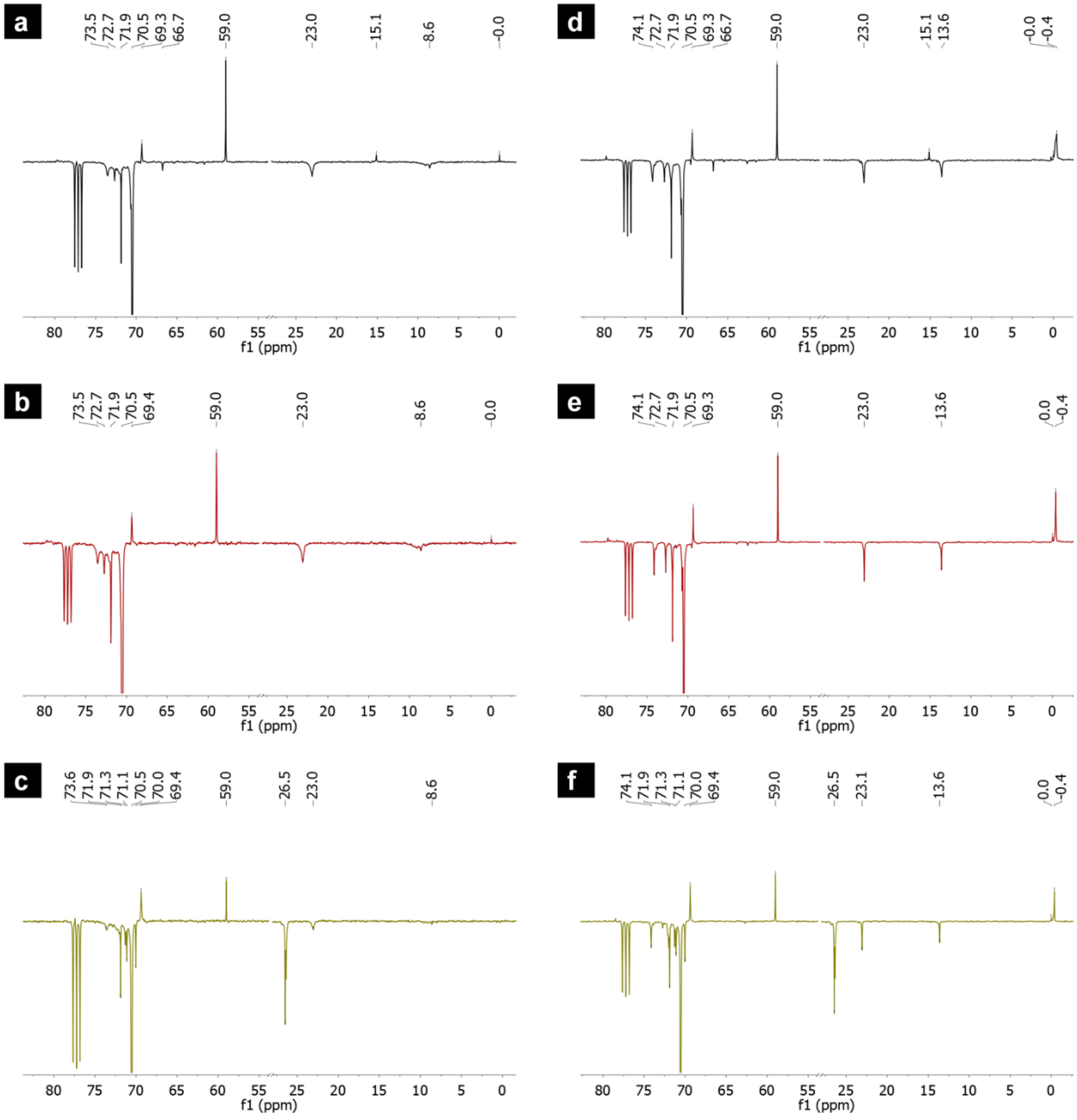

Figure 6.4: ^{13}C-DEPTQ-135 NMR spectra of – (a) PEG-GLY-POSS-Chloroform (b) PEG-GLY-POSS-Toluene (c) PEG-GLY-POSS-THF (d) PEG-GDMS-POSS-Chloroform (e) PEG-GDMS-POSS-Toluene (f) PEG-GDMS-POSS-THF.

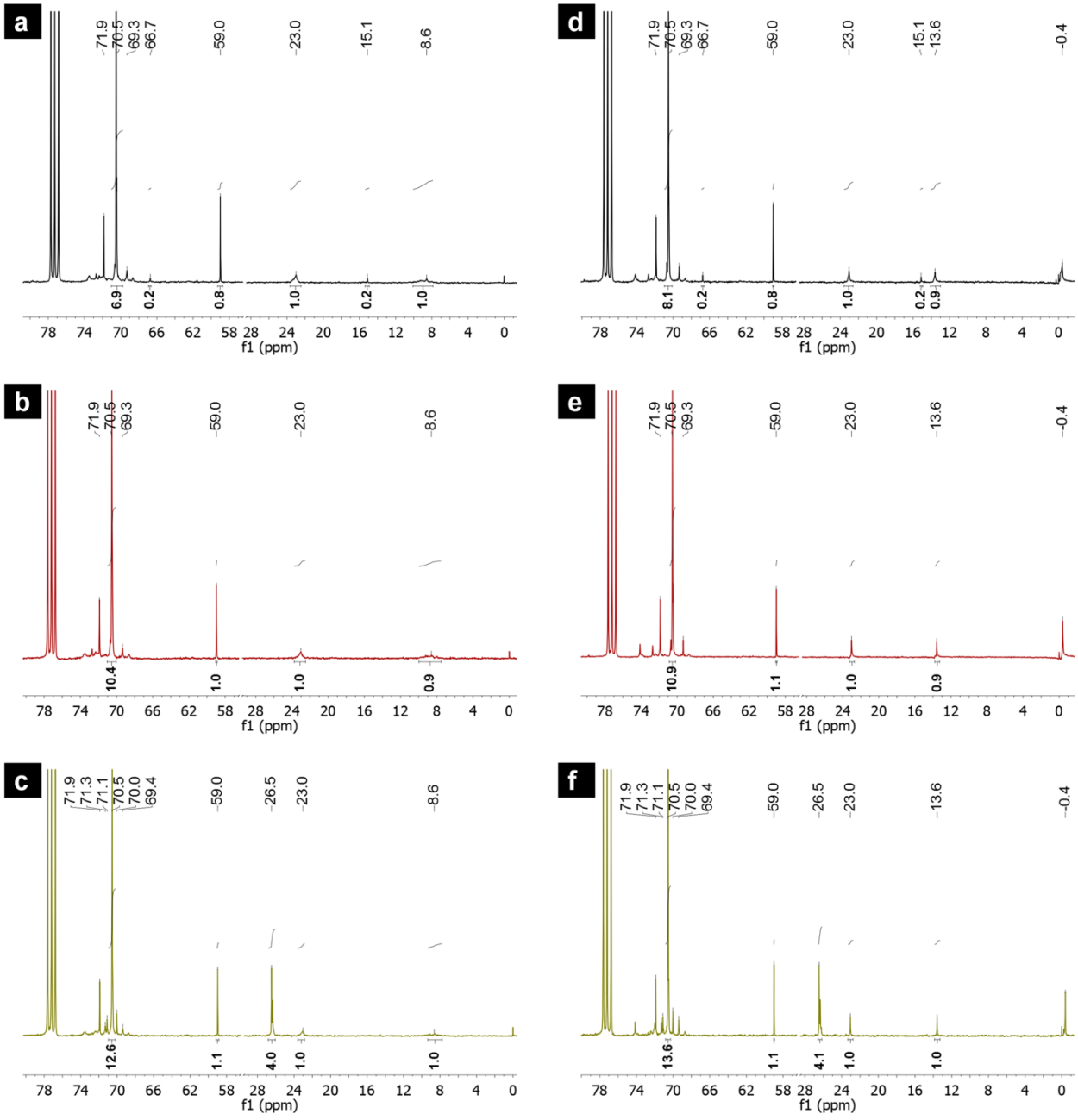

Figure 6.5: Quantitative ^{13}C (inverse gated decoupled) NMR spectra of – (a) PEG-GLY-POSS-Chloroform (b) PEG-GLY-POSS-Toluene (c) PEG-GLY-POSS-THF (d) PEG-GDMS-POSS-Chloroform (e) PEG-GDMS-POSS-Toluene (f) PEG-GDMS-POSS-THF.

Figure 6.3 and 6.4 shows the ^{1}H-NMR and the ^{13}C-DEPTQ-135 NMR spectra of the synthesized nanofillers, respectively (a list of the ^{1}H-NMR and ^{13}C-NMR peaks is provided in Appendix A, Section 12.1). From the position of the –CH peak (in Figure 6.4) after ring opening it is evident that the epoxide ring opening reaction occurred via S_N2 mechanism in all three solvents for both glycidyl POSS® and glycidyldimethylsilyl POSS®. The quantitative ^{13}C (inverse gated decoupled) NMR spectra of the synthesized nanofillers are presented in Figure 6.5. Comparison of these spectra as well as the integration of the area of peaks reveals very important information about the structure of the synthesized nanoparticles. If all the epoxide rings open up due to nucleophilic attack of the –OH group of PEG, the integration of the area of $–CH_2$ peak at 23 ppm and $–CH_3$ peak (originates from the end group of PEG) at 59 ppm should be equal (since it is already evident that there is no unreacted PEG left in the product). In the spectra of both PEG-GLY-POSS-Toluene (Figure 6.5b) and PEG-GDMS-POSS-Toluene (Figure 6.5e) the integral areas of these peaks are nearly equal. Hence, it is clear that toluene as a solvent for the reaction does not lead to any byproducts and the epoxide ring opening occurs merely due to nucleophilic attack of PEG. However, in the spectra of PEG-GLY-POSS-Chloroform (Figure 6.5a) and PEG-GDMS-POSS-Chloroform (Figure 6.5d) two additional peaks are visible at 66.7 ppm and 15.1 ppm. These peaks are a distinct signature of the $–OCH_2CH_3$ group of boron triflouride diethyletherate i.e. the catalyst. Moreover, the integral areas of $–CH_3$ peak at 59 ppm with respect to the areas of $–CH_2$ peak at 23 ppm are not equal. These observations unveil the fact that when chloroform is used as the reaction solvent, although most of the epoxide rings (ca. 80%) are opened by the PEG, a small fraction of epoxide rings are opened by the catalyst itself. Comparison of the integral area of the $–CH_2$ peak at 70.5 ppm (originating from the repeating unit of PEG) of Figures 3a to 3d and Figures 3b to 3e also supports this argument and provides

evidence that PEG-GLY-POSS-Chloroform (Figure 6.5a) and PEG-GDMS-POSS-Chloroform (Figure 6.5d) contain less amount of PEG compared to PEG-GLY-POSS-Toluene (Figure 6.5b) and PEG-GDMS-POSS-Toluene (Figure 6.5e), respectively. However, there is some deviation in the integral areas of this peak due to closely packed peaks (baseline is difficult to be determined) at this region. In the NMR spectra of PEG-GLY-POSS-THF (Figure 6.5c) and PEG-GDMS-POSS-THF (Figure 6.5f), although no peak is observed which may originate from the catalyst, a typical peak for THF is observed at 26.5 ppm and another peak is merged with the repeating unit of PEG at 70.5 ppm. Two individual resonances for protons of the THF are clearly visible in the ^{1}H-NMR spectra at 1.62 ppm and 3.41 ppm (Figure 6.3c and f). Moreover, in ^{13}C-NMR of PEG-GLY-POSS-THF (Figure 6.5c) and PEG-GDMS-POSS-THF (Figure 6.5f) three new peaks are observed at 70 ppm, 71.1 ppm and 71.3 ppm. But the areas of -CH_2 peak at 23 ppm and –CH_3 at 59 ppm are rather similar. Hence it can be concluded that the epoxide rings are opened by a nucleophilic attack of PEG.

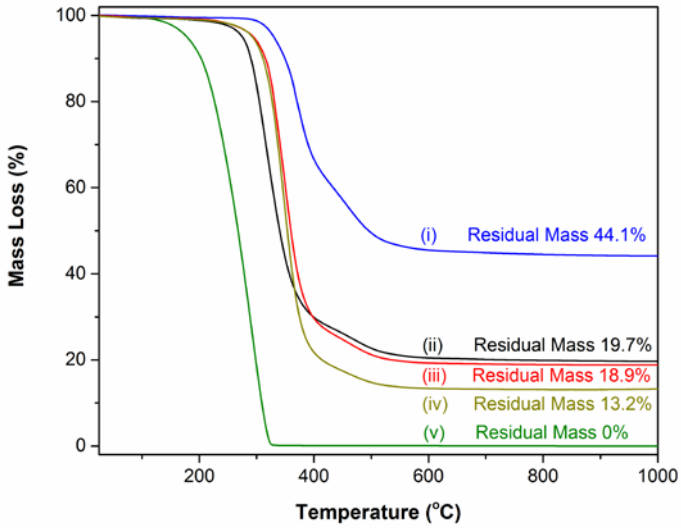

Figure 6.6: Thermogravimetric analysis of – i) glycidyl POSS® ii) PEG-GLY-POSS-Toluene iii) PEG-GLY-POSS-Chloroform iv) PEG-GLY-POSS-THF v) methoxy poly(ethylene glycol) (PEG).

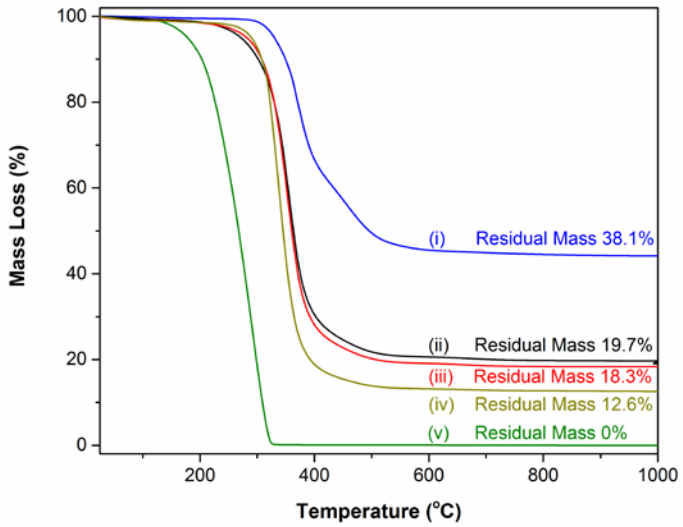

Figure 6.7: Thermogravimetric analysis of – i) glycidyldimethylsilyl POSS® ii) PEG-GDMS-POSS-Toluene iii) PEG-GDMS-POSS-Chloroform iv) PEG-GDMS-POSS-THF v) methoxy poly(ethylene glycol) (PEG).

Thermogravimetric analysis (TGA) of glycidyl POSS® and glycidyldimethylsilyl POSS® before and after PEG modification are presented in Figures 6.6 and 6.7, respectively. The weight loss of PEG starts at 221 ºC and there is no significant residue at the end. It is evident that the thermal stability of the PEG ligand attached to POSS is higher compared to that of pure PEG. For glycidyl POSS® (Figure 6.6) and glycidyldimethylsilyl POSS® (Figure 6.7) the onset temperature of mass loss are 337 ºC and 327 ºC while the residual masses are 44.1% and 38.1%, respectively. After grafting PEG to the POSS nanoparticles the mass loss increases substantially which is attributed to the higher organic functional group content of the POSS. No significant difference is observed in the residual mass of PEG-GLY-POSS-Chloroform, PEG-GLY-POSS-Toluene, PEG-GDMS-POSS-Chloroform and PEG-GDMS-POSS-Toluene. But, both PEG-GLY-POSS-THF (Figure 6.6) and PEG-GDMS-POSS-THF (Figure 6.7) show higher mass loss compared to

the POSS nanoparticles modified using chloroform and toluene as a solvent. The onset of mass loss for PEG-GLY-POSS-THF (Figure 6.6) and PEG-GDMS-POSS-THF (Figure 6.7) are 314 ºC and 310 ºC, respectively. Hence the higher mass loss is not due to the presence of any residual solvent. It must be attributed to an organic moiety which is strongly bound to the POSS nanoparticles. The observations of ^{13}C-NMR and TGA leads to a conjecture that THF forms a complex when it is used as solvent for epoxide ring opening reaction in presence of boron triflouride diethyletherate catalyst i.e. in PEG-GLY-POSS-THF and PEG-GDMS-POSS-THF. Compostion of the PEG functionalized POSS nanoparticles are determined using the NMR data which is provided in Appendix A, Table 12.1.[81]

6.2.3. Gas separation performance of the nanocomposite membranes:

In this section, the gas separation performance of the prepared nanocomposite membranes is compared with that of the pure PEBAX® MH 1657 membrane. The solution-diffusion mechanism is adopted to explain the transport of CO_2 gas through the prepared dense membranes. Figure 6.8 shows the permeability of N_2, H_2 and CO_2 as a function of nanofiller content in the nanocomposite membranes at 30 ºC.

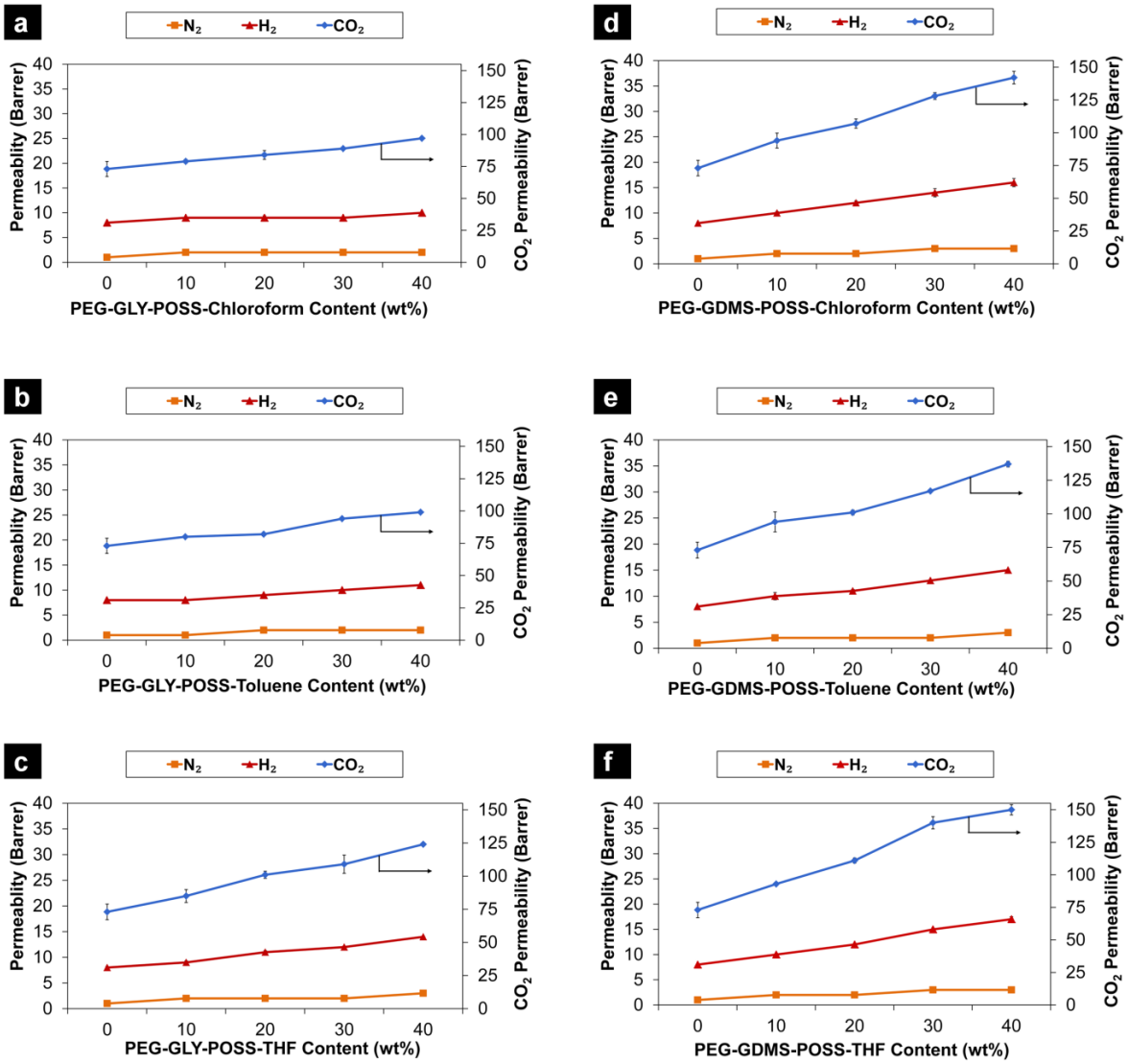

Figure 6.8: Single gas permeability as a function of – a) PEG-GLY-POSS-Chloroform content b) PEG-GLY-POSS-Toluene content c) PEG-GLY-POSS-THF content d) PEG-GDMS-POSS-Chloroform content e) PEG-GDMS-POSS-Toluene content f) PEG-GDMS-POSS-THF content. Permeability of N_2 and H_2 are plotted on left ordinate and that of CO_2 right ordinate.

By comparing the graphs on the left column of Figure 6.8 to those on the right column (i.e Figure 6.8a to 6.8d, 6.8b to 6.8e and 6.8c to 6.8f, respectively) it is possible to study the effect of the

dimethylsilyl spacer between the cage structure of POSS and PEG ligand on the gas permeability of the nanocomposite membranes. On the other hand, comparison of the graphs of one column with each other (e.g. Figure 6.8a, 6.8b and 6.8c) shows the effect of the three different solvents used for synthesis of the nanofillers upon gas permeability of the nanocomposite membranes. The scales of the graphs in Figures 6.8, 6.9 and 6.10 are similar for easier comparison. It is evident from Figure 6.8 that the nanocomposite membranes containing the nanofillers with the dimethylsilyl spacer i.e. PEG-GDMS-POSS-Chloroform (Figure 6.8d), PEG-GDMS-POSS-Toluene (Figure 6.8e) and PEG-GDMS-POSS-THF (Figure 6.8f) have higher permeabilities compared to those containing the nanoparticles without spacer i.e. PEG-GLY-POSS-Chloroform (Figure 6.8a), PEG-GLY-POSS-Toluene (Figure 6.8b) and PEG-GLY-POSS-THF (Figure 6.8c). Comparison of Figure 6.8a to Figure 6.8b shows that incorporation of PEG-GLY-POSS-Chloroform and PEG-GLY-POSS-Toluene in PEBAX® MH 1657 leads to similar values of gas permeability for all four compositions. Figures 6.8d and 6.8e (i.e gas permeability of nanocomposites containg PEG-GDMS-POSS-Chloroform and PEG-GDMS-POSS-Toluene respectively) are also analogous. Therefore, it is clear that although the synthesis of nanofillers in chloroform induces small amounts of byproduct due to ring opening via catalyst instead of PEG, it does not have any significant influence upon gas permeability of the nanocomposite membranes. But Figure 6.8c shows that the PEG-GLY-POSS-THF incorporated nanocomposites have higher gas permeability compared to the nanocomposites containing both PEG-GLY-POSS-Chloroform (Figure 6.8a) and PEG-GLY-POSS-Toluene (Figure 6.8b). Figure 6f shows that the nanocomposites containing up to 30 wt% PEG-GDMS-POSS-THF have higher permeabilities compared to the nanocomposites containing both PEG-GDMS-POSS-Chloroform (Figure 6.8d) and PEG-GDMS-POSS-Toluene (Figure 6.8e) of similar composition.

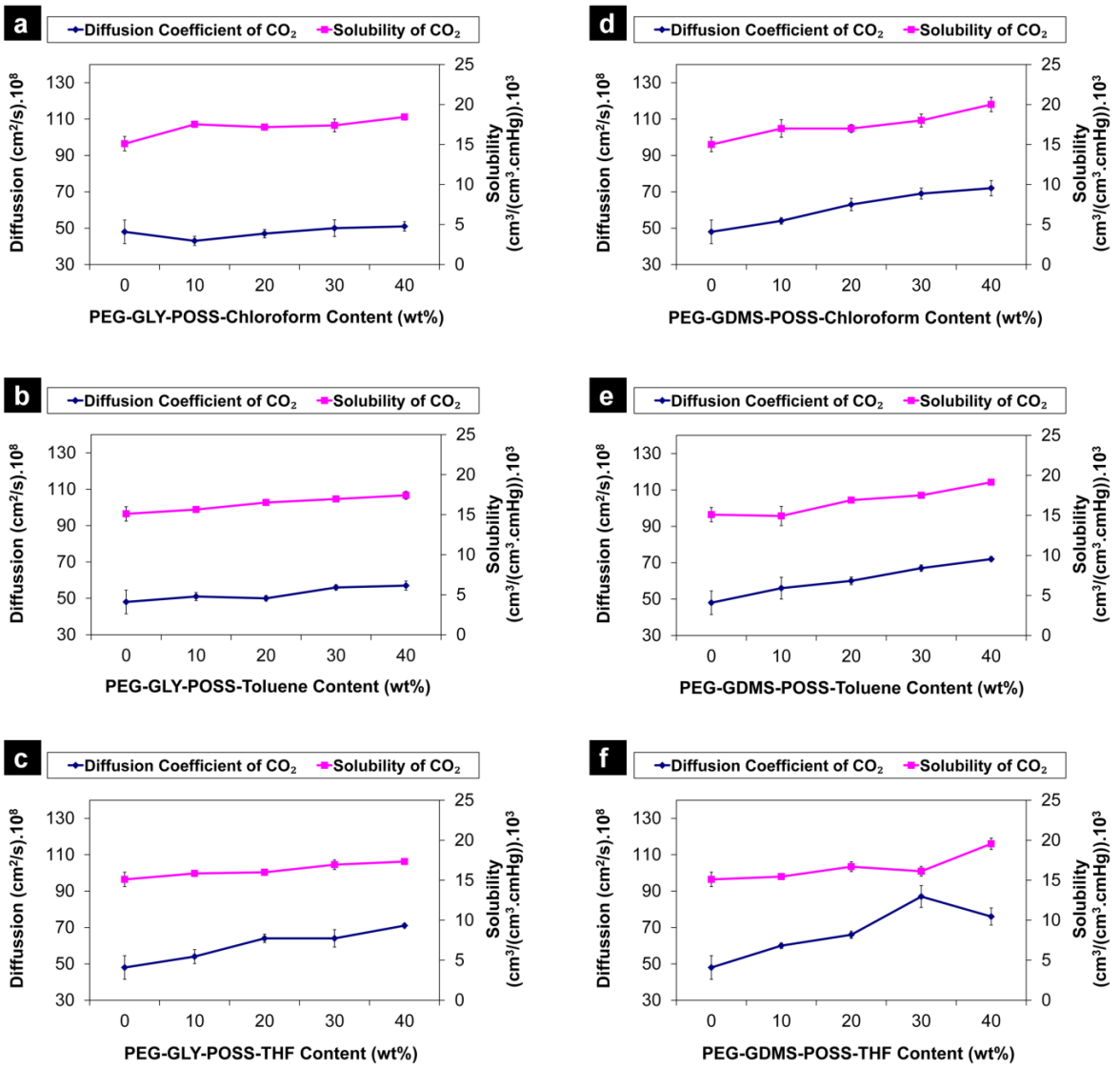

Figure 6.9: Diffusion and solubility coefficients of CO_2 as a function of – a) PEG-GLY-POSS-Chloroform content b) PEG-GLY-POSS-Toluene content c) PEG-GLY-POSS-THF content d) PEG-GDMS-POSS-Chloroform content e) PEG-GDMS-POSS-Toluene content f) PEG-GDMS-POSS-THF content

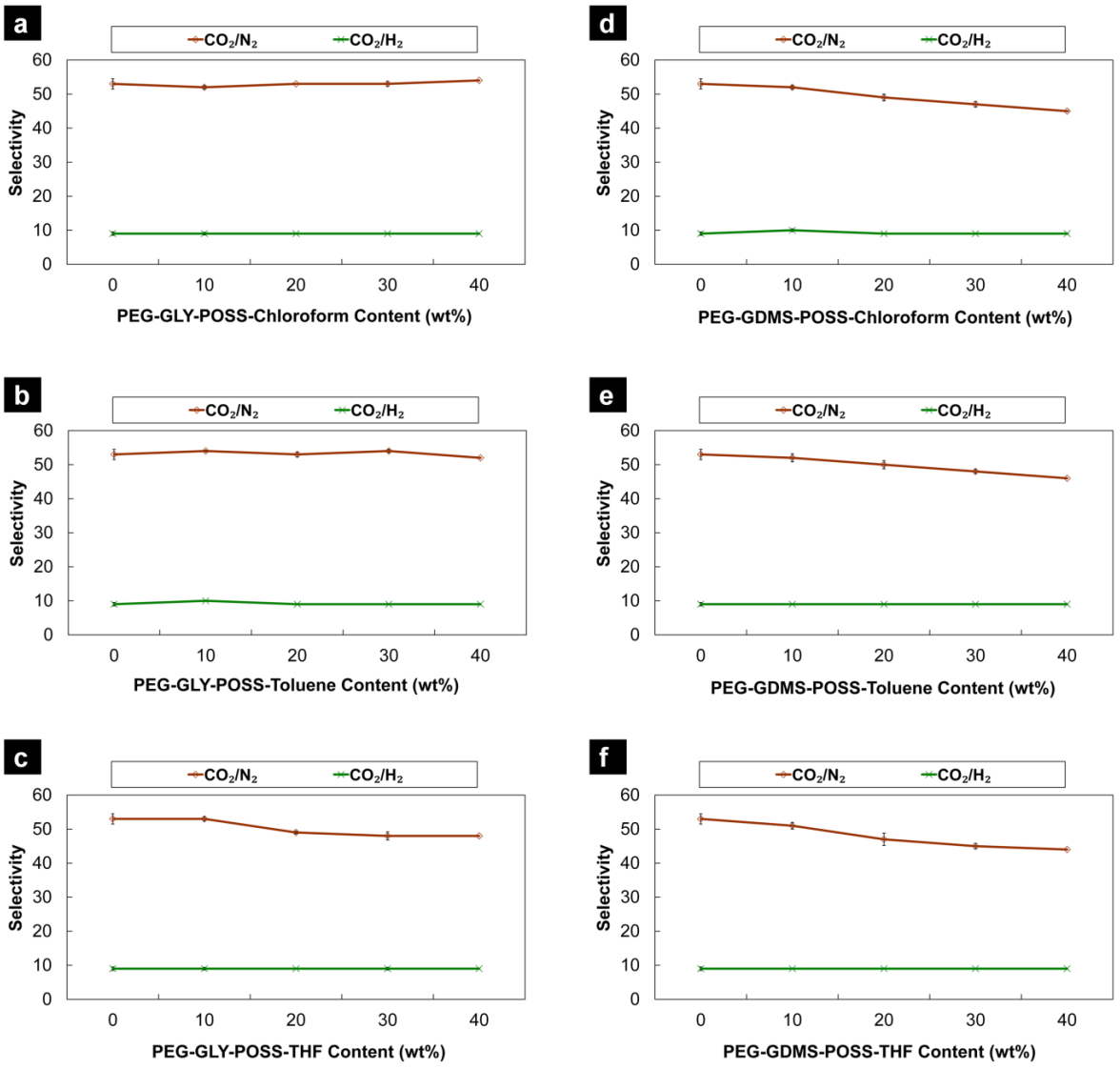

Figure 6.10: CO_2 selectivity over light gases as a function of – a) PEG-GLY-POSS-Chloroform content b) PEG-GLY-POSS-Toluene content c) PEG-GLY-POSS-THF content d) PEG-GDMS-POSS-Chloroform content e) PEG-GDMS-POSS-Toluene content f) PEG-GDMS-POSS-THF content.

The diffusion and solubility coefficients of CO_2 were determined using equation 3.3 and 3.2, respectively. (Figure 6.9) It is clear that the presence of the THF complex and the dimethylsilyl spacer between the cage structure of POSS and PEG ligand both leads to higher CO_2 diffusion coefficient through the nanocomposite membranes which in turn increases the CO_2 permeability. The correlation between gas transport mechanism and structure of the nanofillers are discussed in detail in Chapter 7. Figure 6.10 shows the selectivity of CO_2 over N_2 and H_2 as a function of nanofiller content in the nanocomposite membranes at 30 ºC. The CO_2/N_2 selectivity is unchanged in PEG-GLY-POSS-Chloroform and PEG-GLY-POSS-Toluene containing nanocomposite membranes. However, the nanocomposite membranes containing other fillers show a decreasing trend of CO_2/N_2 selectivity with increasing nanofiller content. The CO_2/N_2 selectivity of PEBAX® MH 1657 membrane is 53. At 40 wt% loading of PEG-GLY-POSS-Chloroform, PEG-GLY-POSS-Toluene, PEG-GLY-POSS-THF, PEG-GDMS-POSS-Chloroform, PEG-GDMS-POSS-Toluene & PEG-GDMS-POSS-THF the CO_2/N_2 selectivity of the nanocomposite membranes were 53, 52, 48, 45, 46 and 44, respectively. Hence, the presence of the THF complex and the dimethylsilyl spacer between the cage structure of POSS and PEG ligand both leads to a loss of CO_2/N_2 selectivity at 30 ºC. However, it is observed that the CO_2/H_2 selectivity did not change at all in the nanocomposite membranes at 30 ºC. Hence, presence of the THF complex and the dimethylsilyl spacer between the cage structure of POSS and PEG ligand both leads to marginal loss of CO_2/N_2 selectivity at 30 ºC. However, it is observed that the CO_2/H_2 selectivity did not change at all in the nanocomposite membranes at 30 ºC.

From an application point of view, an increase in permeability of the membrane material leads to a decrease of capital investment because less membrane area is required to separate a particular amount of gas. Due to the enormous scale of the gas separation plants even small improvement of permeability of the membrane material can lead to a large economic advantage. The investigation of gas separation performance presented in Figure 6.8 and 6.9 shows that compared to the nanocomposite containing PEG-GLY-POSS-Chloroform and PEG-GLY-POSS-Toluene those containing PEG-GLY-POSS-THF, PEG-GDMS-POSS-Chloroform, PEG-GDMS-POSS-Toluene and PEG-GDMS-POSS-THF have remarkably higher CO_2 permeability without substantial loss of CO_2/N_2 and CO_2/H_2 selectivity at 30 ºC. Hence, the structural features of the PEG functionalized POSS nanoparticles introduced in this chapter i.e. the dimethylsilyl spacer and the THF complex are certainly apt to improve the separation efficiency of PEBAX® MH 1657 CO_2 selective membrane.[81]

6.4. Conclusion

The grafting of PEG ligand to epoxide containing POSS nanoparticles in presence of boron triflouride diethyletherate catalyst using chloroform, toluene or THF as solvents is thoroughly investigated. Although the epoxide ring opening occurs merely via S_N2 mechanism in all three investigated solvents for both glycidyl POSS® and glycidyl dimethylsilyl POSS®, the choice of solvent has a substantial effect upon the final product obtained from the synthesis. The reaction in toluene occurred without formation of any byproducts, but in chloroform a small fraction of the epoxide rings are opened by the catalyst itself. When THF was used as a solvent for the reaction, the solvent molecules formed a complex (in PEG-GLY-POSS-THF and PEG-GDMS-

POSS-THF). While the collective information from NMR and TGA indicates formation the of THF complex, the exact nature of this complex remains unclear.

The intriguing structural features of the synthesized nanoparticles have eventually led us to design some innovative block copolymer nanocomposite membranes for CO_2 separation based on the commercial thermoplastic elastomer PEBAX® MH 1657. The single gas permeability results of the nanocomposites containing 10 - 40 wt% of the synthesized nanofillers confirm that the dimethylsilyl spacer between the cage structure of POSS and the PEG ligand enhanced the gas permeability through the nanocomposite membranes. The THF complex (in PEG-GLY-POSS-THF and PEG-GDMS-POSS-THF) also increased the gas permeability of the nanocomposite membranes. Moreover, no substantial loss of CO_2/N_2 selectivity and CO_2/H_2 selectivity was observed. In short, chapter 6 demonstrates that incorporation of the PEG functionalized POSS nanoparticles containing dimethylsilyl spacer and THF complex are very promising to improve the CO_2 separation performance of PEBAX® MH 1657 from N_2 and H_2. Therefore, it is essential to precisely control these structural features of the nanoparticles to design new generation of polymer nanocomposite membranes with controlled molecular functions.[81]

Chapter 7. Influence of temperature upon properties of tailor made PEBAX® MH 1657 nanocomposite membranes for post combustion CO_2 capture

7.1. Introduction

Advances in synthesis and functionalization of nanofillers have opened up myriad of opportunities for tailoring the properties of traditional polymeric materials. However, in a block copolymer-nanoparticle composite the control of nanostructure and localization of nanoparticle as well as the fundamental understanding of structure-property relationship remains a challenge. It is essential to explore new methods and develop fundamental understanding to exploit this interplay in order to design novel functional materials. [28, 49, 50] In this endeavor chapter 6 reports block copolymer nanocomposite membranes containing tailor made PEG functionalized POSS nanofiller in a PEBAX® MH 1657 matrix. In this chapter a thorough investigation regarding the influence of elevated temperature upon CO_2 separation and stability of the PEBAX® MH 1657 nanocomposite membranes containing 40wt% nanofiller is presented. The surface and cross-section morphologies of the nanocomposites are investigated by scanning electron microscopy (SEM). Atomic force microscopy (AFM) is used to find out the location of the nanoparticles in the block copolymer matrix. Separation of CO_2 from N_2 and H_2 is studied by measurements of single gas transport properties of nanocomposite materials using the time-lag method in the temperature range 30 ºC to 70 ºC. The fundamental structure-property relationship of the tailor made nanocomposite membranes are also outlined in this chapter. Thermal properties of the nanocomposite membranes are studied by differential scanning calorimetry (DSC) to assess the stability of the nanocomposite membranes upon melting of polyether and polyamide blocks. The aim of this study (presented in this chapter) is to examine the separation performance and stability of the nanocomposite membranes in the expected temperature range of post combustion carbon capture application i.e. 50 - 60 ºC.

7.2. Results

7.2.1. Location of the nanoparticles in the prepared nanocomposite membranes via atomic force microscopy:

TappingMode™ atomic force microscopy was used to investigate the cross section of PEBAX® MH 1657 block copolymer membrane and its nanocomposites after incorporation of 40 wt% nanofiller. Figure 7.1 shows the phase image of the cross section of PEBAX® MH 1657 membrane. Microphase separation of the polyether and polyamide blocks is clearly visible in this image. The contrast of this image is attributed to the difference in viscoelastic properties of the two blocks. The brighter areas correspond to the polyamide hard phase, while the darker areas correspond to the softer phase of polyether.

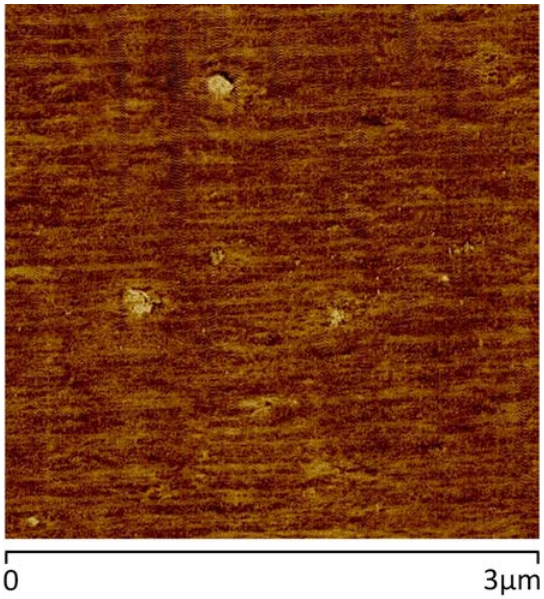

Figure 7.1: TappingMode™ AFM phase image (3 µm ×3 µm) of the cross section of a PEBAX® MH1657 membrane.

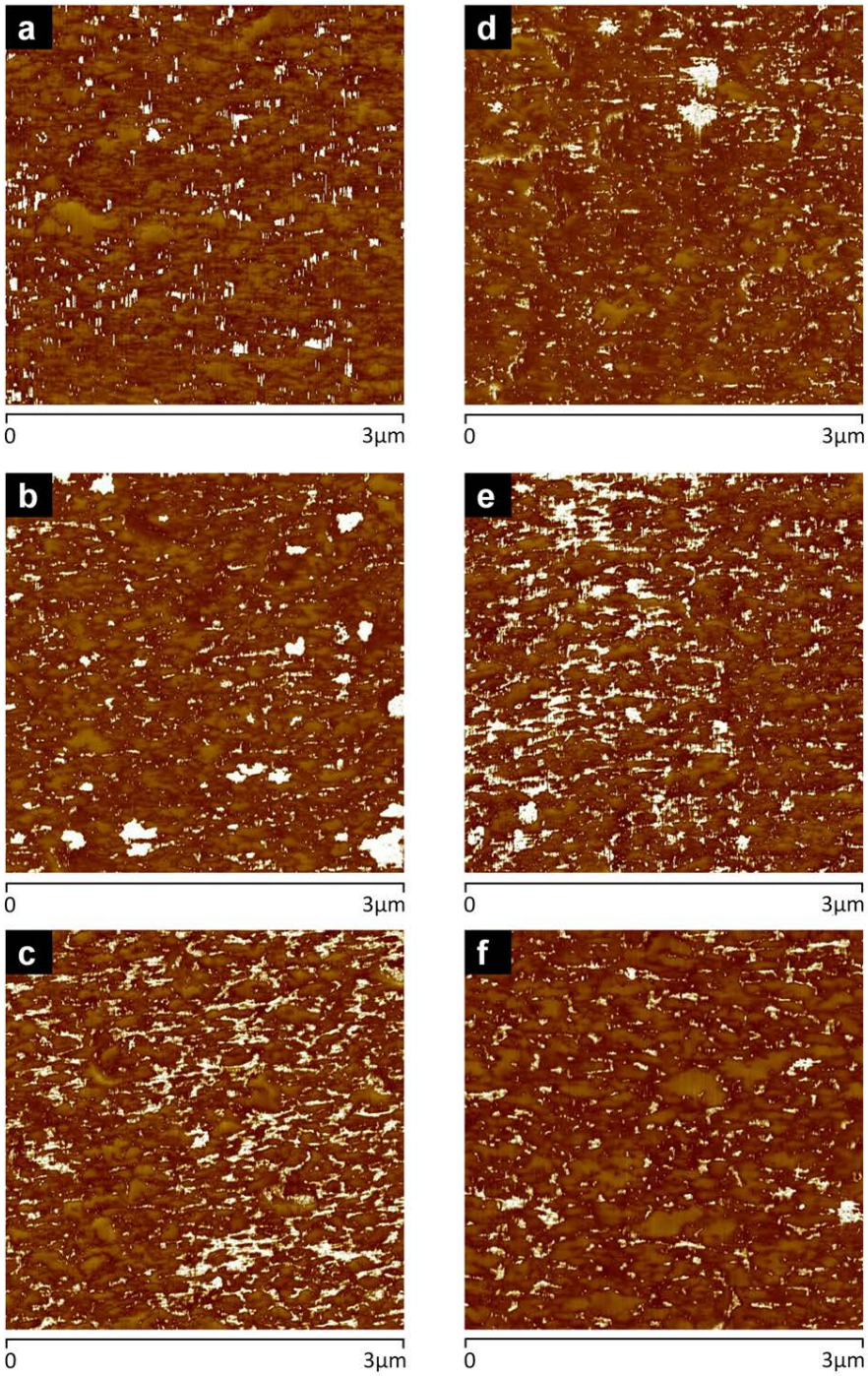

Figure 7.2: TappingMode™ AFM phase image (3 µm ×3 µm) of the cross section of PEBAX® MH 1657 nanocomposite containing 40 wt% – a) PEG-GLY-POSS-Chloroform b) PEG-GLY-POSS-Toluene c) PEG-GLY-POSS-THF d) PEG-GDMS-POSS-Chloroform e) PEG-GDMS-POSS-Toluene f) PEG-GDMS-POSS-THF.

Figure 7.2 depicts the cross section of the nanocomposite membranes. The PEG functionalized POSS nanoparticles appear as white spots in the AFM image. Introduction of functionalized POSS nanoparticles have profound influence on the morphology, since the particle loading is very high. Compared to the pure PEBAX® MH 1657, the size of the polyether domains are increased in the nanocomposites which is attributed to the decrease of total polyamide content due to incorporation of PEG functionalized POSS nanoparticles. It is evident that the nanoparticles are located in the polyether domain of the nanocomposite membranes. This corresponds to the fact that the interaction between the PEG ligands of the nanoparticles with the polyamide domain of PEBAX® MH 1657 is unfavorable, while with the polyether domain it is less incompatible or neutral. Hence the PEG ligand makes the nanoparticles compatible to the polyether domain of PEBAX® MH 1657, regardless of the presence of the dimethylsilyl spacer (in PEG-GDMS-POSS-Chloroform and PEG-GDMS-POSS-Toluene) or the THF complex (in PEG-GLY-POSS-THF and PEG-GDMS-POSS-THF). But the distribution of POSS in the polyether domain is not the same in the studied six nanocomposites. It is worth mentioning that the AFM imaging parameters had to be adjusted for optimal observation of the different phases. As a result the density of white spots in Figures 7.2 a - f differs from each other although in every case the nanocomposite contains 40 wt% nanofiller. A careful comparison of the cross section of nanocomposites (Figure 7.2) shows that the organization of the PEG domains of the nanocomposites is also different. For example, in 40 wt% PEG-GDMS-POSS-THF incorporated PEBAX® MH 1657 nanocomposite (Figure 7.2 f) polyamide domains are bigger in size and in most case completely surrounded by polyether domains. On the other hand, 40 wt% PEG-GLY-POSS-Chloroform shows a more co-continuous nature and finer distribution of polyether and polyamide domains (Figure 7.2 a). Thus the difference in structural features of the nanoparticles

has a pronounced influence upon the final morphology of the nanocomposites. These results agree well with SEM measurements using the nanoscale compositional information available from low-loss backscattered electrons electrons.

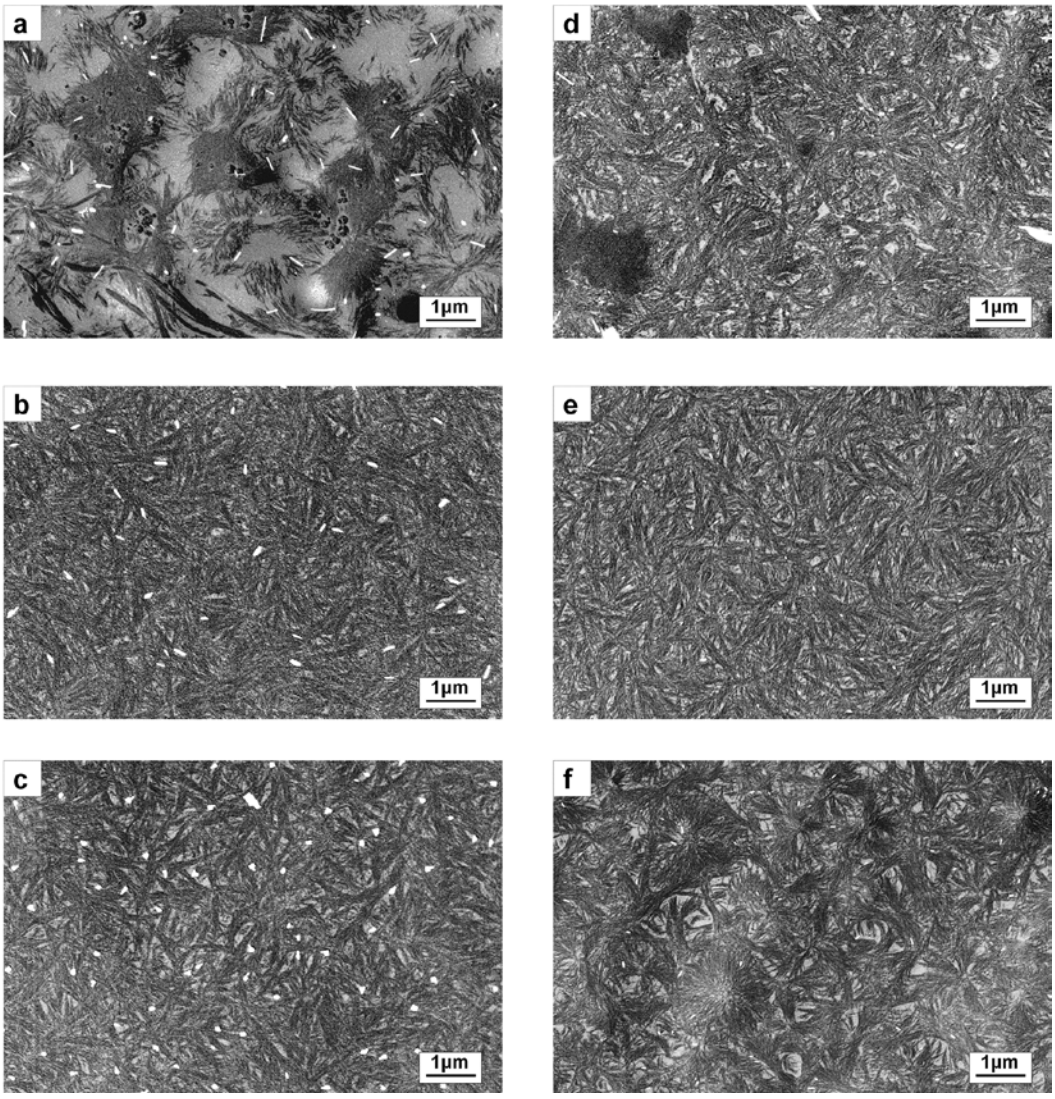

Figure 7.3: SEM micrograph of the surface of the PEBAX® MH 1657 nanocomposites containing 40 wt% of – (a) PEG-GLY-POSS-Chloroform (b) PEG-GLY-POSS-Toluene (c) PEG-GLY-POSS-THF (d) PEG-GDMS-POSS-Chloroform (e) PEG-GDMS-POSS-Toluene (f) PEG-GDMS-POSS-THF.

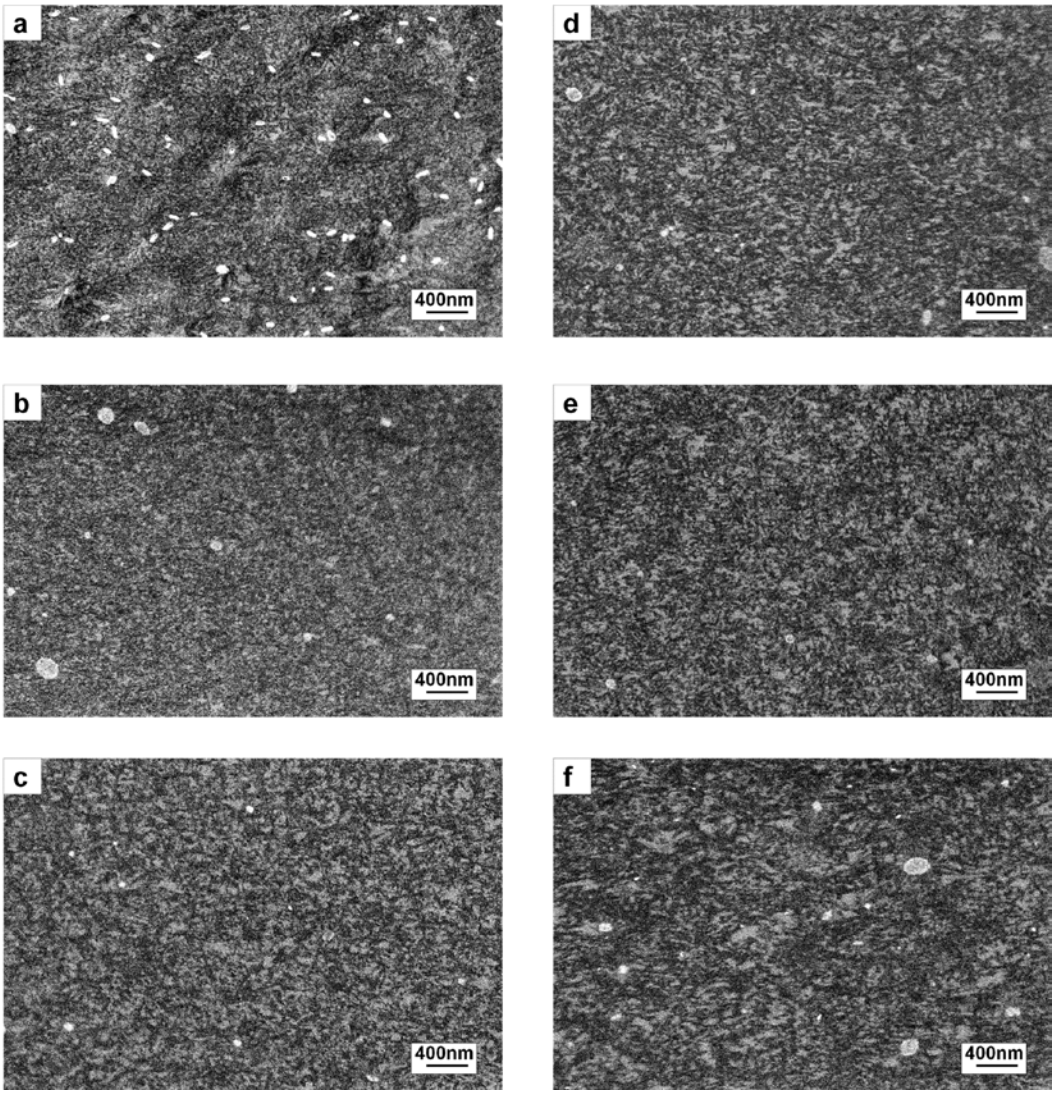

Figure 7.4: SEM micrograph of the cross section of the PEBAX® MH 1657 nanocomposites containing 40 wt% of – (a) PEG-GLY-POSS-Chloroform (b) PEG-GLY-POSS-Toluene (c) PEG-GLY-POSS-THF (d) PEG-GDMS-POSS-Chloroform (e) PEG-GDMS-POSS-Toluene (f) PEG-GDMS-POSS-THF.

Figure 7.3 and 7.4 show the top surfaces and cross sections of the nanocomposite membranes, respectively. In the SEM micrographs the bright features correspond to POSS agglomerates, the dark continuous areas correspond to PEG and the dispersed light areas are polyamide.[82]

7.2.2. Gas separation performance:

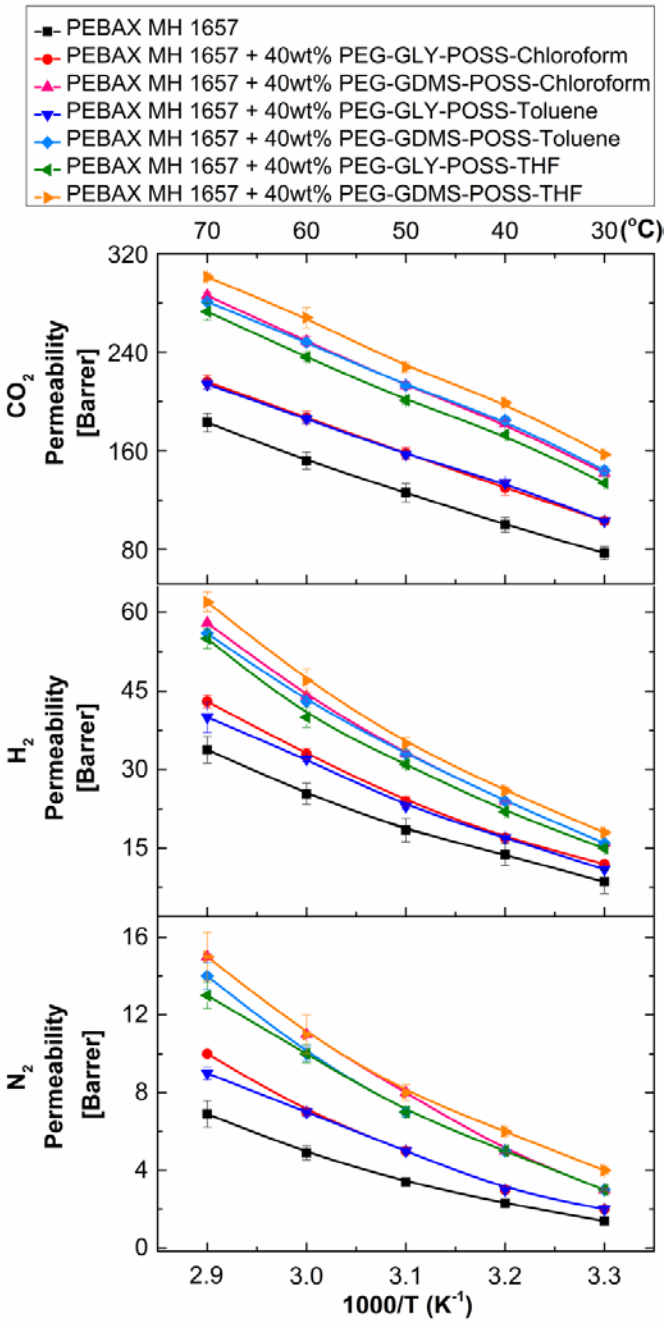

Figure 7.5: Permeability of gases as a function of inverse temperature of PEBAX® MH 1657 and nanocomposites containing 40 wt% nanofiller.

Permeability of N_2, H_2 and CO_2 versus inverse temperature is plotted in Figure 7.5. The gas perameability through the membranes were determined during heating the membranes from 30 ºC to 70 ºC. The measurements were not repeated for a cooling cycle from 70 ºC to 30 ºC. Permeability of all the gases increases sharply with the increase of temperature. The nanocomposite membranes show substantially high N_2, H_2 and CO_2 permeability coefficients compared to the pure PEBAX® MH 1657. A careful comparison of CO_2 permeabilities of the studied nanocomposites reveals that 40 wt% incorporation of PEG-GLY-POSS-Chloroform and PEG-GLY-POSS-Toluene gives similar CO_2 permeability values at all temperatures in the range from 30 ºC to 70 ºC. Compared to these membranes, the nanocomposite membranes containing other nanofillers have significantly higher CO_2 permeability. Among them the nanocomposite membranes containing PEG-GDMS-POSS-Chloroform, PEG-GDMS-POSS-Toluene and PEG-GLY-POSS-THF show similar permeability. But the highest value of permeability is demonstrated by the one containing 40 wt% PEG-GDMS-POSS-THF. Permeability of H_2 and N_2 show a similar trend (like permeability of CO_2) after incorporation of different fillers in PEBAX® MH 1657. The observations from Figure 7.5 confirm that within the temperature range from 30 ºC to 70 ºC, the presence of a dimethylsilyl spacer and a THF complex both lead to higher gas permeability. The nanoparticles synthesized using chloroform and toluene as solvents have similar influence upon gas permeability when incorporated in PEBAX® MH 1657.

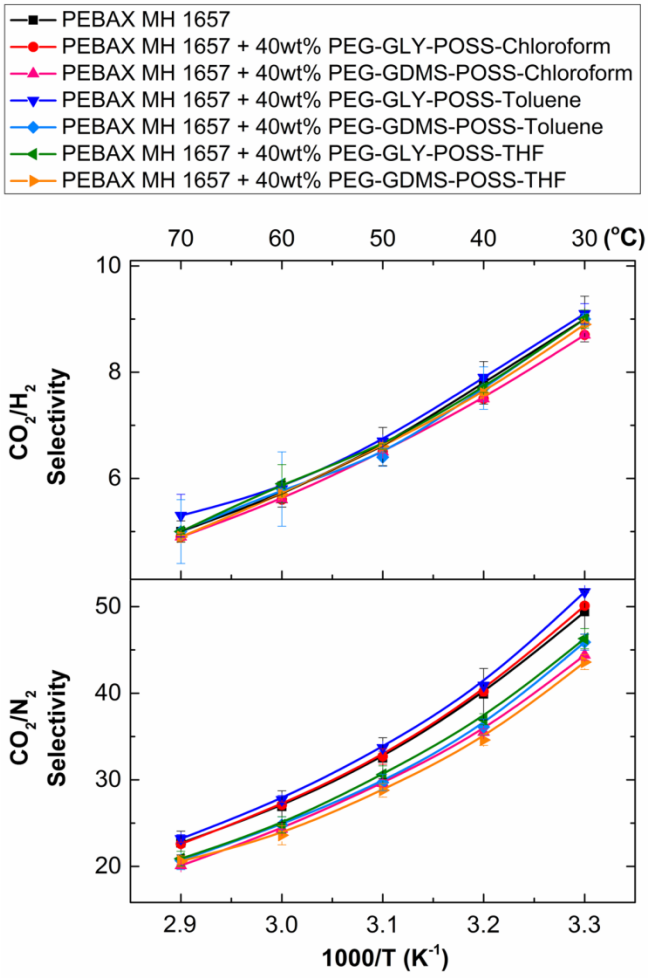

Figure 7.6: CO_2 permeability selectivity over N_2 and H_2 as a function of inverse temperature of PEBAX® MH 1657 and nanocomposites containing 40 wt% nanofiller.

Figure 7.6 depicts the permeability selectivity of CO_2 over H_2 and N_2 in the temperature range of 30 - 70 ºC. CO_2/H_2 permeability selectivity and CO_2/N_2 permeability selectivity drop significantly with the increase of temperature. It is clear that the nanofillers do not have any influence on CO_2/H_2 permeability selectivity in this temperature range. CO_2/N_2 permeability selectivity remains unchanged in PEG-GLY-POSS-Chloroform and PEG-GLY-POSS-Toluene

incorporated nanocomposite membranes. At 30 ºC the CO_2/N_2 permeability selectivities of the nanocomposites containing the other four fillers are lower than that of the pure PEBAX® MH 1657 membrane. But the difference in selectivity becomes narrower as the temperature increases and finally at 70 ºC there is no significant difference in CO_2/N_2 permeability selectivity between PEBAX® MH 1657 and its nanocomposites (discussed in section 7.3.2).

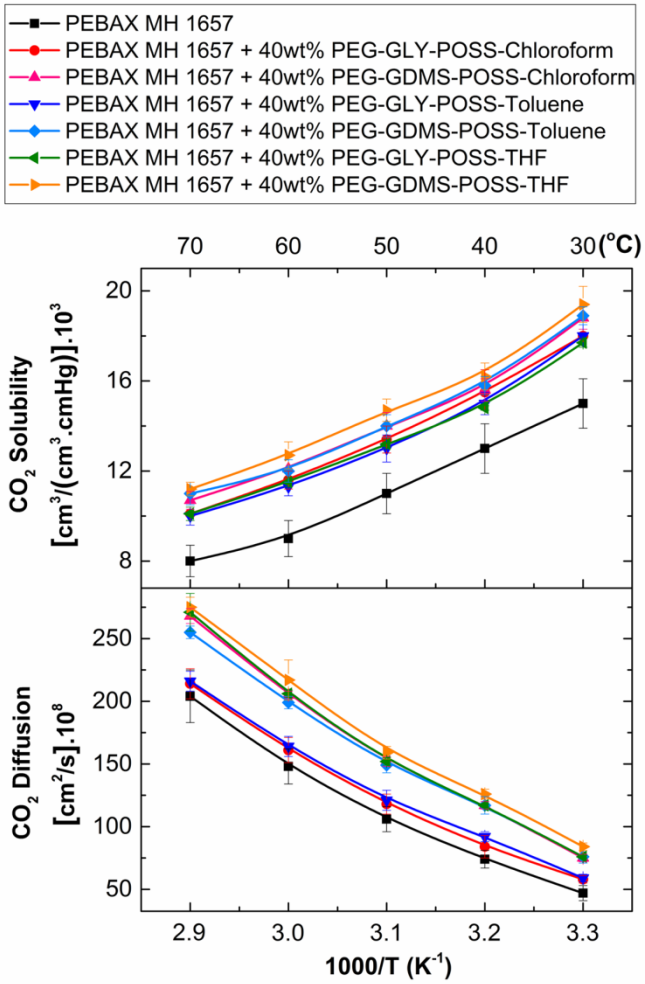

Figure 7.7: Solubility and diffusion coefficient of CO_2 as a function of inverse temperature of PEBAX® MH 1657 and nanocomposites containing 40 wt% nanofiller.

In pure PEBAX® MH 1657 membrane and the nanocomposite membranes the diffusion coefficient of CO_2 shows a sharp rise as the temperature is increased from 30 ºC to 70 ºC (Figure 7.7). Meanwhile the CO_2 solubility follows a decreasing trend with increasing temperature. It is evident that the CO_2 diffusion coefficients of PEG-GLY-POSS-Chloroform and PEG-GLY-POSS-Toluene incorporated nanocomposite membranes are similar to that of pure PEBAX® MH 1657 membrane. The other fillers lead to higher values of diffusion coefficients. On the other hand, CO_2 solubility of all the nanocomposite membranes is higher than that of PEBAX® MH 1657 membrane. But the values of CO_2 solubility of different nanocomposite membranes are analogous as the error bars overlap each other. The permeability, diffusion and solubility of CO_2 are correlated with Arrhenius and van't Hoff equations, in order to further explore the temperature dependence of CO_2 transport.

Table 7.1: Comparison of E_P, E_D and ΔH_S (Chapter 2, equation 2.11, 2.12, 2.14 and 2.15) of CO_2 transport through PEBAX® MH 1657 and its nanocomposites containing different nanofillers.

	E_P of CO_2 (kJ/mol)	E_D of CO_2 (kJ/mol)	ΔH_S of CO_2 (kJ/mol)
PEBAX® MH 1657	18.7	31.8	-13.0
PEBAX® MH 1657 + 40% PEG-GLY-POSS-Chloroform	16.1	28.3	-12.1
PEBAX® MH 1657 + 40% PEG-GDMS-POSS-Chloroform	15.2	26.8	-11.6
PEBAX® MH 1657 + 40% PEG-GLY-POSS-Toluene	15.9	28.1	-12.2
PEBAX® MH 1657 + 40% PEG-GDMS-POSS-Toluene	14.6	26.3	-11.7
PEBAX® MH 1657 + 40% PEG-GLY-POSS-THF	15.4	27.5	-12.1
PEBAX® MH 1657 + 40% PEG-GDMS-POSS-THF	14.3	25.9	-11.6

Table 7.1 presents the E_P (calculated from the slope of ln P vs 1000/T using equation 2.11), E_D (calculated from the slope of ln D vs 1000/T using equation 2.12) and ΔH_S (calculated from equation 2.15) of CO_2 transport through PEBAX® MH 1657 and its nanocomposites. Comparison of E_P, E_D and ΔH_S provides a fundamental guideline to understand the influence of nanofillers upon the transport behavior of CO_2 through the nanocomposite membranes. However, the determination of these parameters encounters the difficulty that in some cases the logarithmic plots do not generate completely straight lines as in the case of CO_2. A linear regression is used to calculate the slope. Therefore, the inherent error in the determination of these parameters must also be taken into account. Only significant changes of the parameters can be used to compare the influence of different structural features of the nanofillers on the CO_2 transport through the nanocomposite membranes. A positive value of E_P corresponds to an increase of permeability with increasing temperature. A significant drop of E_P can be noticed in the nanocomposite membranes compared to the pure polymer membrane. From Table 7.1 it is evident that, the lower value of E_P in the nanocomposite membranes is largely due to the lower value of E_D. Moreover, PEG-GDMS-POSS-Chloroform, PEG-GDMS-POSS-Toluene and PEG-GDMS-POSS-THF contributed more to the drop of E_P and E_D than PEG-GLY-POSS-Chloroform, PEG-GLY-POSS-Toluene and PEG-GLY-POSS-THF, respectively. A negative value of ΔH_S is characteristic for decrease of sorption with increase of temperature. However, it is clear from Table 7.1 that the values of ΔH_S are too close to each other to make any comparison about the sorption environment of the CO_2 molecule in presence of different fillers but for all studied fillers the ΔH_S values never exceed that of pure PEBAX® MH 1657.

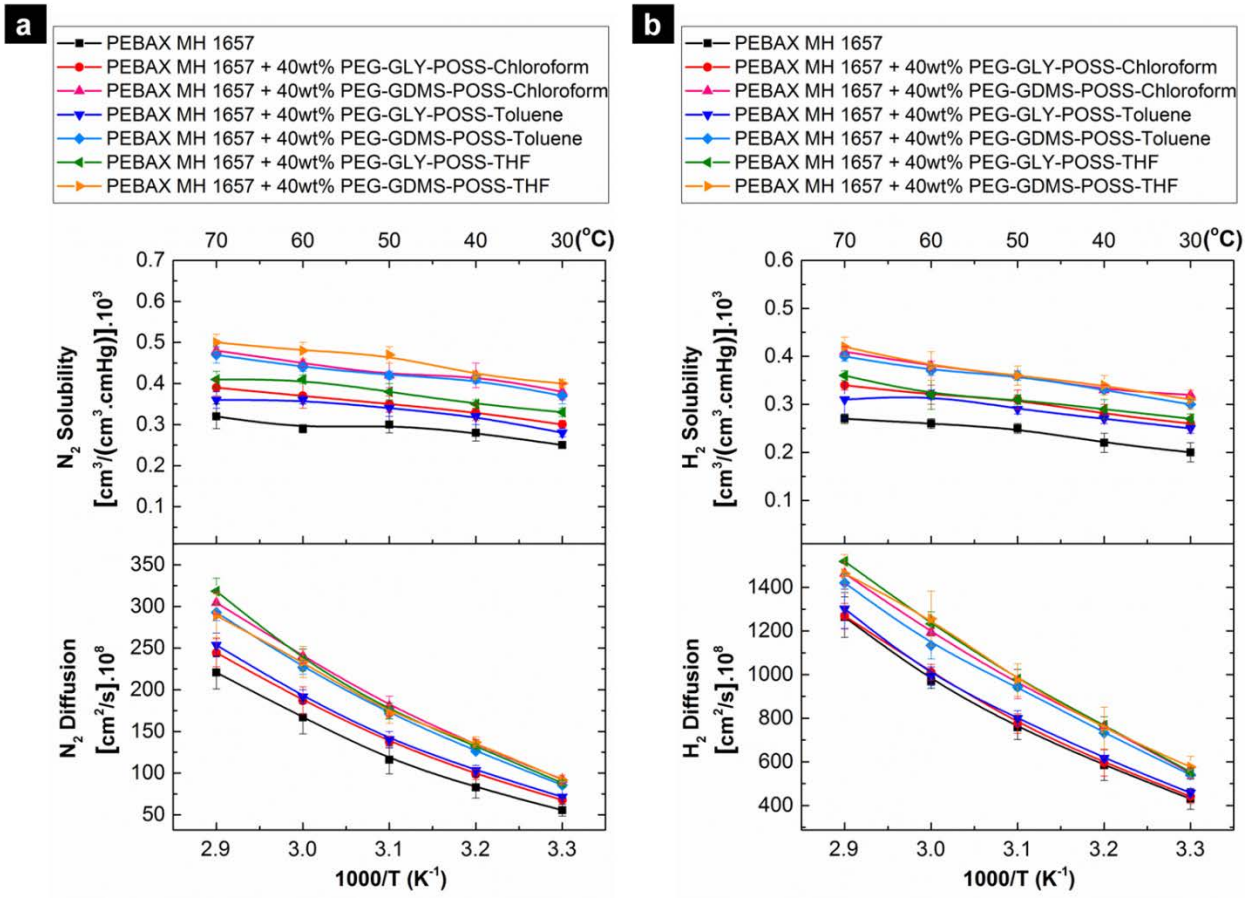

Figure 7.8: Solubility and diffusion coefficient as a function of inverse temperature of PEBAX® MH 1657 and nanocomposites containing 40 wt% nanofiller – a) N_2 and b) H_2.

Solubility and diffusion coefficients of N_2 and H_2 in PEBAX® MH 1657 and its nanocomposites containing 40 wt% nanofiller are plotted in Figure 7.8a and b, respectively. Diffusion of N_2 and H_2 sharply increases with the increase of temperature in all membranes. Similar to CO_2, the diffusion of N_2 and H_2 is higher in the nanocomposites containing the nanofillers which have the dimethylsilyl group and THF complex than those which do not have such moiety. It is clear that N_2 and H_2 have very low solubilities in the PEBAX® MH 1657 and its nanocomposites. Unlike CO_2, the solubilities of N_2 and H_2 do not decrease with increasing temperature. N_2 and H_2 solubilities are analogous in the temperature range of 30 – 70 ºC for all membranes.

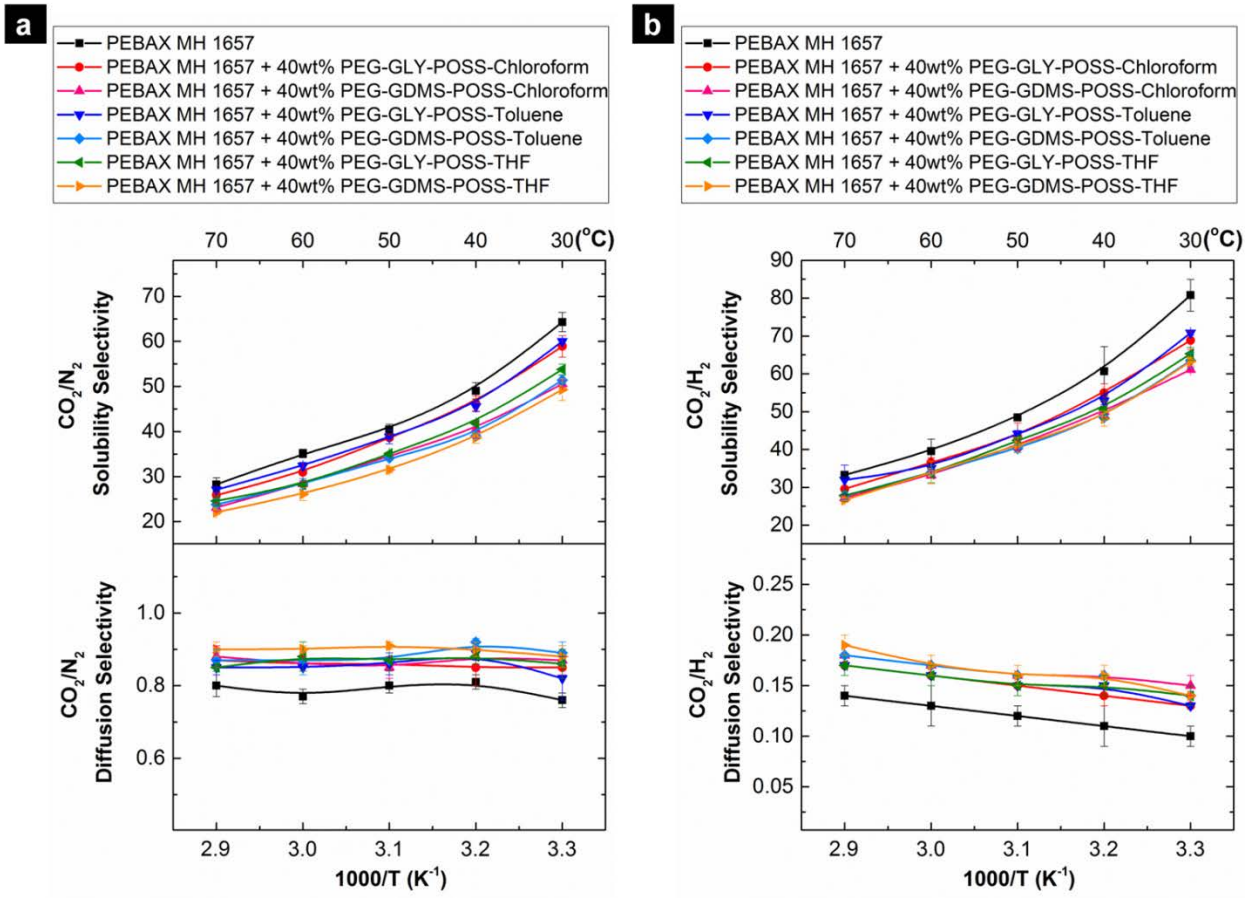

Figure 7.9: Solubility selectivity and diffusion selectivity as a function of inverse temperature of PEBAX® MH 1657 and nanocomposites containing 40 wt% nanofiller – a) CO_2/N_2 and b) CO_2/H_2.

Figure 7.9 shows the diffusion selectivity and solubility selectivity of CO_2 over N_2 and H_2 in the temperature range 30 - 70 ºC. CO_2/N_2 and CO_2/H_2 solubility selectivities drop sharply with the increase of temperature. From figure 7.7 and 7.8 it is clear that this loss of solubility selectivity stems from decrease of CO_2 solubility with increasing temperature. The diffusion selectivity of CO_2/N_2 is close to 1 while that of CO_2/H_2 is in the range 0.1 to 0.2 (discussed in section 7.3.2). [82]

7.2.3. Differential scanning calorimetry:

Table 7.2: Glass transition temperature of PEBAX® MH 1657, the nanofillers and the nanocomposites.

	T_g (ºC)					
	PEG-GLY-POSS-Chloroform	PEG-GDMS-POSS-Chloroform	PEG-GLY-POSS-Toluene	PEG-GDMS-POSS-Toluene	PEG-GLY-POSS-THF	PEG-GDMS-POSS-THF
Nanofiller	-59 ±0.1	-67 ± 0.1	-59 ± 0.1	-64 ± 0.4	-69 ± 0.1	-71 ± 0.1
PEBAX® MH 1657 + 40 wt% nanofiller	-54 ± 0.3	-59 ± 0.8	-54 ± 0.6	-58 ± 0.8	-59 ± 1.1	-
PEBAX® MH 1657	-51 ± 0.5					

The glass transition temperature (T_g) of the polyether blocks of PEBAX® MH 1657, the nanofillers and the nanocomposites are tabulated in Table 7.2. The PEG ligands of the nanofillers have lower T_g compared to the polyether segments of PEBAX® MH 1657. It implies that the mobility of the PEG ligands is higher compared to the polyether segments of PEBAX® MH 1657. T_g's of the polyether segment of the nanocomposites are lower compared to that of PEBAX® MH 1657. Since the nanofillers are located in the polyether domain (section 7.2.1) and the T_g of the blocks of PEBAX® MH 1657 decreases after incorporation of the nanofillers it is evident that the PEG ligand of the nanofillers plasticizes the polyether segments of PEBAX® MH 1657. Moreover, the glass transition temperatures of PEG-GDMS-POSS-Chloroform and PEG-

GDMS-POSS-Toluene are significantly lower than those of PEG-GLY-POSS-Chloroform and PEG-GLY-POSS-Toluene. Interestingly, PEG-GLY-POSS-THF and PEG-GDMS-POSS-THF exhibit lower glass transition temperatures than the other nanoparticles. The nanocomposite membranes show lower T_g compared to PEBAX® MH 1657. The decrease of T_g is more significant for nanocomposites containing PEG-GDMS-POSS-Chloroform, PEG-GDMS-POSS-Toluene and PEG-GLY-POSS-THF, compared to PEG-GLY-POSS-Chloroform and PEG-GLY-POSS-Toluene containing nanocomposites (discussed in section 7.3.1). In case of PEG-GDMS-POSS-THF incorporated nanocomposite the T_g is not clearly visible.

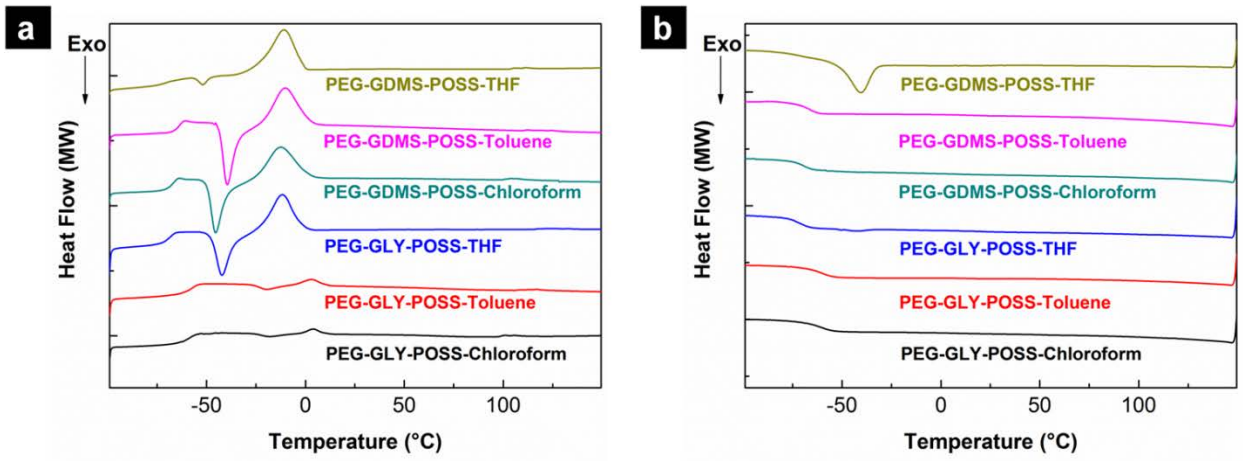

Figure 7.10: DSC thermogram of synthesized nanofillers – a) 2nd heating trace b) 2nd cooling trace.

To investigate the melting and crystallization behavior of the functionalized nanoparticles the thermal history was erased by heating up to 100 ºC and then they were cooled down to -100 ºC. Figures 7.10a & Figure 7.10b show the second heating and second cooling trace of the DSC run. Except PEG-GDMS-POSS-THF the ligand attached to other synthesized nanoparticles exhibit

cold crystallization on the heating cycle and do not crystallize during the cooling cycle of the DSC run. The weight of PEG ligands attached to nanoparticles is M_n=350 g/mol and it is probably too small to crystallize during the cooling cycle at 10 K/min, which accounts for the cold crystallization behavior observed during heating cycle. For PEG-GDMS-POSS-Chloroform and PEG-GDMS-POSS-Toluene the onset of cold crystallization are -50 ºC and -44 ºC while the heat of cold crystallization are 20 J/g and 21 J/g. But for both PEG-GLY-POSS-Chloroform and PEG-GLY-POSS-Toluene the onsets of cold crystallization are -26 ºC and the heat of cold crystallization is 2 J/g. The enthalpies of crystallization are normalized to the total mass of sample on the pan. Thus on the heating cycle of the DSC run the nanoparticles containing the dimethylsilyl spacer exhibit the cold crystallization at significantly lower temperature and evolve approximately 10 times more heat per unit mass of the nanoparticle. Interestingly the onset and heat of cold crystallization of PEG-GLY-POSS-THF is -47 ºC and 18 J/g, respectively. For PEG-GDMS-POSS-THF nanoparticles although a small trace of cold crystallization was observed during heating cycle, major portion of the crystallization starts at -33 ºC already while cooling down from the melt and the heat of crystallization is 18 J/g. It is worth mentioning that third and fourth heating and cooling cycles in the temperature range -100 ºC to 150 ºC produce thermograms similar to the second heating & cooling cycle presented in Figure 7.10. Hence it is evident that the presence of dimethylsilyl spacer as well as the THF complex (in PEG-GLY-POSS-THF and PEG-GDMS-POSS-THF) facilitates the crystallization of PEG ligand.

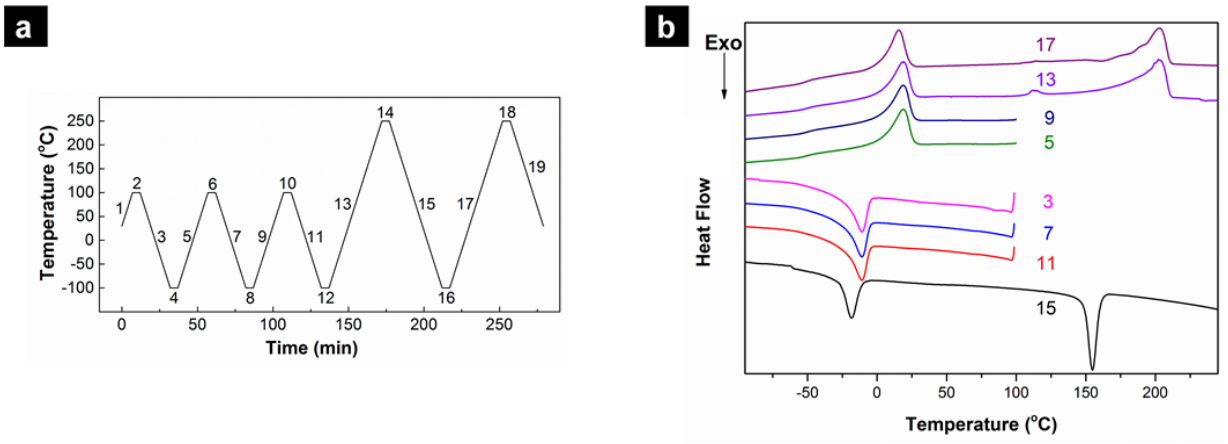

Figure 7.11: a) Temperature protocol of DSC run b) DSC thermogram of PEBAX® MH 1657.

Figure 7.11a depicts the temperature protocol of DSC runs for PEBAX® MH 1657 and its nanocomposites while Figure 7.11b illustrates the DSC thermogram of PEBAX® MH 1657. This temperature protocol is designed to study the influence of melting of the polyether blocks and the polyamide blocks upon the stability of nanocomposites. The sample is heated up to 100 ºC (step 1) to remove the residual solvents, followed by a 5 min isotherm at 100 ºC (step 2). At this stage only the polyether block of PEBAX® MH 1657 is in molten form. The crystallization of polyether block starts at -5 ºC and ends at -22 ºC as the sample is cooled down to -100 ºC (step 3). The sample is heated to 100 ºC and cooled down to -100 ºC for two more times (steps 4 - 12). The cooling traces of step 7 and 11 show that while cooling down from 100 ºC the exothermic peak of crystallization of polyether blocks appears at the same temperature. In step 13 the sample is heated up to 250 ºC to melt both the polyether and the polyamide block. The cooling trace of step 15 shows that the crystallization exotherm of polyether blocks shifts to a lower temperature (onset -11 ºC and endset -26 ºC) compared to those observed in step 3, 7 and 11. The heating trace of step 17 shows that the melting endotherm of polyether blocks is slightly shifted to a lower temperature, too, but the shape of the peak remains unchanged.

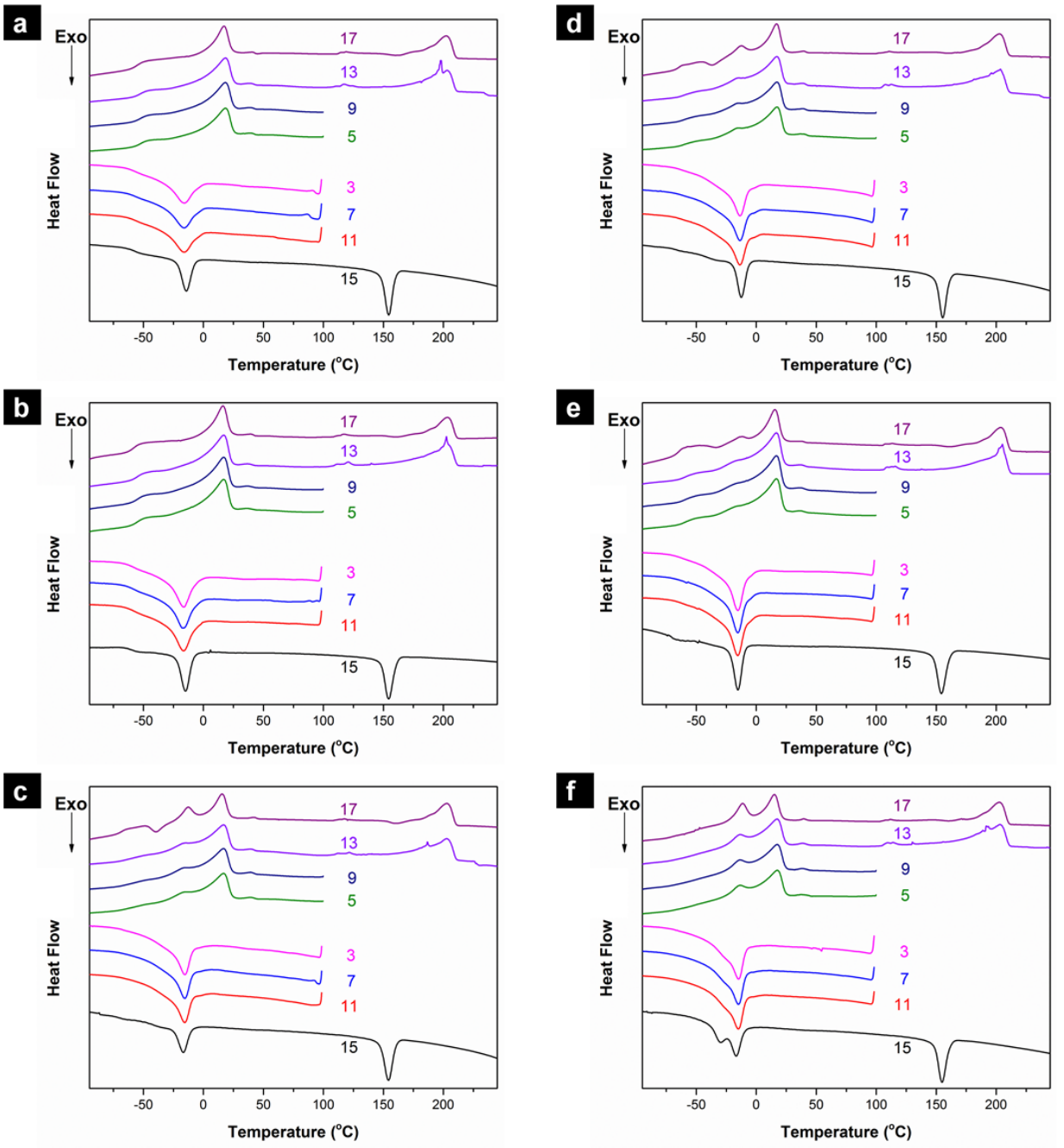

Figure 7.12: DSC thermogram (second cooling trace) of the nanocomposites of PEBAX® MH 1657 containing – (a) PEG-GLY-POSS-Chloroform (b) PEG-GLY-POSS-Toluene (c) PEG-GLY-POSS-THF (d) PEG-GDMS-POSS-Chloroform (e) PEG-GDMS-POSS-Toluene (f) PEG-GDMS-POSS-THF.

DSC thermograms of the nanocomposites (obtained by using the temperature protocol presented in Figure 7.11a) are depicted in Figure 7.12. The cooling traces of step 3, 7 and 11 show that the crystallization exotherms of polyether domain are identical. Similarly in step 5, 9 and 11 the melting endotherms of polyether domains are identical. Moreover, although these nanocomposites contain 40 wt% of nanofiller, no recrystallization of polyether is observed in these steps. It is evident that due to the high compatibility between the PEG ligand of the nanofillers and polyether segment of the block copolymers, they crystallize together during the cooling cycle of the DSC runs. However, compared to pure PEBAX® MH 1657 broadening of the polyether domain melting endotherms and crystallization exotherms was observed in the nanocomposites. Contrariwise, when both the polyether and the polyamide blocks are completely melted (by heating up to 250 ºC in step 13), in the subsequent cooling and heating trace, i.e. step 15 and step 17 substantial changes are observed in the crystallization exotherm and melting endotherm of the polyether blocks. In Figure 7.12c, d and e recrystallization of PEG ligand of the nanofillers is observed prior to the melting endotherm in step 17. In Figure 7.12f two separate crystallization exotherms and melting endotherms are clearly visible for the PEG ligands of the nanofiller and polyether domain of the block copolymer. It is evident from the DSC study that as long as the nanocomposites were heated up to 100 ºC and cooled down to -100 ºC to operate solely with the polyether domains, the nanocomposites were quite stable (since the melting and crystallization of the of the polyether domain remains unchanged even after three thermal cycles), but when the polyamide blocks are completely melted (by heating up to 250 ºC in step 13), in the subsequent cooling step the block copolymer matrix starts to reject a fraction of the nanofillers and they crystallize separately from the polymer matrix.[82]

7.3. Discussion

7.3.1. Influence of structural features of the nanofillers upon gas permeation:

The diffusion coefficient for a given gas molecule in amorphous or rubbery polymer membranes is related to the dynamics or mobility of the polymer chains. E_D is the energy required for a gas molecule to execute a diffusive jump. In rubbery polymers, at elevated temperature the increase of polymer chain motion leads to the formation of transient chain gaps more frequently that enable easier penetrant diffusive jumps from one equilibrium site to another. As a result, higher temperature leads to an enhancement of the diffusion coefficient and it follows ultimately an increased permeability. This phenomenon is apparently well known and is regarded as typical for amorphous polymer membranes.[35]

In the prepared nanocomposite membranes the PEG grafted nanoparticles are located in polyether domains (presented in Figure 7.2). Moreover, the T_g's of the polyether domains of the nanocomposites are significantly lower than that of pure PEBAX® MH 1657 membrane (listed in Table 7.2). As T_g is a crude indicator of the mobility of polymer segments, it is evident that the mobility of polyether segments of the nanocomposites is higher than that of PEBAX® MH 1657 membrane. Additionally, higher diffusion coefficients accompanied with lower values of E_D of the nanocomposite membranes reveal that, due to the higher chain mobility the permeating CO_2 molecules experience lower resistance to diffusive jumps in the nanocomposite membranes compared to pure PEBAX® MH 1657. Besides, T_g (listed in Table 7.2) and E_D (listed in Table 7.1) values are significantly lower for the nanocomposites which contain the nanoparticles that have the dimethylsilyl spacer. These observations indicate that in studied nanocomposite

membranes the mobility of the polyether segments surrounding the nanoparticles having dimethylsilyl spacer is higher compared to the nanocomposites where the nanoparticles do not have such moiety. It is well-known that the polymers containing flexible Si-O linkage in the main and side chains exhibits high gas permeability which stems from the low energy barrier of rotation of the Si-O linkage of the dimethylsilyl group. [83] In the PEG grafted nanoparticles obtained from glycidyl POSS® and glycidyldimethlysilyl POSS® the ligands are connected to the silsesquioxane core through Si-C and Si-O bonds, respectively. For this reason, the presence of the dimethylsilyl group in between the cage structure of POSS and PEG ligand increases the flexibility of PEG ligands (discussed in section 7.2.3) which eventually leads to higher segmental mobility of polyether blocks of PEBAX® MH 1657 in the nanocomposite membranes. Although it is evident that the THF complex (in PEG-GLY-POSS-THF and PEG-GDMS-POSS-THF) leads to similar phenomenon, the interaction between the THF complex and polyether domain of the block copolymer is not completely clear from the results available at present.[82]

7.3.2. Influence of nanofiller upon selectivity of CO_2 over N_2 and H_2

At 30 ºC the CO_2/N_2 permeability selectivity in PEBAX® MH 1657 is five times higher than that of CO_2/H_2 permeability selectivity (Figure 7.6). The diffusion of CO_2 in PEBAX® MH 1657 membrane (Figure 7.7) is analogous to that of N_2 (Figure 7.8a) and lower than that of H_2 (Figure 7.8b) which becomes more obvious from a comparison of the diffusion selectivity of CO_2/H_2 and CO_2/N_2 gas pairs. At 30 ºC the CO_2/N_2 diffusion selectivity (Figure 7.9a) is ca. 0.8 (i.e. close to 1) while the CO_2/H_2 diffusion selectivity is ca. 0.1 only. This phenomenon is attributed to the ratio of kinetic diameters of CO_2, N_2 and H_2. [36] But CO_2 enjoys much higher

solubility in PEBAX® MH 1657 (Figure 7.7) membrane compared to N_2 and H_2 (Figure 7.8) which is attributed to high condensability of CO_2 and the quadrapole-dipole interaction between CO_2 and polar ether oxygen of the membrane. [36] Therefore the relatively higher permeation of CO_2 compared to H_2 i.e. CO_2/H_2 selectivity suffers from the fact that the advantage of higher solubility of CO_2 is largely offset by higher diffusion of H_2 which leads to a very low CO_2/H_2 selectivity.

In the nanocomposite membranes the CO_2/H_2 permeability selectivity remains unchanged. At 30 ºC the nanocomposites containing PEG-GLY-POSS-THF, PEG-GDMS-POSS-Chloroform, PEG-GDMS-POSS-Toluene, and PEG-GDMS-POSS-THF show slightly lower values of CO_2/N_2 permeability selectivity than PEBAX® MH 1657. Hence, the nanofillers containing the dimethylsilyl spacer and the THF complex have a small but statistically significant influence on CO_2/N_2 permeability selectivity of the nanocomposite membranes but not on CO_2/H_2 permeability selectivity. In these nanocomposite membranes the solubilities of N_2 and H_2 are slightly higher and the solubility selectivities of CO_2/N_2 and CO_2/H_2 are lower compared to PEBAX® MH 1657 (Figure 7.8 and 7.9). This small change of solubility leads to marginal loss of CO_2/N_2 permeability selectivity at 30 ºC (as the diffusion selectivity is close to unity). On the other hand the low value of CO_2/H_2 permeability selectivity (which is highly offset by the much higher diffusion of smaller H_2 compared to that of CO_2) is not influenced by such small change of solubility.

The CO_2/N_2 permeability selectivity decreases in all the membranes with increasing temperature and follows a similar trend. At elevated temperature (e.g. 70 ºC) the values of CO_2/N_2 selectivity

of the membranes differ less from each other. An increase of temperature leads to higher kinetic energy of the permeating gas molecules and higher mobility of polymer chains of the amorphous polyether block. As a result diffusion of the gases increases significantly but solubility decreases. For example, CO_2 diffusion in PEBAX® MH 1657 increases four times as the temperature is increased from 30 ºC to 70 ºC while CO_2 solubility decreases significantly (Figure 7.7). Hence, at elevated temperature (e.g. 70 ºC) the permeation of gas molecules is dominated more by diffusion than by solubility. Under these circumstances the values for CO_2/N_2 selectivity of the nanocomposites and PEBAX® MH 1657 become similar.[82]

7.3.3. Influence of temperature upon stability of the membrane

Thermoplastic elastomeric block copolymers having alternating hard and soft blocks are often considered as systems where the hard blocks (having high glass transition and melting temperature) act as virtual physical crosslinks between the soft blocks.[43, 84] In contrast to the covalently crosslinked systems, in this case at a temperature where the hard block is in a molten state this physical crosslinking does not exist anymore. From section 7.2.1 it is evident that when the nanocomposite membranes are prepared by a solution casting method, the PEG functionalized POSS nanoparticles are located in the polyether domains of the block copolymer nanocomposite system due to unfavorable interaction with the polyamide blocks. Since for post combustion carbon capture the application temperature is between 50 ºC and 60 ºC, [3] the gas permeability measurements were done from 30 ºC to 70 ºC (plotted in Figure 7.5). In this temperature range the polyether block is molten but the polyamide block remains in a crystalline state. From the DSC study in section 7.2.3 it is clear that the nanocomposite membranes are quite

stable in a temperature range where the polyamide block is not in a molten state. In other words, in the expected temperature range of post combustion carbon capture the physical crosslinking provided by the crystalline polyamide blocks exists and the nanoparticles are securely trapped in the amorphous polyether block domains. Once the hard block melts the physical crosslinking is destroyed and the nanocomposite obtains the possibility for reorganization of block copolymer's domains during the material cooling. Under this circumstance the matrix starts to reject the nanoparticles from the polyether domains and the nanocomposites are not stable anymore. Hence, the application of the nanocomposite membranes presented in this chapter is limited to a temperature range where the melting of the hard domain does not occur.[82]

7.4. Conclusion

Chapter 7 demonstrates that it is possible to regulate the gas transport through PEG functionalized POSS nanoparticle incorporated PEBAX® MH 1657 membrane by taking advantage of the flexibility of Si-O bond as a linkage between the core and the ligand of the nanoparticle. Furthermore, it shows that the THF complex (in PEG-GLY-POSS-THF and PEG-GDMS-POSS-THF) is also a useful structural feature to fabricate nanocomposite membranes. Both the dimethylsilyl spacer between the cage structure of POSS and PEG ligand and the THF complex can substantially improve the CO_2 permeability of the PEBAX® MH 1657 nanocomposite membrane without significant loss of selectivity. This concept can be instrumental in designing next generation nanocomposite membranes for post combustion carbon capture. The operation temperature of the separation process implementing the studied block copolymer based nanocomposite membranes is limited by the melting temperature of hard

domains of the block copolymer. As the expected temperature range (50 - 60 ºC) of CO_2 separation process in post combustion carbon capture technology is significantly below the melting temperature of hard block (above 100 ºC) the nanocomposites presented here are suitable materials for this application.[82]

Chapter 8. Functionalization of Carbon Nanotubes and Fabrication of Nanocomposite Membranes

The work described in this chapter is a part of the project named "High Aspect Ratio Carbon-based Nanocomposites (HARCANA)" funded by the European Community's 7th Framework Programme for Research and Technological Development under the grant agreement NMP3-LA-2008-213277. Since this is a collaborative project the content of this chapter refers also to the results obtained by other project partners.

8.1. Introduction

Carbon nanotubes (CNT) are referred to as rolled up graphite sheets having diameters up to 100 nm but lengths in micrometers. For several nanotechnological applications CNTs are attractive candidates, but the lack of solubility and the tendency to agglomerate due to π-π stacking have imposed great limitation to their use. Functionalization of carbon nanotubes via covalent attachment and non-covalent adsorption has been used to overcome these problems. The functionalization approaches of CNT can be classified into three general categories – a) covalent attachment of chemical groups b) non-covalent adsorption or wrapping of molecules c) endothermal filling of inner cavity. Numerous approaches have been utilized for covalent functionalization of CNT such as- oxidation, halogenation, cycloaddition, radical addition etc. [85] Recently, Murali et. al. [18] have reported the effect of multiwalled carbon nanotubes (MWCNT) incorporation on the permeability of hydrogen, nitrogen, oxygen and carbon dioxide and selectivity of each of these gases over others in both crosslinked and non-crosslinked PEBAX 1657 membranes. In the non-crosslinked membrane after incorporation of MWCNT, CO_2 appeared to have greater solubility and CO_2/N_2 selectivity increased. The MWCNT incorporated crosslinked membrane showed higher CO_2/N_2 selectivity, but lower permeability. However, MWCNT appeared as bundles or aggregates in the PEBAX matrix. To employ CNT's effective incorporation in polymer nanocomposites, a proper dispersion in the polymer matrix has to be guaranteed, for which functionalization of CNT is a promising approach.

8.2. Functionalization of Carbon Nanotube with poly(ethylene glycol) (Mn=200 g/mol)

Grafting of polymer to the surface of CNT is carried out by two main methods- a) grafting to and b) grafting from. In the "grafting to" method an already synthesized polymer is attached on the surface of the CNT by end group termination or radical addition. The "Grafting from" method is based on covalently attaching a polymer precursor on the surface of the CNT followed by in-situ propagation of the polymer chain. [85, 86] In this work the "grafting to" approach is used to decorate the multiwalled carbonanotube (MWCNT) with poly(ethylene glycol) (PEG). The MWCNTs were prepared by FutureCarbon GmbH, Germany (FutureCarbon-MWCNT) and CSIC, Spain (CSIC-MWCNT). The FutureCarbon-MWCNT are produced by a standard chemical vapor deposition (CVD) method followed by a purification step (Batch no – R11081023-01). The CSIC-MWCNT are prepared by a supported CVD injection method using toluene as the carbon source and ferrocene as the catalyst in a hot quartz tube reactor at 760 ºC under inert argon atmosphere. [87-89] The MWCNT obtained from both manufacturers are used without further purification. MWCNT are oxidized to introduce carboxylic functional groups (-COOH). The oxidized MWCNTs are chlorinated using thionyl chloride ($SOCl_2$) to convert the –COOH group to –COCl group. Finally, PEG (Mn=200 g/mol) is grafted to the MWCNT by hydroxyl terminated esterification reaction (depicted in Scheme 8.1). [90]

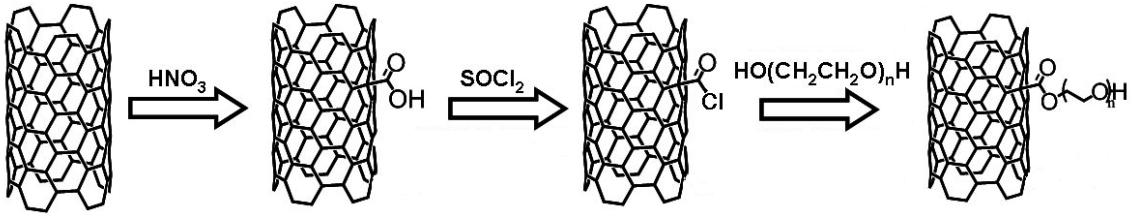

Scheme 8.1: Schematic diagram of grafting oligomeric hydroxyl terminated poly(ethylene glycol) chain on pristine MWCNT.

8.2.1. TGA and TGA-FTIR study

Thermogravimetric analysis is used to determine the functional group content of the MWCNTs after oxidation and PEG functionalization. The percentage mass loss at 600 ºC is recorded in this regard. No significant mass loss is observed for CSIC-MWCNT and FutureCarbon-MWCNT at this temperature. But degradation of the organic functional groups is expected to be completed at 600 ºC. At higher temperature the mass loss observed in TGA might also be associated with the degradation of MWCNT which may lead to misleading results.

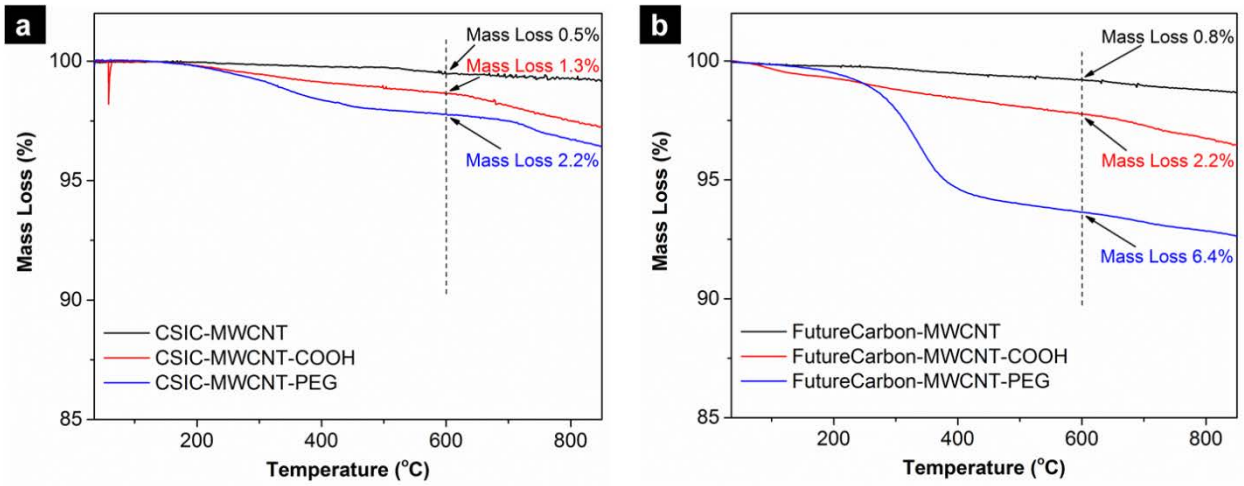

Figure 8.1: Thermogravimetric Analysis at 10 K/min (mass loss (%) at 600 ºC) of unfunctionalized, oxidized and PEG grafted – a) CSIC-MWCNT and b) FutureCarbon-MWCNT.

Figure 8.1 shows that at 600 ºC mass loss of CSIC-MWCNT and FutureCarbon-MWCNT are analogous. FutureCarbon-MWCNT after oxidation (FutureCarbon-MWCNT-COOH) and after PEG functionalization (FutureCarbon-MWCNT-PEG) looses 2.2% and 6.4% mass, respectively.

But the mass loss of CSIC-MWCNT after oxidation (CSIC-MWCNT-COOH) and after PEG functionalization (CSIC-MWCNT-PEG) is 1.3% and 2.2%, respectively. It is evident that after functionalization the PEG content of the CSIC-MWCNT is significantly lower than that of FutureCarbon-MWCNT. Thus there might be some unreacted –COOH group left in the CSIC-MWCNT after PEG functionalization. Further investigation of the CSIC-MWCNT is carried out using TGA-FTIR to support this hypothesis.

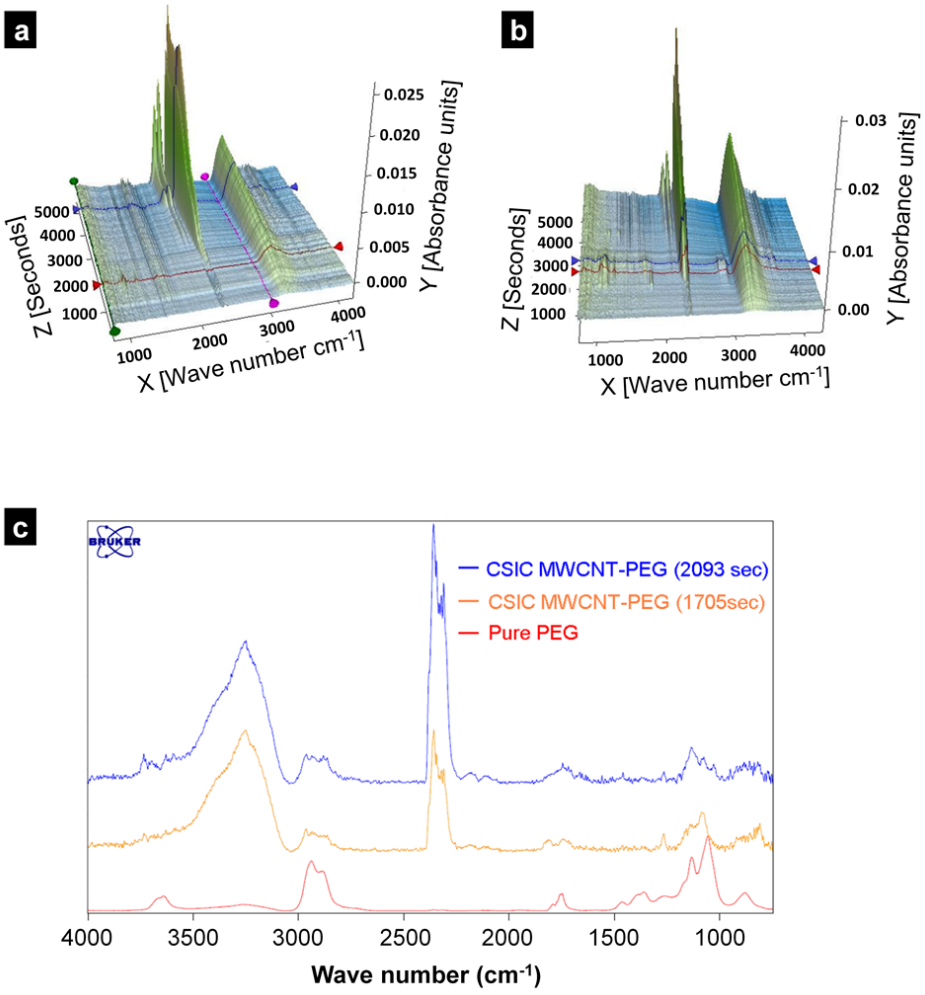

Figure 8.2: TGA-FTIR – a) CSIC-MWCNT after oxidation b) CSIC-MWCNT after PEG functionalization c) Comparison of pure PEG with CSIC-MWCNT PEG.

The TGA- FTIR spectra of CSIC-MWCNT after oxidation and after PEG functionalization are presented in Figure 8.2. From the 3-d image it is clear that the IR spectra originated from the degradation of –COOH group of oxidized CSIC MWCNT have very low intensity. A 2-d IR spectrum was extracted from two points (represented by red and blue arrows) but the signal to noise ratio was too high to evaluate them. After PEG- functionalization the 2-d IR spectrum was extracted from 1705 seconds and 2093 seconds (represented by red and blue lines in the 3-d image). From comparison of the extracted 2-d IR spectrum (presented by orange and blue lines) with spectrum of pure PEG (presented by red line) it is clear that the nanotubes contain covalently bonded PEG. However, it is not possible to comment on the presence of unreacted -COOH group. Note that in the TGA-FTIR spectra an artifact was observed between wave numbers 3000 - 3500 cm^{-1} which does not belong to the sample.

8.2.2. Raman spectroscopy

Raman spectroscopy gives information of the type of hybridization of the carbon atoms, the introduction of chemical impurities or defects etc. In this work the comparison between the G band and the D band was used to analyses the defects present in the MWCNTs. The G band originates from the carbon-carbon bonds in-plane tangential stretching and the D band is attributed to the presence of amorphous carbon or defects in the graphene structure.[91] The Raman spectra obtained from mapping experiments of both FutureCarbon-MWCNT and CSIC-MWCNTs before and after functionalization are presented in Figure 8.3. From the 3-D image it is evident that the intensity of D-band (which corresponds to the defects) is significantly lower in CSIC-MWCNT compared to FutureCarbon-MWCNT.

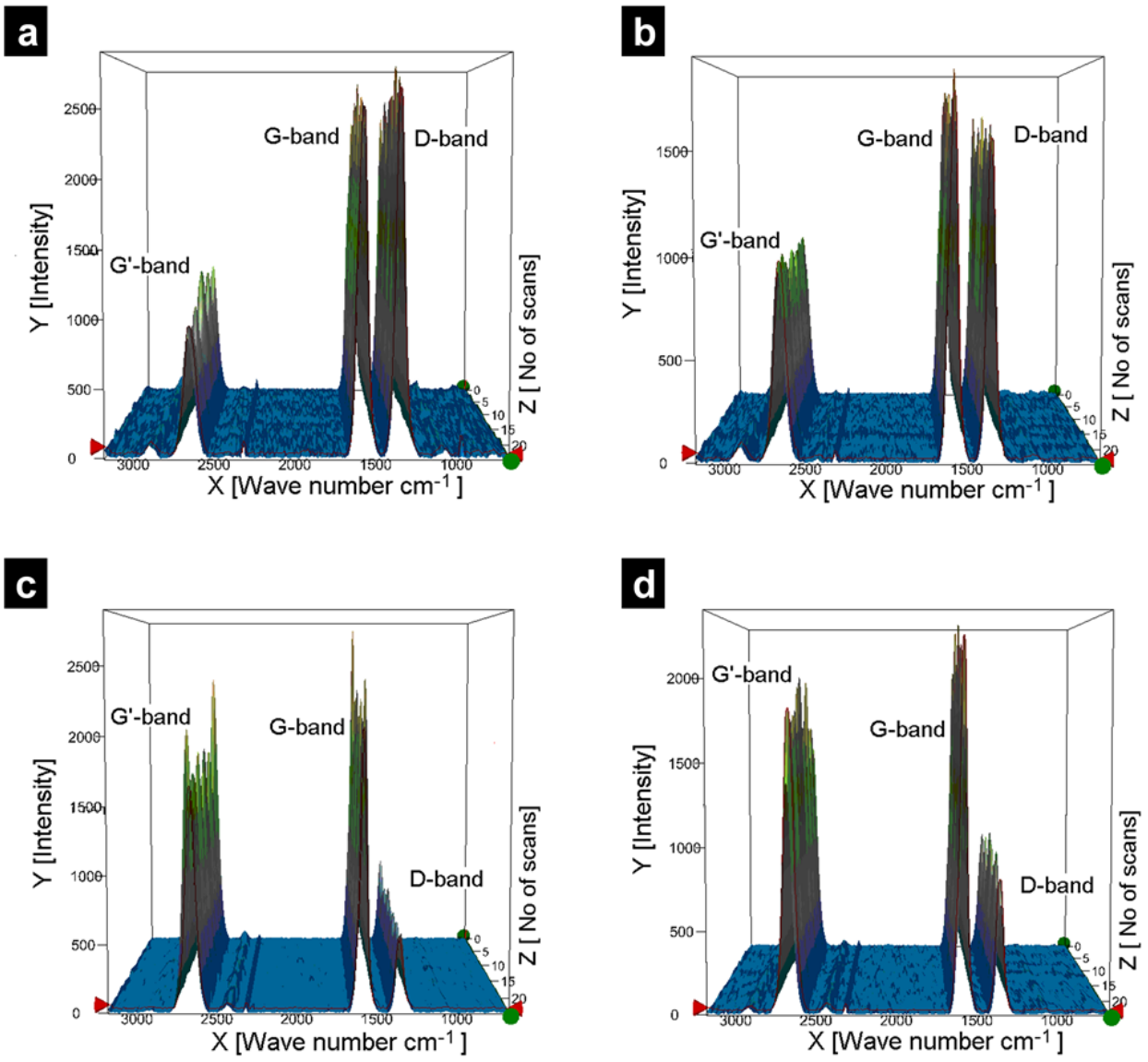

Figure 8.3: Raman spectra – a) CSIC-MWCNT before functionalization b) CSIC-MWCNT after functionalization c) FutureCarbon-MWCNT before functionalization d) FutureCarbon-MWCNT after functionalization.

The area of D-band and G-band of the spectra are determined by OPUS software and the ratios of D band to G band as well as the standard deviation of 25 scans are listed in Table 8.1.

Table 8.1: Average ratio of area and standard deviation of D-band to G-band

Type of MWCNT	Average Ratio of area of D-band to G-band (Area of D/ Area of G)	Standard deviation of ratios
FutureCarbon-MWCNT (Before Functionalization)	0.99	0.05
FutureCarbon-MWCNT (After PEG Functionalization)	0.83	0.04
CSIC-MWCNT (Before Functionalization)	0.29	0.05
CSIC-MWCNT (After PEG Functionalization)	0.40	0.05

The ratio of area of D to G band is 3 times lower in case of CSIC nanotubes than that of FutureCarbon nanotubes (before functionalization) what reveals the fact that FutureCarbon nanotubes contain almost 3 times more defect than CSIC nanotubes. Moreover, the change of D and G band ratio after functionalization in both FutureCarbon and CSIC nanotubes are beyond the standard deviation. Hence, it is possible to comment on the defect generated on the nanotubes during functionalization. The ratio changed from 0.29 to 0.4 after functionalization in case of CSIC-MWCNT which means during the 3 step functionalization some new defects might have been generated on these nanotubes. But, in case of FutureCarbon-MWCNT the ratio changed from 0.99 to 0.83 which means the functionalized nanotubes contain fewer defects than unfunctionalized nanotubes. However, it is not expected that any of the 3 steps of functionalization (oxidation, chlorination and esterification) can generate new sp^2 hybridized carbon on the surface of nanotube. So, during the functionalization and subsequent purification

(washing with water and THF) some carbonaceous impurities might have been washed away as amorphous carbons. As a result, the functionalized nanotubes contain fewer defects. But after functionalization the FutureCarbon carbon nanotubes still contain 2 times more defects than the CSIC carbon nanotubes.

8.3. PEBAX® MH 1657 nanocomposite membranes with FutureCarbon-MWCNT-PEG

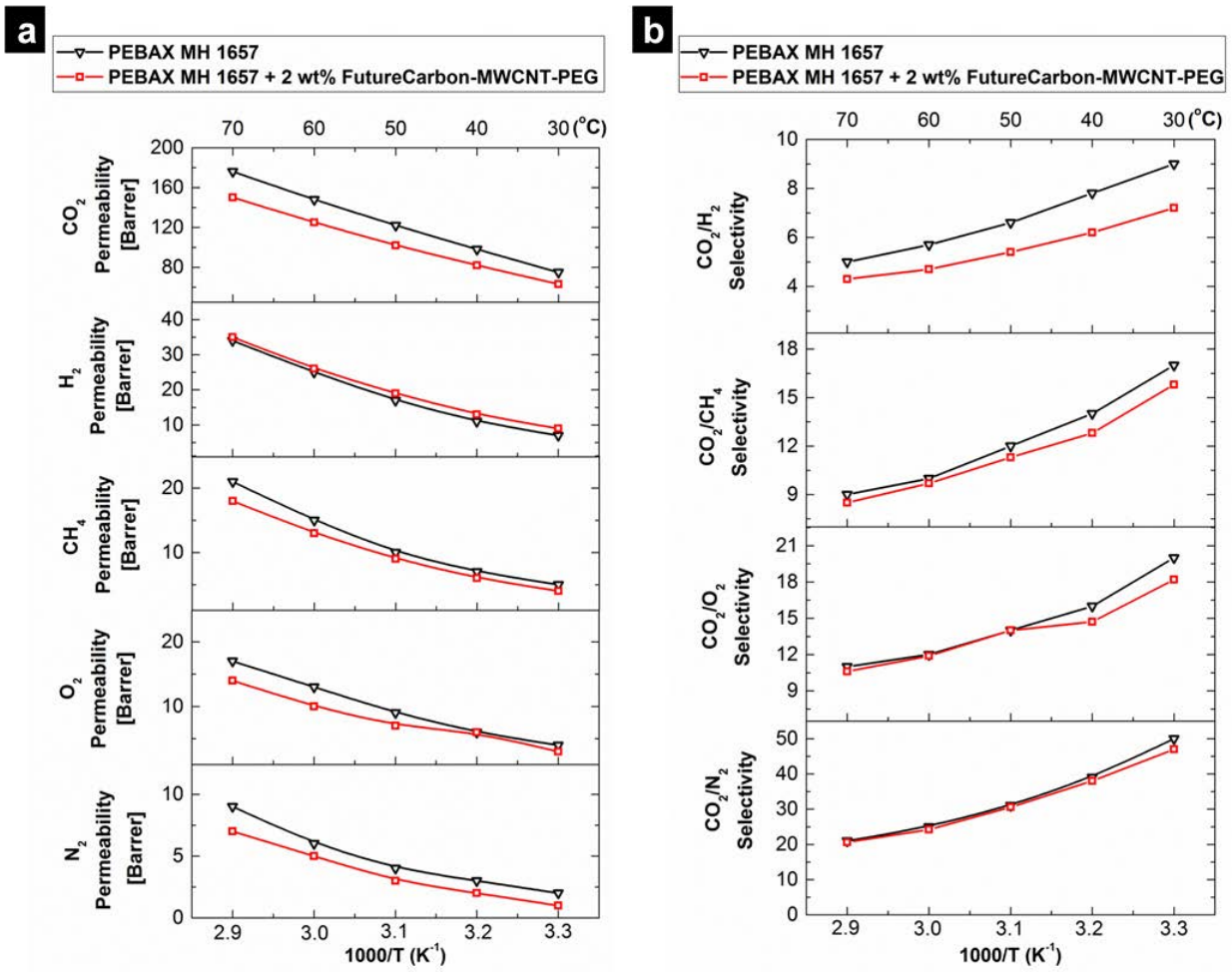

Figure 8.4: Gas separation performance of PEBAX® MH 1657 membranes before and after 2 wt% FC-MWCNT-PEG incorporation as a function of temperature – a) Permeability b) Selectivity of CO_2 over other gases.

Permeabilities of CO_2, H_2, CH_4, O_2 and N_2 in PEBAX® MH 1657 membrane and 2 wt% FutureCarbon-MWCNT-PEG incorporated PEBAX® MH 1657 membranes are plotted as a function of temperature in Figure 8.4a. CO_2 and N_2 permeability in the nanocomposite membrane is lower than the PEBAX® MH 1657 membrane between 30 ºC to 70 ºC. No significant differences are observed in the permeabilities of H_2 and CH_4 between the nanocomposite and pure polymer membrane in this temperature range. O_2 permeability in the nanocomposite membrane is similar to the pure polymer membrane at 30 ºC and 40 ºC. But at higher temperature the nanocomposite has a slightly lower permeability compared to PEBAX® MH 1657 membrane. Figure 8.4b shows that the selectivity of CO_2 over other gases in PEBAX® MH 1657 membrane and its nanocomposite containing 2 wt% FutureCarbon-MWCNT-PEG. CO_2/N_2 selectivity of the nanocomposite and pure polymer membrane are the same while the CO_2/H_2 selectivity dropped sharply in the nanocomposite membrane. The nanocomposite has slightly lower CO_2/O_2 and CO_2/CH_4 selectivity at 30 ºC and 40 ºC compared to the pure polymer membrane. At higher temperature CO_2/O_2 and CO_2/CH_4 selectivities of the membranes are equal. From Figure 8.4 it is evident that PEBAX® MH 1657 is a better membrane material for CO_2 separation compared to its nanocomposite containing 2 wt% FutureCarbon-MWCNT-PEG.

8.4. Polyurethane based electromagnetic interference (EMI) shielding foam

CSIC-MWCNT and FutureCarbon-MWCNT after PEG functionalization was supplied to other project partners of HARCANA for fabrication of polyurethane based electromagnetic interference (EMI) shielding foam material. The most representative EMI shielding results are provided in Appendix B, Table 12.2. Incorporation of CSIC-MWCNT leads to better conductivity compared to FutureCarbon-MWCNT. The PEG functionalized CSIC-MWCNT increased the conductivity of the foam even further. From the Raman spectroscopy study presented in section 8.2.2 it is clear that the better performance of the nanocomposite foams fabricated using CSIC-MWCNT stems from higher crystallinity or fewer defects of the CSIC-MWCNT. The better performance of CSIC-MWCNT after PEG functionalization can be also related to better percolation of the nanotubes. However, there is no experimental evidence to support this hypothesis. [1]

PS: 1. Note that the author of this thesis is responsible for functionalization of the MWCNTs and characterization of the MWCNT before and after the functionalization which helped to understand the better performance of the CSIC-MWCNT incorporated nanocomposite foams. The nanocomposite foams are prepared and characterized by other project partners.

8.5. Conclusion

MWCNT prepared by both FutureCarbon and CSIC are successfully functionalized with PEG. From Raman spectroscopy it is evident that CSIC nanotubes contain significantly lower defects compared to FutureCarbon nanotubes both before and after functionalization. Although the TGA-FTIR spectra prove the presence of covalently bonded PEG on CSIC-MWCNT-PEG it is not possible to comment on the presence of unreacted –COOH groups. FutureCarbon-MWCNT-PEG is incorporated in PEBAX® MH 1657 to prepare nanocomposite membrane. The CO_2 separation performance of the nanocomposite membrane is worse compared to pure PEBAX® MH 1657 membrane. Thus the PEG functionalized MWCNT is not a suitable nanofiller for PEBAX® MH 1657 membrane.

Part- E:

Chapter 9. Outlook

9.1. Post modification of PEG-GLY-POSS-Toluene

The aforementioned research work on tailor made POSS incorporated PEBAX® MH 1657 nanocomposite membranes (presented in chapter 6 and 7) demonstrates the potential utility of functionalized nanoparticles to design the next generation gas separation membranes with better separation performance. The gas transport properties of the block copolymer nanocomposite membranes are readily tunable by deliberate induction of surface functionality to the nanofiller. An advantage of using epoxide ring opening reaction for grafting PEG ligand to POSS nanoparticle is that it creates a –OH group which can be used for post modification. Hereinafter, some initial works to explore the possibilities towards this endeavor are presented. As the preliminary study, acylation and mesylation reactions are performed on PEG-GLY-POSS-Toluene (depicted in Scheme 9.1).

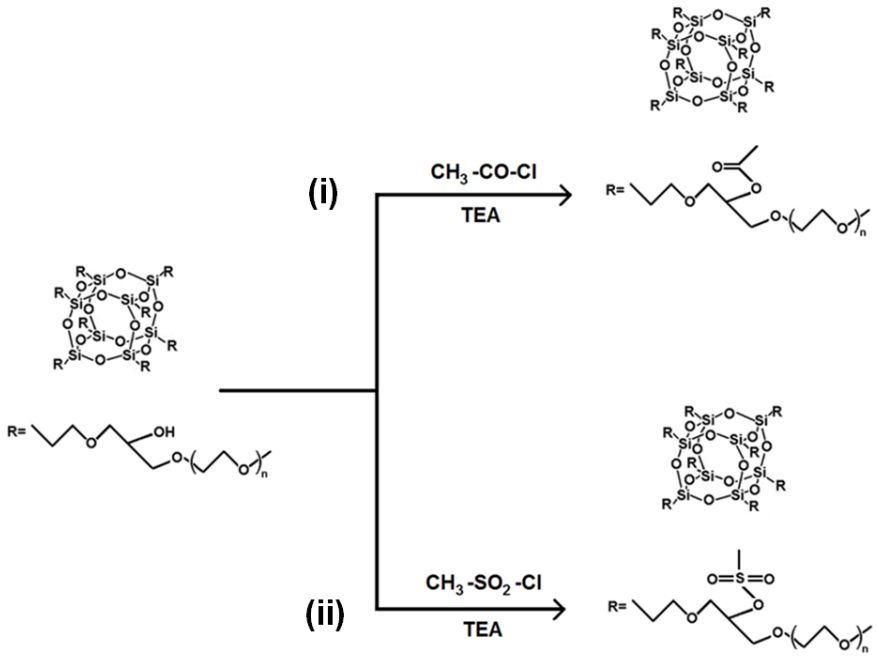

Scheme 9.1: Post modification of PEG-GLY-POSS- i) Acylation ii) Mesylation.

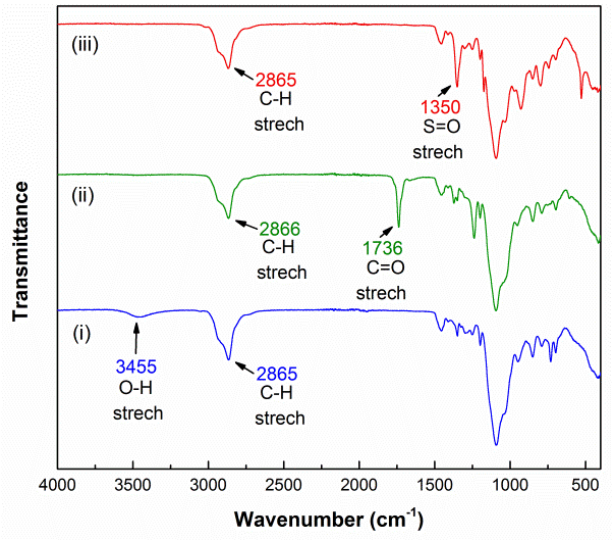

Figure 9.1: FT-IR spectra – i) PEG-GLY-POSS ii) PEG-GLY-POSS after acylation iii) PEG-GLY-POSS after mesylation.

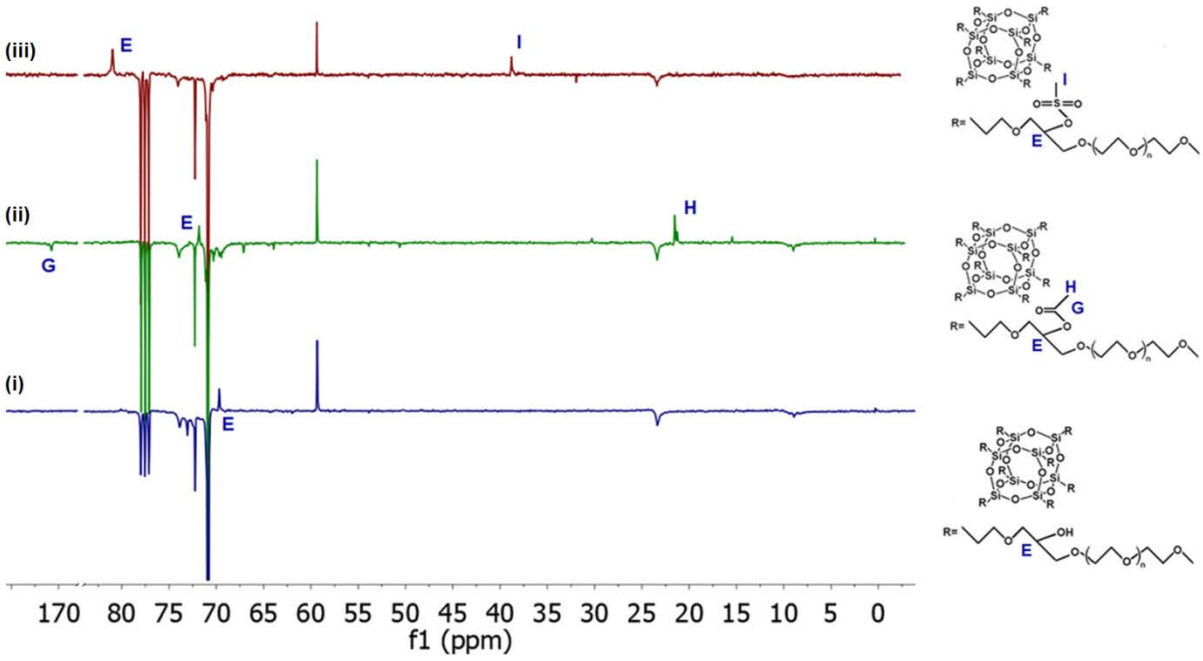

Figure 9.2: ^{13}C-DEPTQ-135 NMR spectra – i) PEG-GLY-POSS-Toluene ii) PEG-GLY-POSS after acylation iii) PEG-GLY-POSS after mesylation.

Figure 9.1 shows that the characteristic FT-IR peak of –OH group at 3455 cm^{-1} (spectra i) disappears completely after acylation (spectra ii) and mesylation (spectra iii). The C=O stretching from acyl group and S=O stretching from mesyl group are also visible at 1736 cm^{-1} (spectra ii) and 1350 cm^{-1} (spectra iii), respectively. Moreover, in ^{13}C-DEPTQ-135 NMR after both acylation and mesylation (Figure 9.2), the peak E i.e. the –CH peak (attached to the -OH group in PEG-GLY-POSS-Toluene) appears shifted more downfield. Hence, the FT-IR and ^{13}C NMR prove the success of acylation and mesylation. Mesylate is an excellent leaving group in nucleophilic substitution. Azidation is performed at this site using sodium azide as a nucleophile.

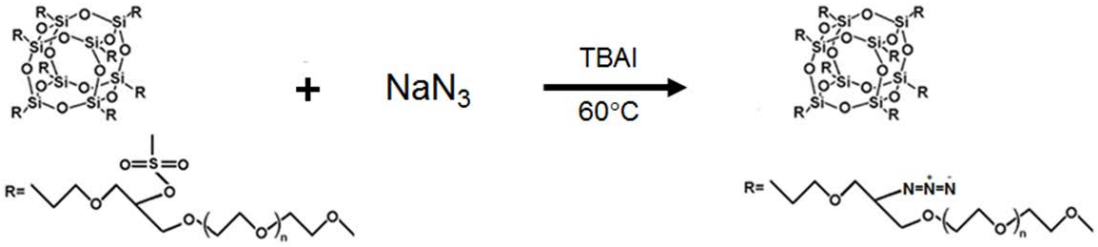

Scheme 9.2: Azidation of mesylated PEG-GLY-POSS-Toluene.

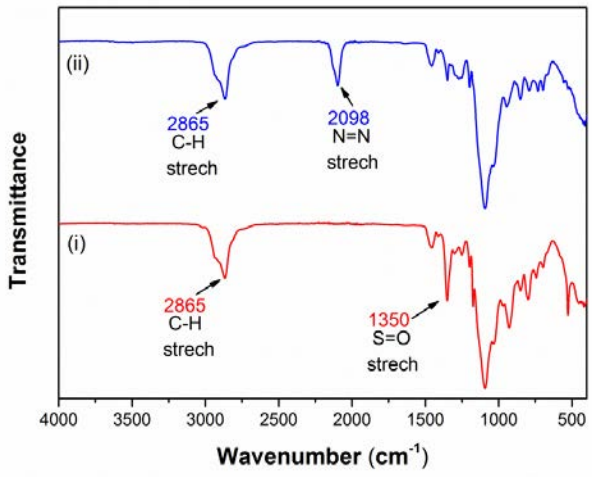

Figure 9.3: FT-IR spectra – i) Mesylated-PEG-GLY-POSS ii) Azide -PEG-GLY-POSS.

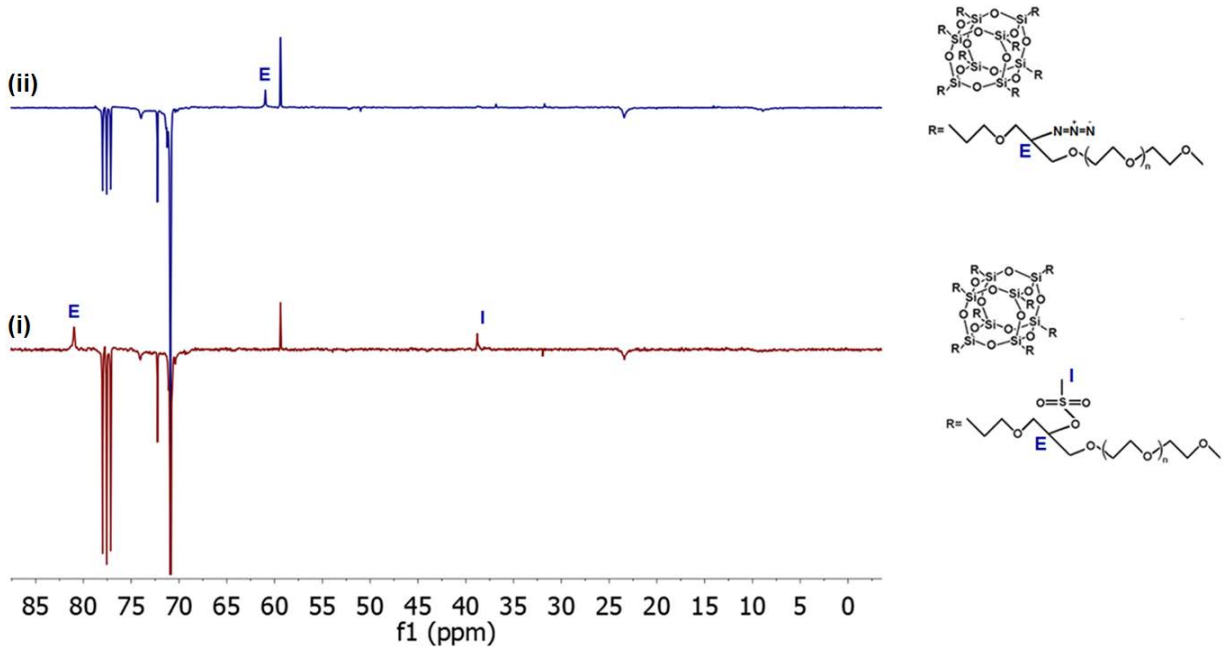

Figure 9.4: ^{13}C-NMR spectra – i) Mesylated-PEG-GLY-POSS ii) Azide -PEG-GLY-POSS.

FT-IR and ^{13}C-NMR spectra provided in Figure 9.3 and 9.4 respectively prove the success of azidation. The S=O stretching vibration at 1350 cm-1 disappeared and the N=N stretching vibration appeared in FT-IR (Figure 9.3) after the reaction. Moreover, in ^{13}C-NMR spectra peak E (which originates from the neighboring C of the mesylate group in Mesylated-PEG-GLY-POSS) shifts upfield after azidation.

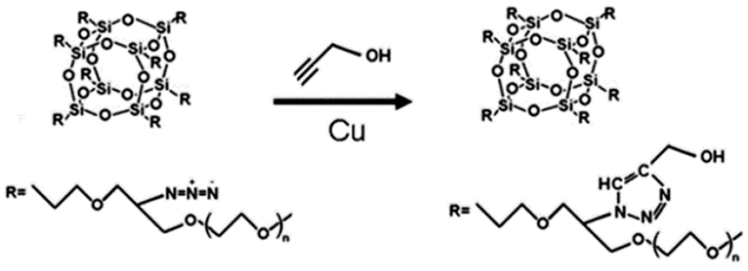

Scheme 9.3: Copper catalyzed “Click”reaction of Azide-PEG-GLY-POSS.

The azide-alkyne cycloaddition in presence of copper catalyst (termed as “Click chemistry” since 2001[92]) was performed on this site (Scheme 9.3). However, the reaction was not completely under control. Further investigation is required to ensure the success of this reaction.

The “Click” reaction is widely used for affixation of ligands by post modification because of its high efficiency. Irrespective of the ligand structure, often more than 95% yield is obtained at moderate reaction temperature (25 – 70 ºC) from “Click” reaction. [93, 94] Therefore, POSS nanoparticles can be tailored with a combination of different ligands by using the functionalization approach described in this thesis i.e. epoxide ring opening reaction followed by “Click” reaction. Consequently, it brings about myriad of opportunities to design block copolymer nanocomposite membrane with controlled molecular function. Considering the vast potential of block copolymer nanocomposite membranes further research in this direction is warranted.

Part – F:

Chapter 10. Summary

10.1. Summary

The multidisciplinary research work presented in this thesis is focused on designing block copolymer nanocomposite membranes for CO_2 separation that can be used in post-combustion carbon capture technology. In this regard, several polymer-nanofiller combinations are extensively investigated within the scope of the present work. Both commercial and tailor made nanoparticles are employed for fabrication of the nanocomposite membranes. Pros and cons of incorporation of the nanofillers in the block copolymer matrices are critically discussed in the context of physical property and gas separation performance of the nanocomposite membranes.

The commercial PEG POSS® nanoparticle is incorporated in five different commercial polymers namely PEBAX® MH 1657, PEBAX® 2533, PolyActive™1500PEGT77PBT23, PolyActive™3000PEGT77PBT23 and PolyActive™4000PEGT77PBT23 (Chapter 4 and 5). Among these five polymers only PEBAX® 2533 has poly(tetramethylene oxide) as a polyether segment. It is observed that incompatibility of the PEG ligand of the nanoparticle and the polyether block of PEBAX® 2533 leads to agglomeration of nanoparticles and eventually diffusion of CO_2 is hindered. In the case of PEBAX® MH 1657 and three grades of PolyActive™ the ligand of the nanoparticles and the polyether segments of the block copolymer have the same polyether i.e. poly(ethylene oxide) (PEO). The length of the PEO segment plays a vital role on the stability and separation performance of the membrane, since it dictates the crystallinity of the PEO block. The nanocomposites prepared from PolyActive™3000PEGT77PBT23 and PolyActive™4000PEGT77PBT23 are not stable in the expected temperature range of application in post combustion carbon capture technology. In these polymers the PEO blocks undergo a

thermal transition between 30 - 70 ºC and the nanofillers are rejected by the polymer matrix during the transition. The nanocomposites of PolyActive^{TM}1500PEGT77PBT23 are stable in this temperature range. It is observed that there is a significant difference in the gas transport mechanism of 20 wt% and 30 wt% PEG POSS® incorporated nanocomposites. The addition of another 10 wt% PEG POSS® after 20 wt% leads to a morphological change of the nanocomposite membranes as a result CO_2 solubility increases dramatically. PEG POSS® is highly compatible with the block copolymer matrix PEBAX® MH 1657. From the detail investigation of gas separation performance, thermal properties and morphological features of the nanocomposite membrane it is clear that PEBAX® MH 1657 is the most suitable block copolymer matrix among the five investigated polymers. The PEG ligands of the nanofillers plasticizes the polyether segment of the block copolymer and the diffusion of CO_2 improves significantly. Moreover, it is observed that PEG POSS® acts as a nucleating agent for the crystallization of polyether domain of PEBAX® MH 1657.

In the next part of the thesis (Chapter 6 and 7) poly(ethylene glycol) (PEG) is grafted to two commercially available POSS nanoparticles (namely glycidyl POSS® and glycidyldimethylsilyl POSS®) via epoxide ring opening reaction using three different solvents (chloroform, toluene and tetrahydrofuran). Since in the initial exploratory work it is found that PEG POSS® is compatible with PEBAX® MH 1657, this polymer is used as matrix material to prepare the nanocomposite membranes using the synthesized nanoparticles. The influence of two novel structural features of the synthesized nanofillers on the gas separation performance is subsequently studied. These are – i) presence of a dimethylsilyl group between the cage structure of POSS and the PEG ligand and ii) formation of a tetrahydrofuran (THF) complex. Single gas

permeability is remarkably increased in both cases. But the application of these membranes is limited to a temperature range where the polyamide domain of the block copolymer is not in a molten state. PEG functionalized MWCNT is also used as nanofiller for PEBAX® MH 1657 (Chapter 8). Unfortunately the gas separation performance of the MWCNT incorporated nanocomposite membranes are worse compared to the pure polymer membrane.

Undoubtedly, the functionalized POSS nanoparticles used in the present work are promising nanofillers to improve the gas permeability of PEBAX® MH 1657 membranes for post combustion carbon capture. From an application point of view, an increase of the membrane permeance reduces the membrane area required for a desired separation which results in reduced footprint and investment costs. However, these nanofillers could not prevent the sharp loss of CO_2 selectivity of the membranes with the increase of temperature. To pave the way for application of membrane technology in post combustion carbon capture there are critical needs to design membrane materials which can lead to higher CO_2 selectivity at the operating condition of the power plant stack. Therefore, future considerations should be directed towards synthesizing the nanofillers which can overcome this limitation. The initial work on functionalization of the POSS nanoparticle presented in this thesis (Chapter 9) offers a plethora of opportunities to rationally design nanoparticles with a combination of chemically distinct functionalities. It is reasonable to expect that novel nanocomposite membrane materials with potential functions will emerge in future using this functionalization approach. Nevertheless, the success of designing the block copolymer nanocomposite membranes depends not only in choosing the right nanofillers but also in precisely tailoring the collective properties of the nanocomposite.

10.2. Zusammenfassung

Die interdisziplinäre Forschungsarbeit, die im Rahmen dieser Promotion geleistet worden ist, fokussiert sich auf Blockcopolymer-basierte Nanocompositmembranen für die Abtrennung von CO_2 aus Post-Combustionströmen für die CarbonCapture-Technologie. Mit Hinblick auf die Arbeit wurden unterschiedliche Kombinationen von Polymeren und Nanofüllstoffen untersucht und bewertet. Sowohl kommerzielle als auch selbst hergestellte Nanopartikel wurden für die Herstellung der Nanokompositmembranen verwendet. Die Vor- und Nachteile der Verwendung solcher Nanofüllstoffe in Blockcopolymermembranen sind kritisch in Hinblick auf die physikalischen und Gastrenneigenschaften diskutiert und die Ergebnisse mit dem Stand der Technik verglichenworden.

Die kommerziell erhältlichen Nanopartikel PEG POSS® wurden in 5 verschiedene ebenfalls kommerzielle Polymertypen eingebracht: PEBAX® MH 1657, PEBAX® 2533, PolyActive™1500PEGT77PBT23, PolyActive™3000PEGT77PBT23 und PolyActive™4000PEGT77PBT23 (Kapitel 4 und 5). Unter diesen 5 verfügt nur PEBAX® 2533 über Poly(tetramethylenoxid) als Polyethersegment. Bei diesem war zu beobachten, dass es zu einer Unverträglichkeit zwischen dem PEG-Liganden auf dem Nanopartikel und dem Polyetherblock kam, was in weiterer Folge zur Agglomeration der Nanpartikel geführt hatte und vermutlich dadurch die CO_2 Diffusion vermindert hat. Im Fall von PEBAX® MH 1657 und den drei unterschiedlichen PolyActive™ verfügen die Liganden auf den Nanopartikeln über dieselben funktionellen Ethergruppen, nämlich Poly(ethyleneoxid) (PEO). Gerade die Länge des PEO Segmentes spielt eine wichtige Rolle bei der Stabilität und den Gastrenneigenschaften der

Membran, da diese Einfluss auf die Kristallinität des PEO Blocks hat. Bei den Experimenten hat sich gezeigt, dass die Nanocompositmembranen auf Basis von PolyActive™3000PEGT77PBT23 und PolyActive™4000PEGT77PBT23 nicht im gewünschten Temperaturbereich (50 - 60 ºC), wie er in der Nachverbrennung für CO_2-Sequestrierung vorliegt, stabil sind. Bei beiden kommt es zu einem thermischen Übergang zwischen 30 - 70 ºC, der in weiterer Folge dafür sorgt, dass es zu einer Entmischung zwischen der Polymermatrix und den Nanopartikeln kommt. Nur Nanocomposite aus PolyActive™1500PEGT77PBT23 sind über den gewünschten Temperaturbereich stabil. Im Laufe der Arbeit hat sich herausgestellt, dass die Konzentration der Nanopartikel auch einen großen Einfluss auf den Gastransport hat. Beispielsweise ist ein signifikanter Unterschied zwischen 20 und 30 Gewichtsprozent zu beobachten, was durch eine Änderung der Morphologie der Nanocompositmembranen zu erklären ist. So ist bei 30 wt% eine starke Zunahme der CO_2 Löslichkeit gegenüber 20% wt zu beobachten. PEG POSS® ist gut verträglich mit der Blockcopolymermatrix PEBAX® MH 1657. Aus der detaillierten Untersuchung der Gastrenneigenschaft, der Morphologie sowie der thermischen Charakteristika wird klar, dass PEBAX® MH 1657 die geeignete Copolymer-Matrix für die Herstellung der Nanocomposite ist. Dies erklärt sich durch die Plastifizierung der Polyethersegmente durch die PEG-Liganden des Nanofillers wodurch sich wiederum die CO_2-Diffusion positiv beeinflussen lässt. Darüber hinaus fungiert PEG POSS® als Nukleierungsmittel für die Kristallisation des Polyetherbereichs des PEBAX® MH 1657.

Der zweite große Teil der Dissertation (Kapitel 6 und 7) beschäftigt sich mit der Poly(ethylenglycol) (PEG) Funktionalisierung zweier POSS Nanopartikel (glycidyl POSS® und glycidyldimethylsilyl POSS®) mit Hilfe einer Ringöffnung der Epoxidgruppe in verschiedenen

Lösungsmitteln (Chloroform, Toluol und Tetrahydrofuran). Da in der vorangegangenen Untersuchung bereits gezeigt werden konnte, dass PEG POSS® gut verträglich ist mit PEBAX® MH 1657, wurde dieses Polymer als Matrixmaterial für die neu synthetisierten Nanopartikel verwendet. Im weiteren wurde der Einfluss dieser strukturellen Modifizierung auf die Gastrenneigenschaften untersucht. Im Detail handelt es sich um i) eine Dimethylsilyl-Gruppe zwischen der Käfigstruktur des POSS und dem PEG-Liganden und ii) und die Bildung eines THF-Komplexes. Die Einzelgasmessergebnisse haben sich deutlich gegenüber dem unmodifizierten Aufbau verbessert. Allerdings gibt es eine Temperatureinschränkung auf einen Bereich wo die Polyamid-Domänen des Blockcopolymers sich im nicht-geschmolzenem Zustand befinden. Schlussendlich wurde noch versucht MWCNT (multi wall carbon nano tubes) in das Polymer einzuarbeiten (Kapitel 8). Allerdings waren die Ergebnisse im Vergleich zum reinen Matrixpolymer schlechter und das Thema wurde nicht weiter verfolgt.

Zweifelsohne sind die POSS-funktionalisierten Nanopartikel ein vielversprechender Baustein um die Gastrenneigenschaften von PEBAX® MH 1657 in Hinblick auf seinen Einsatz in der CO_2-Abtrennung zu optimieren. Die verbesserten Trenneigenschaften erlauben es bei gleichbleibender Leistung die Membranfläche zu reduzieren und somit Kosten als auch negative Umweltkonsequenzen zu minimieren. Allerdings waren die hier vorgestellten Nanofüllstoffe nicht in der Lage, den für PEBAX typischen starken Verlust der Selektivität bei erhöhten Temperaturen zu verhindern. Doch gerade die Funktionalität der Membranen bei der Anwendungstemperatur, wie man sie in der Nachverbrennungstechnologie in Kraftwerken vorfindet, ist ein kritischer Erfolgsparameter für den Einsatz von Membrantechnologien. Daher muss der Fokus zukünftiger Arbeiten auf Nanofüllstoffen liegen, die die temperaturbedingten

Nachteile von PEBAX ausgleichen können und zu guten Selektivitäten führen. Die anfänglichen Arbeiten zur Funktionalisierung von POSS-Nanopartikeln (Kapitel 9) bieten eine Fülle von Ansatzmöglichkeiten zur chemischen Modifikation um spezielle Eigenschaften zu erreichen. Es darf folglich erwartet werden, dass der Fortschritt in diesem Bereich neuer Nanocompositmembranen mit zusätzlichen Funktionalitäten schnell voranschreiten wird. Nichts destotrotz ist der Erfolg neuer Nanocompositmembranen nicht nur auf die Auswahl geeigneter Füllstoffe beschränkt, sondern auch auf das Zusammenspiel dieser mit den Blockpolymer, um so maßgeschneiderte Eigenschaften zu erhalten.

Part- G:

Chapter 11. References

[1] S. Shafiee, E. Topal, When will fossil fuel reserves be diminished?, Energy Policy, 37 (2009) 181-189.

[2] F.R. Pazheri, M.F. Othman, N.H. Malik, A review on global renewable electricity scenario, Renewable and Sustainable Energy Reviews, 31 (2014) 835-845.

[3] T.C. Merkel, H. Lin, X. Wei, R. Baker, Power plant post-combustion carbon dioxide capture: An opportunity for membranes, Journal of Membrane Science, 359 (2010) 126-139.

[4] A. Brunetti, F. Scura, G. Barbieri, E. Drioli, Membrane technologies for CO_2 separation, Journal of Membrane Science, 359 (2010) 115-125.

[5] E. Favre, Membrane processes and postcombustion carbon dioxide capture: Challenges and prospects, Chemical Engineering Journal, 171 (2011) 782-793.

[6] M. Freemantle, Membranes for gas separation, Chemical & Engineering News 83 (2005) 3.

[7] P. Bernardo, G. Clarizia, 30 Years of Membrane Technology for Gas Separation, Chemical Engineering Transactions, 32 (2013).

[8] W.J. Koros, Gas separation membranes: needs for combined materials science and processing approaches, Macromolecular Symposia, 188 (2002) 13-22.

[9] B.D. Freeman, I. Pinnau, Polymeric Materials for Gas Separations, in: Polymer Membranes for Gas and Vapor Separation, American Chemical Society, 1999, pp. 1-27.

[10] Y. Gupta, K. Hellgardt, R.J. Wakeman, Enhanced permeability of polyaniline based nano-membranes for gas separation, Journal of Membrane Science, 282 (2006) 60-70.

[11] P. Bernardo, E. Drioli, G. Golemme, Membrane Gas Separation: A Review/State of the Art, Industrial & Engineering Chemistry Research, 48 (2009) 4638-4663.

[12] H. Lin, B.D. Freeman, Materials selection guidelines for membranes that remove CO_2 from gas mixtures, Journal of Molecular Structure, 739 (2005) 57-74.

[13] H. Lin, B.D. Freeman, Gas solubility, diffusivity and permeability in poly(ethylene oxide), Journal of Membrane Science, 239 (2004) 105-117.

[14] A. Car, C. Stropnik, W. Yave, K.-V. Peinemann, Tailor-made Polymeric Membranes based on Segmented Block Copolymers for CO_2 Separation, Advanced Functional Materials, 18 (2008) 2815-2823.

[15] S.J. Metz, M.H.V. Mulder, M. Wessling, Gas-Permeation Properties of Poly(ethylene oxide) Poly(butylene terephthalate) Block Copolymers, Macromolecules, 37 (2004) 4590-4597.

[16] V.I. Bondar, B.D. Freeman, I. Pinnau, Gas transport properties of poly(ether-b-amide) segmented block copolymers, Journal of Polymer Science Part B: Polymer Physics, 38 (2000) 2051-2062.

[17] S. Sridhar, R. Suryamurali, B. Smitha, T.M. Aminabhavi, Development of crosslinked poly(ether-block-amide) membrane for CO_2/CH_4 separation, Colloids and Surfaces A: Physicochemical and Engineering Aspects, 297 (2007) 267-274.

[18] R.S. Murali, S. Sridhar, T. Sankarshana, Y.V.L. Ravikumar, Gas Permeation Behavior of Pebax-1657 Nanocomposite Membrane Incorporated with Multiwalled Carbon Nanotubes, Industrial & Engineering Chemistry Research, 49 (2010) 6530-6538.

[19] W. Yave, A. Car, S.S. Funari, S.P. Nunes, K.-V. Peinemann, CO_2-Philic Polymer Membrane with Extremely High Separation Performance, Macromolecules, 43 (2009) 326-333.

[20] A. Car, C. Stropnik, W. Yave, K.-V. Peinemann, PEG modified poly(amide-b-ethylene oxide) membranes for CO_2 separation, Journal of Membrane Science, 307 (2008) 88-95.

[21] W. Yave, A. Car, K.-V. Peinemann, Nanostructured membrane material designed for carbon dioxide separation, Journal of Membrane Science, 350 (2010) 124-129.

[22] T.C. Merkel, B.D. Freeman, R.J. Spontak, Z. He, I. Pinnau, P. Meakin, A.J. Hill, Ultrapermeable, Reverse-Selective Nanocomposite Membranes, Science, 296 (2002) 519-522.

[23] T.C. Merkel, Z. He, I. Pinnau, Effect of Nanoparticles on Gas Sorption and Transport in Poly(1-trimethylsilyl-1-propyne), Macromolecules, 36 (2003) 6844-6855.

[24] J. Ahn, W.-J. Chung, I. Pinnau, M.D. Guiver, Polysulfone/silica nanoparticle mixed-matrix membranes for gas separation, Journal of Membrane Science, 314 (2008) 123-133.

[25] N.P. Patel, A.C. Miller, R.J. Spontak, Highly CO_2-Permeable and Selective Polymer Nanocomposite Membranes, Advanced Materials, 15 (2003) 729-733.

[26] M. Sadeghi, M.A. Semsarzadeh, H. Moadel, Enhancement of the gas separation properties of polybenzimidazole (PBI) membrane by incorporation of silica nano particles, Journal of Membrane Science, 331 (2009) 21-30.

[27] J.H. Kim, Y.M. Lee, Gas permeation properties of poly(amide-6-b-ethylene oxide)–silica hybrid membranes, Journal of Membrane Science, 193 (2001) 209-225.

[28] A.C. Balazs, T. Emrick, T.P. Russell, Nanoparticle Polymer Composites: Where Two Small Worlds Meet, Science, 314 (2006) 1107-1110.

[29] E. Ayandele, B. Sarkar, P. Alexandridis, Polyhedral Oligomeric Silsesquioxane (POSS)-Containing Polymer Nanocomposites, Nanomaterials, 2 (2012) 445-475.

[30] H. Cong, M. Radosz, B.F. Towler, Y. Shen, Polymer–inorganic nanocomposite membranes for gas separation, Separation and Purification Technology, 55 (2007) 281-291.

[31] http://www.co2crc.com.au/aboutccs/cap_membranes.html.

[32] R.W. Baker, Gas Separation, in: Membrane Technology and Applications, John Wiley & Sons, Ltd, 2004, pp. 301-353.

[33] S.A. Stern, H.L. Frisch, The Selective Permeation of Gases Through Polymers, Annual Review of Materials Science, 11 (1981) 523-550.

[34] S. Matteucci, Y. Yampolskii, B.D. Freeman, I. Pinnau, Transport of Gases and Vapors in Glassy and Rubbery Polymers, in: Materials Science of Membranes for Gas and Vapor Separation, John Wiley & Sons, Ltd, 2006, pp. 1-47.

[35] K. Ghosal, B.D. Freeman, Gas separation using polymer membranes: an overview, Polymers for Advanced Technologies, 5 (1994) 673-697.

[36] H. Lin, B.D. Freeman, Materials selection guidelines for membranes that remove CO_2 from gasmixtures, Journal of Molecular Structure, 739 (2005) 57-74.

[37] H.L. Frisch, S.A. Stern, Diffusion of small molecules in polymers, Critical Reviews in Solid State and Materials Sciences, 11 (1983) 123-187.

[38] S.A. Stern, S. Trohalaki, Fundamentals of Gas Diffusion in Rubbery and Glassy Polymers, in: Barrier Polymers and Structures, American Chemical Society, 1990, pp. 22-59.

[39] S. Kanehashi, K. Nagai, Analysis of dual-mode model parameters for gas sorption in glassy polymers, Journal of Membrane Science, 253 (2005) 117-138.

[40] C.M. Zimmerman, W.J. Koros, Polypyrrolones for membrane gas separations. II. Activation energies and heats of sorption, Journal of Polymer Science Part B: Polymer Physics, 37 (1999) 1251-1265.

[41] V. Abetz, A. Boschetti-de-Fierro, J.-F. Gohy, Morphologies in Block Copolymers, in: Controlled and Living Polymerizations, Wiley-VCH Verlag GmbH & Co. KGaA, 2010, pp. 493-554.

[42] R.J. Spontak, N.P. Patel, Thermoplastic elastomers: fundamentals and applications, Current Opinion in Colloid & Interface Science, 5 (2000) 333-340.

[43] J.P. Sheth, J. Xu, G.L. Wilkes, Solid state structure–property behavior of semicrystalline poly(ether-block-amide) PEBAX® thermoplastic elastomers, Polymer, 44 (2003) 743-756.

[44] F.S. Bates, G.H. Fredrickson, Block Copolymers-Designer Soft Materials Physics Today, 52 (1999) 32-38.

[45] Y. Mai, A. Eisenberg, Self-assembly of block copolymers, Chemical Society Reviews, 41 (2012) 5969-5985.

[46] V. Abetz, T. Goldacker, Formation of superlattices via blending of block copolymers, Macromolecular Rapid Communications, 21 (2000) 16-34.

[47] F.S. Bates, G.H. Fredrickson, Block copolymer thermodynamics: theory and experiment, Annual Review of Physical Chemistry, 41 (1990) 525-557.

[48] K.I. Winey, R.A. Vaia, Polymer Nanocomposites, MRS Bulletin, 32 (2007) 314-322.

[49] M.R. Bockstaller, R.A. Mickiewicz, E.L. Thomas, Block Copolymer Nanocomposites: Perspectives for Tailored Functional Materials, Advanced Materials, 17 (2005) 1331-1349.

[50] A.C. Balazs, Nanocomposites: Economy at the nanoscale, Nature Materials, 6 (2007) 94-95.

[51] B. Sarkar, P. Alexandridis, Self-Assembled Block Copolymer–Nanoparticle Hybrids: Interplay between Enthalpy and Entropy, Langmuir, 28 (2012) 15975-15986.

[52] J. Kao, K. Thorkelsson, P. Bai, B.J. Rancatore, T. Xu, Toward functional nanocomposites: taking the best of nanoparticles, polymers, and small molecules, Chemical Society Reviews, 42 (2013) 2654-2678.

[53] L. Lui, PhD Thesis - Gas separation by poly(ether block amide) membranes, in: Chemical Engineering, University of Waterloo, Waterloo, Ontario, Canada, 2008.

[54] V.I. Bondar, B.D. Freeman, I. Pinnau, Gas transport property of poly(ether-b-amide) segmented block copolymers, Journal of Polymer Science Part B: Polymer Physics, 38 (2000) 2051-2062.

[55] A. Car, C. Stropnik, W. Yave, K.-V. Peinemann, PEG modified poly(amide-b-ethylene oxide) membranes for CO_2 separation, Journal of Membrane Science, 307 (2008) 88-95.

[56] W. Yave, A.Car, K.-V. Peinemann, Nanostructure membrane material designed for carbondioxide separation, Journal of Membrane Science, 350 (2010) 124-129.

[57] S.R. Reijerkerk, M.H. Knoef, K. Nijmeijer, M. Wessling, Poly(ethylene glycol) and poly(dimethyl siloxane): Combining their advantages into efficient CO_2 gas separation membranes, Journal of Membrane Science, 352 (2010) 126-135.

[58] Y. Li, T.-S. Chung, Molecular-level mixed matrix membranes comprising Pebax® and POSS for hydrogen purification via preferential CO_2 removal, International Journal of Hydrogen Energy, 35 (2010) 10560-10568.

[59] K. Madhavan, B.S.R. Reddy, Structure–gas transport property relationships of poly(dimethylsiloxane–urethane) nanocomposite membranes, Journal of Membrane Science, 342 (2009) 291-299.

[60] V.I. Bondar, B.D. Freeman, I. Pinnau, Gas sorption and characterization of poly(ether-b-amide) segmented block copolymers, Journal of Polymer Science Part B: Polymer Physics, 37 (1999) 2463-2475.

[61] M.M. Rahman, V. Filiz, S. Shishatskiy, C. Abetz, S. Neumann, S. Bolmer, M.M. Khan, V. Abetz, PEBAX® with PEG functionalized POSS as nanocomposite membranes for CO_2 separation, Journal of Membrane Science, 437 (2013) 286-297.

[62] T.K. Kwei, W.M. Arnheim, The diffusion of gases through filled polymers, Journal of Polymer Science Part C: Polymer Symposia, 10 (1965) 103-110.

[63] P. Meares, The Diffusion of Gases Through Polyvinyl Acetate, Journal of the American Chemical Society, 76 (1954) 3415–3422.

[64] S. Fakirov, Poly(ether-b-amide) thermoplastic elastomers: Structure, properties and applications, in: Handbook of Condensation Thermoplastic Elastomer, WILEY-VCH Verlag Gmbh & Co, 2005, pp. 263-267.

[65] S.T. Correale, N.S. Murthy, Secondary crystallization and premelting endo- and exotherms in oriented polymers, Journal of Applied Polymer Science, 101 (2006) 447-454.

[66] R.R.L. De Oliveira, D.A.C. Albuquerque, T.G.S. Cruz, F.M. Yamaji, F.L. Leite, Measurement of the Nanoscale Roughness by Atomic Force Microscopy: Basic Principles and Applications, Atomic Force Microscopy - Imaging, Measuring and Manipulating Surfaces at the Atomic Scale, Dr. Victor Bellitto (Ed.), 2012, ISBN: 978-953-51-0414-8, InTech, DOI: 10.5772/37583. .

[67] S.A. Stern, H.L. Frisch, The Selective Permeation of Gases through Polymers, Annual Review of Materials Science, 11 (1981) 523-550.

[68] E.R. Hensema, Polymeric Gas Separation Membranes, Advanced Materials, 6 (1994) 269-279.

[69] H. Cong, M. Radosz, B.F. Towler, Y. Shen, Polymer-inorganic nanocomposite membranes for gas separation, Separation and Purification Technology, 55 (2007) 281-291.

[70] S. Fakirov, T. Gogeva, Poly(ether/ester)s based on poly(butylene terephthalate) and poly(ethylene glycol), 2. Effect of polyether segment length, Die Makromolekulare Chemie, 191 (1990) 615-624.

[71] M.M. Rahman, V. Filiz, S. Shishatskiy, C. Abetz, P. Georgopanos, M.M. Khan, S. Neumann, V. Abetz, Influence of Poly(ethylene glycol) Segment Length on CO_2 Permeation and Stability of PolyActive Membranes and Their Nanocomposites with PEG POSS, ACS Applied Materials & Interfaces, (2014) DOI: 10.1021/am504223f.

[72] F.T. Simon, J.M. Rutherford, Crystallization and Melting Behavior of Polyethylene Oxide Copolymers, Journal of Applied Physics, 35 (1964) 82-86.

[73] A. Fina, D. Tabuani, A. Frache, G. Camino, Polypropylene–polyhedral oligomeric silsesquioxanes (POSS) nanocomposites, Polymer, 46 (2005) 7855-7866.

[74] H. Ríos-Dominguez, F.A. Ruiz-Treviño, R. Contreras-Reyes, A. González-Montiel, Syntheses and evaluation of gas transport properties in polystyrene–POSS membranes, Journal of Membrane Science, 271 (2006) 94-100.

[75] N. Hao, M. Böhning, A. Schönhals, CO_2 Gas Transport Properties of Nanocomposites Based on Polyhedral Oligomeric Phenethyl-Silsesquioxanes and Poly(bisphenol A carbonate), Macromolecules, 43 (2010) 9417-9425.

[76] P. Iyer, G. Iyer, M. Coleman, Gas transport properties of polyimide–POSS nanocomposites, Journal of Membrane Science, 358 (2010) 26-32.

[77] M.L. Chua, L. Shao, B.T. Low, Y. Xiao, T.-S. Chung, Polyetheramine–polyhedral oligomeric silsesquioxane organic–inorganic hybrid membranes for CO_2/H_2 and CO_2/N_2 separation, Journal of Membrane Science, 385–386 (2011) 40-48.

[78] B. Sarkar, E. Ayandele, V. Venugopal, P. Alexandridis, Polyhedral Oligosilsesquioxane (POSS) Nanoparticle Localization in Ordered Structures Formed by Solvated Block Copolymers, Macromolecular Chemistry and Physics, 214 (2013) 2716-2724.

[79] R.C.D. Muniz Filho, S.A.A.d. Sousa, F.v.d.S. Pereira, M.r.M.C. Ferreira, Theoretical Study of Acid-Catalyzed Hydrolysis of Epoxides, The Journal of Physical Chemistry A, 114 (2010) 5187-5194.

[80] J. Mu, S. Zheng, Poly(N-isopropylacrylamide) nanocrosslinked by polyhedral oligomeric silsesquioxane: Temperature-responsive behavior of hydrogels, Journal of Colloid and Interface Science, 307 (2007) 377-385.

[81] M.M. Rahman, V. Filiz, M.M. Khan, B.N. Gacal, V. Abetz, Functionalization of POSS nanoparticles and fabrication of block copolymer nanocomposite membranes for CO_2 separation, Reactive and Functional Polymers, DOI: 10.1016/j.reactfunctpolym.2014.1007.1006.

[82] M.M. Rahman, S. Shishatskiy, C. Abetz, P. Georgopanos, S. Neumann, M.M. Khan, V. Filiz, V. Abetz, Influence of temperature upon properties of tailor-made PEBAX® MH 1657 nanocomposite membranes for post-combustion CO_2 capture, Journal of Membrane Science, 469 (2014) 344-354.

[83] Y. Kawakami, I. Imae, Functionality and stereochemical design of silicon-containing polymers, Macromolecular Chemistry and Physics, 200 (1999) 1245-1256.

[84] T. Kamal, S.-Y. Park, J.-H. Park, Y.-W. Chang, Structural evolution of poly(ether-b-amide12) elastomers during the uniaxial stretching: An in situ wide-angle X-ray scattering study, Macromolecular Research, 20 (2012) 725-731.

[85] D. Tasis, N. Tagmatarchis, A. Bianco, M. Prato, Chemistry of carbon nanotubes, Chemical Reviews, 106 (2006) 1105-1136.

[86] P. Liu, Modifications of carbon nanotubes with polymers, European Polymer Journal, 41 (2005) 2693-2703.

[87] M.M. Bernal, M. Liras, R. Verdejo, M.A. López-Manchado, I. Quijada-Garrido, R. París, Modification of carbon nanotubes with well-controlled fluorescent styrene-based polymers using the Diels–Alder reaction, Polymer, 52 (2011) 5739-5745.

[88] R. Verdejo, S. Lamoriniere, B. Cottam, A. Bismarck, M. Shaffer, Removal of oxidation debris from multi-walled carbon nanotubes, Chemical Communications, (2007) 513-515.

[89] C. Singh, M.S.P. Shaffer, K.K.K. Koziol, I.A. Kinloch, A.H. Windle, Towards the production of large-scale aligned carbon nanotubes, Chemical Physics Letters, 372 (2003) 860-865.

[90] J. Albuerne, A. Boschetti-de-Fierro, V. Abetz, Modification of multiwall carbon nanotubes by grafting from controlled polymerization of styrene: Effect of the characteristics of the nanotubes, Journal of Polymer Science Part B: Polymer Physics, 48 (2010) 1035-1046.

[91] C. Zenkel, J. Albuerne, T. Emmler, A. Boschetti-de-Fierro, J. Helbig, V. Abetz, New strategies for the chemical characterization of multi-walled carbon nanotubes and their derivatives, Microchimica Acta, 179 (2012) 41-48.

[92] H.C. Kolb, M.G. Finn, K.B. Sharpless, Click Chemistry: Diverse Chemical Function from a Few Good Reactions, Angewandte Chemie International Edition, 40 (2001) 2004-2021.

[93] W.H. Binder, R. Sachsenhofer, ‘Click’ Chemistry in Polymer and Materials Science, Macromolecular Rapid Communications, 28 (2007) 15-54.

[94] W.H. Binder, R. Sachsenhofer, ‘Click’ Chemistry in Polymer and Material Science: An Update, Macromolecular Rapid Communications, 29 (2008) 952-981.

Chapter 12. Acknowledgement

I am grateful to Prof. Volker Abetz for his wonderful supervision during the last three and a half years. The PhD position at Helmholtz-Zentrum Geesthacht (HZG) under his supervision availed me the opportunity to benefit from his experience. The scientific discussions with him were always fruitful and in many cases opened up new dimensions in my research. Working under him as a PhD student has been a privilege.

I appreciate the guidance and support of Dr. Volkan Filiz, Head of PMS department. I was really influenced by his positive approach and encouragement to try new things in the research work. His friendly attitude provided me a great working environment at HZG. I express my heartfelt gratitude to Dr. Sergey Shishatskiy for his valuable inputs and continuous interest in my research. He was always eager to discuss which was highly motivating. It was a pleasure to work with this dedicated scientist. My special thanks to Clarissa Abetz for the morphological characterization and helpful discussion. It would not be possible to analyze the complicated morphology of my samples without her diligence and hard work. I would also like to thank Prokopios Georgopanos and Sabrina Bolmer for morphological characterization using Atomic Force Microscopy. Many thanks to Silvio Neumann for fast and accurate DSC, NMR, TGA-FTIR and Raman spectroscopy analyses.

I am thankful to Carsten Scholles, Thomas Emmler, Mona Wombach, Ivonne Ternes and Petra Merten for their valuable suggestion and support in my work. I would like to thank Muntazim Munir Khan, Bing Du, Wiebke junior, Bahadir Gacal, Judith Grünauer, Shaheed Majeed and the other PhD students of PMS, PMM and PMV. It is because of these people every working day in HZG was a nice day.

I acknowledge the financial support of European Union (EU) and Helmholtz Association during this whole period of my PhD research. This work was financially supported by the 7th Framework Program research EU-project “HARCANA” (Grant Agreement no. NMP3-LA-2008-213277) and the Helmholtz Association of German Research Centers through the Helmholtz Portfolio MEM-BRAIN.

Chapter 13. Appendix

Appendix A

13.1. List of NMR Peaks

a) PEG-GLY-POSS-Chloroform

^{1}H NMR ($CDCl_3$, 300 MHz): δ (ppm): 0.61(s, 2H), 1.21 (t, 3H), 1.65 (s, 2H), 3.38 (s, 3H), 3.4-4.0 (m, -CH_2CH_2O- of PEG).

$^{13}C\{^{1}H\}$ NMR ($CDCl_3$, 75 MHz): δ (ppm): 8.6, 15.1, 23.0, 59.0, 66.7, 69.3, 70.5, 71.9, 72.7, 73.5.

b) PEG-GLY-POSS-Toluene

^{1}H NMR ($CDCl_3$, 300 MHz): δ (ppm): 0.62 (s, 2H), 1.65 (s, 2H), 3.38 (s, 3H), 3.4-4.0 (m, -CH_2CH_2O- of PEG).

$^{13}C\{^{1}H\}$ NMR ($CDCl_3$, 75 MHz): δ (ppm): 8.6, 23.0, 59.0, 69.4, 70.5, 71.9, 72.7, 73.5.

c) PEG-GLY-POSS-THF

^{1}H NMR ($CDCl_3$, 300 MHz): δ (ppm): 0.61(s, 2H), 1.62 (s, overlapped -CH_2 of THF and –CH_2 of glycidyl arm), 3.38 (s, 3H), 3.4-4.0 (m, overlapped -CH_2 of THF & -CH_2CH_2O- of PEG).

$^{13}C\{^{1}H\}$ NMR ($CDCl_3$, 75 MHz): δ (ppm): 8.6, 23.0, 26.5, 59.0, 69.4, 70.0,70.5, 71.1, 71.3, 71.9, 73.6.

d) PEG-GDMS-POSS-Chloroform

^{1}H NMR ($CDCl_3$, 300 MHz): δ (ppm): 0.14, (s, 6H), 0.58 (s, 2H),1.21 (t,3H), 1.61 (s, 2H), 3.38 (s, 3H), 3.4-4.0 (m, -CH_2CH_2O- of PEG).

$^{13}C\{^{1}H\}$ NMR ($CDCl_3$, 75 MHz): δ (ppm): -0.4, 13.6, 15.1, 23.0, 59.0, 66.7, 69.3, 70.5, 71.9, 72.7, 74.1.

e) PEG-GDMS-POSS-Toluene

^{1}H NMR ($CDCl_3$, 300 MHz): δ (ppm): 0.14, (s, 6H), 0.58 (s, 2H), 1.61 (s, 2H), 3.38 (s, 3H), 3.4-4.0 (m, -CH_2CH_2O- of PEG).

$^{13}C\{^{1}H\}$ NMR ($CDCl_3$, 75 MHz): δ (ppm): -0.4, 13.6, 23.0, 59.0, 69.3, 70.5, 71.9, 72.7, 74.1.

f) PEG-GDMS-POSS-THF

^{1}H NMR ($CDCl_3$, 300 MHz): δ (ppm): 0.14, (s, 6H), 0.61(s, 2H), 1.62 (s, overlapped -CH_2 of THF and -CH_2 of glycidyl arm), 3.38 (s, 3H), 3.4-4.0 (m, overlapped –CH_2 THF & -CH_2CH_2O- of PEG).

$^{13}C\{^{1}H\}$ NMR ($CDCl_3$, 75 MHz): δ (ppm):-0.4, 13.6, 23.1, 26.5, 59.0, 69.4, 70.0,70.5, 71.1, 71.3, 71.9, 74.1.

13.2. Composition of PEG functionalized POSS nanoparticles

Table 13.1: Composition of the functionalized POSS nanoparticles after modification with PEG.

Name of POSS	POSS cage content (wt%)	Total ligand content (wt%)	Dimethylsilyl spacer content (wt%)	PEG content (wt%)	THF complex content (wt%)	Diethyletharate content (wt%)	Rest of the ligand content (wt%)
PEG-GLY-POSS-Chloroform	12	88	-	61	-	3	24
PEG-GDMS-POSS-Chloroform	10	90	14	52	-	3	21
PEG-GLY-POSS-Toluene	10	90	-	68	-	-	22
PEG-GDMS-POSS-Toluene	9	91	12	59	-	-	20
PEG-GLY-POSS-THF	8	92	-	53	22	-	17
PEG-GDMS-POSS-THF	7	93	10	48	20	-	15

Note- Glycidyl groups are attached to the POSS cage and dimethylsilyl spacer of Glycidyl POSS® and Glycidyldimethlysilyl POSS® respectively. Weight percentage of this part after modification with PEG is denoted as “Rest of the ligand content”.

13.3. DSC thermograms

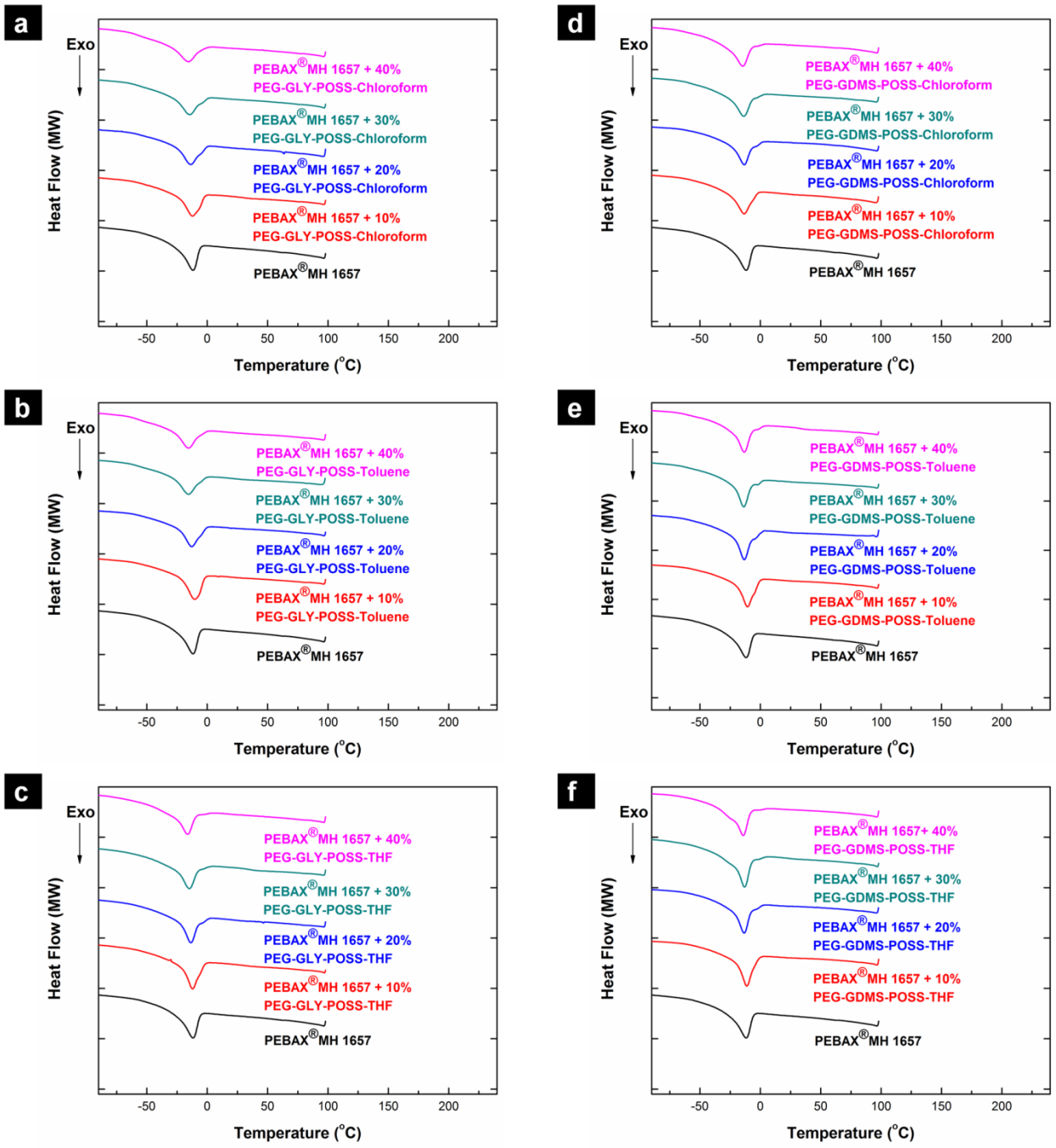

Figure 13.1: DSC thermograms (first cooling trace) of PEBAX® MH 1657 and its nanocomposites containing – a) PEG-GLY-POSS-Chloroform b)PEG-GLY-POSS-Toluene c)PEG-GLY-POSS-THF d) PEG-GDMS-POSS-Chloroform e)PEG-GDMS-POSS-Toluene f)PEG-GDMS-POSS-THF

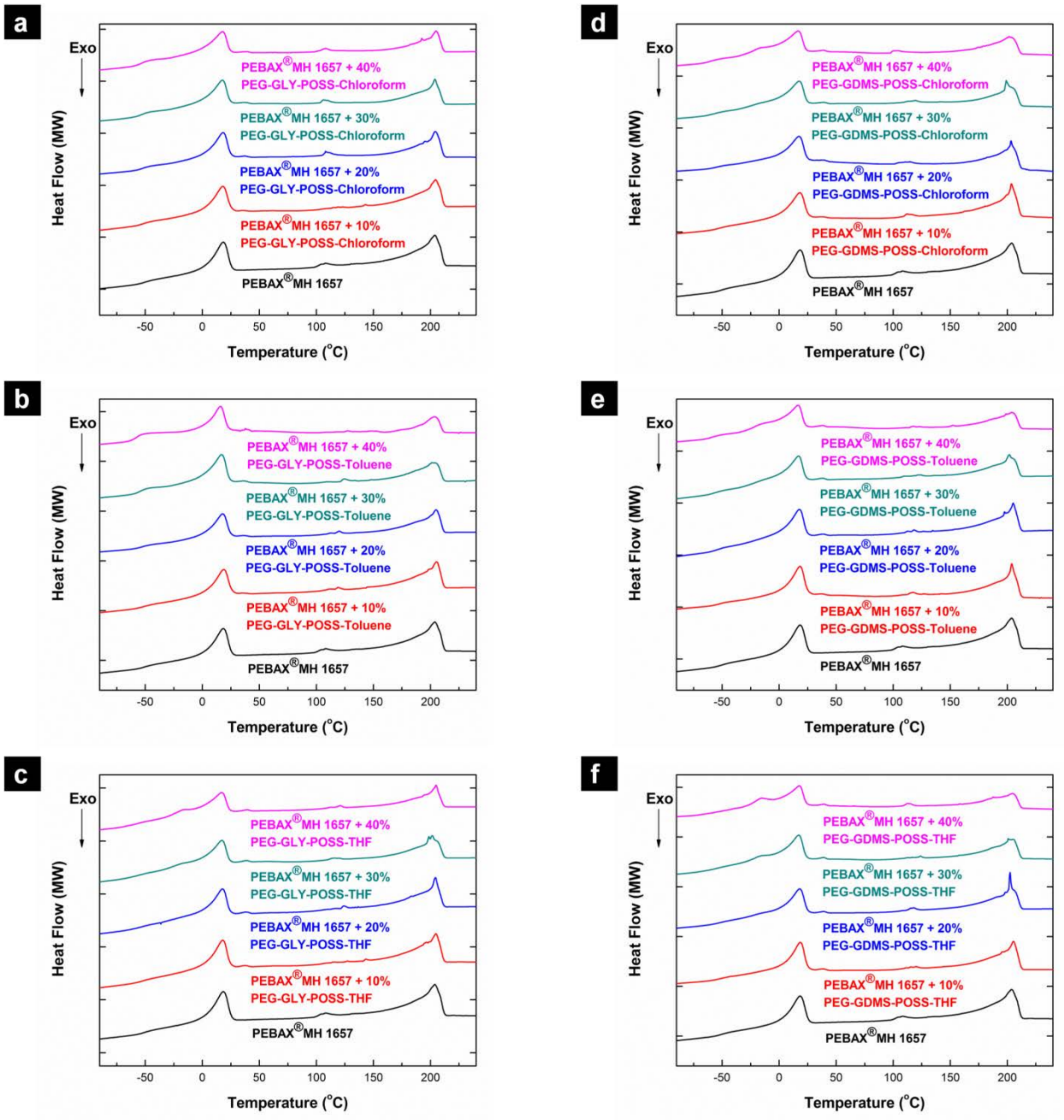

Figure 13.2: DSC thermograms (second heating trace) of PEBAX MH 1657 and its nanocomposites containing – a) PEG-GLY-POSS-Chloroform b)PEG-GLY-POSS-Toluene c)PEG-GLY-POSS-THF d) PEG-GDMS-POSS-Chloroform e)PEG-GDMS-POSS-Toluene f)PEG-GDMS-POSS-THF

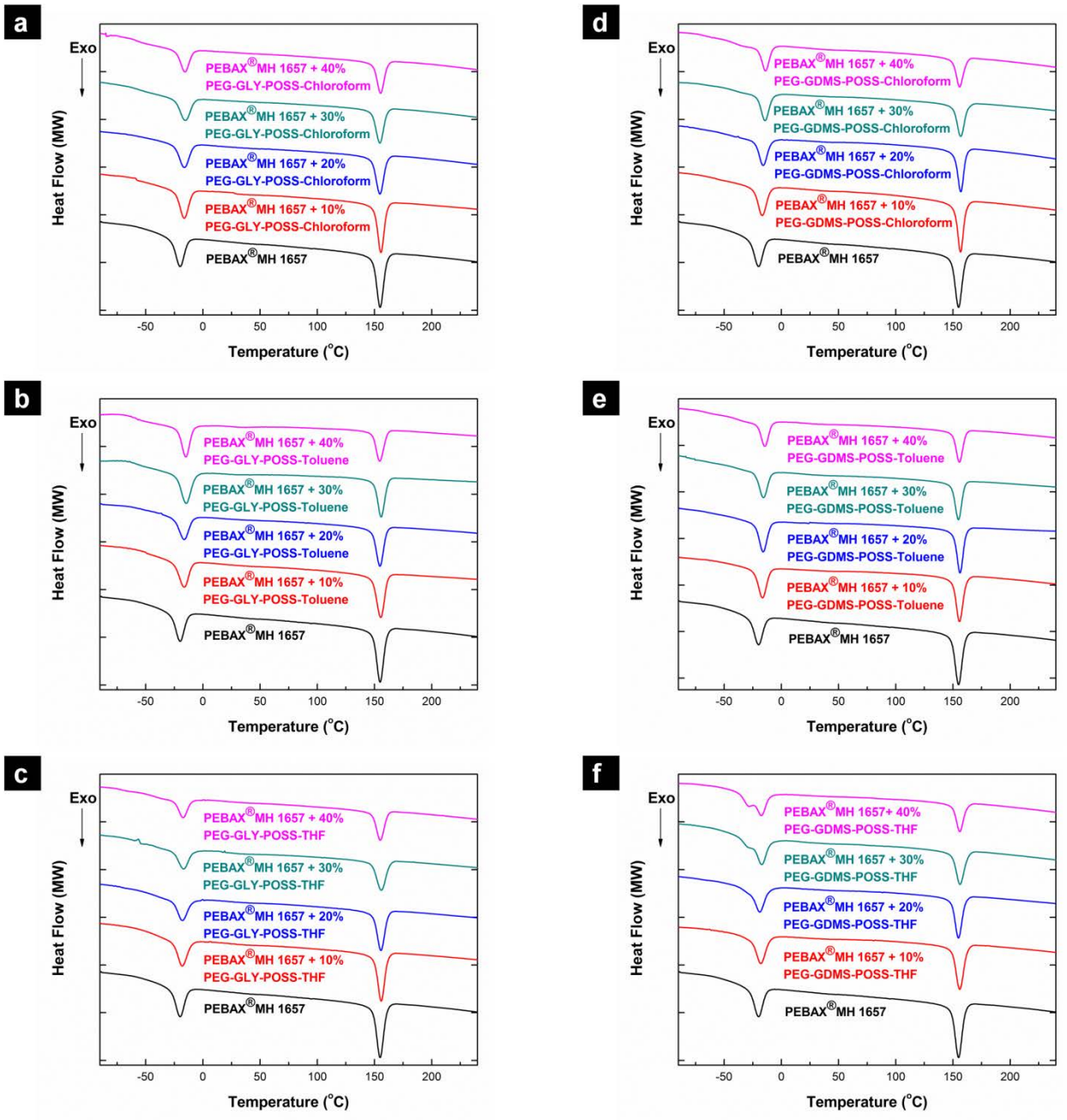

Figure 13.3: DSC thermograms (second cooling trace) of PEBAX MH 1657 and its nanocomposites containing – a) PEG-GLY-POSS-Chloroform b)PEG-GLY-POSS-Toluene c)PEG-GLY-POSS-THF d) PEG-GDMS-POSS-Chloroform e)PEG-GDMS-POSS-Toluene f)PEG-GDMS-POSS-THF

Appendix B

13.4. Conductive Foam

MWCNTs were dispersed in polyol following two dispersing protocols, one developed by CSIC and the other by FutureCarbon. These samples were then sent to ECCOSORB for the development and characterisation of rigid PU foams with different loading fractions of MWCNTs. A set of samples was developed using CSIC-MWCNT-PEG and FutureCarbon-MWCNT-PEG (functionalization and characterization MWCNT are presented in Chapter 8).

Table 13.2: Conductivity values as a function of density, MWCNT type and dispersion protocol.

CNT by	Functionalized by	Dispersed by	Loading fraction in polyol (wt.-%)	Density ($kg \cdot m^{-3}$)	Conductivity (S/m)
CSIC	-	CSIC	0.8	70	0.04
CSIC	-	FC	0.8	65	0.02
CSIC	-	FC	4	300	0.15
FC	-	FC	3	300	0.14
FC	-	FC	3	480	0.30
FC	-	FC	4	345	0.04
CSIC	HZG	CSIC	0.6	202	0.35
CSIC	HZG	CSIC	1	190	0.20
CSIC	HZG	FC	1	190	0.22
CSIC	HZG	FC	3	230	0.55
FC	HZG	FC	4	260	0.07

Table 13.2 summarises the most representative EMI shielding results obtained by ECCOSORB at 10 Hz of the developed foams. The results show clearly that the addition of CSIC CNTs gives better conductivity. PEG functionalised MWCNTs raised even further the conductivity of the samples. The sample with CSIC-MWCNT-PEG dispersed by CSIC almost met the conductivity requirement for ECCOSORB of 0.4 S/m at a filler loading of only 0.6% in polyol.

Appendix C

13.5. Toxicity of Chemicals

Table 13.3 List of chemicals with GHS symbol, H- and P-data.

Substances	GHS Symbol	Hazard Statements	Precautionary Statements
Chloroform	GHS02, GHS07, GHS09	H302, H332, H315, H319, H351,H361d H336, H373	P261, P281, P305+P351+P338
Copper(I) bromide	GHS07	H315-H319-H335	P261-P305 + P351 + P338
Dichloromethane	GHS07, GHS08	H315-H319-H335-H336-H351-H373	P261-P281-P305 + P351 + P338
N,*N*-Dimethylformamide	GHS02, GHS07, GHS08	H226-H312 + H332-H319-H360D	P201-P280-P305 + P351 + P338-P308 + P313
Ethanol	GHS02, GHS07, GHS08	H225-H302-H371	P210-P260
Glycidyl POSS®	–	–	–
Glycidyldimethylsilyl POSS®	–	–	–
Hydrochloric acid	GHS05, GHS07	H314-H335	P261-P280-P305 + P351 + P338-P310

Magnesium sulfate	–	–	–
Methanesulfonyl chloride	GHS05, GHS06	H300 +H310 + H330-H314-H335	P260-P264-P280-P284-P301 + P310-P302 + P350
Multiwalled carbon nanotube	GHS02, GHS07 GHS08, GHS13	H319, H335,	P261, P305+P351+P338
PEBAX® MH 1657	–	–	–
PEBAX® 2533	–	–	–
PEG POSS®	–	–	–
PolyActive™ 1500PEGT77PBT23	–	–	–
PolyActive™ 3000PEGT77PBT23	–	–	–
PolyActive™ 4000PEGT77PBT23	–	–	–
Poly(ethylene glycol)	–	–	–
Sodium azide	GHS06, GHS09	H300-H410	P264-P273-P301 + P310-P501
Sodium chloride	–	–	–
Sodium hydroxide	GHS05	H314	P280-P305 + P351 + P338-P310
Tetrahydrofuran	GHS02, GHS07, GHS12	H225, H319, H351	P210, P261, P305+P351+P338
Tetrabutylammonium iodide	GHS07	H302-H315-H319-H335	P261-P305 + P351 + P338
Thionyl chloride	GHS03, GHS07, GHS08	H302, H331, H314	P261, P280, P305+P351+P338
Toluene	GHS02, GHS07, GHS08	H225-H304-H315-H336-H361d-H373	P210-P261-P281-P301 + P310-P331
Triethylamine	GHS02, GHS05, GHS07	H225-H302-H312-H314-H332	P210-P280-P305 + P351 + P338-P310

List of Publications

1) “Influence of poly(ethylene glycol) segment length on CO_2 permeation and stability of PolyActive™ membranes and their nanocomposites with PEG POSS®”; Md. Mushfequr Rahman, Volkan Filiz, Sergey Shishatskiy, Clarissa Abetz, Prokopios Georgopanos, Silvio Neumann, Muntazim Munir Khan, Volker Abetz, **ACS Applied Materials and Interfaces** (2014) DOI: 10.1021/am504223f.

2) “Functionalization of POSS nanoparticle and fabrication of block copolymer nanocomposite membranes for CO_2 separation”; Md. Mushfequr Rahman, Volkan Filiz, Muntazim Munir Khan, Bahadir N. Gacal, Volker Abetz, **Reactive and Functional Polymers** (2014) DOI: 10.1016/j.reactfunctpolym.2014.07.006.

3) “Influence of temperature upon properties of tailor made PEBAX® MH 1657 nanocomposite membranes for post combustion CO_2 capture”; Md. Mushfequr Rahman, Sergey Shishatskiy, Clarissa Abetz, Prokopios Georgopanos, Silvio Neumann, Muntazim Munir Khan, Volkan Filiz, Volker Abetz; **Journal of Membrane Science** (2014) 469, 344-354.

4) “Synthesis, characterization and gas permeation properties of anthracene maleimide-based polymers of intrinsic microporosity”; Muntazim Munir Khan, Gisela Bengtson, Silvio Neumann, Md. Mushfequr Rahman, Volker Abetz, Volkan Filiz, **RSC Advances** DOI: 10.1039/c4ra03663h.

5) “PEBAX® with PEG functionalized POSS as nanocomposite membranes for CO_2 separation”; Md. Mushfequr Rahman, Volkan Filiz, Sergey Shishatskiy, Clarissa Abetz, Silvio Neumann, Sabrina Bolmer, Muntazim Munir Khan, Volker Abetz; **Journal of Membrane Science** (2013) 437, 286-297.

6) “Enhanced Gas Permeability by Fabricating Mixed Matrix Membranes of Functionalized Multiwalled Carbon Nanotubes and Polymers of Intrinsic Microporosity (PIM)”; Muntazim Munir Khan, Volkan Filiz, Gisela Bengtson, Sergey Shishatskiy, Md. Mushfequr Rahman, Jelena Lillepaerg, Volker Abetz; **Journal of Membrane Science** (2013) 436, 109-120.

7) “Cross-linking of Polymer of Intrinsic Microporosity (PIM-1) via nitrene reaction and its effect on gas transport property”; Muntazim Munir Khan, Gisela Bengtson, Sergey Shishatskiy, Bahadir N. Gacal, Md. Mushfequr Rahman, Silvio Neumann, Volkan Filiz, Volker Abetz; **European Polymer Journal** (2013) 49, 4157-4166.

8) “Functionalized carbon nanotubes mixed matrix membranes of polymers of intrinsic microporosity for gas separation”; Muntazim Munir Khan, Volkan Filiz, Gisela Bengtson, Sergey Shishatskiy, Md. Mushfequr Rahman, Volker Abetz; **Nanoscale Research Letters** (2012) 7, 504.

9) “PEG Functionalized POSS Incorporated PEBAX Nanocomposite Membranes”; Md. Mushfequr Rahman, Volkan Filiz, Sergey Shishatskiy, Silvio Neumann, Muntazim Munir Khan, Volker Abetz; **Procedia Engineering 44 (Euromembrane Conference 2012)** (2012) 1523-1526.

10) “Functionalized Carbon Nanotube Mixed Matrix Membranes of Polymers of Intrinsic Microporosity (PIMs) for Gas Separation”; Muntazim Munir Khan, Volkan Filiz, Gisela Bengtson, Md. Mushfequr Rahman, Sergey Shishatskiy, Volker Abetz; **Procedia Engineering 44 (Euromembrane Conference 2012)** (2012) 1899-1901.

Curriculum Vitiate

Md. Mushfequr Rahman

Contact details:

Helmholtz Zentrum Geesthacht (HZG)

Max-Planck Street 1, 21502 Geesthacht, Germany.

Email: mushfequr.rahman@hzg.com

mushfeq007@gmail.com

Cell Phone No: +49015225685543

Office Phone No: +49 (0) 4152 87-2453

Present address: Wald Street 5, 21502 Geesthacht, Germany

Educational qualification:

09/2014 – till date	Post-doctoral researcher, Department of Polymer Synthesis, Institute of Polymer Research, HZG, Germany
02/2011 – 07/2014	PhD Student, Department of Polymer Synthesis, Institute of Polymer Research, HZG, Germany
2009 – 2010	Master of Science in Applied Chemistry & Chemical Engineering, University of Dhaka, Bangladesh
2002 – 2008	Bachelor of Science in Applied Chemistry & Chemical Engineering, University of Dhaka, Bangladesh
2002	Higher Secondary Certificate, Ispahani Public School & College, Chittagong, Bangladesh
2000	Secondary School Certificate, Ispahani Public School & College, Chittagong, Bangladesh

Personal Information:

Father's Name :	Md. Shafiqur Rahman
Mother's Name :	Kaniz Zahra Rahman
Spouse Name :	Nazia Noor
Date of Birth :	29th Octoberber, 1984.
Permanent address :	5/4, 1-C, Mirpur, Dhaka, Bangladesh.
Nationality :	Bangladeshi (By birth)
Religion :	Islam

Declaration on oath

I hereby declare that this doctoral thesis has never been submitted in the present form or smilar to any other University or board of examiners. I declare under the penalty of perjury, that the present dissertation was prepared independently and solely by me maintaining the Rules of Good Scientific Practice of the German Research Foundation.

Md. Mushfequr Rahman